VARIABLE FLUX, DC BUS VOLTAGE CONTROL, AND SELF-SENSING FOR FLUX INTENSIFYING IPMSM

by

Chen-Yen Yu

A dissertation submitted in partial fulfillment of the

requirements for the degree of

Doctor of Philosophy

(Mechanical Engineering)

at the

University of Wisconsin – Madison

2014

Date of final oral examination: 5/6/14

The dissertation is approved by the following members of the Final Oral Committee:

Lorenz, Robert D., Professor, Mechanical Engineering

Duffie, Neil A., Professor, Mechanical Engineering

Jahns, Thomas M., Professor, Electrical and Computer Engineering

Sarlioglu, Bulent, Assistant Professor, Engineering Professional Development

Han, Yehui, Assistant Professor, Electrical and Computer Engineering

Acknowledgements

First of all, I would like to thank Prof. Lorenz, for giving me the opportunity to study in WEMPEC and his guidance and support during my research. His knowledge, enthusiasm and energy guide me through all the challenges in my research. As he always asks me, "Do you learn something? Do you have fun?" Yes! I really learn a lot and have lots of fun when working with you during all the 5 years.

Second, I would like to thank the committee members, Professor Thomas M. Jahns, Professor Neil A. Duffie, Professor Yehui Han and Professor Bulent Sarlioglu for all the comments and suggestions on the thesis. It's always fun to discuss experts like all of you.

Third, I would like to thank the whole WEMPEC family for making my life in Madison an enjoyable and unforgettable experience. The discussions with you always inspire me and remind me of the meaning of Ph.D: love of wisdom. I would like to thanks for WEMPEC fellow graduate students, especially Larry, Wei, Di, Yang, James, Phil, Yichao, Wanjun, Wenying, Seth Avery, Tyler, Chris, Bryan, Caleb, Brent, Teng Apoorva, Jiyao , Ruxiu, Brian, Hao, Kang, Yuying, Shang-Chuan, Yukai, Gilsu, and Seth McElhinney. I would also like to thank my Nissan colleagues, Yuichi, Takashi Kato, Jun Tamura, Takashi Kato, Takashi Fukushige, and Kensuke Sasaki for providing lots of industrial experiences and useful insights.

Finally, I would like to thanks to my parent’s and my family support, without them nothing would be possible. I would like to give a special thanks to my wife, Wen-Hsin. With her support and encouragement, I can finally go through this journey. In the end, I would like to present this thesis to our future daughter, Summer; your coming gives me the final barrel of fuel to accomplish my degree.

Abstract

Having good dynamic performance, power conversion properties, and a low cost are always goals for every drive system. This research follows these goals as motivation and focuses on control methods for FI type PM machine drives. Several approaches are investigated to achieve these goals. First, injection signals selections, effects of DC bus voltage, and control methods for FI-IPMSM are explored to improve the position self-sensing accuracy and drive reliability. Secondly, it is shown that reducing DC bus voltage used during low speed condition will improve inverter efficiency and self-sensing performance. However, the required DC bus voltage value is difficult to calculate precisely due to machine parameter estimation errors and spatial harmonics. An online optimum DC bus voltage calculation is proposed to solve these issues while achieving energy savings. Finally, this research also focuses on control methods of VFI-IPMSM: flux manipulation methods, MS selection methods to achieve energy savings and MS estimation. The conventional MS manipulation methods cause pulsating torque or require lookup tables, which rely on time consuming experiments. New control methods featuring relatively low sensitivity to parameter estimation errors and smooth torque control during magnetization manipulation are presented. A MS manipulation method to achieve loss savings is proposed and the VF machine is shown to have a better loss saving properties compared to a commercial IPM machine. The MS information is shown to be the key for properly selecting the MS to achieve energy savings. A new MS self-sensing methodology is proposed by using high frequency injection and achieves reliable MS estimation. Ultimately, energy savings are achieved by properly manipulating MS with the correct MS estimation information.

Table of Contents

Nomenclature

Symbol	*Definition*
$f_{dq} \equiv f_d + \boldsymbol{j} f_q$	definition of a complex vector
$\boldsymbol{j}$	complex number operator $\sqrt{-1}$
β	current angle. An angle by which the stator current leads the q-axis.
ξ	saliency ratio. $\frac{L_d}{L_q}$ for IPM; $\frac{L_q}{L_d}$ for FI-IPM
λ_{PM}	magnet flux linkage
ω_e	synchronous electrical frequency [rad/sec]
ω_r	rotor electrical frequency [rad/sec]
ω_f	fundamental electrical frequency [rad/sec]
ω_c	carrier electrical frequency [rad/sec]
θ	Angular position [rad]
ϕ	Phase offset [rad]
ΣL	average transient inductance
ΔL	differential transient inductance

Subscripts	*Definition*
d	d-axis component
q	q-axis component
s	quantity in stator side
pc	positive sequence component
nc	negative sequence component

Superscripts	*Definition*
s	quantity in the stationary reference frame
r	quantity in the rotor reference frame
e	quantity in the synchronous reference frame

Abbreviations	*Definition*
EMF	electromotive force
MMF	magnetomotive force
FW	flux-weakening
FI	flux-intensifying
PM	permanent magnet
SM	synchronous machine
IPM	interior permanent magnet
FEA	finite element analysis
MS	magnetization state
VF	variable flux
VMS	variable magnetization state
VLF	variable leakage flu

Introduction

I 1. Project Overview

This thesis presents position self-sensing control methods and the integration of self-sensing and a variable DC bus drive on FI-IPMSMs. It also demonstrates MS manipulation methods, MS selection methods to achieve energy savings, and MS estimation methods for VFI-IPMSMs.

The injection signal selection and decoupling techniques for improving self-sensing on FI-IPMSMs are one of the major the focuses of the project. In saliency-based self-sensing control techniques, a crucial issue is the tracking error caused by non-linear inverter effects and the distortion of the saliency image due to machine saturation. Therefore, robust and load insensitive techniques are important for tracking saliency images. Three high frequency vector signal injection methods (rotating vector, pulsating, square wave) are used to investigate the position self-sensing performance of a FI-IPMSM. A 90 degree offset is observed with the square wave injection for FIP-IPMSMs. An alternative square wave injection method to estimate FI-IPMSM rotor position is presented. Both simulation and experimental results show that the estimation accuracy and system robustness are improved with the alternative square wave injection. Tracking disturbances caused by cross-coupling inductances, magnetic saturation, and inverter dead-time effects are investigated and associated decoupling techniques are presented. With proper injection signal selection, decoupling techniques, and an accurate estimation method, reliable rotor position estimation capability for FI-IPMSMs can be achieved in simulation and is demonstrated experimentally. Furthermore, integration of self-sensing with variable DC voltage is also investigated. It is experimentally shown that self-sensing performance with a variable DC bus voltage can achieve better position estimation than fixed DC bus voltage.

Secondly, it is known from an empirical inverter model that inverter system efficiency can be improved with decreased DC voltage. This has also been demonstrated experimentally. The key issue is how to decide the optimum DC bus voltage, such that the machine can simultaneously achieve desired output torque and minimum losses. With the physical model of the machine, an optimum DC bus voltage at each operating point can be selected to achieve minimum losses. However, DC bus calculation errors can occur due to inductance saturation, machine parameter estimation errors, or temperature effects. The existing method requires time-consuming experiments to create a lookup table for optimal DC bus voltage. Therefore, an online method to calculate the optimum DC bus voltage in variable DC bus voltage drive system is proposed. The machine parameter estimation errors and spatial harmonics in the machine cause calculation errors for the required DC bus voltage. A voltage disturbance state filter (VDSF) is used to mitigate the voltage calculation errors. Both the simulations and experimental results show that the proposed method can calculate the nearly optimum DC bus voltage even with the presence of machine spatial harmonics or parameter estimation errors.

Thirdly, a design of a variable flux, IPMSM which exploits magnets with low coercive force, and a FI-IPM type rotor has shown potential benefits in reducing losses in applications with considerable cyclical partial loads [1, 2]. Due to an ability to vary magnetization state, the magnetic flux can be changed to obtain a suitable balance between copper loss and iron loss that yields a reduction in total losses for any given torque and speed operating condition. In general, the magnetization state can be lowered at low torque conditions such that iron losses can be decreased. For high-speed conditions, by operating at lowered magnetization levels, excessive copper loss associated with flux-weakening current can be reduced or eliminated as well. With an FI-IPM type rotor, the effect of demagnetizing load current can be reduced and positive

$+I_d$ can be applied to produce positive reluctance torque and maintain MSat the same time.

From the above description, it follows that the machine efficiency can be improved by changing the magnetization state. The next important issue is how to dynamically change magnetic flux during loaded conditions. Since a magnetization/demagnetization current must be injected into the machine to change the magnetization state, therefore, a significant torque change (a pulsating torque) can be produced. An evaluation of the relationship between pulsating torque and injected current should be done to examine the machine response. Furthermore, a method should be developed to solve this issue.

To achieve smooth transient torque performance during magnetization state manipulation as discussed above, the machine properties and magnetization state manipulation methods of the VFI-IPMSM are investigated in this research. It is experimentally demonstrated that d-axis current can be used to successfully control the magnetization state. Different control methods for the magnetization state manipulation are discussed as well. It has been shown that a pulsating torque is generated if a magnetization pulse current is injected into a machine. To solve this issue, an observer-based current decoupling control method is proposed to achieve smooth torque output during the magnetization state manipulation process.

Fourthly, to change the MS for reducing overall loss, a current pulse must be injected into the machine. Although the additional loss during MS change can be reduced by reducing the total duration of the current pulse injection, there is still additional copper loss. Therefore, manipulating the MS too frequently would result in larger net losses, as the loss caused by the magnetization current would be greater than the reduced losses from optimal MS. Thus, a control method is required to balance the additional loss due to

changing MS and the loss saving from using the optimal MS for the torque and speed operating condition.

An optimum magnetization state manipulation for loss minimization is proposed in this research. First of all, efficiency contours for different magnetization states of the low coercive force magnets are obtained by a series of experiments. The contours are then compared with the finite element analysis (FEA) simulation results. The discrepancy between the experiment and the simulation is investigated. The designed machine shows the benefit of improving efficiency when magnetization state is optimally operated. Subsequently, with the obtained efficiency maps, the losses over a driving cycle are simulated. An algorithm to properly change the magnetization state during the driving cycle is introduced. As a result, changing the magnetization state is evaluated in terms of loss minimization over a driving cycle.

Finally, variable flux machines are shown to have total loss reduction with appropriate MS manipulation. To manipulate the MS to a desired level, the magnitude of the current pulse can be chosen according to an offline calibration table. The calibration table can be obtained by measuring EMF voltage after various current pulses under various speed conditions. However, this type of off-line technique requires additional effort to deal with MS variation due to imperfections from manufacturing (individuality of the magnet property or magnet corrosion effects), thus an on-line technique is preferable. A flux observer could be a better solution for MS estimation. However, flux observer methods work well only in medium and high speed conditions and estimation accuracy deteriorates in zero/low speed conditions as the EMF signal reduces with decreasing speed. Therefore, a robust MS estimation method suitable for zero/low speed conditions is needed.

A methodology is proposed by using HF injection techniques combined with closed-loop current vector control (CVC) for MS estimation at zero/low speed conditions,

To combine these, a fundamental current observer (FCO) and a synchronous reference frame filter (SRFF) were implemented to separate the fundamental frequency component from the HF component, so that the impact of EMF at rotating conditions on MS estimation accuracy can be reduced. In addition, the immunity to noise could be improved since the vector tracking technique is used for obtaining the amplitude of HF current instead of using a single point current detection method.

I 2. Research contributions

The main contributions of the research is the development a general control methodology for flux intensifying machines including position self-sensing, optimum DC bus selection for variable DC bus voltage, and variable flux control. More specifically the contributions can be summarized as following.

1. Development of a rigorous self-sensing control methodology for FI-machines
2. Development the methodology for online optimum DC bus voltage selection for variable DC bus voltage system
3. Development of smooth torque control methodologies during magnetization manipulation process
4. Development of MS selection method to achieve loss saving
5. Development of MS self-sensing methodology with high frequency injection
6. Assessment of the advantages, disadvantage and limitations to the methodologies mentioned above.

I 3. Overview of chapters

The thesis is divided into seven parts:

In Chapter 1, the state-of-the-art of self-sensing, direct torque control, variable DC bus voltage drive and variable flux machine are reviewed.

In Chapter 2, three kinds of injection signals are used to analyze self-sensing performance of FI-IPMSM. An alternative rotor position estimation method is proposed to increase the accuracy and robustness for self-sensing control. Variable DC bus voltage control for self-sensing is also presented.

In Chapter 3, a control method to calculate nearly optimum DC bus voltage with low sensitivity to machine estimation parameters is presented. The effectiveness of proposed method is evaluated with simulation and experimental results.

In Chapter 4, smooth torque control of VFI-IPMSM during magnetization manipulation process is presented. It is shown that the magnetization state can be changed by the proposed method without pulsating torque.

In Chapter 5, the magnetization selection methodology for loss minimization is presented. By using the proposed hysteresis controller, the loss minimization can be achieved.

In Chapter 6, magnetization state estimation without using voltage sensors is presented. It is shown that a reliable magnetization state estimation can be achieved without using voltage sensors.

In Chapter 7, the key conclusions and outlines for future work are summarized.

Chapter 1 - The State-of-the-Art Review

This chapter reviews the-state-of-art review in current solutions for both self-sensing control and loss minimization control method with fix DC bus voltage and adjustable DC bus voltage. First, major self-sensing techniques are presented and discussed. The rotor position estimation schemes include saliency tracking method, back EMF tracking, and other types of self-sensing techniques. Challenge and implementation at low speed self-sensing control are a major focus. Secondly, several loss minimization control methods with fix and variable DC bus voltage are introduced. Advantages and limitations of each method are discussed. Thirdly, characteristics of variable flux machine are discussed. The impact of flux manipulation method, machine's energy saving, and pulsating torque will be the major focus. Finally, opportunities for this research are proposed.

1.1 Permanent magnet synchronous machine types

PMSMs have a wide variety of design configuration. For the stator, distributed stator windings are usually used since they are easy to achieve sinusoidal flux distribution. The advantage of sinusoidal flux distribution is that machine has less ripple torque and iron loss induced by harmonic. Concentrated winding designs also have attracted lots of attention recently due to short ending winding (i.e. low copper loss), short machine total length and higher slot fill factor [3-6]. However, the major drawback for concentrated winding motor is its large torque ripple and reducing the torque ripple is still a very important research topic.

According to the rotor configuration; the PMSM can be divided into three categories as shown in Fig. 1.1. The first one is surface PM synchronous machine (SPMSM) with magnets glued in the surface of the rotor. The second one is interior PM synchronous machine (IPMSM) with magnets inset or buried in the rotor. Recently, FI-IPMSM starts to attract attentions because they can achieve both good self-sensing performance and power conversion. In the research, the FI-IPMSM with distribution winding will be the main focus.

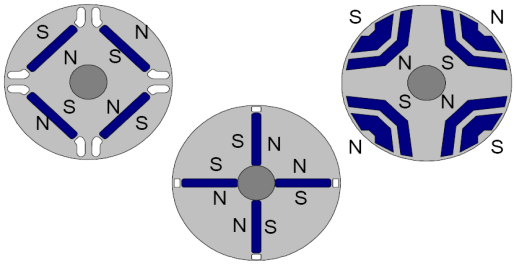

(a) SPM [7]

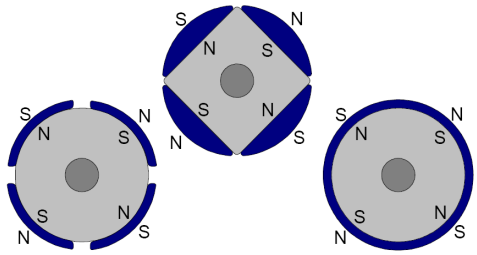

(b) IPM machines [7]

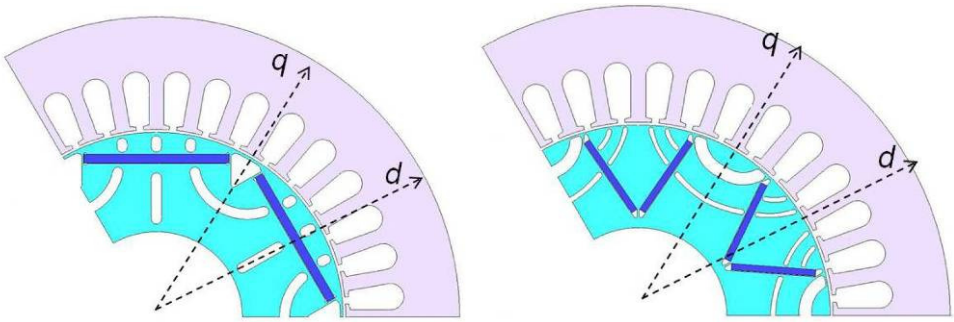

(c) FI-IPMSM[8, 9]

Fig. 1.1 The geometry features of three different kinds of motor

In this chapter, two major techniques for the self-sensing control are reviewed. One is based on the fundamental excitation. It is also referred to as the back electromotive force (EMF) tracking. Another trend is using the position-dependent saliency for position estimation. Their advantages and limitations and implementation issues will be reviewed in the following sections.

1.2 Self-sensing control for medium and high speed

The basic idea of back-EMF tracking is to use machine back EMF to find flux position. The position information embedded in back EMF can be extracted from the machine model in either a synchronous (1-1) or stationary reference frame (1-2). To have better flux space vector, system identification of stator resistance and inductance are usually required.

$$v_{dqs}{}^{r} = \begin{Bmatrix} v_{ds}{}^{r} \\ v_{qs}{}^{r} \end{Bmatrix} = \begin{bmatrix} r_s + pL_d & -\omega_r L_q \\ \omega_r L_d & r_s + pL_q \end{bmatrix} \begin{Bmatrix} i_{ds}{}^{r} \\ i_{qs}{}^{r} \end{Bmatrix} + \begin{bmatrix} 0 \\ \omega_r \lambda_{pm} \end{bmatrix} \tag{1-1}$$

$$v_{dqs}{}^{s} = r_s \begin{bmatrix} i_{ds}^{s} \\ i_{qs}^{s} \end{bmatrix} + p \begin{bmatrix} \Sigma L + \Delta L \cos 2\theta_e & \Delta L \sin 2\theta_e \\ \Delta L \sin 2\theta_e & \Sigma L - \Delta L \cos 2\theta_e \end{bmatrix} \begin{bmatrix} i_{ds}^{s} \\ i_{qs}^{s} \end{bmatrix} + \omega_r \lambda_{pm} \begin{bmatrix} -\sin\theta_e \\ \cos\theta_e \end{bmatrix} \tag{1-2}$$

where $\Sigma L \equiv \frac{L_d + L_q}{2}$, $\Delta L \equiv \frac{L_d - L_q}{2}$

The basic method is to detect the conducting interval of free-wheeling diodes connected in anti-parallel with power transistors[10]. Matsui presents back EMF position estimation methods, which are based on the voltage model and current model [11-13]. An estimated frame shown as Fig. 1.2 is used to estimate flux position. For the voltage model method, the estimated voltage is calculated by transforming the current to the estimated frame and using estimated machine parameter. Because the error is proportional to the sine and cosine of difference between the real and estimated frame, a PI type controller is used to force the error to zero to estimate the rotor position. For the current model method, error between estimated current calculated by current observer and measured current in the estimated rotor reference frame is used to estimate rotor position.

These methods cannot be applied to interior PMSM directly without approximation because the complication of mathematical model. However, approximation could result in instability of the system.

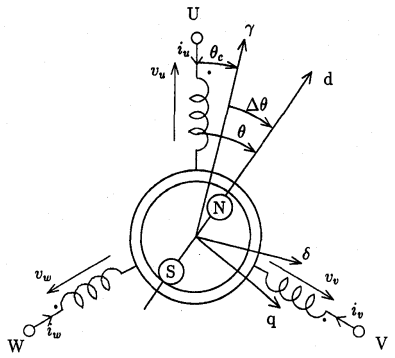

Fig. 1.2 Analytical model of PM brushless DC motor[11].

Later, an extended electromotive force Model is proposed to solve this problem [14-16]. It solves the complex mathematical model problem by manipulating the machine model. Arctan method is used to estimate the machine position. To improve the phase lag property, Kim and Lorenz used an tracking observer to achieve zero phase lag property[17]. They compare several different estimation methods and show that the tracking observer can achieve zero phase lag and good tracking performance. The structures of different estimation methods are shown as Fig. 1.3.

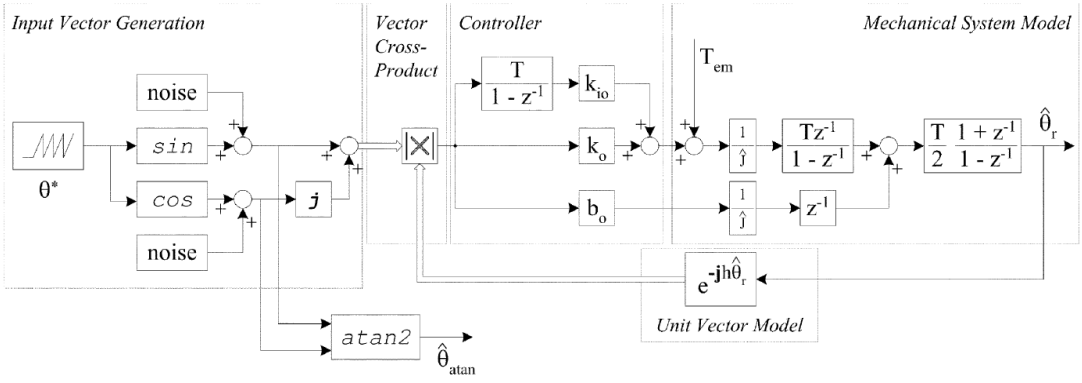

Fig. 1.3 Block diagram of the simulation comparing (a) observer-based, (b) state-filter-based, and (c) arctan-calculation-based position estimation. [17]

The machine parameters are required in all of the methods discussed above. Since the inductance value changes with the magnetic saturation level, the position estimation is also affected. The accuracy can be increased by using the on-line parameter identifications and adaptive parameter adjustment of the controller. It is similar to the

model reference adaptive system (MRAS). Morimoto proposed a system identification method which identified machine and inverter parameters at standstill to improve the self-sensing performance. The parameter estimations include the machine resistance, the d-axis and q-axis inductances, inverter turn on resistance and the voltage error which is caused by the dead time of the inverter[18]. The flux linage is estimated under the self-sensing operation based on the extended EMF estimation method. The same research group also proposes a nonlinear inverter model and a voltage compensation method for voltage errors caused by inverter nonlinearity to improve the accuracy and the stability[19]. The major drawbacks of the PM flux based tracking method are 1) the parameter estimation accuracy 2) Back-EMF magnitude become very low or zero in the low and zero speed 3) the disturbance rejection ability degrade as the speed decrease. Henry and Lorenz demonstrated that even the command tracking can be achieved, the system disturbance rejection property degraded seriously [20]. As can be seen in the Fig. 1.4, the machine dynamics stiffness in the low frequency became very low as machine operated at 25 [rad/sec]. The stiffness of the machine was very weak in the low speed region which caused difficult of external force rejection. As a result, saliency-based method in the low or zero speed is preferred and will be discussed in the next section.

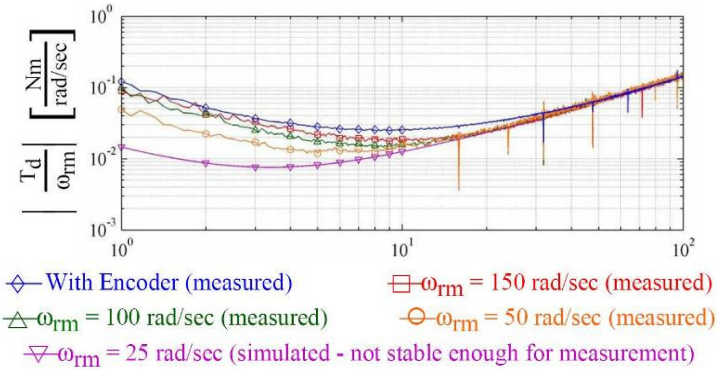

Fig. 1.4 Experimental dynamic stiffness for
closed loop speed control with encoder and back-EMF tracking feedback for
varying ω_{rm} with a span from 0 – 100 Hz and f_b = 0.0833 Hz[20]

1.3 Self-sensing control for zero and low speed

The major drawbacks of back EMF method for self-sensing are the signal decrease with the drop of machine speed and the weak dynamic stiffness in the low speed conditions. It causes the difficulty of position estimation in the low speed region. Therefore, high frequency injection methods were proposed to extract the machine position in the low speed region. These techniques use machine inherent saliencies for the position estimation. To achieve high bandwidth position estimation in the zero–low speed range, it requires a position dependent saliency, persistent excitation and proper signal processing and state estimation. First of all, the saliency normally exists in machines, but the saliencies reduce in the high load conditions because of saturation. Secondly, the excitation signal acts like examination tool. The excitation should have sufficiently high frequency or sampling to have high bandwidth position estimations. It also makes the low fundamental signal can be easily separated from the high frequency signal. Last but not least, the position information is extracted from the response signals by signal processing. Therefore, the performance of the filters and fundamental current observer directly affects the estimation bandwidth. Normally, three command methods: Arctan function, state filter and state observer are usually used. Several methods and their advantages and limitation were reviewed and discussed in this section.

1.3.1 ***Rotating vector injection***

A rotating vector high frequency injection method is first proposed by Jansen and Lorenz[21]. This method injects the rotating vector (voltage/current) in the stationary frame. Since the voltage source inverter is usually used in normal drive, the voltage injection is usually used instead of current. It has been demonstrated that the results of two methods are analogous[22]. If a balance rotating voltage is injected in the stationary frame, the negative sequence component of the induced current is a phase modulated of

the saliency model which is the second harmonic of the rotor position. The position can be estimated by using tracking observer to track the phase of negative sequence current[23]. The illustration of rotating vector method is shown as Fig. 1.5 and Fig. 1.6.

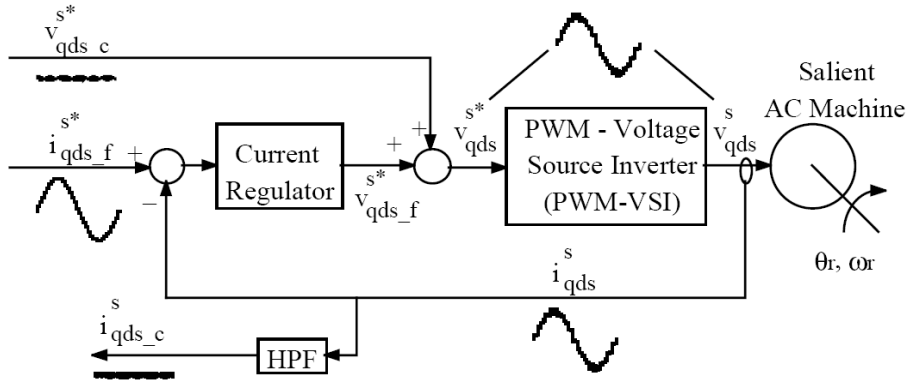

Fig. 1.5 A high-frequency signal injection scheme utilizing a PWM voltage source inverter with high pass filter to synthesize both fundamental and high-frequency components[23]

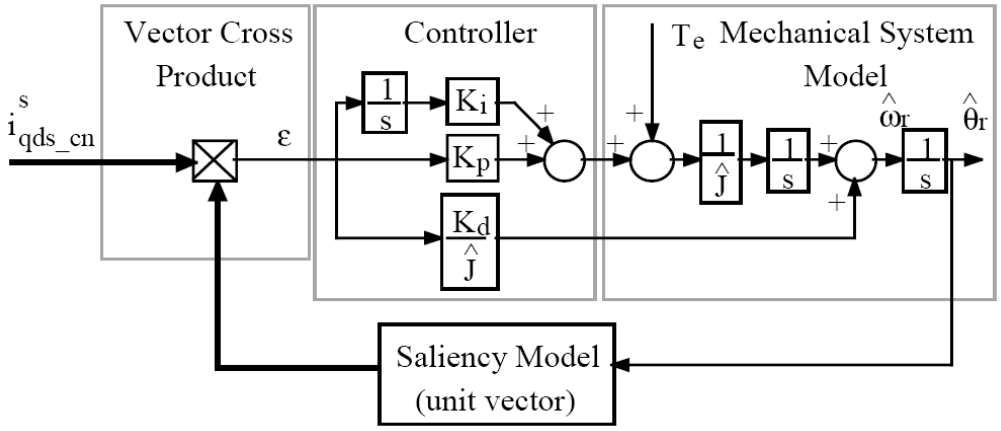

Fig. 1.6 Vector Cross-Product Observer with a Unit Vector Saliency Model[23]

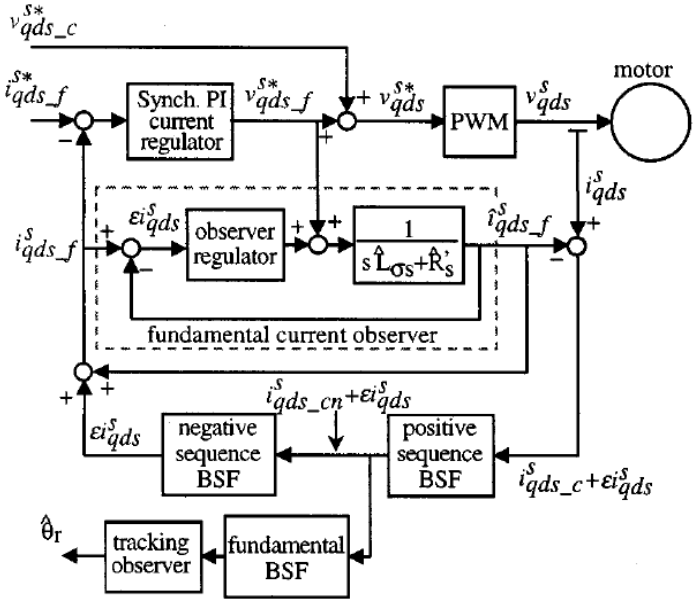

Fig. 1.7 Dynamic elimination of the fundamental current by means of a fundamental current observer [24]

Briz *et al.* further investigate that harmonics close to carrier frequency can be introduced by the fundamental current transients. A fundamental current observer was proposed to decouple the harmonics and thereby the accuracy of the estimated rotor position or flux angle is increased[24].

Consoli uses a peak detection of the resulting high frequency current to estimation the rotor position [25, 26]. However, this method is relatively sensitive to noise.

The nonlinearity effect including multi-saliency [23, 27], induced saliency because of saturation[28], and transient resistance will be discussed in the subsequent section. Their decoupling techniques is also addressed[29].

1.3.2 ***Pulsating vector injection***

Corley and Lorenz first propose injecting carrier pulsating voltage vector in estimated synchronous frame in 1998[30] as shown in Fig. 1.8. The induced current is demodulated to a signal proportional to the estimated position error. The signal is further feed into a rotor position observer to have a high–bandwidth position estimation. Other research group injected the pulsating vector in the estimated d-axis synchronous frame only [31-34] or other axis [35]. Aihara use FFT to extract rotor position from induced current. Sul's research group demodulates the induced current and then uses a PI type controller to extract rotor position [32, 33]. The procedure is shown as Fig. 1.10.

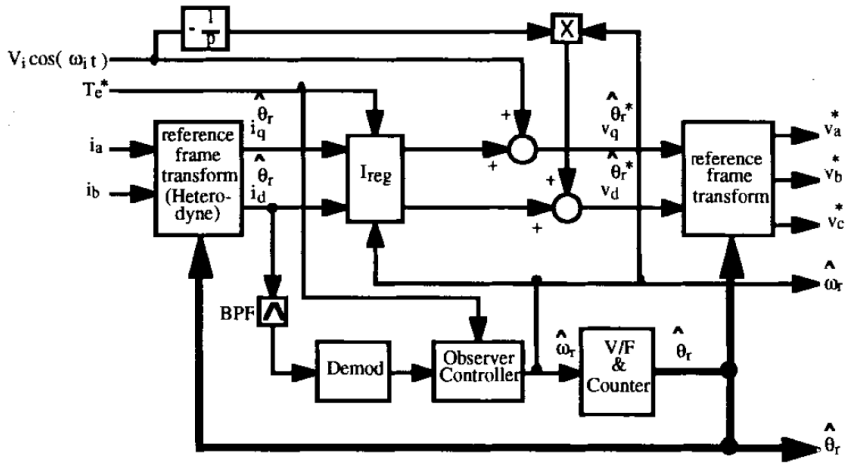

Fig. 1.8 Pulsating carrier signal in estimated frame[30]

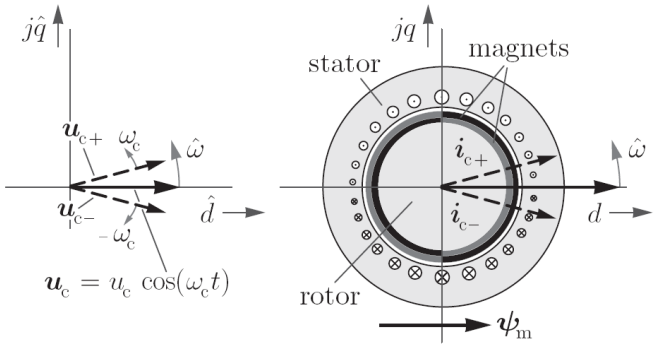

Fig. 1.9 Pulsating carrier signal is composed by superposition of 2 rotating carrier signals[34]

Comparing to the rotating vector method which injects a rotating vector in the stationary frame, the pulsating vector injection method can be represented as superposition of two rotating vector injected in the estimated rotating frame. The carrier signal is injected in the estimated frame which is dynamically adjusted by the estimated rotor position. Once the estimated frame is oriented to the real rotating frame, the rotor position can be estimated. The pulsating vector is shown as Fig. 1.9. Since an additional high frequency signal is injected, the torque ripple would be an important issue. In [36], the author claim that once the position is tracked (i.e. estimated rotor flux angle coincides with the actual angle), virtually no ripple torque, no vibration, and less audible noise caused by the d-axis injected signal. The reason is that d-axis current normally doesn't contribute to torque production. As a result; d-axis voltage injection might be better for torque ripple reduction and power conversion reservation. The detailed comparison has not been investigated and is an important issue for many applications.

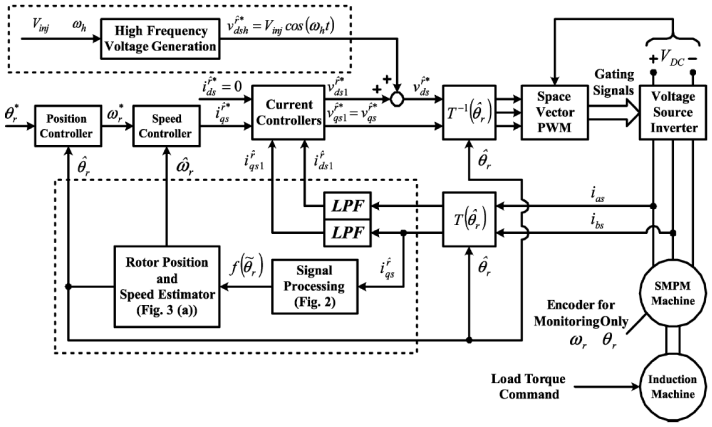

(a) Block diagram of self-sensing drive system of an SMPM machine

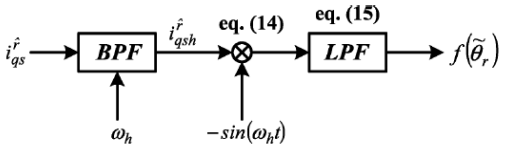

(b) Block diagram of signal processing)

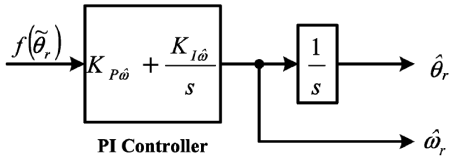

(c) PI regulator and integrator. for rotor position and speed estimation

Fig. 1.10 Implementation of self-sensing block diagram with d-axis pulsating injection [33]

1.3.3 ***Square wave injection***

Recently, square-wave type voltage injection is proposed [37-43]. A relatively high frequency injection (5 kHz) is used and the authors claim that no low pass filter is required in this method; therefore, high bandwidth motion controller is achieved[38]. Hammel and Kennel propose a demodulation process which uses a linear and quadratic term to model the induced current. The estimate carrier current can be obtained after 4 PWM cycle then the rotor position is estimated by the carrier frequency. The illustration of resulting current is shown as Fig. 1.11 and the system diagram is shown in Fig. 1.12 [44]. Sul's research group proposed different demodulation method[38, 41]. The current in the stationary frame is used to estimate the rotor position. By taking arctan of stator d- and q-axis current, rotor position can be estimated and a position observer is then used to further have clear estimated rotor position signal.

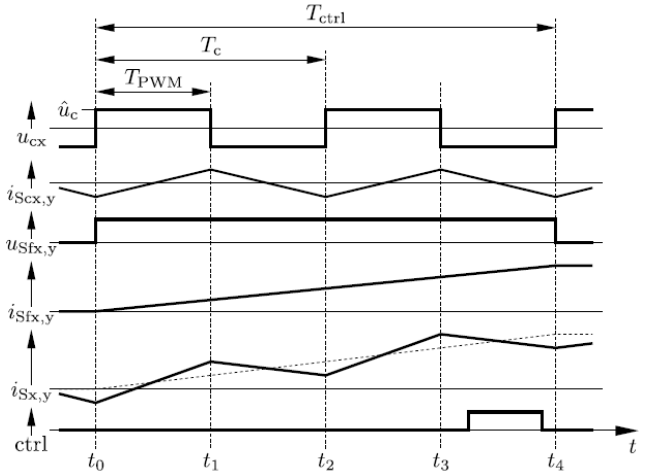

Fig. 1.11 Square wave pulsating vector injection;
Traces from top: carrier voltage, carrier current, fundamental voltage, fundamental current, resulting current, task embodying current controller. All signals are in the estimated reference frame. Current sampling instances are indicated by t0-t4[39]

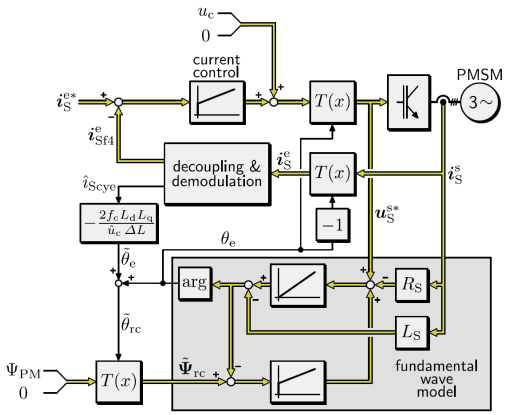

Fig. 1.12 Control scheme for the low frequency range showing carrier injection, separation and demodulation of carrier current [44]

A PWM frequency injection method has been developed recently[43]. By using a non symmetric PWM switching patent in one PWM cycle[45], an addition PWM frequency signal can be injected. This method requires a addition sampling point in every PWM switching cycle to have the information of current response as shown in Fig. 1.13.

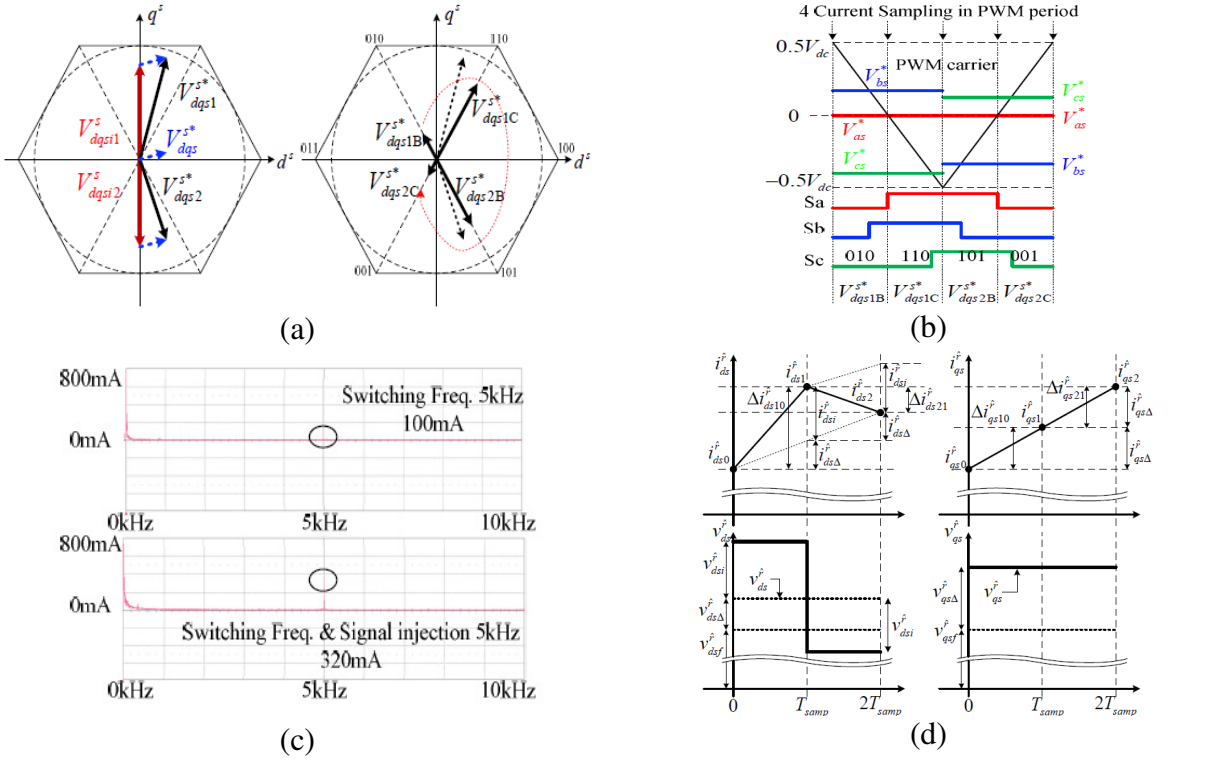

Fig. 1.13 PWM frequency injection voltage reference (a) and a non symmetric PWM sequence to inject high frequency signal (b) response current (c) addition current sampling (d) [43]

The basic fundamental theory of this method is the same as the method of Akagi's research group which has published in late 90's [46-48]. By changing the PWM switching pattern, an additional signal can be injected achieve an addition signal injection. Therefore, they are all based on single point detection method. One of the disadvantages of point detection method is usually from the noise rejection ability. More details of the point detection methods which will be discussed in next section.

For the square wave injection method, since impedance increase with frequency, the injection voltage is increased as the frequency increase. As a result, electrical and acoustic noise is a potential issue and has not been addressed. A PWM frequency injection signal can be used to avoid acoustic noise. However, it is good for acoustic noise but not for EMI noise. In addition, large offset of PWM sequence is required to achieve high injection voltage due to the increased impedance. It results in additional PWM harmonics so the efficiency can be seriously affected.

1.3.4 ***Pulse-based measurement techniques***

As shown in (1-2), the inductance matrix contains the rotor information. The pulse-based use the transient excitation to estimate the machine inductance. The basis is that once a pulse voltage is given to a machine, and the resulting rise of current is measured, the inductance can be estimated from (1-29).

$$v = L\frac{di}{dt} \tag{1-3}$$

Schrödl utilize this characteristic and propose a rotor position estimation method "INFORM" by using a pulse-based excitation and measuring di/dt to estimate inductance variation [49-51]. The rotor position information can be extracted from tracking the variation of inductance. The limitation of this technique comes from current sensor offset and transient resistance. The decoupling technique can be used to achieve further improvement.

Akagi's research team proposed a special PWM modulation which is able to estimate the inductance matrix from the current induced by the PWM harmonic voltage [46-48]. With the induced current, the di/dt and voltage terms can be used to calculate the inductance matrix. Then the estimated rotor position can be obtained from inductance matrix. Since only PWM pattern is changed, no additional signal injection is required in the method. This method could have lower losses since no additional voltage injection is required. Furthermore, the DC bus voltage can be fully used for the fundamental excitation. However, the drawback is that accurate di/dt term is hard to obtain because of noisy environment in drive system [52].

To reduce the noise problem, Juliet and Holtz use a coaxial current transformer to measure *di/dt* which is induced from a special PWM modulation pattern[53]. As Fig. 1.14 shows, less noise current signal can be obtained with this measurement method. No

additional injection is required in this method. To extract the rotor position, *arctan* function is used calculate to the angle of the rotating vector.

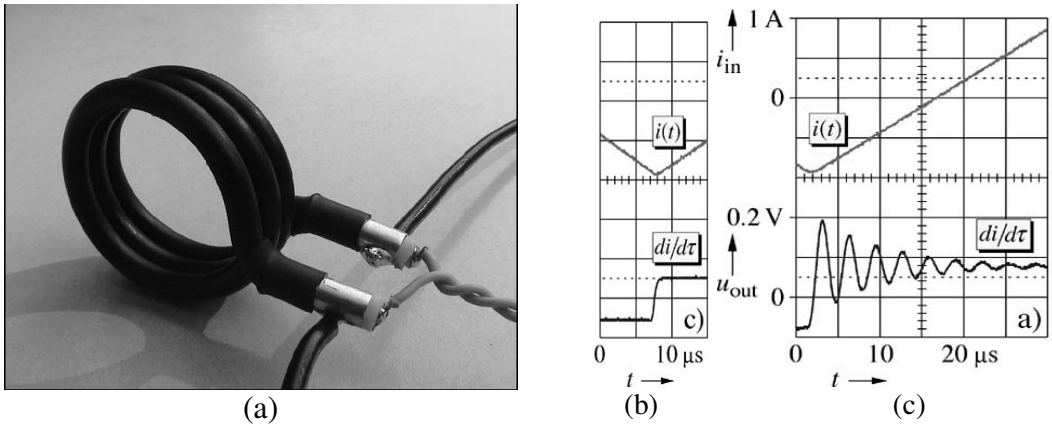

Fig. 1.14 (a) the coaxial current transformer is used to measure *di/dt* Measured signal from coaxial current transformer(b) Measured signal from Rogowski coils [53]

Actually, all the methods mentioned in this section use special PWM pattern to achieve “injection” voltage signal. Though no additional voltage injection is claimed by the authors, the harmonic voltage is indeed injected by the special PWM Pattern. Therefore, the methods can still be classified as one kind of voltage injection with di/dt method for rotor position estimation.

*1.3.5 **Zero sequence based position estimation***

The zero-sequence spectrum also contains saliency information and can be used to extract rotor position information. Researchers investigated rotor position information can be extracted from zero sequence by using carrier voltage injection [54-56]. The idea is that if inductance model includes zero sequence harmonics due to machine unbalanced saliency affect, both the zero voltage for wye connection and the zero current for delta connection contain the position information because of the inductance variations.

The zero sequence voltage in wye connection can be written as:

For h=1,4,7

$$v_{0sc}^{s} = V_{0ch}\cos(\omega_c t - h\theta_e) - V_{0c2h}\cos(\omega_c t + 2h\theta_e) \quad (1\text{-}4)$$

For h=2,5,8

$$v_{0sc}^{s} = V_{0ch}\cos(\omega_c t + h\theta_e) - V_{0c2h}\cos(\omega_c t - 2h\theta_e) \quad (1\text{-}5)$$

The zero sequence current in delta connection can be written as:

For h=1,4,7

$$i_{0sc}^{s} = I_{0ch}\cos(\omega_c t - h\theta_e) + I_{0c2h}\cos(\omega_c t + 2h\theta_e) \quad (1\text{-}6)$$

For h=2,5,8

$$i_{0sc}^{s} = I_{0ch}\cos(\omega_c t + h\theta_e) + I_{0c2h}\cos(\omega_c t - 2h\theta_e) \quad (1\text{-}7)$$

The measurement of zero sequence voltage for wye connection and zero sequence current for delta connection are shown as Fig. 1.15 and Fig. 1.16.

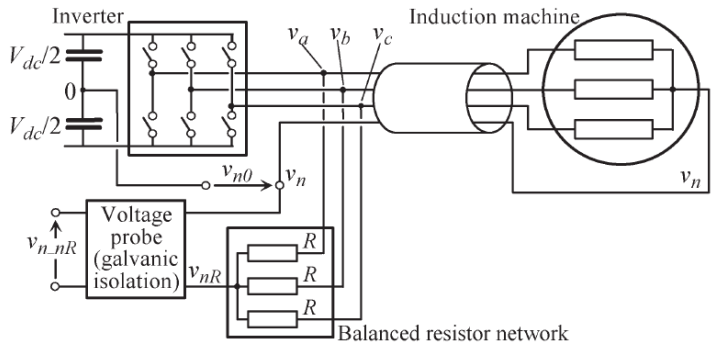

Fig. 1.15 Zero-sequence voltage measurement in a wye-connected machine

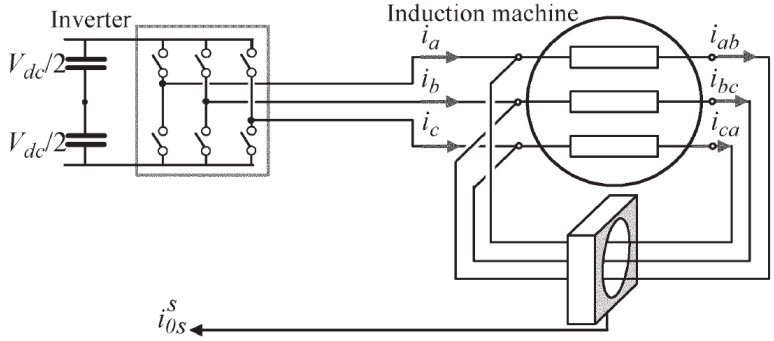

Fig. 1.16 Zero-sequence current measurement in a delta-connected machine

Briz *et al.* compare the three different saliency-based sensorless methods for ac machines: negative-sequence carrier-signal-current-based methods, zero-sequence carrier-signal-voltage-based methods, and zero-sequence PWM-switching-voltage-based[57]. Server observations are made 1) all the methods can be used for rotor position estimation and field orientation and the same restrictions have been observed for all of the methods. Restrictions include rotor-position-dependent saliencies, specifically rotor–stator slotting saliencies, coupling with the stator windings. 2) Saturation-induced saliencies are independent to the zero-sequence-voltage methods. It is an advantage for zero sequence based method. 3) Zero-sequence-voltage carrier-based methods and PWM-switching zero-sequence-voltage-based methods share the same the same physical principles and provide similar results. The differences between them would be the implementation issues.

1.4 Position estimation error caused by non-ideal effect

The models and rotor position estimation methods discussed above ignore nonlinearity effects in the real applications. Large errors can be made by the nonlinearity effects. Many researchers try to mitigate the nonlinearity effects to improve the rotor position accuracy. Significant improvements have been made during recent decades and are discussed in this section.

1.4.1 Machine multiple saliency and induced saliency

The saliency of machine is not perfect sinusoidal distribution because of the slot/pole distribution, winding, and machine distribution. As a result, machines have several other saliencies which are called as multi-saliencies. The machine inductance including multi-saliencies can be model as:

$$L_{dq}^{s} = \Sigma L \begin{bmatrix} 1 & 0 \\ 0 & 1 \end{bmatrix} + \sum_{h=1}^{\infty} \Delta L_i \begin{bmatrix} cos(h\theta_e) & \mp sin(h\theta_e) \\ \mp sin(h\theta_e) & -cos(h\theta_e) \end{bmatrix} \tag{1-8}$$

For the induced current component, spatial harmonics equal to h = 2, 5, 8…, result in same rotating direction. The spatial harmonics equal to h = 1, 4, 7… creates the negative rotating direction with respect to the saliency harmonics. Because of three-phase balanced, the spatial harmonics which are the integer multiple of 3 (h = 3, 6, 9…) usually don't create position dependent currents. It can be seen that the current spectrum will have other frequency components which is shown as Fig. 1.17[23].

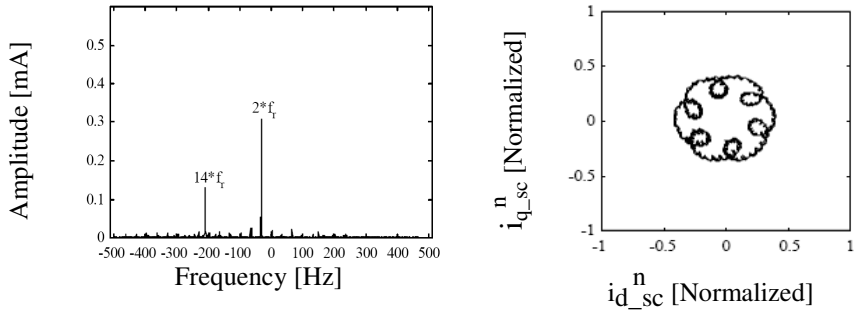

Fig. 1.17 (a) FFT of the Stator Current (b) saliency image without any fundamental excitation present in the machine [23]

It can be expected that the estimation accuracy will be affected by the multi-saliencies. Degner investigated the effects and developed a decoupling technique to improve the estimation accuracy with an induction machine [23, 27]. As shown in Fig. 1.18, he proposed a decoupling observer to decouple multi-saliencies. Several observer topologies are also proposed to investigate the stability and performance.

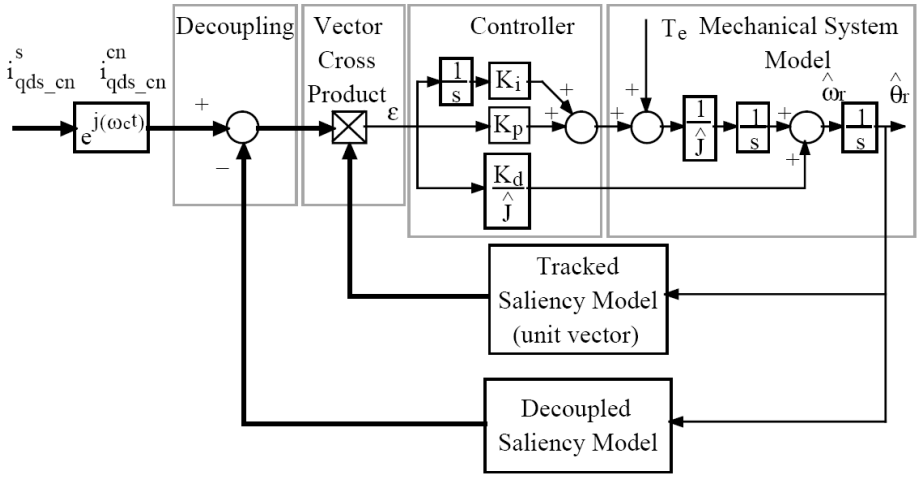

Fig. 1.18 Multiple saliency decoupling observer for a machine with rotor position dependent Saliencies [23]

Induced saliencies appear because of iron saturation effects. It can be categories as the multi-saliencies. Briz investigated the effect of induced saliencies and used lookup tables to decouple the induced saliencies [28]. To avoid time consuming of constructing lookup tables, García utilized structured neural networks (SNN) for automatic commissioning and decoupling of secondary saliencies including saturation-induced saliencies[29]. The existing method mainly focused on FW-machines. The applicability and limitations for FI- machines is still unknown due to reverse saliency characteristic. In addition, these methods mainly focus on the mitigation of multi-saliencies effect. However, sensitivity of multi-saliencies to injection signal has not been explored yet.

1.4.2 ***High frequency resistance***

High frequency resistance is also a source causing rotor estimation error. Normally, the high frequency resistance and stator resistance is small and can be ignored. However, it is not true in all cases. The high frequency resistance could come from rotor resistance which is caused by the eddy current reflect to the stator side. Reigosa proposed an adaptive decoupling method to mitigate this effect[58].

1.4.3 ***Inverter nonlinearity effects***

One of the major nonlinearity effects cause errors of the self-sensing control is from inverter. Since voltage source inverter is usually for common drive, non-ideal behavior of the switching devices affect the estimation accuracy because additional fake saliencies are created by the inverter. Guerrero et al investigate the effect which simulations and experimental tests and propose a simple compensation method[59].

- Dead-time(shoot-through delay, dwell time, or interlock time)

To prevent the short through which will make a permanent damage to the switch device, a delay time is needed to add to ensure the one switch is fully switch off before the switch turn on since switches cannot turn off instantaneously. However, short voltage error pulses are caused by Dead-time with respect to the commanded voltage. In addition the current polarity is the opposite of the sign of the error pulse in the switch leg.

- Turn-on and turn-off times of semiconductors

A short period is needed for the switch device to fully turn on or off. Normally, this term is small and typically neglected. Some of the Dead-time compensation methods include solutions for this problem.

- Parasitic capacitance of semiconductors

Turn-on and turn-off times of the switch devices are also affected by parasitic capacitance. Since the current is very small during the low-current region, it will take

more time to change the output voltage (i.e. the slope of rising and falling of output voltage become flat).

- Zero-current clamping effect

When the phase current is near zero, the extinction of the current in the freewheeling diode cause the phase leg disconnect from the bus during a portion of the deadtime period. This problem becomes more serious for low-frequency signals, since it remain in the zero-current-clamping region much longer.

- Additional voltage drop

Additional voltage drop which is across the switch devices causes the error of the output voltage. This can be modeled as an equivalent resistor and can be compensated by a lookup table.

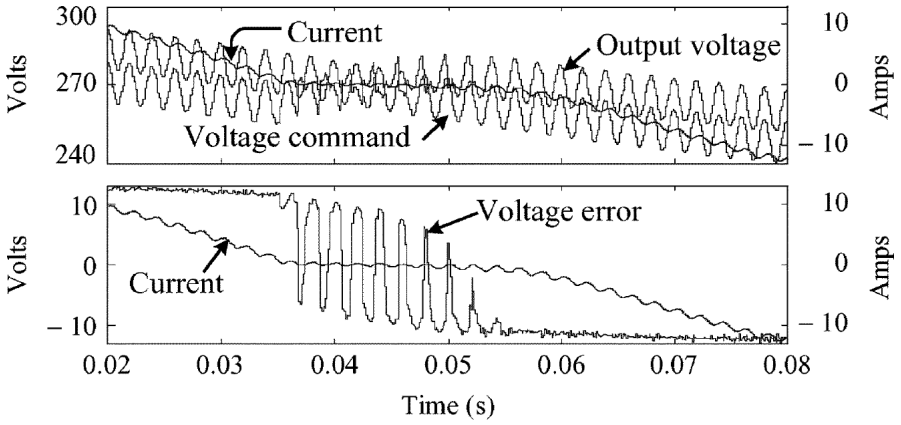

Fig. 1.19 Simulation of injection of fundamental and high-frequency voltage[59]

Based on the Guerrero et al's work, the major cause of the errors for the high frequency injection method is the parasitic capacitance in the devices. The effect is dominant in the low current region and it can be seen from the Fig. 1.19[59]. To mitigate the dead-time effect, they suggest including the modeling of the parasitic capacitances to mitigate the dead-time effect.

In addition to decoupling based on the open-loop inverter model, an observed based voltage disturbance decoupling is reported [60]. The idea is that the current is estimated

by the current observer with ideal motor model so the current difference between the ideal and measured current is the error caused by the dead-time effect. The dead time effect can be decoupled with the knowledge of the current error. Since estimated current is from the model of the machine, the estimation accuracy is dependent on the estimation accuracy machine parameters.

It is shown that lower DC bus voltage can effectively mitigate inverter non-ideal effect [61]. The author use low DC bus voltage in the low speed region because of only low voltage is required. However, dynamically changing the DC bus voltage and its impact on the self-sensing performance are not been explored yet.

*1.4.4 **Magnetic cross-saturation***

Magnetic cross-coupling effect has been reported as one of the source causing the rotor estimation error[62]. It also can refer as a d- and q- axis cross-saturation. In theory, it is assumed d- and q-axis are perpendicular and don't affect each other. However, the magnetic saturation result in d-axis is impacted by in q-axis or vice versa. This effect is usually small in the light load conditions and become server in the heavy load conditions because of saturation.

The cross-saturation causes a constant phase offset φ for saliency tracking. As discussed above, cross-saturation depends on magnetic saturation which is dependent operation point conditions. This phase offset φ can be expressed as[62]

$$\varphi = \frac{1}{2}\arctan\left[\frac{L_{dq}}{\Delta L}\right] \tag{1-9}$$

It can be seen that the phase offset is relative to cross-saturation inductance L_{dq} and differential inductance ΔL.

Prediction and decoupling of cross-coupling effect has been report on several literatures. Since the cross-saturation effect depends on the loaded conditions, a simple machine model is difficult to fully model the cross-saturation effect. An offset of lookup table on different operating points from experimental result is used to compensate the estimated rotor position error[62-64] or adaptive decoupling[65]. Cross-saturation effects can also be predicted by using finite element analysis[63, 66]. Cross-effect can also be mitigated by machine design since machine geometry or nonlinearity behavior in magnetic materials is the result of cross-coupling effect [8, 66, 67]. The geometry of FI-IPMSM is designed to reduce the d and q axis cross-coupling[8].

1.5 **Permanent magnet synchronous machine torque and flux control**

1.5.1 ***Current vector control method***

In the modern field oriented control, both the torque-producing part of the current vector and the flux vector of AC machines can be manipulated. Torque and flux can be decoupled if they are perpendicular in the spatial space. Under this circumstance, PMSM behaves like a separately excited DC machine. Two control state variable direct axis current (i_{ds}^{r}) and quadrature axes currents (i_{qs}^{r}) are used to simulate DC machine. Magnet flux axis is usually defined as direct axis so the direct axis current which acts like the field current in the DC machine and quadrature current is proportional to the torque command. The torque equation can be written as

$$T_{em} = \frac{3}{4} P[\lambda_{pm} i_{qs}^{r} - (L_q - L_d) i_{ds}^{r} i_{qs}^{r})] \tag{1-10}$$

It can be seen that PMSM torque is comprised of magnet torque (Lorentz force torque) and reluctance torque (if d-axis and q-axis inductance are not equal). For SPMSM ($L_q = L_d$), field oriented control is suitable since there is almost no reluctance torque. However, for IPMSM and FI-IPMSM (($L_q = L_d$)), it is very obvious only field oriented control is not a good solution.

For the manipulation of torque, current vector control (CVC) is widely used in PMSMs. For CVC, the manipulated input is the stator voltage vector to achieve closed loop control of the stator current vector (i_{ds}^{r} and i_{qs}^{r}). The current vector components are computed to achieving the desired torque while yield minimum losses. The loss minimization can be based on copper losses, iron losses, inverter losses, or some combination. The loss minimization based on the copper losses is shown as Fig. 1.20. More detail discussion is shown in next section.

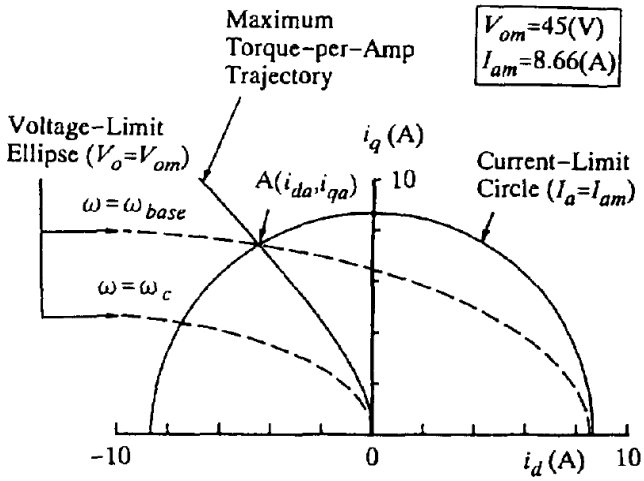

Fig. 1.20 Maximum torque-per-ampere trajectory with CVC [68]

1.5.2 ***Direct torque control - Hysteretic direct torque control (H-DTC) and Deadbeat-direct torque flux control (DB-DTFC)***

DTC has been developed initially in induction machine in mid 1980's [69-72] and was presented to have faster dynamic property [73-76]. For DTC, the major difference is that stator flux linkage magnitude and torque is the controlled states. Inverter voltage vector commands are directly manipulated by the controller input in DTC while voltage vector commands are regulated by an intermediate current regulator in CVC. It is clear that dynamic property of the drive system can be improved with stator flux magnitude and torque is directly controlled.

The equation for stator flux linkage is shown (1-11)

$$p\lambda_{dqs} = V_{qds} - R_s i_{qds} \tag{1-11}$$

Normally, the voltage drop on stator resistance is considered small and neglected, so the stator flux linkage is almost directly manipulated by the stator voltage. In common three phase voltage source inverter (VSI), seven voltage vectors can be applied to the stator at any instant of time and it is graphically depicted in Fig. 1.21

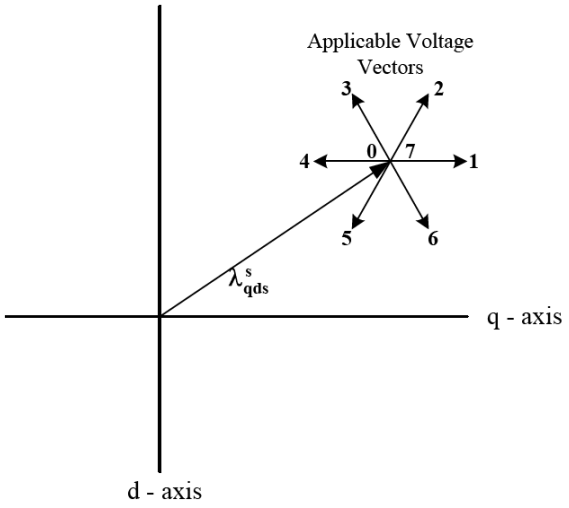

Fig. 1.21 Stator flux linkage vector and possible voltage vectors [72]

Classical DTC utilized a lookup table and hysteresis control strategy for both stator flux and torque control. One hysteretic switch is used to control torque and the other is used to control stator flux. Control block diagram is shown in Fig. 1.22. It can be seen that bang/bang hysteresis control with a switching table was the primary implementation.

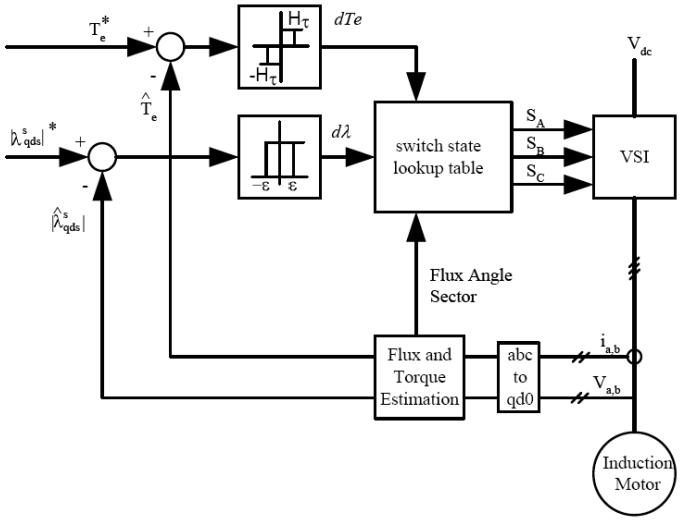

Fig. 1.22 The block diagram of an IPMSM drive with DTC [72]

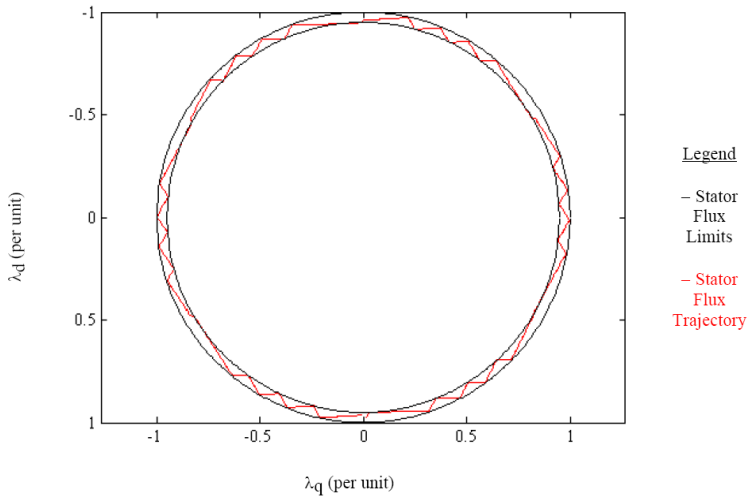

Fig. 1.23 Typical stator flux linkage orbit for classical DTC[72]

Fig. 1.23 shows the flux trajectory in the classical DTC. It can be observed that switching frequency in DTC method is unpredictable due to the bang/bang hysteresis control. However, continuous change and unpredictable of switching frequency of inverter is usually not preferred. First, additional switching losses can be raised which results in heating problem. Secondly, unpredictable torque ripple occurs due to variable switching frequency. Thirdly, for low self inductance machine, the unpredictable torque ripple can exceed inverter limit so the dynamic property can be degraded.

Although classical DTC has the unpredictable switching frequency, it still has the advantage of fast dynamic property compared to CVC. For loss issues, Similar to the CVC, the stator flux linkage command also can be calculated and manipulated to have copper loss minimization. Rahman proposed maximum torque-per-ampere for DTC and the control trajectory is shown as Fig. 1.24[76].

From discussion above, DTC has fixed switching frequency technique is preferred to have better loss control. Furthermore, only fundamental model is considered in the classical DTC control. If transient model is also considered, DTC has fast dynamic property which provides a “knob” to manipulate the transient loss.

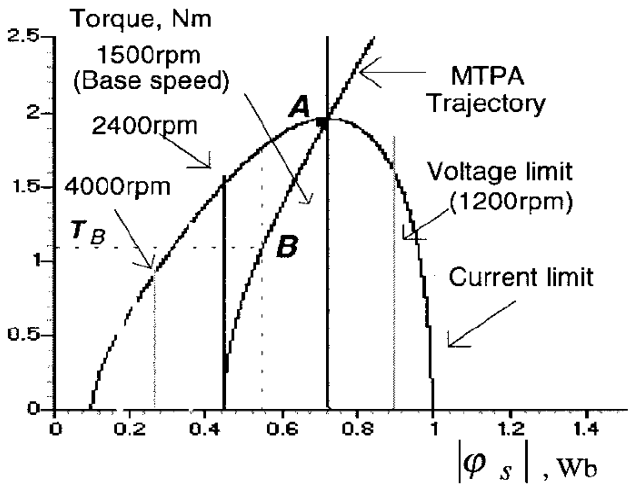

Fig. 1.24 Control trajectories in torque–stator flux plane [68]

A significant improvement to the classical DTC has been made by B. Kenny and Lorenz[77]. An inverse of physical plant model which include the cross-coupling is utilized to apply stator voltage vectors instead of using bang/bang controller.

Several advantages are shown in this control law. First, by using the inverse model, the torque output and stator flux linkage can be achieved only in one switching cycle i.e. deadbeat. Deadbeat control is fastest possible law in digital system. It drives the error signal to zero in one time step and becomes a good choice for high performance control. Secondly, the cross-coupling term is included in the inverse model. As a result, overshoot and oscillations will not exist in the transient torque dynamics. Thirdly, fix switching cycle can be achieved. It increases the system stability and reduces the inverter losses.

Deadbeat-direct torque and flux control has been investigated and well-established in induction machine and permanent magnet synchronous machine in WEMPEC [77-82]. This permanent magnet synchronous machine is the focus of this research so it will be the main discussion.

Equations in the rotor reference frame can be written as d-q complex vector notation where $f_{dq} = f_d + jf_q$

$$v_{dqs}^{r} = R_s\, i_{dqs}^{r} + \dot{\lambda}_{dqs}^{r} + j\omega_r\, \lambda_{dqs}^{r}$$
$$\text{Where } \lambda_{ds}^{r} = L_d\, i_{ds}^{r} + \lambda_{pm} \text{ and } \lambda_{qs}^{r} = L_q\, i_{qs}^{r} \tag{1-12}$$

For the short time period of typical PWM frequencies, the discrete time form of (1-12) is shown as (1-13)

$$\lambda_{dqs}^{r}(k+1) = \lambda_{dqs}^{r}(k) + v_{dqs}^{r}(k)\, T_s - \left(\frac{R_s}{L_s} + j\omega_r\right)\, \lambda_{dqs}^{r}(k)\, T_s + \frac{R_s}{L_s}\lambda_{pm}\, T_s \tag{1-13}$$

The inverse model derivation starts with the air-gap torque equation which is developed in (1-14).

$$T_{em} = \frac{3}{4}P\, [\, \lambda_{ds}^{r}\, i_{qs}^{r} - \lambda_{qs}^{r}\, i_{ds}^{r}\,] \tag{1-14}$$

The time rate of change of torque can be defined as

$$\dot{T}_{em} = \frac{3}{4}P\, [\, \dot{\lambda}_{ds}^{r}\, i_{qs}^{r} + \lambda_{ds}^{r}\, \dot{i}_{qs}^{r} - \dot{\lambda}_{qs}^{r}\, i_{ds}^{r} - \lambda_{qs}^{r}\, \dot{i}_{ds}^{r}\,] \tag{1-15}$$

Substituted the differential stator flux linkage and stator current into (1-15) leads to the torque differential equation which is shown as following:

$$\dot{T}_{em} = \frac{3}{4}P\Big[\, v_{ds}^{r}\, \lambda_{qs}^{r}\, \left(\frac{L_d - L_q}{L_d\, L_q}\right) + v_{qs}^{r}\frac{(L_d - L_q)\, \lambda_{ds}^{r} + \lambda_{pm}\, L_q}{L_d\, L_q} +$$
$$\frac{\omega_r}{L_d\, L_q}\left(\,(L_q - L_d)\left(\lambda_{ds}^{r\,2} - \lambda_{qs}^{r\,2}\right) - L_q\, \lambda_{ds}^{r}\, \lambda_{pm}\right) + \frac{R_s\, \lambda_{qs}^{r}}{L_d^2\, L_q^2}\left(\,(L_q^2 - L_d^2)\, \lambda_{ds}^{r} - L_q^2\, \lambda_{pm}\right)\Big] \tag{1-16}$$

$$\frac{T_{em}(k+1) - T_{em}(k)}{T_s} = \frac{3}{4}P\, \Big[\, v_{ds}^{r}(k)\, \lambda_{qs}^{r}(k)\left(\frac{L_d - L_q}{L_d\, L_q}\right) + v_{qs}^{r}(k)\frac{(L_d - L_q)\, \lambda_{ds}^{r}(k) + \lambda_{pm}\, L_q}{L_d\, L_q}$$
$$\frac{\omega_r(k)}{L_d\, L_q}\left(\,(L_q - L_d)\left(\lambda_{ds}^{r\,2}(k) - \lambda_{qs}^{r\,2}(k)\right) - L_q\, \lambda_{ds}^{r}(k)\, \lambda_{pm}\right) + \tag{1-17}$$
$$\frac{R_s\, \lambda_{qs}^{r}(k)}{L_d^2\, L_q^2}\left(\,(L_q^2 - L_d^2)\, \lambda_{ds}^{r}(k) - L_q^2\, \lambda_{pm}\right)$$

An expression can be developed for the change in torque, (6),

$$\Delta T_{em}(k) \;=\; T_{em}(k+1) - T_{em}(k) \tag{1-18}$$

Equation (1-17) describe a straight line in the d and q-axis stator plane where

$$v_{qs}^{r}(k)\, T_s = \;\mathrm{M}\; v_{ds}^{r}(k)\, T_s + \mathrm{B} \tag{1-19}$$

The slope M is defined as

$$M = \left(\frac{(L_q - L_d)\,\lambda^r_{qs}(k)}{(L_d - L_q)\,\lambda^r_{ds}(k) + L_q\,\lambda_{pm}} \right) \tag{1-20}$$

The q-axis intercept, B, is defined as:

$$B = \left(\frac{L_d\,L_q}{(L_d - L_q)\lambda^r_{ds}(k) + L_q\lambda_{pm}} \right)$$
$$\left[\frac{4\Delta T_{em}}{3P} - \frac{\omega_r T_s}{L_d\,L_q}\left((L_q - L_d)\,(\lambda^r_{ds}(k)^2 - \lambda^r_{qs}(k)^2) - L_q\lambda^r_{ds}(k)\,\lambda_{pm}\right) - \right. \tag{1-21}$$
$$\left. \frac{R_s\,T_s\,\lambda^r_{qs}(k)}{L_d^2\,L_q^2}\left((L_q^2 - L_d^2)\,\lambda^r_{ds}(k) - L_q^2\,\lambda_{pm}\right)\right]$$

From(1-18), the commanded torque can be achieved over the next sample instant with multiple possible stator voltage vectors. Deadbeat-direct torque and flux control can be realized in each of these solutions. Fig. 1.25 depicts the DB-DTFC graphical representation including the desired torque line and stator flux linkage vector for IPMSMs.

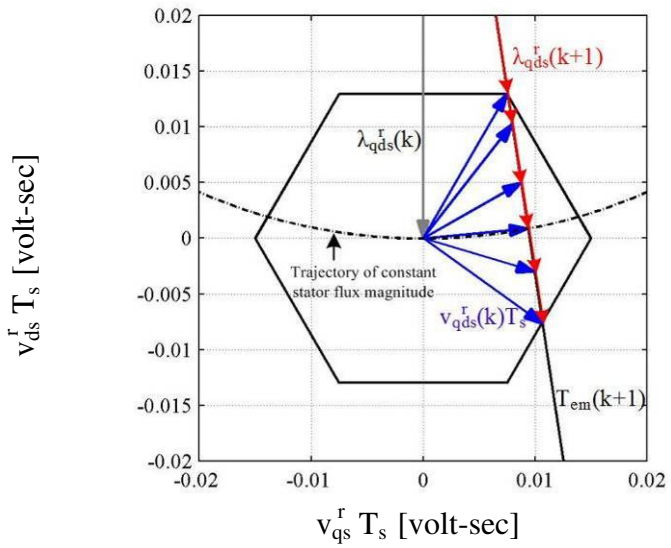

Fig. 1.25 Graphical representation of DB-DTFC voltage solution for IPMSMs[82].

From Fig. 1.25, several key observations can be found. First, the desired air gap torque can be achieved in one sample period. Therefore, it can be expected that the dynamic property is fast than CVC. Secondly, the switching frequency is fixed which

helps to manage the inverter losses. Last but not least, since each stator voltage vectors yield different stator flux level ever sample time instant, loss in IPMSMs can be manipulated every sample instant via stator voltage vector selection. This is the key issues for motor loss minimization.

DB-DTFC provides a valuable degree-of-freedom for loss minimizing control since flux level is the manipulated input. First, in feasible operating conditions, manipulating stator flux linkage can yield significant reduction in iron and copper losses. Secondly, the single control law for DB-DTFC can be easily augmented by an appropriate loss minimizing. Thirdly, DB-DTFC provides the opportunity to manipulate dynamic losses which is usually ignored in fundamental model. Lorenz research group took the advantage of DB-DTFC to achieve loss minimization in induction machine [83]. A steady state evaluation in induction machine has been shown in that the losses can be minimized if the optimum flux is chosen.

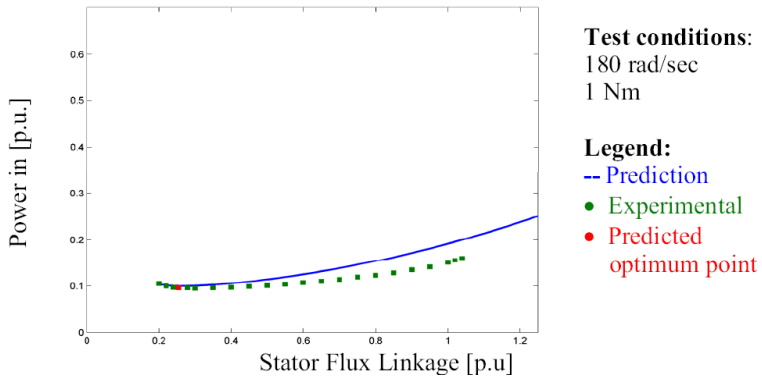

Fig. 1.26 Experimental and predicted power input versus stator flux linkage with the predicted optimal flux point at constant rated speed and constant low torque[83]

1.6 **Loss minimization control of PMSM with fixed DC bus voltage**

The torque production of non-salient pole machine can be written as

$$T_{em} = \frac{3}{4} P[\lambda_{pm} i_{qs}^{r} - (L_q - L_d) i_{ds}^{r} i_{qs}^{r})] \tag{1-22}$$

Where T_{em}: torque, P: pole pair, λ_{pm} : magnet flux linkage, L_q : q-axis inductance, L_q : d-axis inductance. The first term is magnet aliened torque (Lorentz torque) and the second term is reluctance torque. From the torque equation, it can be seen that the torque production can be optimized between reluctance torque and Lorentz torque to have (i.e. Maximum torque-per-ampere (MTPA). Jahns propose this method which can also be viewed as copper loss minimization method because the theoretical maximum torque with minimal current vector is computed[84]. It should be noted that inductances and resistances used to model iron loss vary with load condition and copper resistance vary with temperature. As a result, the parameter can be adjust based on off-line parameter estimation[85] or on line parameter estimation[86].

In the MTPA method, iron loss is neglected so the losses are not fully minimized. Morimoto propose a new control method which adds d-axis and q-axis resistances representing the iron loss and block diagram is shown as Fig. 1.1. The optimization point can be obtained by differentiating the iron and copper loss equations[87]. Similar method is also proposed by other research group[88]. However, effectiveness of these methods depends on the estimated parameter accuracy.

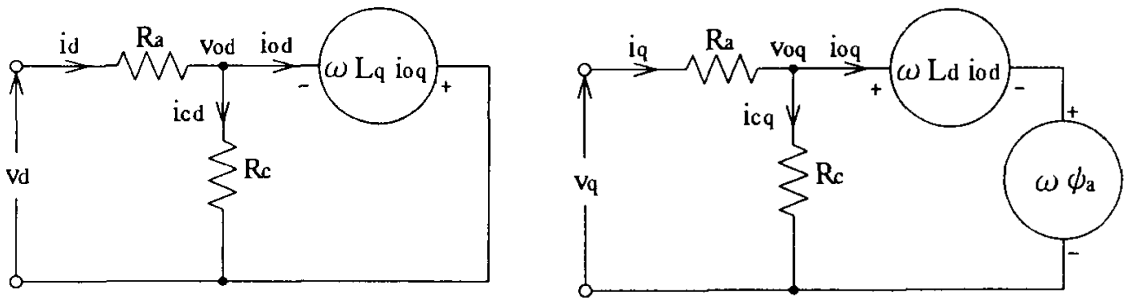

(a) d-axis equivalent circuit (b) q-axis equivalent circuit

Fig. 1.27 equivalent circuit of permanent magnet synchronous machine[87]

In mid-80s, an online loss minimization search method has been demonstrated with the induction machine [89-91]. As shown in Fig. 1.28, the target is to find the minimal input power line. Recently, similar idea has been demonstrated by other research groups. A high frequency current signal (300Hz) is be injected to search the minimal input power operating point [92-94]. As shown in Fig. 1.29. They used that the input power variation according to the current angle on the constant torque locus should be zero at the maximum power per torque operating point.

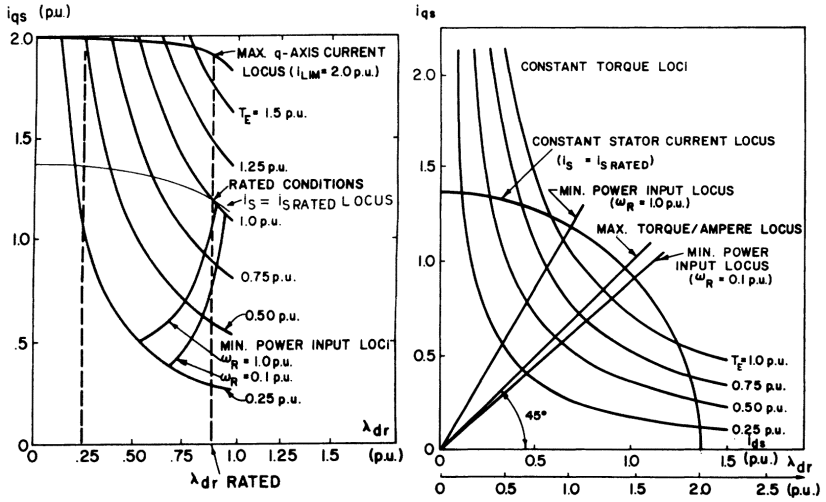

Fig. 1.28 Characteristic loci of 7.5-hp induction machine in field-oriented reference frame, neglecting saturation.[90]

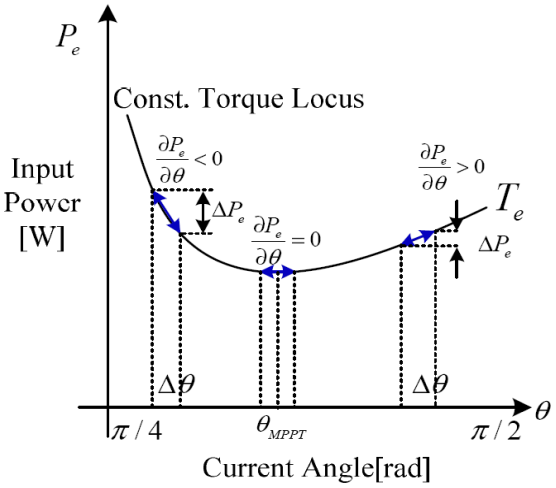

Fig. 1.29 Plot of input power variation with respect to the current injection angle onto the constant torque locus[93]

Both of the two methods have the disadvantage of relatively low dynamic property. As a result, the techniques are not suitable for transient operation. During the transient operation, machine model changes, so the methods are inferior solution for the transient states. Wei and Lorenz has proposed a dynamic loss model with DB-DTFC to achieve dynamic loss minimization[95]. The voltage sec selection is based on the loss minimized transient operation point which is calculated from the dynamic loss model as shown in Fig. 1.30. The Experimental results have been demonstrated that dynamic loss minimizing models in DB-DTFC can improve energy efficiency when compared to existing steady state loss minimization control techniques.

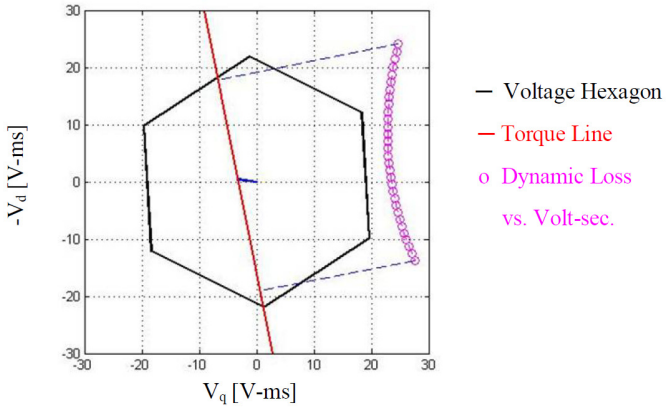

Fig. 1.30 Dynamic loss curve vs. Volt-sec selections[95].

1.7 Loss minimization control with variable DC bus voltage

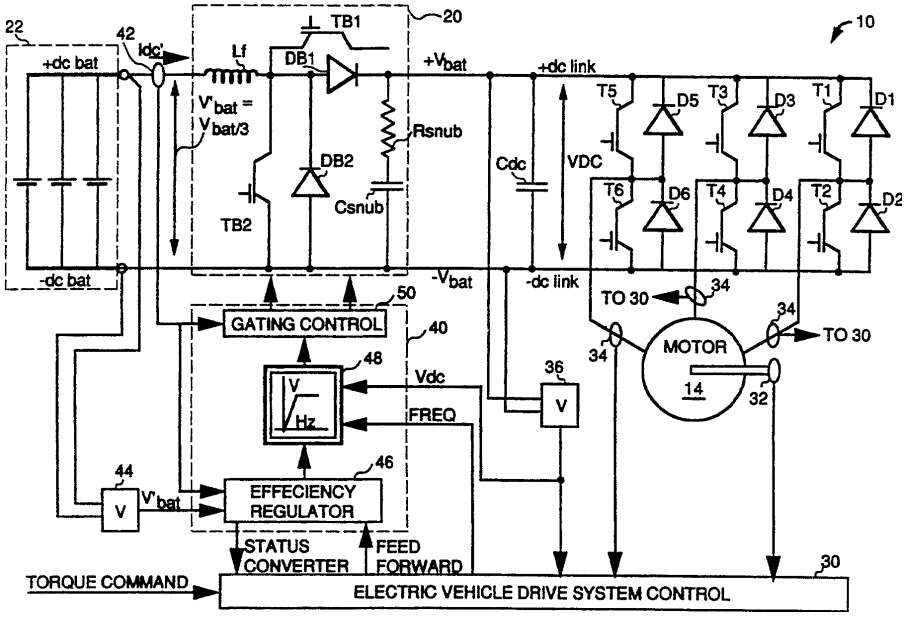

Fig. 1.31 System configuration of PWM inverter with voltage booster [96]

Drive system having a DC/DC converter which is connected to inverter has been proposed [96-99] and widely used in hybrid car. The system block diagram is shown as Fig. 1.31. Characteristics and control issues for adjustable DC bus voltage drive system are addressed as following.

1.7.1 Copper losses in flux weakening region

Traditionally, flux-weakening control is used to expend the machine operating speed. The drawback is that d-axis current must be generated to suppress permanent magnet flux linkage. Since the total current is increased, losses including conduction loss of inverter, and motor iron losses are increased. If adjustable DC-bus voltage is used, no d-axis is required to suppress the magnet flux linkage during the high speed region. As a result, total current is reduced so the conduction loss of inverter and copper loss of motor can be reduced [100-102]. Actually, the interactions of loss reduction and boost voltage

highly depend on system design. With a proper design, efficiency can be improved as shown in Fig. 1.32.

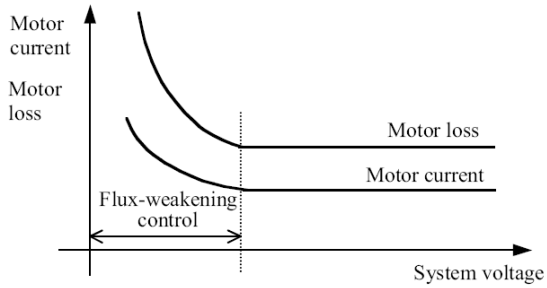

(a) DC-link voltage versus motor losses

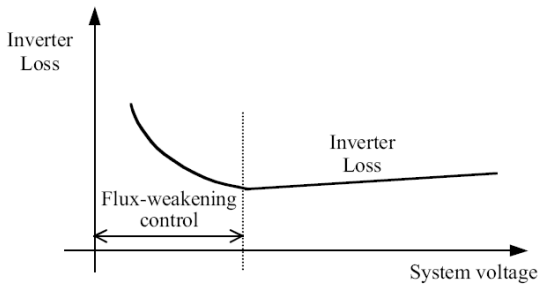

(b)DC-link voltage versus inverter losses

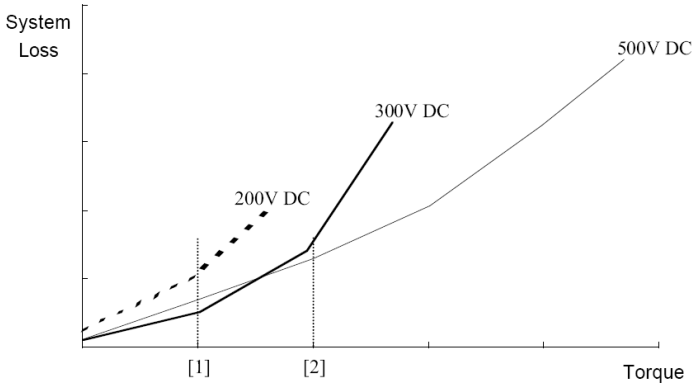

(c) DC-link voltage versus system losses

Fig. 1.32 The relationship between DC-link voltage and losses [103]

1.7.2 The impact of input voltage variation on drive

With the boost converter, the DC-link voltage of inverter can be independent of input system DC bus voltage. For example, if the energy source comes from battery, input voltage varies with the state of charge of battery. Since machine performance (torque-speed curve, maximum power) depends on the DC bus voltage, maximum power can be reduced due to the reduction of DC bus voltage. With the DC/DC converter, the DC link voltage can be kept constant so the desired machine operation can be maintained.

Researchers in Toyota corp. propose dynamic boost voltage and successfully adopt this topology in their commercial hybrid vehicles. The DC-bus voltage is dynamic boost depending on the vehicle operating point as shown in Fig. 1.33. The DC bus selection is based on the control flowchart shown in Fig. 1.34. Other research groups also propose similar idea and implement a constant boost voltage system, but no efficiency analysis is presented [104].

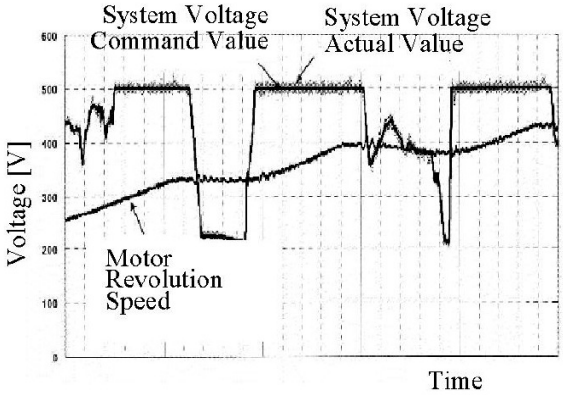

Fig. 1.33 The relationship between DC-link voltage and operating condition [105]

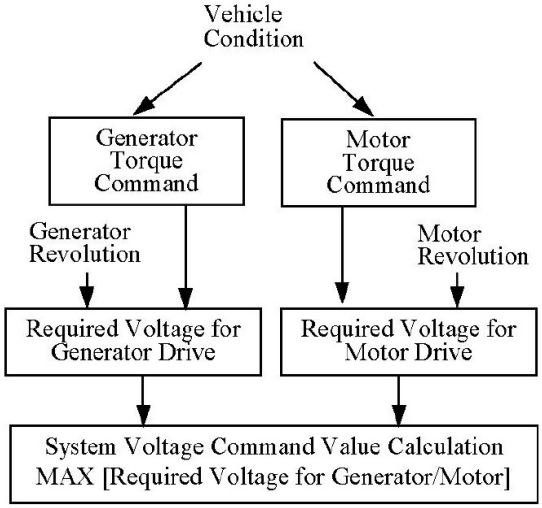

Fig. 1.34 Control flowchart for the boost converter[105]

1.7.3 DC bus voltage level selection for variable DC bus drive system

To achieve efficiency improvement for a variable DC bus voltage system, the voltage selection for the DC bus voltage is the curial point. Researchers used the machine fundamental component model to calculate the required DC bus voltage[97]. In this control algorithm, the drive system will not operate in the flux weakening region until reach the maximum boost DC bus voltage. Based on the boost voltage calculated from machine fundamental model, the machine operating regions can be divided into several regions as shown in Fig. 1.35.

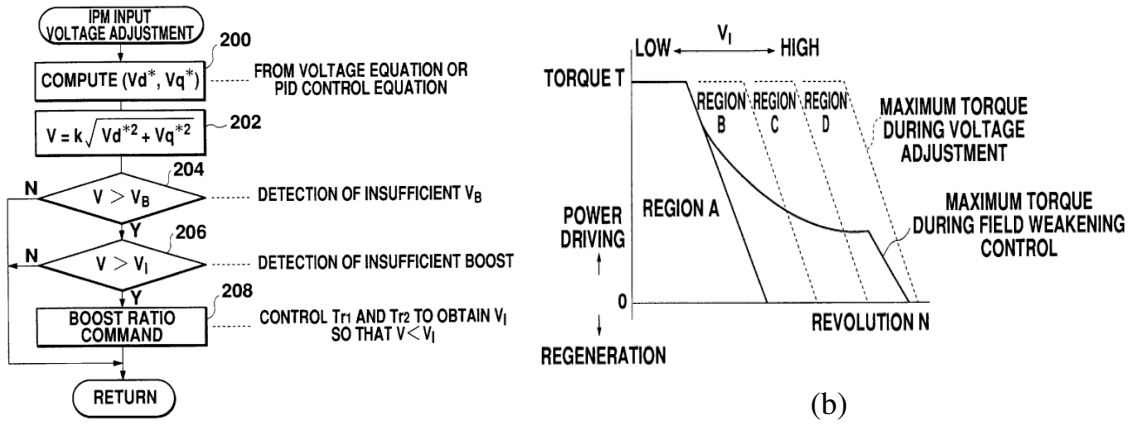

Fig. 1.35 (a) DC bus voltage level calculation based on the machine fundamental model (b) Machine operating region based on the boost DC bus voltage[97]

Other researchers also investigated this topology and try to find the optimum DC bus voltage selection point. Due to the unmodeled spatial harmonic components, the required DC bus voltage is higher than fundamental component model. To solve this issue, a certain gain from try and error method is used for adjusting the calculation DC bus voltage as shown in Fig. 1.36. Other Researchers used a lookup table method to solve this issues[106]. The major drawback for lookup table is the intensively experimental efforts.

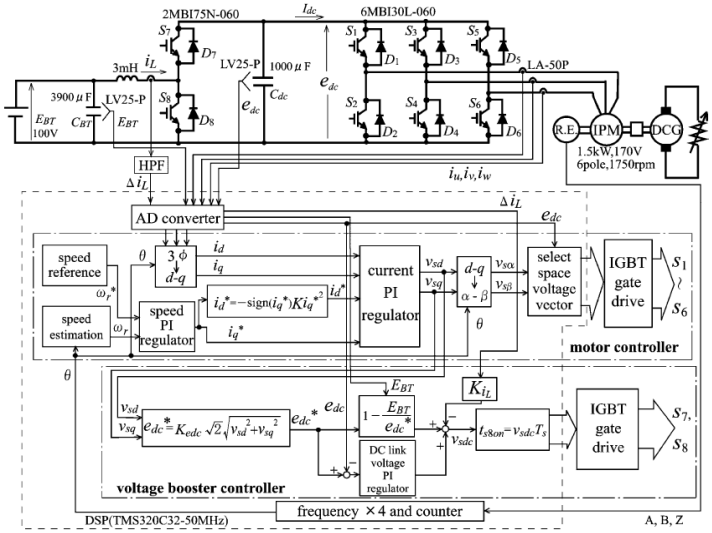

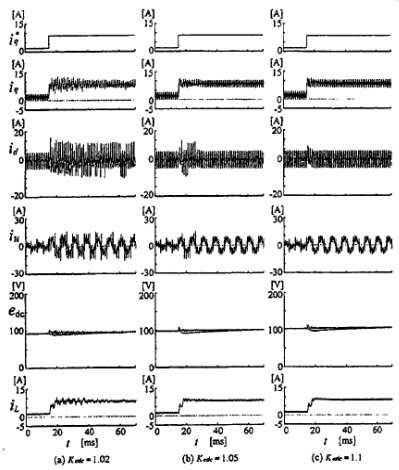

Fig.8. Transient state waveforms of voltage booster and PM motor for step change of q-axis current reference i_q^* (Kpv = 5.0, K_{iL} = 5.0, 4000rpm)

(a) (b)

Fig. 1.36 (a) Adjustable DC bus voltage drive topology and DC bus voltage calculation (b) Using a gain from testing results to correct the calculation errors[105]

1.8 Variable flux machine

1.8.1 Introduction of variable flux machine

Wide speed operation is required for machines in many applications, e.g. electrical vehicles. To achieve wide speed operation, flux weakening control in high speed operation machines is commonly used. However, it results in additional energy loss due to the required flux weakening current. A variable magnetic flux machine (or memory motor) has been proposed to achieve "true" wide speed operation as shown in [107-110]. By using low coercive force permanent magnets, magnetization state can be changed by a stator current pulse, allowing flux weakening control current to be greatly reduced and corresponding losses are reduced. The illustrations are shown in Fig. 1.39. Recently, variable flux machines have been successfully commercialized in duty-cycle based application such as washing machines[111-113] as shown in Fig. 1.40.

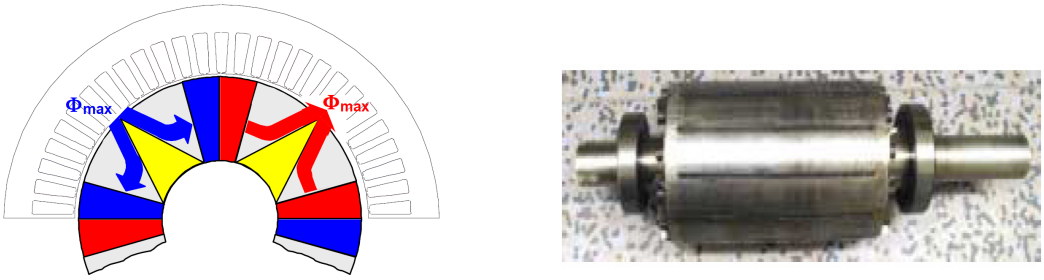

Fig. 1.37 Cross-sectional view of a memory motor and its rotor prototype [107, 108]

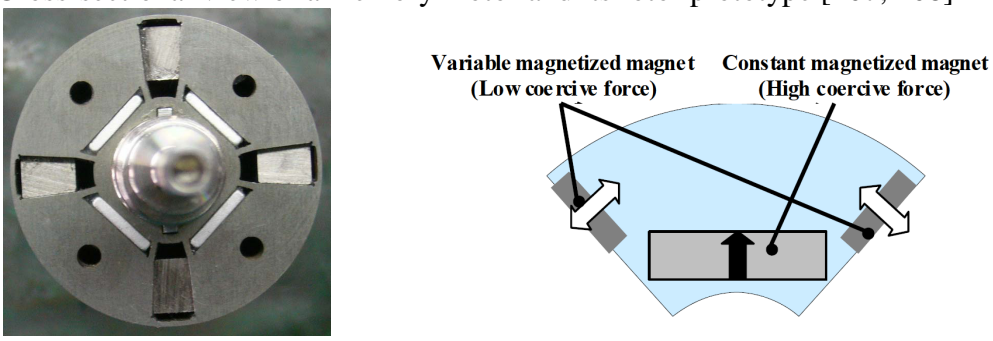

Fig. 1.38 Cross-sectional view of a memory motor and its rotor prototype [110]

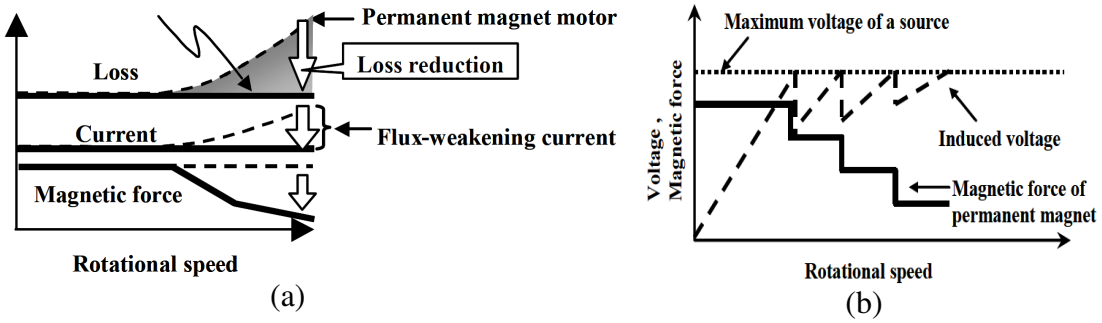

Fig. 1.39 (a) Loss at variable-speed operation (b) Voltage regulation at variable-speed using the variable magnetic-force [110]

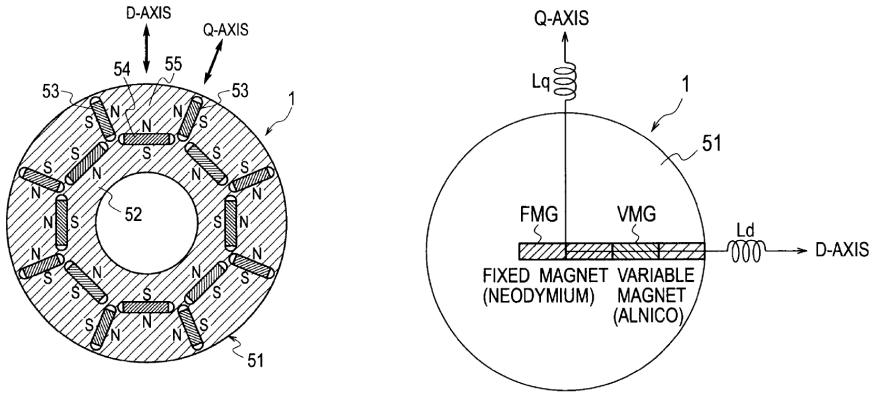

Fig. 1.40 Structure of the variable flux motor in washing machine [113]

1.8.2 Features of variable flux intensifying machine

The VF machines mentioned in last section are all in FW topology. Flux weakening current is required to achieve maximum torque per ampere (MTPA) or maximum torque per input power (maximum efficiency control(MEC)) due to the L_d<L_q property. However, if MTPA (negative i_d in FW machine topology) is used, demagnetizing flux will act on the magnet. Under these circumstances, it is difficult to avoid demagnetization so the magnet flux linkage is reduced and cannot be fully utilized. On the other hand, if a FI topology is used, then positive i_d current is used to achieve MTPA or MEC. The relationships between current and torque in FW and FI machines are shown as Fig. 1.41.

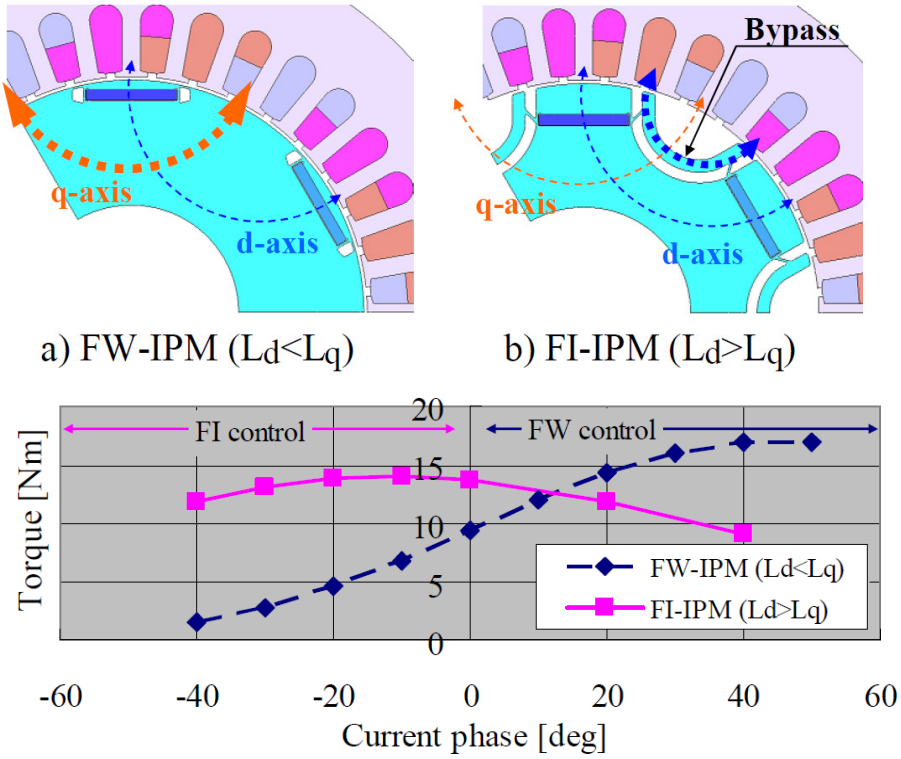

Fig. 1.41 Current phase and torque relationship [114]

In order to fully use magnet flux linkage, a combined concept of flux intensified machine and variable flux properties has been proposed recently[114, 115]. The advantage of using FI topology is that positive i_d current is used during MTPA or MEC operation. Under this condition, no demagnetization occurs so a better magnet utilization design could be achieved.

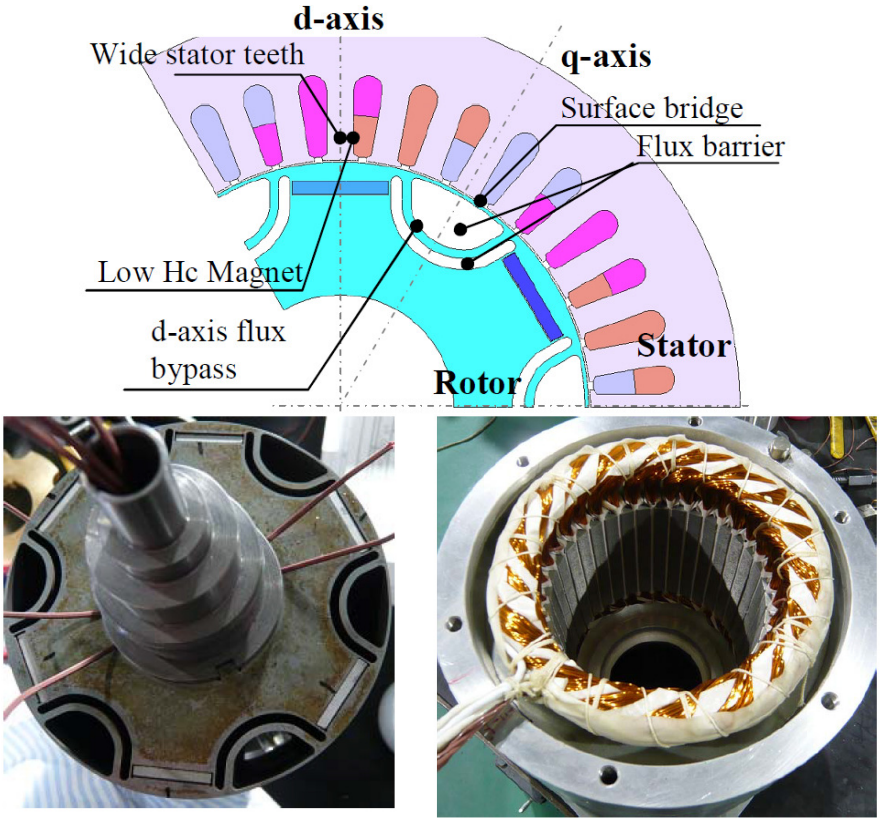

Fig. 1.42 Geometry and prototype of a variable-flux flux-intensifying interior permanent magnet machine

1.8.3 Magnetization state manipulation and pulsating torque mitigation methods

As shown in Fig. 1.39, the magnetization state should be changed based on the operation conditions to have energy loss minimization and wide speed operation. Therefore, how to perform magnetization state manipulation will be the key issues for variable machine operations. In this section, the magnetization state manipulation is discussed.

In Fig. 1.43, magnetization state manipulation is performed with current pulse method [108]. Since a current pulse is injected into the machine to change the magnetization state, severe pulsating torque could be produced due to change of magnetization state and the reluctance torque generated by the i_d current pulse. To avoid the pulsating torque, the magnetization state manipulation can be implemented at zero speed, zero load condition or by using pre-defined current vector control based on a lookup table under non-zero speed and loaded conditions. The control methodology is shown as Fig. 1.44 and Fig. 1.45. However, the last method requires a look up table which must be calibrated by time intensive experiments. Furthermore, if machine parameters vary due to temperature drifting, even more experiments are required. In addition, machine parameters are not identical even with same design due to imperfect manufacturing process. Therefore, if this method is applied to application (e.g. electric vehicle) time intensive experiments will be expected.

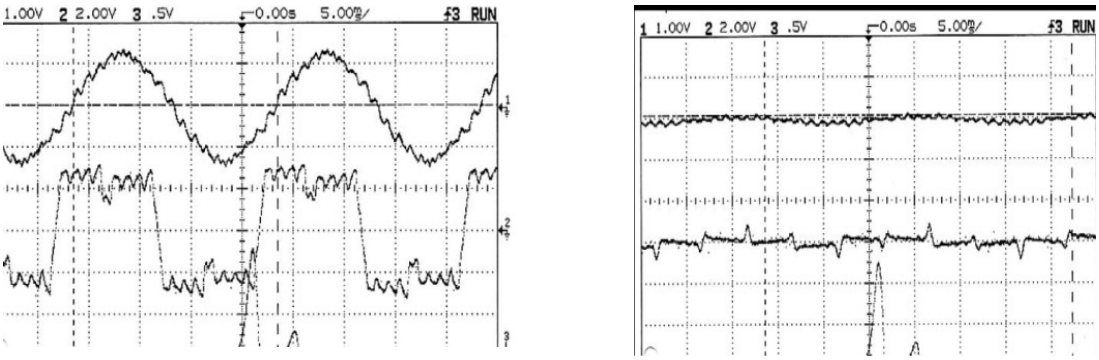

Fig. 1.43 Magnetization state manipulation with current pulse (Left: after magnetization current, Right: zero magnetization level) [108]

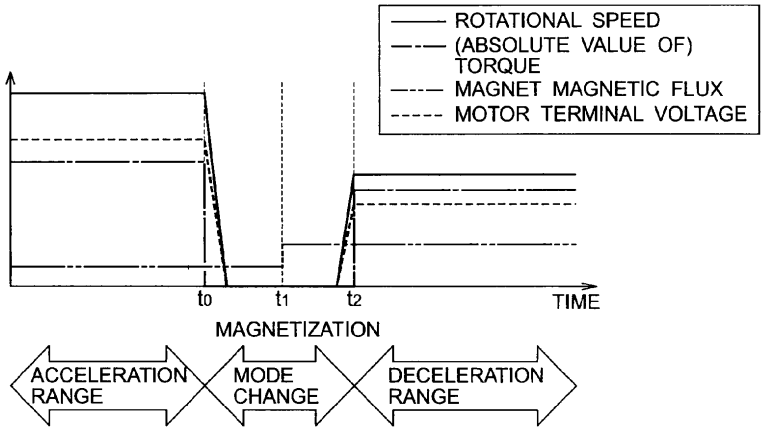

Fig. 1.44 Magnetization manipulation during zero load, zero speed condition [113]

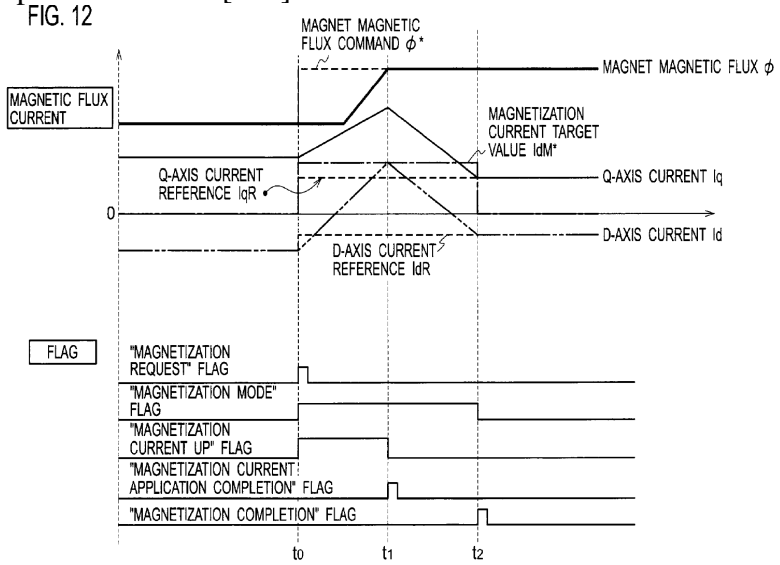

Fig. 1.45 Using predefined current vector for the magnetization state manipulation during loaded, non zero speed condition[113]

1.8.4 ***Magnetization state estimation***

For the variable flux machine, it is important to know the MS information in order to manipulate MS to proper state to perform losses minimization control. To manipulate the MS to a desired level, the magnitude of the current pulse can be chosen according to an offline calibration table [116]. The calibration table can be obtained by measuring EMF voltage after various current pulses under various speed conditions. However, this type of off-line techniques requires additional efforts to deal with MS variation due to imperfect manufacturing, individuality of the magnet property or magnet corrosion effects [117], thus on-line technique is preferable. A flux observer could be a better solution for MS estimation. However, flux observer methods work well only in medium and high speed conditions and estimation accuracy deteriorates in zero/low speed conditions as the EMF signal reduces as speed decreases [118]. In [119], the torque constant of BLDC machines with trapezoidal flux is estimated and used as an indicator for magnet demagnetization. A significant limitation of this method for MS estimation is that the back EMF is reduced at low speed conditions and sensitivity to stator resistance becomes dominant.

Other researchers estimate MS condition by monitoring the zero sequence voltage component of the stator phase voltage. However, the zero sequence voltage also decreases at zero/low speed conditions and an additional voltage sensor is required for zero sequence voltage measurement [120]. The system is shown as Fig. 1.46 and the experimental result is shown in Fig. 1.47. It can be seen that the zero sequence voltage is much smaller than the fundamental voltage (1/5th) so the signal to noise ratio could be also small. Therefore, achieving high accuracy estimation could be difficult.

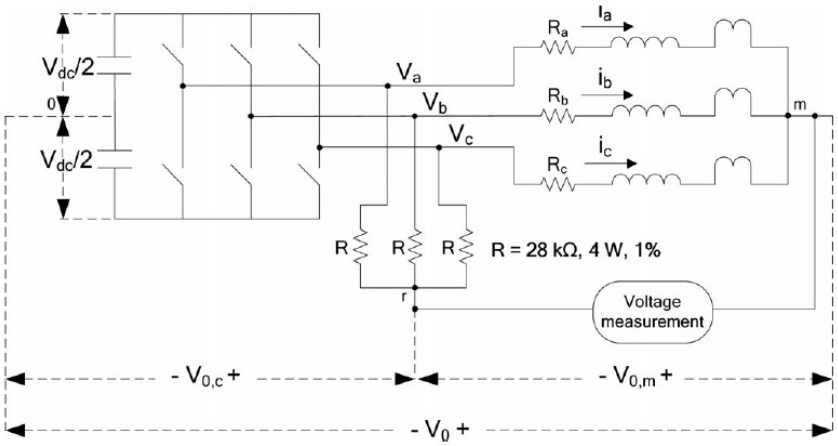

Fig. 1.46 Scheme diagram of SPMSM connection with the inverter, the stator windings, and the resistor network used to generate an artificial neutral point [120]

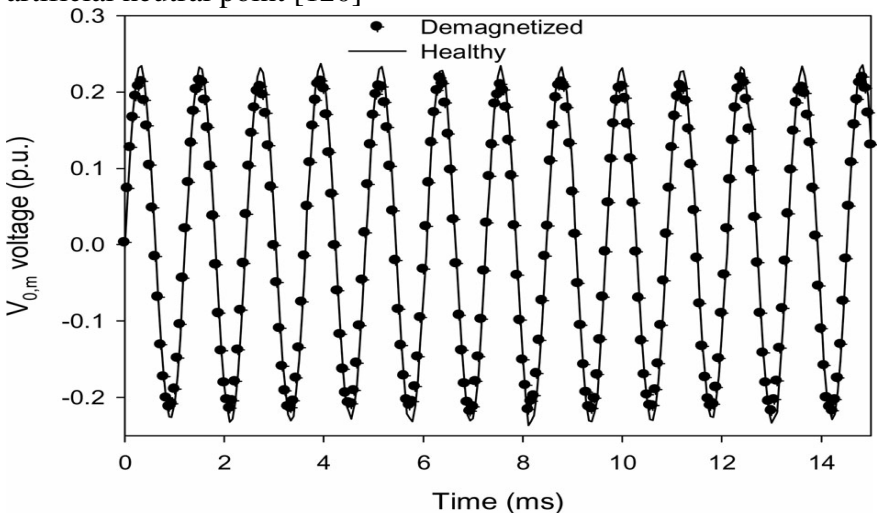

Fig. 1.47 Experimental ZSVC voltage of a healthy and a partially demagnetized SPMSM operating at 6000 r/min[120]

In [121, 122], a 200 Hz pulsating square wave at different angular positions was injected in the machine at standstill under no load conditions and the magnet condition was detected from the pattern of the resulting stator current. The current response to the pulsating field is a function of inductance, which is influenced by magnetic saturation. When the magnet MS changes (e.g. demagnetized or damaged), the magnetic saturation level is decreased, which is reflected in the stator current response as shown in Fig. 1.50.

However, only standstill, no load operating conditions is presented in [121, 122] for MS estimation.

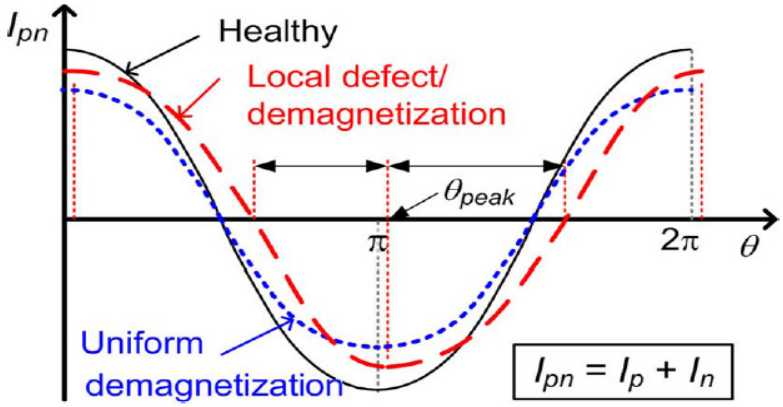

Fig. 1.48 I_{pn} pattern for magnets with uniform and local magnetizations[121, 122]

Several online system identification estimation methods for has been proposed for the parameter estimations [18, 123, 124]. Underwood proposed an iteration method with machine model to estimate machine parameters as shown Fig. 1.49. However, it still suffers from lacking of ranks since there are 4 unknowns with 2 voltage equations. In addition, it is difficult to know the PM flux linkage during the loaded condition due to the variation of inductance condition.

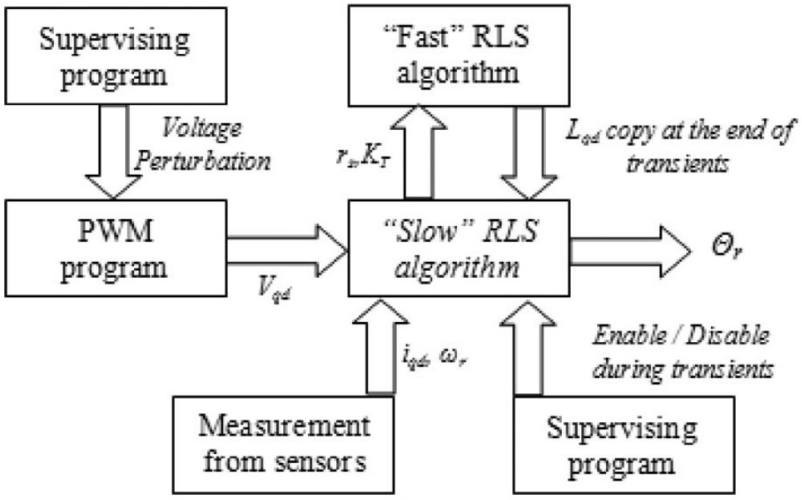

Fig. 1.49 Machine system identification with two loop (fast and slow) based on the machine model [123]

1.8.5 ***Losses minimization with variable machines***

In Fig. 1.39, it is known that the flux level selections are highly based on the operation condition and will affect the losses minimization. In addition, the operations will also high affected by the application. For the duty cycle load as washing machine, the operation condition can be shown as Fig. 1.50.

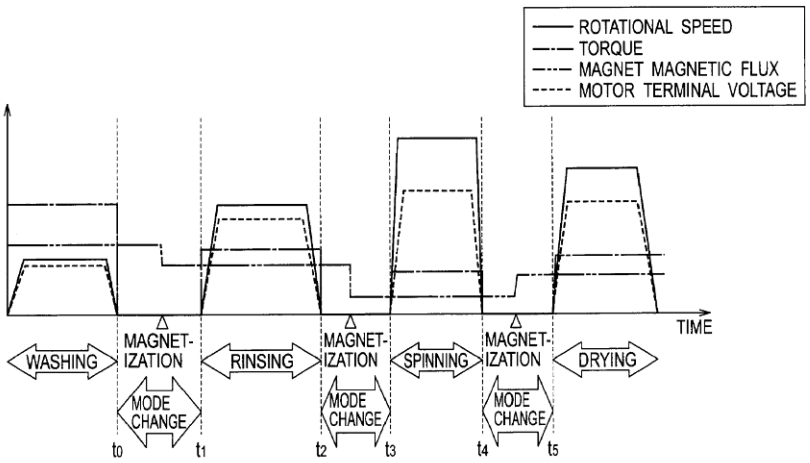

Fig. 1.50 operation mode with the magnetization condition [113]

It is obvious that high magnetization level is selected in the low speed condition to achieve losses reduction and low magnetization level to have high speed operation. However, the details of flux selection strategy are not mentioned by the author and are also not shown in other literature.

1.9 Opportunities for research

1.9.1 Position self-sensing control of FI-IPMSM:

- **Evaluations, limitations, and control methodologies for FI-IPMSM**

Based on the state-of-the-art review, machine design modifications have been shown to reduce the sources of noise caused by the machine itself. The FI-IPMSM is designed for relatively low cross saturation effects and improving self-sensing capability, but implementation alternatives and comparative performance evaluation of the low speed position tracking self-sensing of FI-machines has not yet been investigated. Most of the existing methods have focused on the FW machines and shown acceptable effectiveness. However, applicability and limitations of existing self-sensing methodology to FI-machines are unknown. The impact of reverse saliency (L_d>L_q) of FI-machines on accuracy and robustness is not explored yet and is important for the development of a rigorous methodology for self-sensing control in FI machines.

- **Multi-saliencies sensitivity to injection signals**

Because of a large flux barrier rotor design, the FI-IPMSM often has multiple saliencies that are of significant magnitude. Existing techniques for rotating vector injection use decoupling methods to mitigate spatial harmonic effects, but a series of setup and tuning are required. It is well established that some point tracking methods can be less sensitive to such multi-saliencies. If multi-saliencies are less sensitive to specific injection signal and tracking methodology, it could be possible to use injection signal selection to mitigate the impact of multi-saliencies of FI-machines. A comparison of the results for all the different injection technologies can be used to systematically identify the most effective for multi-saliencies mitigation in FI-machines and this topic has not yet been addressed.

- **The impact of reflected resistance effects on FI-machines self-sensing**

Reflected resistance effects are often ignored in most self-sensing techniques using saliency-based tracking with high frequency injection at low speed. This non-ideal effect could also lead to degradation of self-sensing performance in FI-machines. In this state-of-the-art review, it was found that the degradation of self-sensing performance is more serious in machines designed with large magnets. Since FI-machines feature less magnet material compared to FW-machines, it could have the benefit of lower reflected resistance effects. The investigation of reflected resistance effects in FI-machines can help to identify the limitations they impose position self-sensing performance.

1.9.2 ***Optimum DC voltage selection for FI-machine drive to achieve loss minimization with variable DC bus voltage control***

- **Optimum DC selection control method**

From the state-of-the-art review, it has been found that it is possible to reduce the losses with the variable DC bus voltage. However, if we rely only on the ideal machine parameters to decide the optimum DC bus voltage, the machine parameter estimation errors and the unmodeled machine spatial harmonics usually cause errors in the calculation. The FI-machines feature large spatial harmonics, which can lead even worse calculation errors. To solve this issue, existing methods usually use a lookup table. However, it usually requires time-consuming offline experiments to prepare the table. Therefore, this research aims to develop a control method which can dynamically and accurately minimize the losses, is easy to implement in real time, and has decreased sensitivity to parameter errors and unknown spatial harmonics.

- **The impact of optimum DC selection on self-sensing capability**

From past research, it is known that the inverter dead time effects can significant impact self-sensing performance and that such effect vary with DC bus voltage. Since loss minimization control strategies vary the DC bus voltage, self-sensing performance

can be affected. This combined effect has not yet been investigated. The research will focus on how self-sensing performance can be dynamically improved by integrating it with the optimum DC voltage selection algorithm.

1.9.3 Variable flux via magnetization state control in VFI-IPMSMs

- **Variable flux characteristics via magnetization states in VFI-IPMSMs**

VFI-IPMSMs are designed to have variable magnetization state capability. The influence of magnetization state manipulation on torque output and energy losses of VFI machine will be crucial for the development of control methods. From the state-of-the-art review, the magnetization level can be changed by the d-axis current pulse. However, because of the change of magnetization state during the manipulation process, the output torque could be affected and the pulsating torque could be induced. However, the limitations (e.g. pulsating torque, voltage limits) during magnetization manipulation have not yet been explored. In addition, the current requirement for magnetization manipulation could also cause additional losses and has not been investigated so far. Therefore, the limitations will be investigated and identified for the development of a rigorous methodology for the magnetization level manipulation in this research.

- **Magnetization state manipulation for VFI-IPMSM during loaded condition**

It has been shown in the state-of-the-art review that magnetization has been performed by using a d-axis current pulse that produces zero torque under zero load and zero speed conditions. However, most applications (e.g. vehicles) require dynamically changing the magnetizations level during loaded conditions at normal operating speeds. Under such conditions, methods must be used to reduce the pulsating torque due to the magnetization state change. In the state-of-the-art review, a prerecorded current vector is used to mitigate the pulsating torque for loaded conditions. However, this method requires a detailed lookup table. The main challenge is that every flux state requires a

lookup table for the necessary current vector trajectory. If a continuous and wide range of magnetization state control is required, infinite lookup tables are required, which is difficult to achieve. As a result, only a limited number of magnetization states can be used. Since the losses and the machine's torque/speed region are directly affected by the magnetization state, the reduction in losses is limited and the limited number of torque/speed regions could have unwanted quantization properties. In addition, lookup table methods need identical machines properties (e.g. magnet property, air gap distance). Variations due to manufacturing imperfections could lead to performance degradation. Therefore, this research will focus on developing magnetization state manipulation control methods that achieve a continuous and wide range of magnetization state change (so loss minimization on duty cycle loaded conditions and smooth torque/speed regions can be achieved). Such methods will also mitigate torque pulsations to yield smooth torque control during magnetization state manipulation without using lookup tables during non-zero speed and loaded conditions.

1.9.4 Loss minimization methodology for variable flux machines

- **Loss profiles analysis of the proof-of-concept VFI-IPMSMs under different MS conditions**

From the state-of-the-art review, VFI-IPMSMs are designed to have a variable magnetization state capability which influences on energy loss profiles and T-N capability. However, the experimental evaluation of loss profiles are not presented or documented in any previous research. Since the loss profiles are important for the optimum MS selection strategy for energy savings, it would be very crucial to implement the experimental evaluation. Therefore, this research will focus on the demonstration and documentation of the energy loss characteristic of VF machine. To achieve that, the

inverter capability will be increased from 350V to 600V to implement the full speed range in experiments (6000 rpm).

- **MS selection methodology for loss minimization of VF machines**

In the state-of-the-art review, very few documents discussed the MS selection method. Since the loss varies with MS, a loss minimization MS selection methodology should be developed for VF machine. In addition, because changing the MS requires a current pulse injection which results in additional loss, the control method will need to optimize energy savings from MS selection and minimize the loss from injected current. Therefore, this research will focus on an optimum magnetization state manipulation with respect to loss minimization. In addition, a driving cycle will subsequently be used to evaluate the proposed methodology. Such evaluation explores not only the applicability of proposed method in duty cycle applications but also energy savings of VF machine comparing to normal FW machines.

- **Scalability analysis of vehicle-sized VF machine with the MS selection methodology**

The experimental loss evaluation in the state-of-the-art and the research are based on reduced scale machine for proof-of-concept. Therefore, a scalability analysis is necessary for real applications. A vehicle-sized VF machine could be used for the evaluation of the developed MS selection methodology. In addition, vehicle driving cycle could be the suitable metrics to evaluate the loss of the VF machine.

1.9.5 Magnetization state estimation in zero/low speed conditions

- **An alternative method without relying on EMF signal**

It has been shown in the state-of-the-art review that EMF MS estimation methods work acceptably at high conditions. However, most duty cycle applications (e.g. vehicles) require various speed (zero to high) operations. Under such conditions, EMF methods

cannot work in zero/low speed condition due to the reduced EMF signal. In the state-of-the-art review, a high frequency injection with a single point current detection method is used to extract MS information at machine standstill condition. However, there is no MS estimation methodology provided for machine at rotating conditions. In addition, the single point detection method also suffers from noise issues. Therefore, this research will focus a robust MS estimation method suitable for zero/low speed conditions. A high frequency injection method with closed-loop current vector control (CVC) for MS estimation can be used to extract MS information in zero/low speed conditions. To combine these, a fundamental current observer (FCO) and a synchronous reference frame filter (SRFF) were implemented to separate the fundamental frequency component from the HF component, so that the impact of EMF at rotating conditions on MS estimation accuracy can be reduced. In addition, the system noise immunity could be improved since the vector tracking technique is used for obtaining the amplitude of HF current instead of using a single point current detection method.

- **The impact of varying speed and machine properties on MS estimation**

In previous research, standstill operation or constant speed conditions are used to evaluate the MS estimation method. The impact of varying speed conditions on the MS estimation is unknown. Since duty cycle applications require dynamic speed changes, the impact of variable speed should be investigated. In addition, there are very few documents showing the effect of the machine properties (inductivity, resistivity and magnet resistivity) on MS estimation. The machine modeling in the state-of-the-art demonstrates that the machine property should affect the MS estimation accuracy. Therefore, this research will explore the impact of variable speed varying and variable machine properties on MS estimation. If a decoupling method is needed, a decoupling should be also developed.

Chapter 2 - Position Self-sensing Estimation in FI-IPMSM based on High Frequency Signal Injection

The FI-IPMSM, lends itself to designing for good self-sensing properties. In this section, it begins by evaluating the self-sensing position estimation performance of a suitably designed FI-IPMSM using different high frequency injection methods. An alternative square wave injection method is used to estimate FI-IPMSM rotor position. The experimental results show that the estimation accuracy and system robustness are improved. The results indicate that the proposed method can work well in both FW-IPMSMs and FI-IPMSMs. It is known that secondary saliencies and saliency offset caused by the saturation of the machine can degrade estimation accuracy. Secondary saliencies and saliency offset caused by machine saturation can degrade the estimation accuracy. The modeling, measurement, and decoupling methods that mitigate these undesirable effects are also implemented. Estimation accuracy and dynamics, and torque ripple caused by the injection current are examined for the experimental FI-IPMSM. Comparisons of the methods are also presented.

2.1 Machine Modeling and Properties of Carrier Signal Injection Methods

The machine modeling equation can be expressed as

$$\begin{bmatrix} v_{ds}^r \\ v_{qs}^r \end{bmatrix} = \begin{bmatrix} r_s + pL_d & -\omega_r L_q \\ \omega_r L_d & r_s + pL_q \end{bmatrix} \begin{bmatrix} i_{ds}^r \\ i_{qs}^r \end{bmatrix} + \begin{bmatrix} 0 \\ \omega_r \lambda_{pm} \end{bmatrix} \tag{2-1}$$

If carrier frequency is much higher than the fundamental frequency and the low speed conditions are assumed, carrier frequency components are only considered in this equation. The stator resistance, machine back-emf and off-diagonal term in the above equation can ignored. The carrier frequency model in the rotation reference frame of the machine can be expressed via (2-2) because diagonal term values will much higher than the cross-coupling term. It should be noticed that the diagonal term is proportional to change of the current.

$$\begin{bmatrix} v_{dsh}^r \\ v_{qsh}^r \end{bmatrix} = \begin{bmatrix} R_{drh}^r + L_{dsh}p & 0 \\ 0 & R_{qrh}^r + L_{qsh}p \end{bmatrix} \begin{bmatrix} i_{dsh}^r \\ i_{qsh}^r \end{bmatrix} \tag{2-2}$$

where R_{drh}^r , $R_{qrh,}^r$ L_{dsh} and L_{qsh} are the rotor high frequency resistances and the stator frequency inductance in the d-axis and q-axis respectively. In the steady state, the high frequency ω is injected and the equation above can be expressed as following.

$$\begin{aligned} \begin{bmatrix} v_{dsh}^r \\ v_{qsh}^r \end{bmatrix} &= \begin{bmatrix} R_{drh}^r + j\omega L_{dsh} & 0 \\ 0 & R_{qrh}^r + j\omega L_{qsh} \end{bmatrix} \begin{bmatrix} i_{dsh}^r \\ i_{qsh}^r \end{bmatrix} \\ &= \begin{bmatrix} Z_{dh}^r & 0 \\ 0 & Z_{qh}^r \end{bmatrix} \begin{bmatrix} i_{dsh}^r \\ i_{qsh}^r \end{bmatrix} \end{aligned} \tag{2-3}$$

Z_{dh}^r , and Z_{qh}^r are the high frequency impendence in the d- and q-axis at the rotor reference frame, respectively. If the rotating matrix is defined as:

$$R=\begin{bmatrix} cos\theta_e & -sin\theta_e \\ sin\theta_e & cos\theta_e \end{bmatrix} \tag{2-4}$$

Then, the equation in the rotor reference frame can be transformed into stator reference frame:

$$\begin{bmatrix} v^s_{dsh} \\ v^s_{qsh} \end{bmatrix} = R\begin{bmatrix} Z^r_{dh} & 0 \\ 0 & Z^r_{qh} \end{bmatrix}R^{-1}\begin{bmatrix} i^r_{dsh} \\ i^r_{qsh} \end{bmatrix} \tag{2-5}$$

$$\begin{bmatrix} v^s_{dsh} \\ v^s_{qsh} \end{bmatrix} = \begin{bmatrix} \Sigma Z + \Delta Z cos2\theta_e & \Delta Z sin2\theta_e \\ \Delta L sin2\theta_e & \Sigma Z - \Delta Z cos2\theta_e \end{bmatrix}\begin{bmatrix} i^s_{dsh} \\ i^s_{qsh} \end{bmatrix} \tag{2-6}$$

Where, $\Sigma Z \equiv \frac{Z^r_{dh} + Z^r_{qh}}{2}$, $\Delta Z \equiv \frac{Z^r_{dh} - Z^r_{qh}}{2}$, the ΣZ and ΔZ are the average impendence and differential impendence, respectively. The key models used for the three high frequency injection methods commonly used for saliency tracking and implemented in this work are discussed as following section.

2.1.1 ***Rotating vector injection***

In this method, a rotating signal (voltage/current) is injected in the stationary frame. Voltage is usually preferred as injection signal with VSI (Voltage Source Inverter). The equation is shown as (2-7):

$$v^s_{dqsh} = \begin{bmatrix} v^s_{dqsh} \\ v^s_{dqsh} \end{bmatrix} = v_c \begin{bmatrix} cos\omega_c t \\ sin\omega_c t \end{bmatrix} = v_c e^{j\omega t} \tag{2-7}$$

Where ω_c is the injection frequency, v_c is the injection voltage amplitude. The induced current can be calculated from equation (2-3) [27].

$$\begin{bmatrix} i^s_{dsh} \\ i^s_{qsh} \end{bmatrix} = \frac{1}{Z^r_d Z^r_q}\begin{bmatrix} \Sigma Z + \Delta Z cos2\theta_r & -\Delta Z sin2\theta_e \\ -\Delta L sin2\theta_e & \Sigma Z - \Delta Z cos2\theta_e \end{bmatrix} v_c \begin{bmatrix} cos\omega_c t \\ sin\omega_c t \end{bmatrix} \tag{2-8}$$

$$= I_{c\_p}\begin{bmatrix} cos\omega_c t \\ sin\omega_c t \end{bmatrix} - I_{c\_n}\begin{bmatrix} 2\theta_e - cos\omega_c t \\ 2\theta_e - sin\omega_c t \end{bmatrix}$$

Where $I_{c\_p} = v_c \frac{\Sigma Z}{Z_d^r Z_q^r}$, $I_{c\_n} = v_c \frac{\Delta Z}{Z_d^r Z_q^r}$

It also can be written in the pharos form. The equation is written as

$$i_{dqsh}^s = I_{c\_p} e^{j\omega_c t} - I_{c\_n} e^{j(2\theta_e - \omega_c t)} \tag{2-9}$$

It can be seen from equation (2-9) that the phase of the negative sequence current contains the rotor position information. It should be noted that the saliency difference is required to have the negative sequence signal. Fig. 2.1 illustrates rotating vector injection.

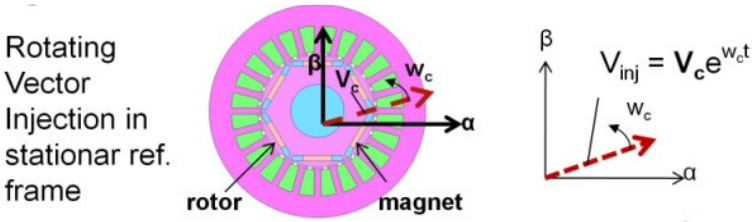

Fig. 2.1 Rotating vector injection in the stationary frame

2.1.2 ***Pulsating vector injection***

A pulsating signal is injected in d-axis or q-axis and the induced current (both in the estimated rotor reference frame) can be used to estimate rotor position. If an estimated d-axis voltage signal is used to inject, the voltage signal is expressed as (2-10).

$$\begin{bmatrix} \hat{v}_{dsh}^r \\ \hat{v}_{qsh}^r \end{bmatrix} = v_c \begin{bmatrix} cos\omega_c t \\ 0 \end{bmatrix} = \frac{1}{2}\boldsymbol{v}_c e^{j\omega_c t} + \frac{1}{2}\boldsymbol{v}_c e^{-j\omega_c t} \tag{2-10}$$

The injection voltage can be seen as injecting a signal point voltage vector in the machine. It also shows the voltage is the combination of two rotating vector. If a position difference between actual machine rotor frame position and injection position is defined:

$$\theta_{err} \equiv \theta_r - \hat{\theta}_r \tag{2-11}$$

The corresponding induced current in the estimated rotor frame can be derived from (2-3)

$$\begin{aligned}\begin{bmatrix} \hat{i}^r_{dsh} \\ \hat{i}^r_{qsh} \end{bmatrix} &= R(\theta_{err}) \begin{bmatrix} 1/Z^r_{dh} & 0 \\ 0 & 1/Z^r_{qh} \end{bmatrix} R^{-1}(\theta_{err}) \begin{bmatrix} \hat{v}^r_{dsh} \\ \hat{v}^r_{qsh} \end{bmatrix} \\ &= \frac{1}{Z^r_{dh}Z^r_{qh}} \begin{bmatrix} \Sigma Z + \Delta Z\cos 2\theta_{err} & -\Delta Z\sin 2\theta_{err} \\ -\Delta L\sin 2\theta_{err} & \Sigma Z - \Delta Z\cos 2\theta_{err} \end{bmatrix} \begin{bmatrix} \hat{v}^r_{dsh} \\ \hat{v}^r_{qsh} \end{bmatrix}\end{aligned} \tag{2-12}$$

From (2-12), it can be seen that the induced high frequency current contains rotor position information. The equation in the cross-coupling term doesn't have DC term so position information can be extracted by using null regulator tracking observer. If injecting voltage in the d-axis is assumed in this case, the estimated q-axis current is expressed as:

$$\hat{i}^r_{qsh} = -\frac{v_c \cos\omega_c t}{2Z^r_{dh}Z^r_{qh}} \Delta Z \sin 2\theta_{err}, \tag{2-13}$$

Where $\Delta Z = \frac{Z^r_{dh} - Z^r_{qh}}{2} = \Delta R_{rh} + j\omega_c \Delta L_{sh,}$ $\Delta R_{rh} = \frac{R^r_{drh} - R^r_{qrh}}{2}$, and $\Delta L_{sh} = \frac{L^r_{dsh} - L^r_{qsh}}{2}$ the induced current model can be written as (2-14)

$$\begin{aligned}\hat{i}^r_{qsh} &= -\frac{v_c \sin 2\theta_{err}}{2(R^r_{drh} + j\omega_c L_{dsh})(R^r_{qrh} + j\omega_c L_{qsh})} \bullet [\Delta R_{rh}\cos(\omega_c t) + j\omega_c \Delta L_{sh}\cos(\omega_c t)] \\ &= \frac{v_c \sin 2\theta_{err}}{2\omega_c^2 L_{dsh}L_{qsh}} [\Delta R_{rh}\cos(\omega_c t) + j\omega_c \Delta L_{sh}\mathrm{Re}(e^{j\omega_c t})] \\ &\approx \frac{v_c \sin 2\theta_{err}}{2\omega_c^2 L_{dsh}L_{qsh}} [\Delta R_{rh}\cos(\omega_c t) - \omega_c \Delta L_{sh}\sin(\omega_c t)]\end{aligned} \tag{2-14}$$

(It is assumed that $\omega_c^2 L_{dsh}L_{qsh}$ is dominant for high frequency injection)

A demodulation (multiplied by $\sin(\omega_c)$ or $\cos(\omega_c)$ and passed through a low pass filter) can be used to separate the signals induced by resistance or inductance. The current induced by the differential inductance and resistance can both be used to extract rotor position signal. The corresponding models are shown as following:

For inductance signal:

$$L_{signal} = \mathrm{LPF}(\hat{i}^{r}_{qsh} \sin(\omega_c t)) = -\frac{v_c}{2\omega_c L_{dsh} L_{qsh}} \Delta L_{sh} \sin 2\theta_{err} = K_L \Delta L_{sh} \sin 2\theta_{err} \quad (2\text{-}15)$$

For resistance signal:

$$R_{signal} = \mathrm{LPF}(\hat{i}^{r}_{qsh} \cos(\omega_c t)) = \frac{v_c}{2\omega_c^{2} L_{dsh} L_{qsh}} \Delta R_{rh} \sin 2\theta_{err} = K_R \Delta R_{rh} \sin 2\theta_{err} \quad (2\text{-}16)$$

Where $K_L = -\frac{v_c}{2\omega_c L_{dsh} L_{qsh}}$, and $K_R = \frac{v_c}{2\omega_c^{2} L_{dsh} L_{qsh}}$

Therefore, both the inductance and resistance signal can be used for the position estimation. It should be noted that the injection voltage can be either q-axis injection or d-axis injection. If an estimated q-axis injection is used, the estimated d-axis current should be used to estimate the rotor position. Fig. 2.2illustrates pulsating vector injection.

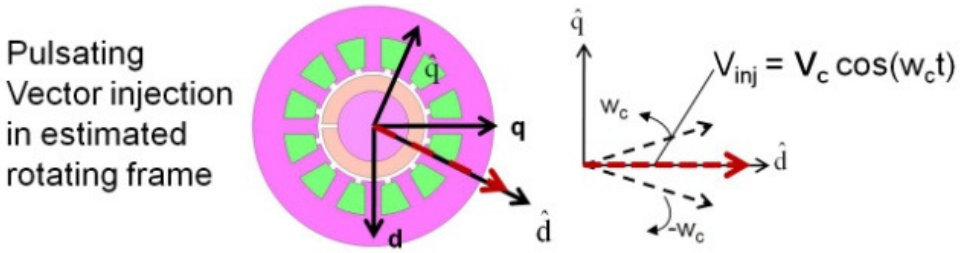

Fig. 2.2 Illustration of pulsating vector injection

2.1.3 ***Square-wave injection***

A square-wave pulsating signal is injected in the estimated frame d-axis or q-axis and the current in the stationary frame can be used to estimate rotor position [38]. It is assumed that a square-wave type voltage $v_{sq}(t)$, with zero average value, is injected.

$$\begin{bmatrix} \hat{v}^{r}_{dsh} \\ \hat{v}^{r}_{qsh} \end{bmatrix} = \begin{bmatrix} v_{sq}(t) \\ 0 \end{bmatrix} \quad (2\text{-}17)$$

The corresponding current model in the stationary frame is used to estimate rotor position.

$$\begin{bmatrix} i^s_{dsh} \\ i^s_{qsh} \end{bmatrix} = \begin{bmatrix} cos(\theta_e) & -sin(\theta_e) \\ sin(\theta_e) & cos(\theta_r) \end{bmatrix} \begin{bmatrix} 1/Z^r_{dh} & 0 \\ 0 & 1/Z^r_{qh} \end{bmatrix} \begin{bmatrix} cos(\theta_{err}) & sin(\theta_{err}) \\ -sin(\theta_{err}) & cos(\theta_{err}) \end{bmatrix} \begin{bmatrix} \hat{v}^r_{dsh} \\ \hat{v}^r_{qsh} \end{bmatrix}$$
$$= \begin{bmatrix} \frac{cos(\theta_e)cos(\theta_{err})}{Z_{dh}} + \frac{sin(\theta_e)sin(\theta_{err})}{Z_{qh}} & \frac{cos(\theta_e)sin(\theta_{err})}{Z_{dh}} - \frac{sin(\theta_e)cos(\theta_{err})}{Z_{qh}} \\ \frac{sin(\theta_e)cos(\theta_{err})}{Z_{dh}} - \frac{cos(\theta_e)sin(\theta_{err})}{Z_{qh}} & \frac{sin(\theta_e)sin(\theta_{err})}{Z_{dh}} + \frac{cos(\theta_e)cos(\theta_{err})}{Z_{qh}} \end{bmatrix} \begin{bmatrix} \hat{v}^r_{dsh} \\ \hat{v}^r_{qsh} \end{bmatrix} \quad (2\text{-}18)$$

If a square-wave type voltage $v_{sq}(t)$, with zero average value, is injected in the d-axis. From (2-18), the corresponding current model which contains the rotor position can be obtained and shown as (2-19).

$$\begin{bmatrix} \Delta i^s_{dsh} \\ \Delta i^s_{qsh} \end{bmatrix} = v_{sq}(t)\,\Delta T \begin{bmatrix} \frac{cos(\theta_e)cos(\theta_{err})}{Z_{dh}} + \frac{sin(\theta_e)sin(\theta_{err})}{Z_{qh}} \\ \frac{sin(\theta_e)cos(\theta_{err})}{Z_{dh}} - \frac{cos(\theta_e)sin(\theta_{err})}{Z_{qh}} \end{bmatrix} \quad (2\text{-}19)$$

Considering the polarity of injection and under the assumption of θ_{err} equals zero, the equations can be modified as (2-20).

$$\begin{bmatrix} \Delta i^s_{dsh\_cal} \\ \Delta i^s_{qsh\_cal} \end{bmatrix} = \text{sign}(v_{sq}(t)) \begin{bmatrix} \Delta i^s_{dsh} \\ \Delta i^s_{qsh} \end{bmatrix} = \frac{v\Delta T}{Z_{dh}} \begin{bmatrix} cos(\theta_e) \\ sin(\theta_e) \end{bmatrix} \quad (2\text{-}20)$$

(Under assumption $\theta_{err} \approx$ zero)

Similar derivation can be applied to the q-axis square-wave type voltage injection, and the position signal equation is shown as (2-21)

$$\begin{bmatrix} \Delta i^s_{dsh} \\ \Delta i^s_{qsh} \end{bmatrix} = v_{sq}(t)\,\Delta T \begin{bmatrix} \frac{cos(\theta_e)sin(\theta_{err})}{Z_{dh}} - \frac{sin(\theta_e)cos(\theta_{err})}{Z_{qh}} \\ \frac{sin(\theta_e)sin(\theta_{err})}{Z_{dh}} + \frac{cos(\theta_e)cos(\theta_{err})}{Z_{qh}} \end{bmatrix} \quad (2\text{-}21)$$

(Under assumption $\theta_{err} \approx$ zero)

$$\begin{bmatrix} \Delta i^s_{dsh\_cal} \\ \Delta i^s_{qsh\_cal} \end{bmatrix} = \frac{v\Delta T}{Z_{qh}} \begin{bmatrix} -sin(\theta_e) \\ cos(\theta_e) \end{bmatrix}$$

From the equation above, it can be observer that the $\Delta i^s_{dqsh\_cal}$ signal contain the rotor position information.

*2.1.4 **Alternative square-wave injection method***

In [38], a square-wave pulsating signal was injected in the estimated frame d-axis or q-axis, and the current in the stationary frame was used to estimate rotor position in previous section. However, it was assumed that θ_{err} is equal to zero and it is not true for all operating conditions and machines. In this chapter, an alternative estimation model is used. The current in the estimated frame is used to estimate rotor position. If a square-wave voltage, $v_{sq}(t)$, is injected in the estimated d-axis, the corresponding current model in the estimated q-axis frame is shown in (2-22)

$$\hat{i}^{r}_{qsh} = -\frac{v_{sq}(t)\, sin2\theta_{err}}{2\omega_{sq}^{2} L_{dsh} L_{qsh}} \Delta L_{sh} \tag{2-22}$$

From (2-22), q-axis current induced by the differential inductance can be used to extract rotor position over the full range of operating conditions. Fig. 2.3 illustrates the square wave injection method. The detail rotor estimation process and performance comparison with previous method is discussed in later.

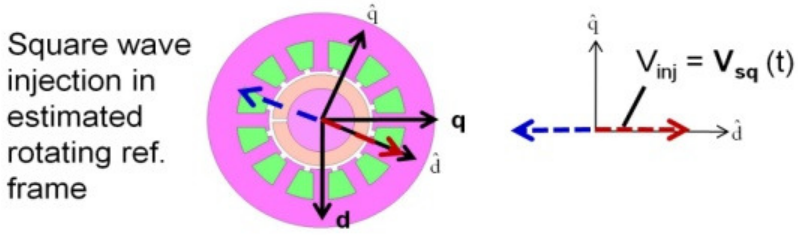

Fig. 2.3. Square wave voltage injection

2.2 Non-ideal Effects

In the real application, the machines usually have other non-ideal effects which cause the some assumptions in the previous section cannot be valid. The nonlinearity effects degrade estimation accuracy. In this section, three critical non-ideal effects that degrade the estimation accuracy are evaluated. These include inverter effects and machine multi-saliency and machine transient (high frequency) resistance effects.

2.2.1 Inverter non-linearity effect

The inverter non-linearity effect causes the voltage error which results in the rotor position estimation errors. Several effects cause the non-linear inverter behavior. It includes zero-current clamping effect, parasitic capacitance of semiconductors, switching dead-time of power device, turn-on and turn-off times of the IGBT's, and voltage drop across the semiconductor. These effects are more apparent during the switching period of power device. As a result, the nonlinearity effects usually cause six times frequency oscillation with respect to the fundamental excitation.

To mitigate the nonlinearity effect, a model of dead time effect can be established. It is reported that the voltage error is directly proportional to the current passing through semiconductor and inversely proportional to the parasitic capacitance[59]. Therefore, the dead-time can be modeled as an active resistance in the inverter circuit. A linear model as a function of the current can be used to describe the voltage error and to decouple the dead-time effect[125]. Two simple methods can be used to decouple the dead-time effect[19]. One method only consider the sign of the phase current and the other use amplitude the phase current and includes the slope relative to the value of phase current for low-current region. The compensation of voltage error based on the two methods is given as (2-23) and (2-24). The two methods are shown as Fig. 2.4.

Method 1:

$$v(i) = \text{sign(i)}\ v_{error} \tag{2-23}$$

Method 2:

$$v(i) = (i \times \frac{1}{k})\ \ v_{error} \ \text{ for } |i| < k$$
$$v(i) = \text{sign(i)}\ v_{error} \quad \text{for } |i| > k \tag{2-24}$$
$$v_{error} = \frac{T_d}{T_s} v_{dc}$$

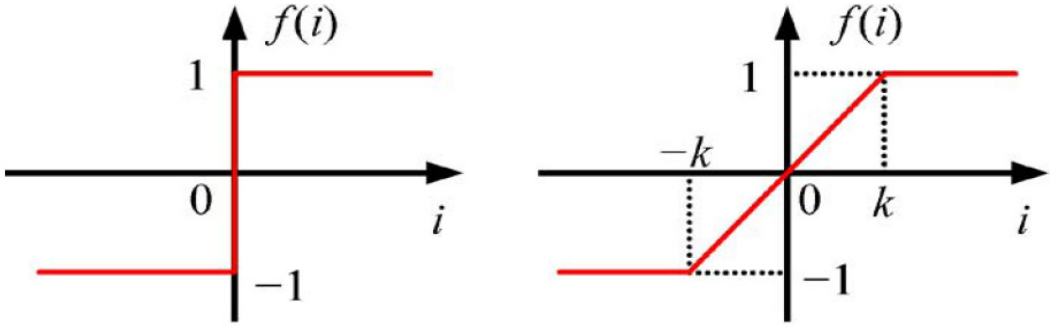

Fig. 2.4 Two simple methods used for deadtime compensation[19]

The experimental results with and without dead-time compensation is shown as Fig. 2.5. It can be seen that it can be seen that the 2nd harmonics and 6th harmonic can be greatly reduced if dead-time effect decoupling is implemented. In the estimation result, it is found that the DC offset of estimation error and is greatly reduced. It can be concluded that the dead-time effect generate a fake saliency superimposed on the 2nd harmonic which is used for extracting the rotor position signal. In addition, the estimation error is also reduced since the additional harmonics (6th harmonics errors) caused by the inverter dead-time are also reduced.

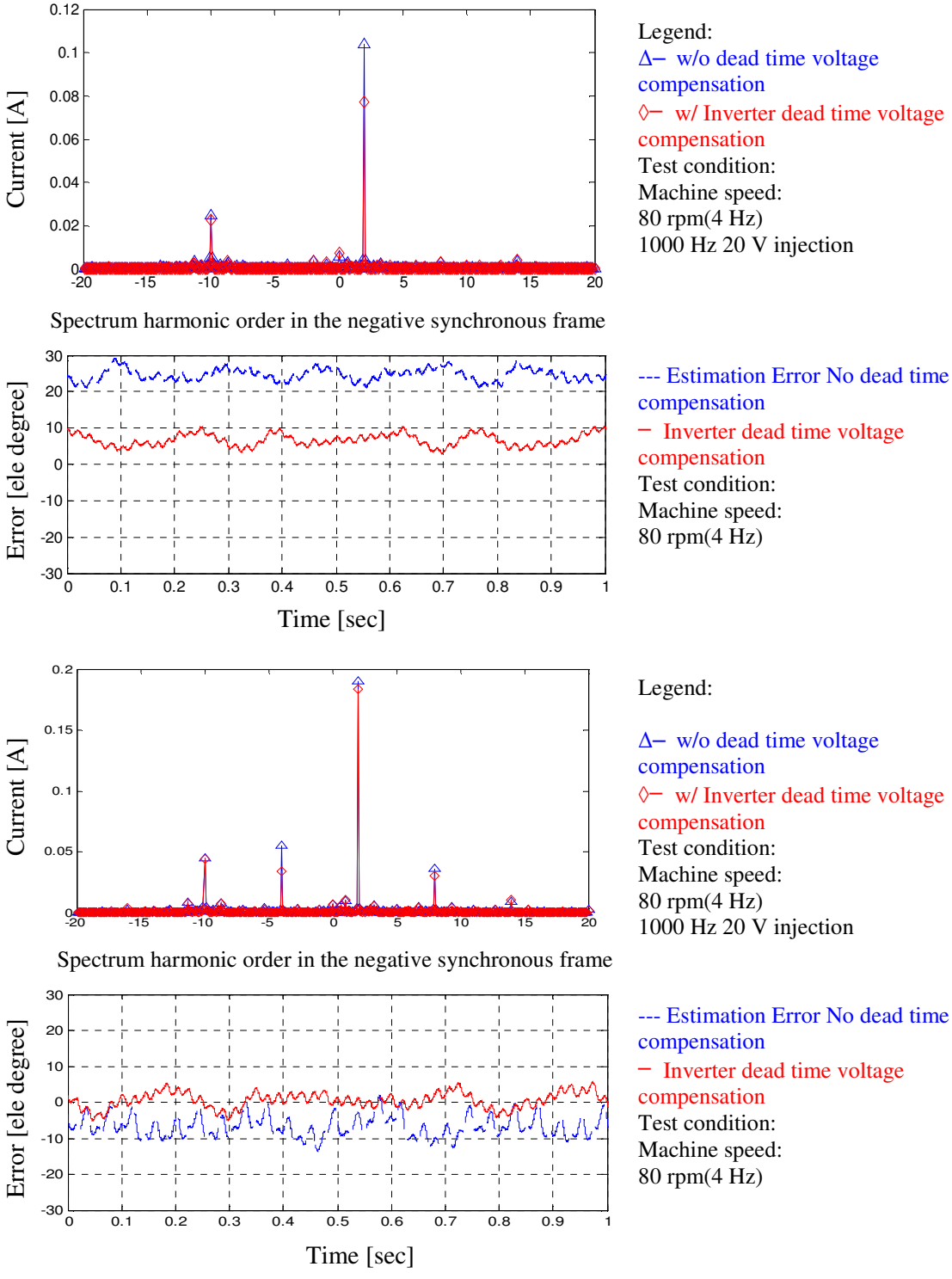

Fig. 2.5 FFT of the phase A current with 0%, 15% rated current (from top to bottom) and the estimation result is based on the rotating vector injection method.

Voltage compensation is based on the phase current direction, however, the current direction is difficult to predict when phase current passing zero. The reasons include the zero-current clamping effect, parasitic capacitor charge and discharge, and additional voltage drop on the switching devices[59]. Therefore, the dead-time effect problem is especially serious when current across zero since non-linear characteristic is difficult to decouple.

From above discussion, it is obvious that reducing the high frequency current passing zero can mitigate dead-time effect. Fig. 2.6 shows the induced current with different voltage injection methods. It can be seen that the carrier voltage would be zero with the q-axis voltage injection so the induced high frequency zero-crossing will be minimized. Therefore, the dead-time effect can be reduced. For d-axis pulsating vector injection and rotating vector injection, high frequency zero-crossing current is not minimized. In conclusion, it is possible to reduce dead time effect with q-axis pulsating voltage injection.

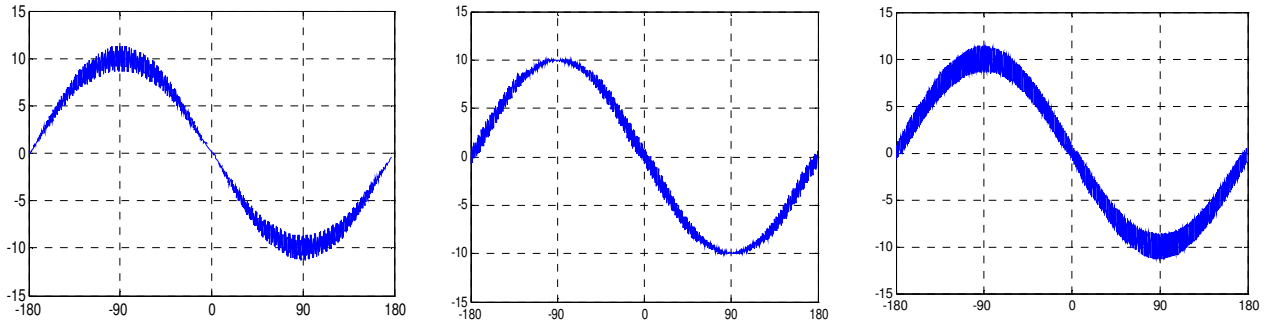

(a) (b) (c)

Fig. 2.6 The experimental result of induced phase current with respect to the rotor position with different voltage injection methods (a) q-axis pulsating vector (b) d-axis pulsating vector(c) rotating vector

Another approach to reduce the dead-time effect is to increase the injection voltage. Dead time effect causes the voltage error so the percentage of voltage error can be reduced with higher injection voltage. In real application, if higher injection voltage is

used, the injection voltage frequency must be increased simultaneously. If the frequency is not increased, the resulting high frequency current will become very high. As a result, the induced current will causes severe pulsating torque and additional losses. To achieve the highest injection voltage, the square wave type injection method is the most suitable candidate. With the square wave injection, the injection frequency can be increased to half PWM switch frequency which is the theoretical maximum limit.

2.2.2 ***FI-IPMSM Saliency image distortion caused by secondary saliencies and inverter nonlinearity effect***

Multiple saliencies and saliencies induced by saturation are investigated in this section. Again, the saliency-based self-sensing assumes that only single position-depend saliency exists in machines and rotates periodic with respect to the rotor electric frequency of $2\omega_e$. As stated before, the inverter nonlinearity effects caused fake saliency which result in the significant limitations on the rotor position estimation. In this section, with inverter dead-time compensation, the negative sequence current in the negative synchronous frame is used to analyze secondary saliencies. The FEA result is compared to the experimental result to evaluate the multiple saliency effects. The purpose is to avoid the impact of the non-linear inverter behavior.

In these tests, 20 V, and 1000 Hz rotating carrier voltage (resulting 4% rated current) is injected to examine the current induced by saliencies. Both fundamental and positive sequence current are removed based on the Synchronous Reference Frame Filter(SRFF)[27].

The FFT plot without the fundamental current excitation and light load conditions (0.15 [pu]) are shown in Fig. 2.7. It can be found the major components of I_{c_n} are quite clean and locate at 2^{nd} order. In addition to the major saliency, both the FEA and experimental result show an additional major component is also found around the $-10\omega_c$ (-40Hz). It shows that a -10^{th} order multi-saliency exists in FI-IPMSM.

In light load conditions (0.15 [pu]), it clearly shows that besides the -10^{th} order harmonics, two major saliencies locate at $+8^{th}$ and -4^{th} order. These two harmonics is exactly the six times of the machine fundamental frequency. However, they are not shown in the FEA results. Therefore, it is very possible that the saliencies are induced by the inverter dead-time effect.

As load is increased to 0.5 pu It can be found that the ratio of harmonics component to the 2^{nd} negative current component (h =2) doesn't have serious change. This is the advantage of FI-IPMSM because L_q will not saturated as the load increased (reversal saliency $L_d < L_q$ and). The additional harmonics of $+8^{th}$ order and -4^{th} order are also decreased. As the load increase, the period of phase current zero-crossing is reduced. Therefore, the dead-time effect can be reduced and the amplitude fake saliencies are decreased. Furthermore, it can be found that an induced saliency (1^{st} order harmonic) increase as the load increase. The induced saliency is mainly introduced by the saturation of the machine.

At 1 [pu] fundamental excitation condition, it clear shows that fake saliency induced by the dead-time effect is much smaller. However, the induced saliency (1^{st} order) becomes more serious.

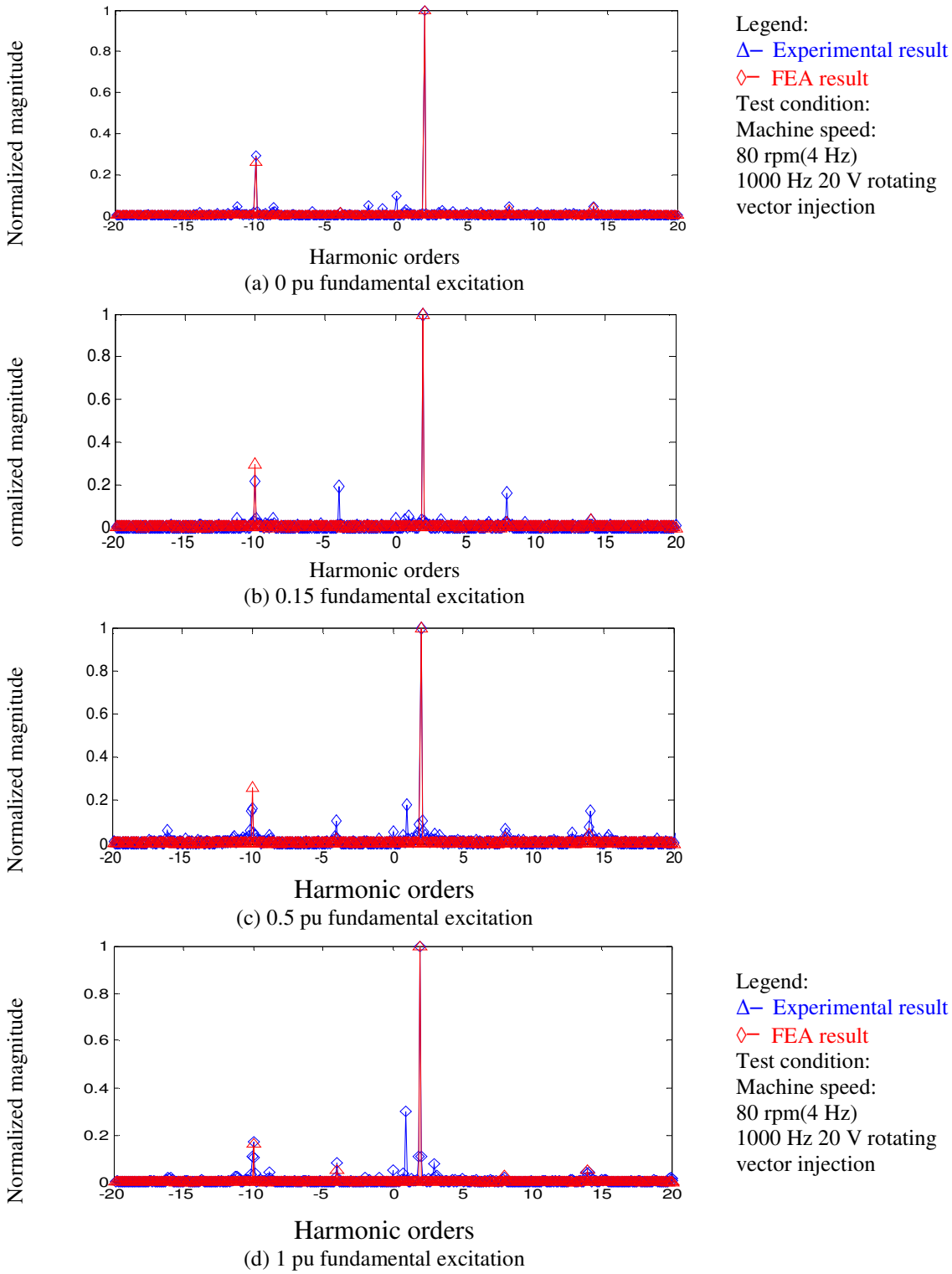

(a) 0 pu fundamental excitation

(b) 0.15 fundamental excitation

(c) 0.5 pu fundamental excitation

(d) 1 pu fundamental excitation

Fig. 2.7 The harmonics comparison of experimental and FEA result

Finally, for more easily to see the variation of saliencies, the experimental result with 3-D plot relative to all the negative current components at different fundamental currents is depicted in Fig. 2.8. It can be seen that -4th and 8th order harmonics are more severe under low load conditions. This content very possibly result from inverter nonlinearity effect (± 6ω_e). The 1st order harmonic harmonics increase as the load increases so it should be the saturation-induced saliency. To improve the estimation accuracy, a decoupling technique is used to remove the effect of the additional harmonics.

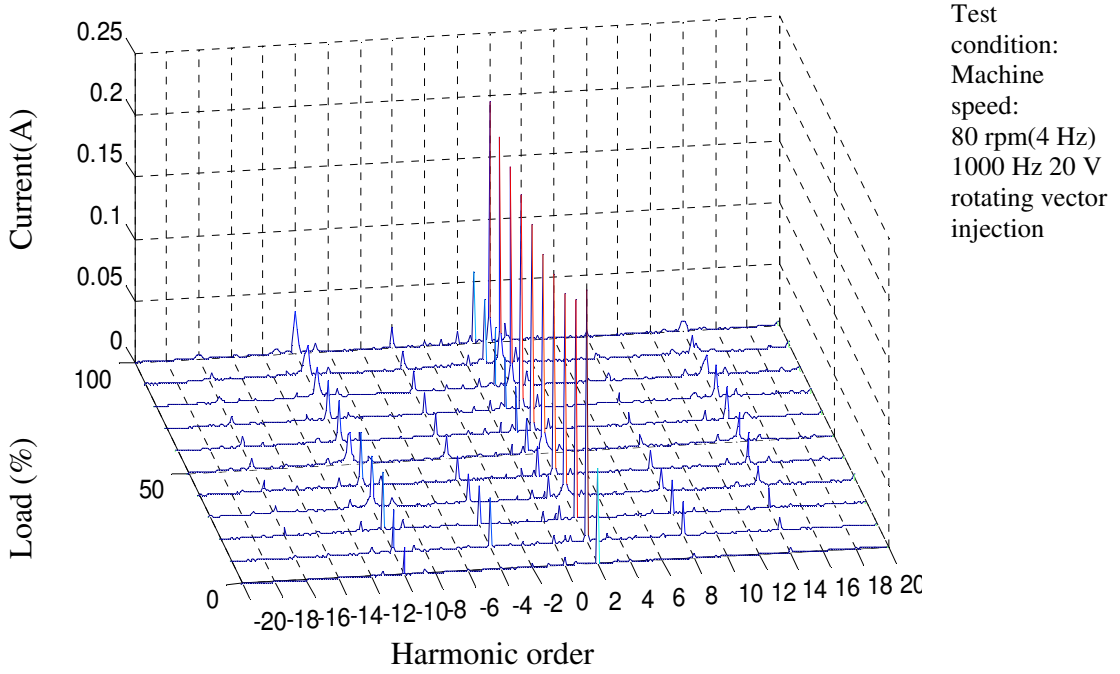

Fig. 2.8 Negative current component at different fundamental current conditions in the negaitve sequence carrier synchous frame

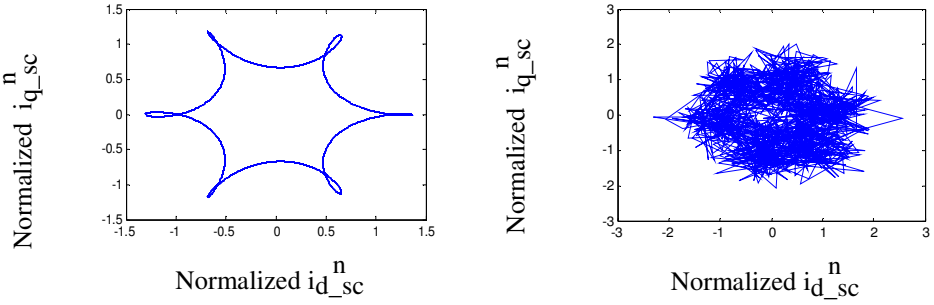

(a) 0 [pu] fundamental excitation

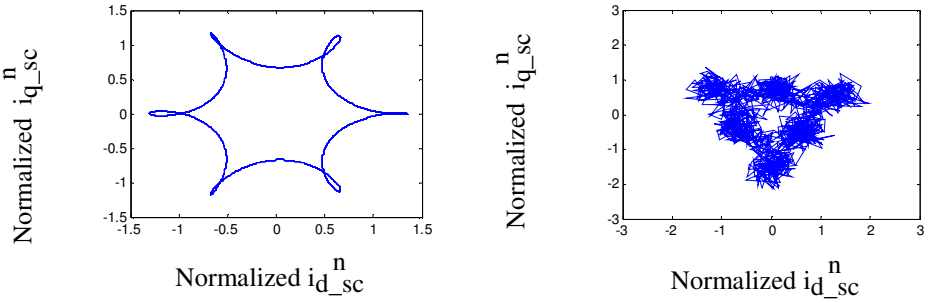

(b) 0.15 [pu] fundamental excitation

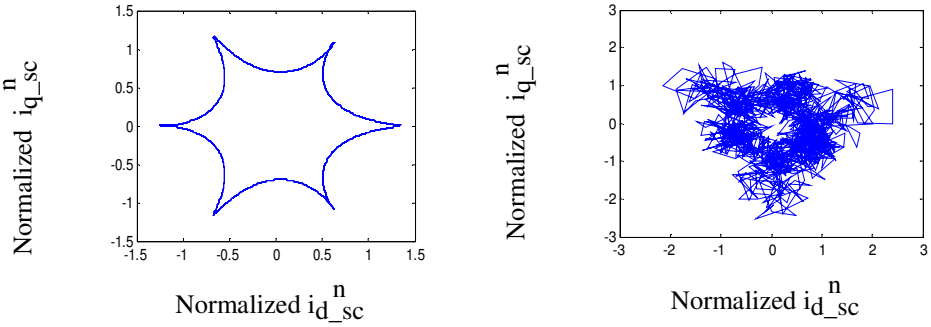

(c) 0.5 [pu] fundamental excitation

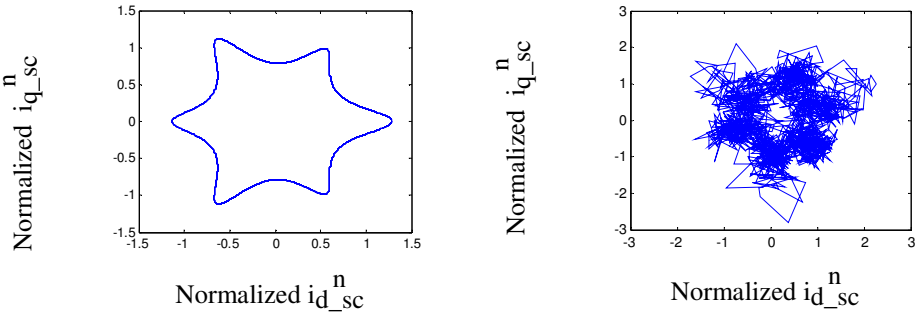

(d) 1 [pu] fundamental excitation

Fig. 2.9 (Left) FEA result of saliency image in the negative sequence carrier synchronous frame (Right) Experimental result in the negative sequence carrier synchronous frame (after removing fundamental and positive current). Experimental test condition: Machine speed:80 rpm(4 Hz) 1000 Hz 20 V rotating vector injection

Fig. 2.9 shows the FEA saliency image result and experimental saliency image result with 0, 0.15, 0.5, and 1 [pu] fundamental excitation. First, it can be seen that the experimental result has more noise compared to FEA results. Normally, the high frequency noise which caused by inverter switch, non-perfect of motor winding, and dead-time effect can be filter out by tracking observer. Secondly, the experimental saliency images have significant change with the load conditions but saliency images FEA don't. From the comparison of FFT result in Fig. 2.7, it can be known that the additional saliencies induced cause the distortion of saliency image. Thirdly, it can be expected that this distorted saliency image degrade the estimation performance. The further compensation and decoupling technique is necessary to provide the reliable saliency tracking and ensure the accuracy of rotor position estimation.

In conclusion, several observations can be made based on Fig. 2.7, Fig. 2.8 and Fig. 2.9. First of all, the 2^{nd} harmonic used for tracking is not reduced as the load increase. As stated before, it is the major advantage of FI-IPMSM.

Secondly, the +8th order and -4th order harmonics is very possibly induced by dead time effect. According to the FEA results, the multiple saliencies induced harmonics at +8th and -4th order is quite small. However, a significant value of +8th and -4th order harmonics are seen in the experimental results compared to the FEA simulation in which the inverter is modeled as an ideal power amplifier. Furthermore, it can be observed that the $+8^{th}$ and -4^{th} harmonics are reduced as the load increases. It is known that dead-time effect reduce as the load increase since zero clamping effect is less severe. As a result, it can be concluded that the +8th order and -4th order harmonics is mainly induced by the inverter dead-time effect.

Thirdly, a significant 1^{st} harmonic is found in FI-IPMSM when the fundamental excitation over 0.5 [pu]. It is known that the induced saliency increases as the increase of

load. The same effect is found in this experiment. As a result, it can be concluded that the 1st harmonic is induced by the induced saliency which is mainly caused by the machine saturation. It can be expected that estimation accuracy will be degrade seriously by the induced saliency. Decoupling must be implemented to mitigate this effect.

Last but not least, the dead-time effect can be reduced if the DC bus voltage can be adjusted to lower voltage. It can be expected that the saliency image distortion will be mitigated A further test can be performed by reducing the DC-bus voltage to mitigate the dead-time effect. If these six times saliencies reduced significantly with low DC bus voltage, it can be concluded that the inverter dead-time effect is mitigated.

2.2.3 ***High frequency resistance***

Normally, in (2-3), the high frequency resistance and stator resistance is small and can be ignored. However, in some cases, the resistance is relatively larger and seriously affects the estimation accuracy. From [126], (2-3) can be further modified as:

$$\begin{bmatrix} v_{dsh}^r \\ v_{qsh}^r \end{bmatrix} = \begin{bmatrix} R_{drh}^r + L_{dsh}p & 0 \\ 0 & R_{qrh}^r + L_{qsh}p \end{bmatrix} \begin{bmatrix} i_{dsh}^r \\ i_{qsh}^r \end{bmatrix} + R_{dqs} \begin{bmatrix} i_{dsh}^r \\ i_{qsh}^r \end{bmatrix} \quad (2\text{-}25)$$

Where, $R_{dqs} = \begin{bmatrix} R_{dds}^r & R_{dds}^r \\ R_{qds}^r & R_{qqs}^r \end{bmatrix}$

The R_{dqs} matrix is transform from stator to the rotor reference frame, and it is physically original from imbalance of stator windings, cabling, and inverter. The high frequency rotor resistance R_{drh}^r and R_{qrh}^r account for the eddy current reflect to the stator side. Therefore, it is important to examine the high frequency resistance effects in the FI-IPMSM. Fig. 2.10 shows high frequency evaluation of the FI-IPMSM (using pulsating vector injection) and it demonstrates a nearly constant power factor. This shows the FI-IPMSM's advantage that the resistance effect can be ignored and no further decoupling is needed.

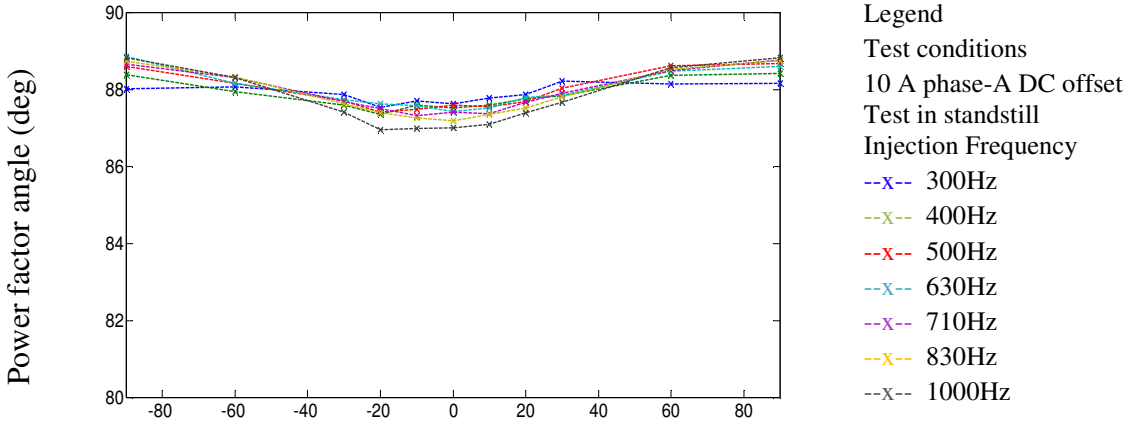

Injection angle with respect to d-axis (ele. deg)

Fig. 2.10 Power factor angle dependent to different injection frequency injection angle for

2.3 Rotor Estimation Methods and Accuracy Improvement Methods

2.3.1 Rotating vector injection with additional harmonics decoupling

The rotor position information extracting method with rotating vector injection is discussed in this section. Estimation accuracy improvement is also discussed.

First of all, the negative sequence current containing rotor position is needed to be extracted. To obtain the negative sequence signal, a SRFF can be used to filter fundamental current and positive sequence current in (2-9). The phase of the negative sequence represents the rotor position which can be extracted by using tracking observer with vector cross product. The error signal feeding into the tracking observer is formed by taking the vector cross-product between the estimated unit vectors of the negative-sequence carrier signal:

$$\varepsilon_{error} = \hat{I}_{c\_n} \text{ x } I_{c\_n} = \sin(2(\hat{\theta}_r - \theta_r)) \tag{2-26}$$

The tracking observer forces the error to become zero, so the phase of negative sequence can be tracked (i.e. rotor position). The signal processing block diagram and the tracking observer with single saliency model is shown as Fig. 2.11.

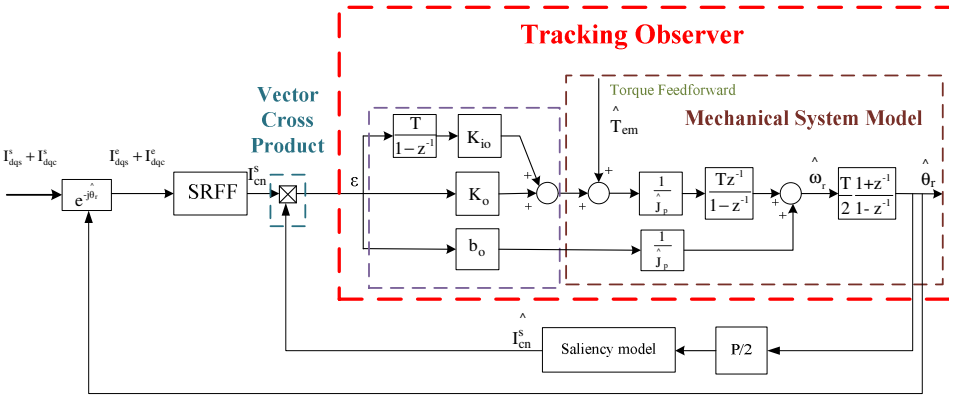

Fig. 2.11 Simplified position estimation single process and tracking observer for rotating vector based injection

In Fig. 2.11, single saliency model is only considered. As stated before, additional saliencies, if present in significant amplitude, must be included in the saliency image [27, 28]. If not included, then the phase of $+2\omega_e$ harmonic used for estimating rotor position will be affected and will degrade the estimation accuracy. These additional saliency harmonics can be introduced by saturation (saturation-induced saliency), machine winding imperfections (multi-saliencies), high frequency rotor/stator resistance and inverter-nonlinearity (fictitious saliency). These additional saliencies exist in every real system. To improve the estimation accuracy, harmonic decoupling methods are usually used to deal with additional saliencies. Based on the discussion above, the model in Fig. 2.11 should be modified to improve the rotor estimation accuracy.

The harmonics decoupling method is usually used to deal with additional saliencies. The measurement and decoupling techniques can be performed by off-line measurement and decoupling [24, 28] or on-line adaptive decoupling [29, 65, 126].

First, for the off-line method, the phase and magnitude of additional saliencies are measured off-line. As shown in last section, the spatial harmonics are dependent on the loading conditions. Therefore, to have the accurate additional saliencies decoupling, their magnitude and phase for every loading condition is needed to be well measured.

Secondly, for the adaptive decoupling techniques, the learning processing is applied to avoid the tedious offline measurement. The learning processes can automatically adaptively decouple load-dependent harmonics. Time consuming measurement is avoided by this method since the estimation parameter used for decoupling is provided by the learning process. Only the off-line measurement and decoupling technique is used at this time. Further on-line decoupling techniques would be the future research work.

The implementation of tracking observer with harmonic decoupling is shown as Fig. 2.12. Two types of harmonics: stationary saliency decoupling and position-dependent saliency decoupling are modeled for decoupling. The causes of stationary saliency are from the induced current unbalance or the current sensor gain error. The causes of position-dependent are stated as in last section. Since the negative current sequence current is used to estimate rotor position, these additional harmonics should be decoupled before the cross-product position estimation of the tracking observer.

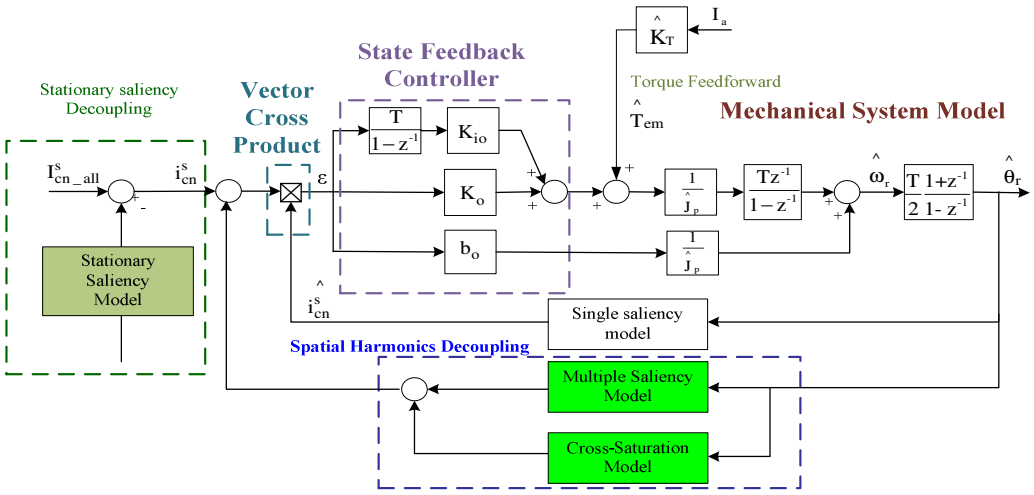

Fig. 2.12 Saliency tracking observer with additional harmonics decoupling

The stationary saliency is not related to the position so it appears as constant offset. As shown in (2-27), it can be modeled as constant current component in the negative synchronous frame.

$$I_{dq\_c\_dc}^{n} = I_{c\_n\_dc} \qquad (2\text{-}27)$$

From the 3-D plot in Fig. 2.8, the dc component is not a major component in this system, but it may be very serious in other system. For the additional harmonic decoupling, since they are position-dependent, the decoupling must be based on the estimation rotor position. The model of the additional can be expressed as

$$I_{dq\_c\_har}^{n} = jI_{c\_n\_dc}\, e^{(-j\omega_c t + h\theta_e)} \tag{2-28}$$

For $(h = 3n \pm 1, 3n \pm 2)$ $n = 0,1,2,3...$

The phase and magnitude measurement result of additional harmonic is shown as Fig. 2.13. The measurement is performed with the encoder to have better parameter estimated accuracy. If the additional saliency-induced current is well estimated, the additional harmonics induced by motile-saliencies and dead-time effect can be reduced greatly by using decoupling technique.

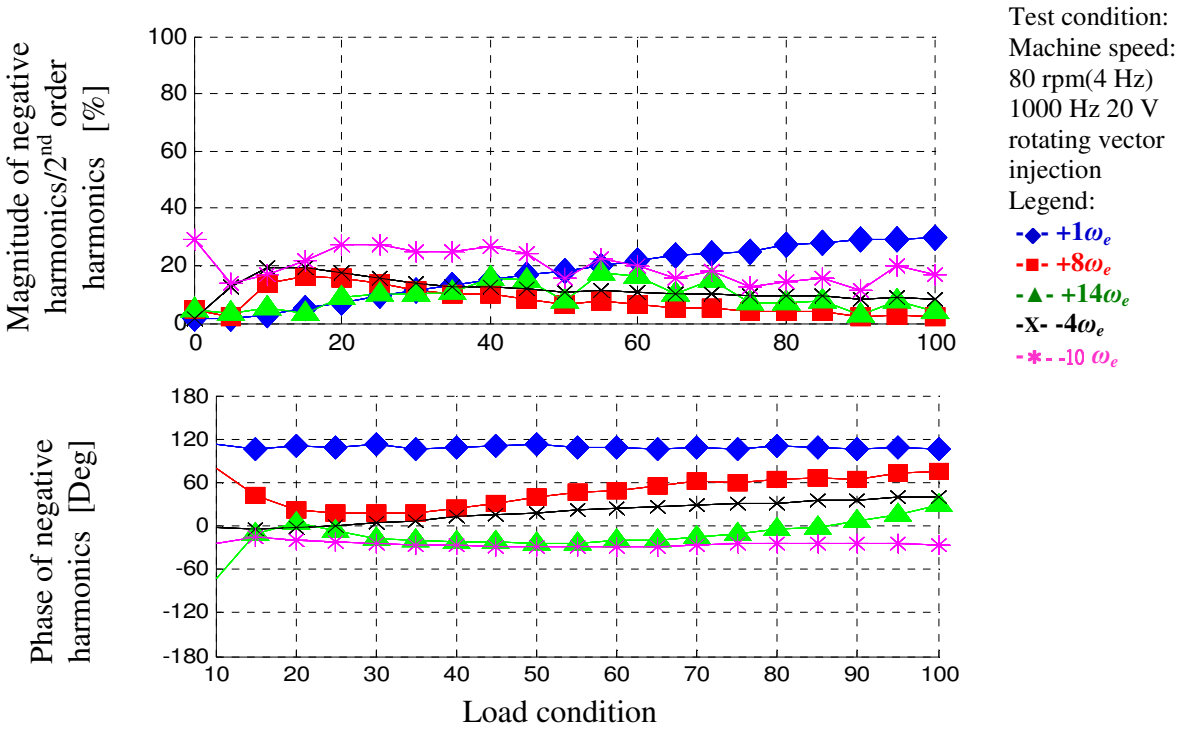

Fig. 2.13 Magnitude and phase of current induced by additional saliencies in the negaitve sequence carrier synchous frame

Fig. 2.14 shows the comparison of with and without decoupling implementation in the negative carrier frequency synchronous frame. From the FFT plot, it can be observed that the additional harmonic is greatly reduced. In addition, the saliency image

is changed to a nearly one unit circle. Therefore, it can be expected that the estimation accuracy can be greatly improved.

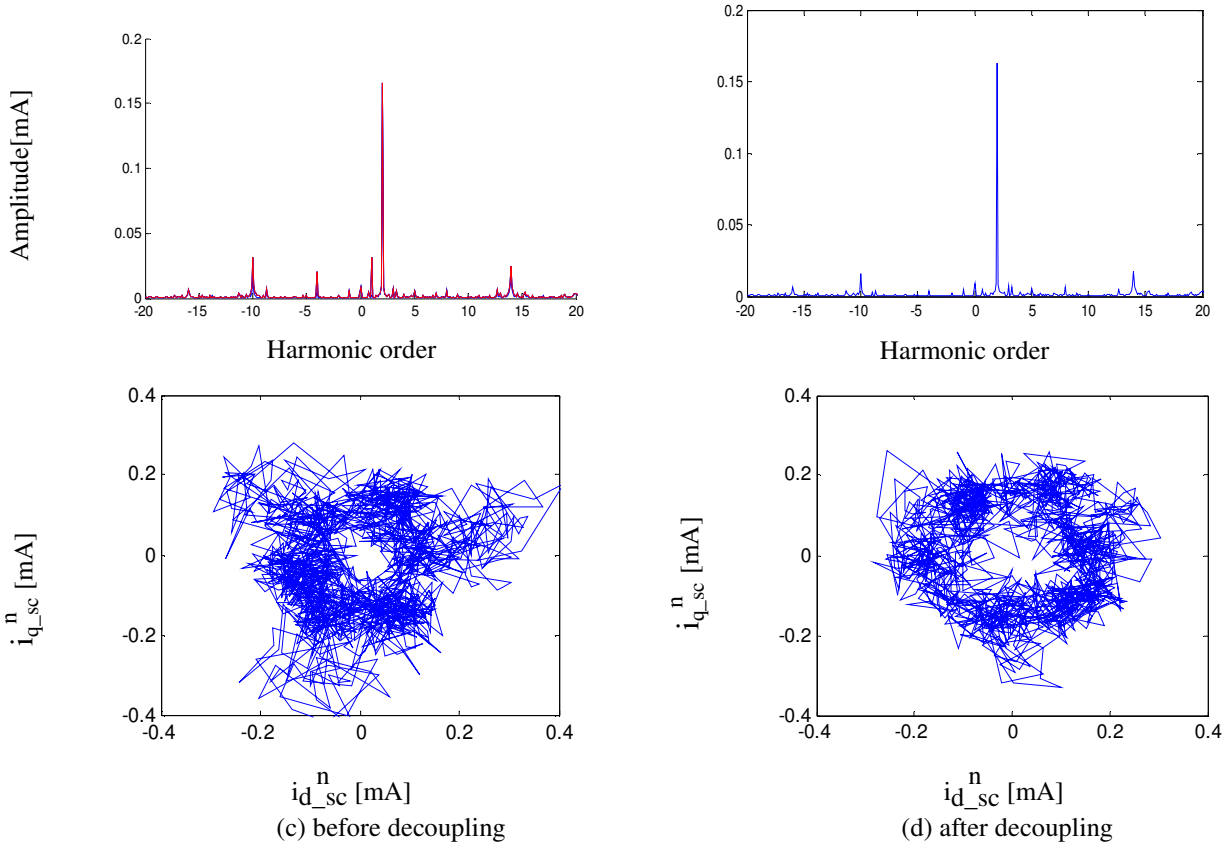

(c) before decoupling (d) after decoupling

Fig. 2.14 (a) Frequency domain analysis with decoupling (b) (without decoupling c) saliency image without decoupling (c) with decoupling (In the negative sequence $-\omega_c$ synchronous frame with the 50% fundamental current excitation experimental and test condition:
Machine speed:80 rpm(4 Hz) 1000 Hz 20 V rotating vector injection)

The saliency tracking result is shown as Fig. 2.15. It can be seen that the error is dominated by the induced 1st harmonics per electric cycle (0.25 sec in this case). After the implementation of the additional harmonics decoupling (1st, 8th, -4th, -10th), the position estimation is significantly improved. It can be observed that small pulsating errors still exist, and they could be possibly from the magnitude and phase change in the transient operation.

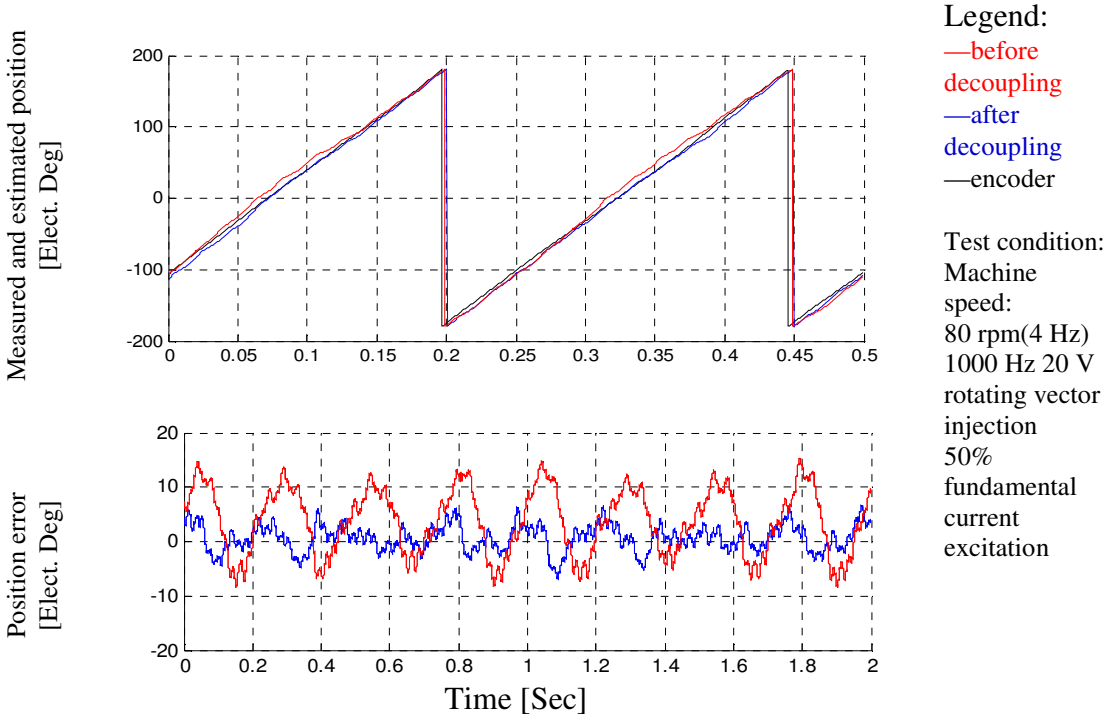

Fig. 2.15 The comparison of rotor position estimation with and without the implementation of additional harmonics decoupling

2.3.2 *Pulsating vector injection*

The rotor position information extracting method with pulsating vector injection is discussed in this section. Cross-coupling effect and estimation accuracy improvement method is also discussed.

After the demodulation process, the signal of estimated current induced from inductance is expressed in (2-15), and it is rewritten here for convenient.

For inductance signal:

$$L_{signal} = \mathrm{LPF}(\hat{i}_q^r \sin(\omega_c t)) = -\frac{v_c}{2\omega_c L_{dsh} L_{qsh}} \Delta L_{sh} \sin 2\theta_{err} = K_L \Delta L_{sh} \sin 2\theta_{err} \quad (2\text{-}29)$$

From (2-29), the current signal can be put into tracking observer which forces θ_{err} become zero so the rotor position can be extracted. The signal processing block diagram is shown as Fig. 2.16. The major difference of pulsating injection and rotating vector injection is that the PHASE of current vector is used to estimate rotor position in the rotating vector injection and the AMPLITUDE of the cross-coupling term is used in the pulsating vector injection method.

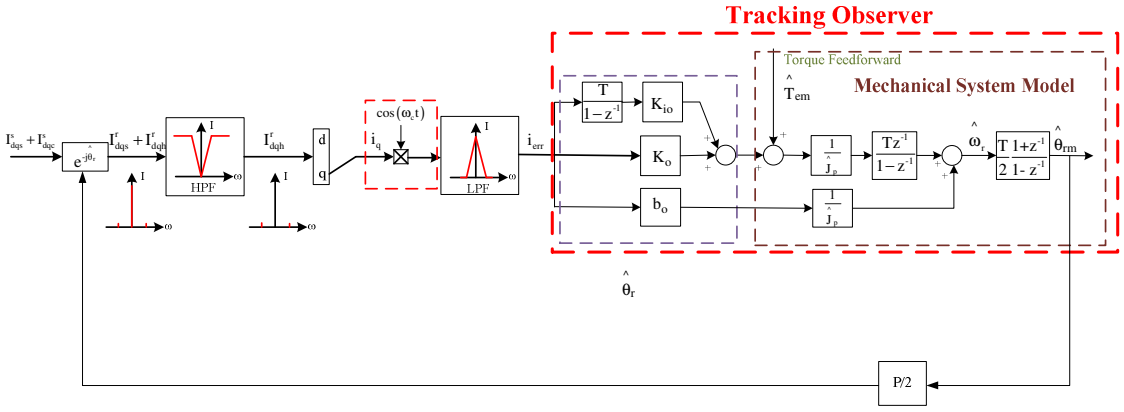

Fig. 2.16 Simplified single process and tracking observer for pulsating base on voltage based position estimation

The pulsating injection method also has non-ideal effect. It is reported that cross-coupling inductances result in phase offset of induced current. The estimation accuracy is

degraded by the cross-coupling inductances [63, 67]. Ideally, the mutual inductance is zero. However, mutual inductance normally exists in every machine, so the flux can no longer align with the real injection axis. It will result in the phase offset of rotor estimation.

If pulsating voltage is injected in estimated d-axis frame and cross-saturation is consider, the induced q-axis current in estimated frame in (2-15)can be modified as

$$\hat{i}^{r}_{q\_modified} = -\frac{v_c \cos\omega_c t}{2L^{r}_{d}L^{r}_{q}-L^{2}_{mh}}\left[\Delta L_{sh}\sin 2\theta_{err} - L_{mh}\cos 2\theta_{err}\right] \tag{2-30}$$

Where L_{mh} is the high frequency mutual inductance

The tracking observer forces the current component in the estimated q-axis current to zero. It leads to

$$\Delta L_{sh}\sin 2\theta_{err} - L_{mh}\cos 2\theta_{err} = 0$$
$$\theta_{offset} = -\frac{1}{2}\times \arctan\left[\frac{L_{mh}}{\Delta L}\right] \tag{2-31}$$

It can be observed that the rotor position estimation error is a function of self and mutual differential inductances. To implement cross-coupling inductance decoupling, the information of cross-saturation inductance L_{mh} and differential inductance ΔL_{sh} is required. Because the mutual inductance is load dependent, the decoupling information in all operating points must be known. The phase offset is estimated by the experimental measurement at each operating points. The offset angle is obtained from curve fitting of the phase offset measurement data. Decoupling techniques is used to decouple the cross-saturation effect. The on-line adaptive decoupling will be the ongoing research.

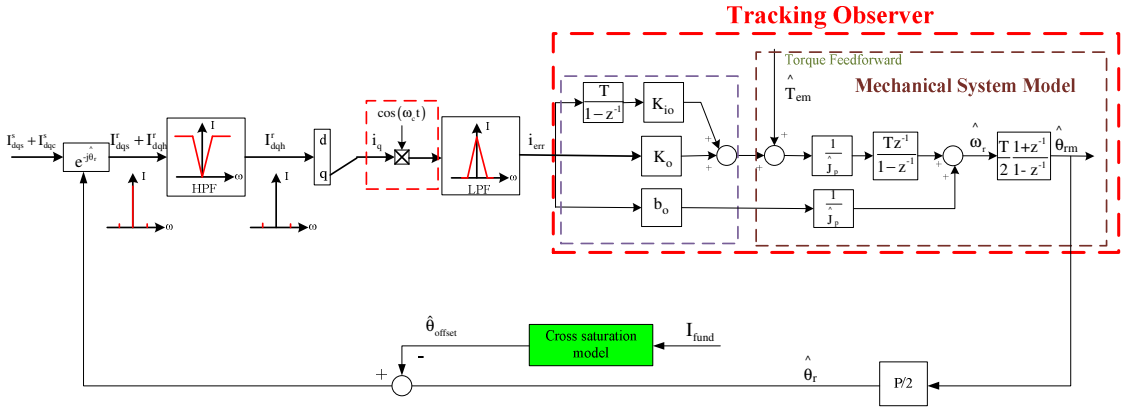

Fig. 2.17 Single process and tracking observer for pulsating voltage based position estimation with the implementation of cross saturation model

*2.3.3 **Alternative square-wave injection rotor position estimation method***

. In the previously published method[42], the rotor position can be extracted by using arctan calculation in (2-20) since θ_{err} equals zero is assumed. The calculated angle θ_{r_est} can be passed through a position tracking observer to have better estimation accuracy. The signal processing block diagram and the tracking observer is shown as Fig. 2.18. However, this method is based on the assumption $\theta_{err} \fallingdotseq$ zero. There is no mechanism in the algorithm to force the θ_{err} to become zero. In the model shown in (2-19), it can be seen that the other steady state condition exists when θ_{err} equals 90 degrees. Therefore, (2-20) should be rewritten as:

$$\begin{bmatrix} \Delta i^s_{dsh\_cal} \\ \Delta i^s_{qsh\_cal} \end{bmatrix} = \frac{v_c \Delta T}{Z_{dh}} \begin{bmatrix} \sin(\theta_e) \\ -cos(\theta_e) \end{bmatrix} \text{ (when } \theta_{err} \approx 90 \text{ degree)}$$
$$= \frac{v_c \Delta T}{Z_{dh}} \begin{bmatrix} cos(\theta_e) \\ sin(\theta_e) \end{bmatrix} \text{ (when } \theta_{err} \approx 0 \text{ degree)} \qquad (2\text{-}32)$$

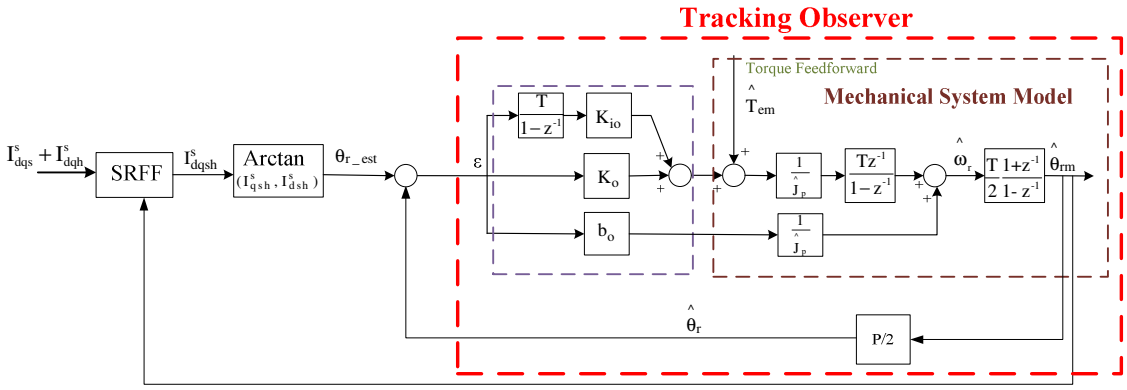

Fig. 2.18 Position estimation single process and tracking observer for square-wave vector based injection

From (2-32), it is clear that if the steady state point falls in $\theta_{err} \approx 90$ degree, it leads to 90 degree offset of estimated rotor position. A modified square wave rotor position estimation method is shown in previous section. The major difference is that current in the estimated frame is used to extract rotor position. In addition, by using synchronous demodulation (multiplication by the injected voltage, v_{sq}), the effect of the square wave on the resulting current can be easily removed as expressed via

$$\begin{aligned} \hat{i}^{r}_{qsignal\_sq} &= \hat{i}^{r}_{qsh} * \text{sign}(v_{sq}(t)) \\ &= -\frac{v_{sq}(t)\, sin2\theta_{err}}{2\omega_{sq}^{2} L_{dsh} L_{qsh}} \Delta L_{sh} = K_{error} sin2\theta_{err} \end{aligned} \tag{2-33}$$

From (2-33) q-axis current induced by the differential inductance (resistance term is usually small and is neglected, especially in FI-IPMSM) can be used to extract rotor position. Similar to the pulsating vector injection method, the cross-coupling inductance also causes phase offset of the estimation rotor position. The same decoupling technique stated in previous section can also be used to improve the accuracy of the estimation rotor position. The signal processing block diagram is shown as Fig. 2.19. Comparing to the prior method, which simply assuming θ_{err} is equals zero, the advantage of this modified method is in using a tracking observer to force θ_{err} to become zero.

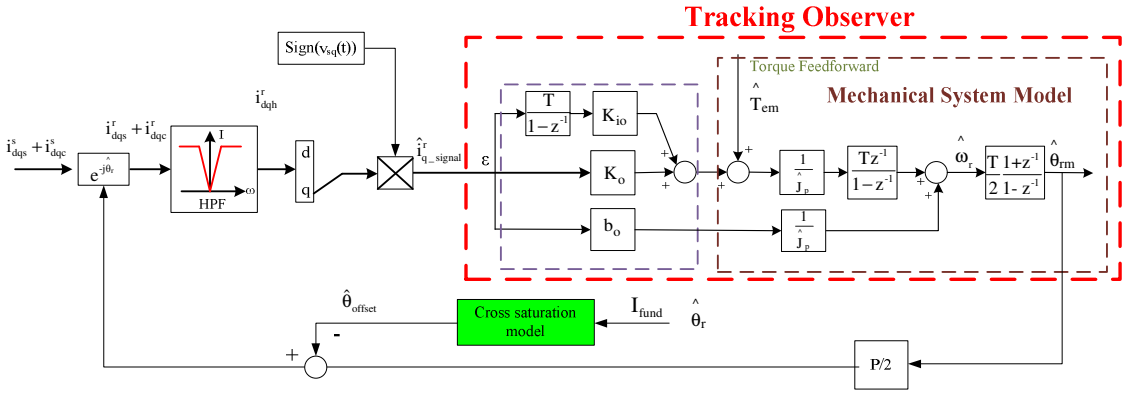

Fig. 2.19 Signal process and tracking observer for d-axis square-wave voltage injection based position estimation method with cross-coupling inductance decoupling

2.3.3.1 Stability analysis of square wave injection

To investigate the stability of rotor position estimation, (2-32) is examined. From, (2-32) the derivative of rotor position with respect to estimation error can be calculated and is shown in Fig. 2.20. It is observed that if a machine d-axis inductance is greater than q-axis inductance, a stable point would occur at $\theta_{err} \approx 90$. On the other hand, if a machine q-axis inductance is greater than d-axis inductance, the stable operating point would occur at $\theta_{err} \approx 0$. It should be noted that rotor position at zero degree was used here, but the results of derivative of rotor position with respect to estimation error remain the same for other rotor positions.

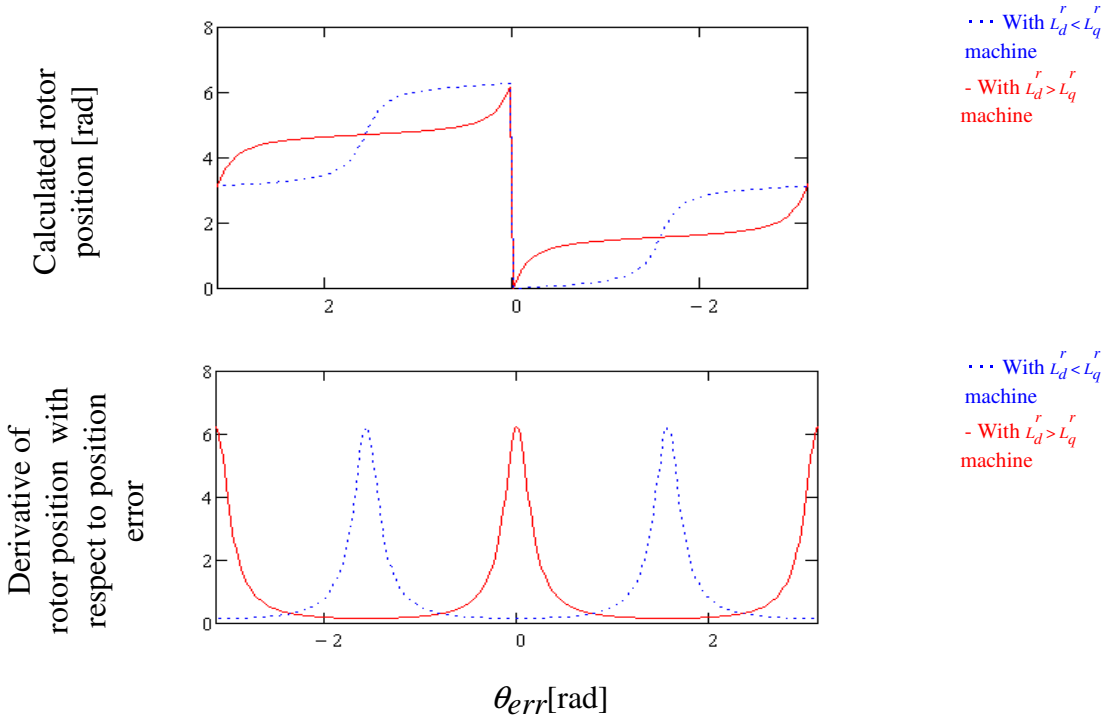

Fig. 2.20. The calculated rotor position and derivative of calculated rotor position with respect to θ_{err} at rotor position at zero degree.

2.3.3.2 Simulation of stability analysis of square wave injection

To evaluate this stable point property, rotor position estimation simulation with both FI-IPMSM and FW-IPMSM were performed and shown as shown in Fig. 2.21and Fig. 2.22. It can be found that the alternative square wave rotor position estimation can estimate rotor position in both type of PMSM. However, a significant phase offset ($\theta_{err} \approx$ 90) is observed when the stationary frame current is used for rotor position estimation in the FI-IPMSM. It will significant degrade the system performance (i.e. no torque output). During real operation, if a certain disturbance or noise occurs, θ_{err} could have significant change leading to a change of the stable point. Therefore, this method could be vulnerable to noise problems. Both methods can estimate the rotor position in FW-

IPMSM without 90 degree error. As a result, it can be concluded that using current in estimated rotor frame to estimate rotor position is valid in both machines.

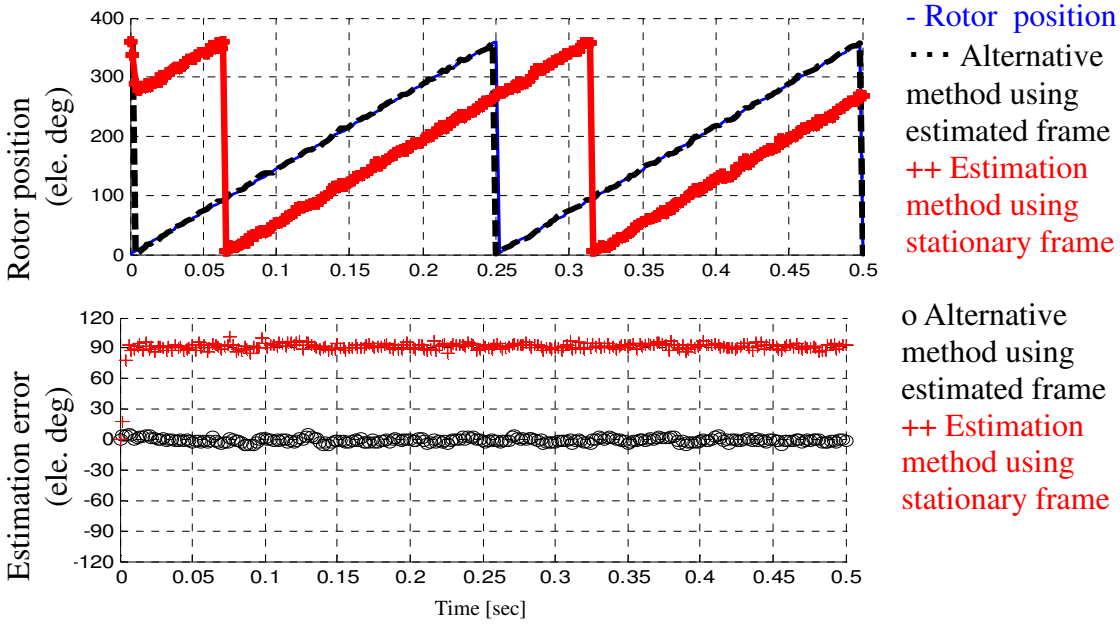

Fig. 2.21. The simulation results of rotor position estimation with FI-IPMSM

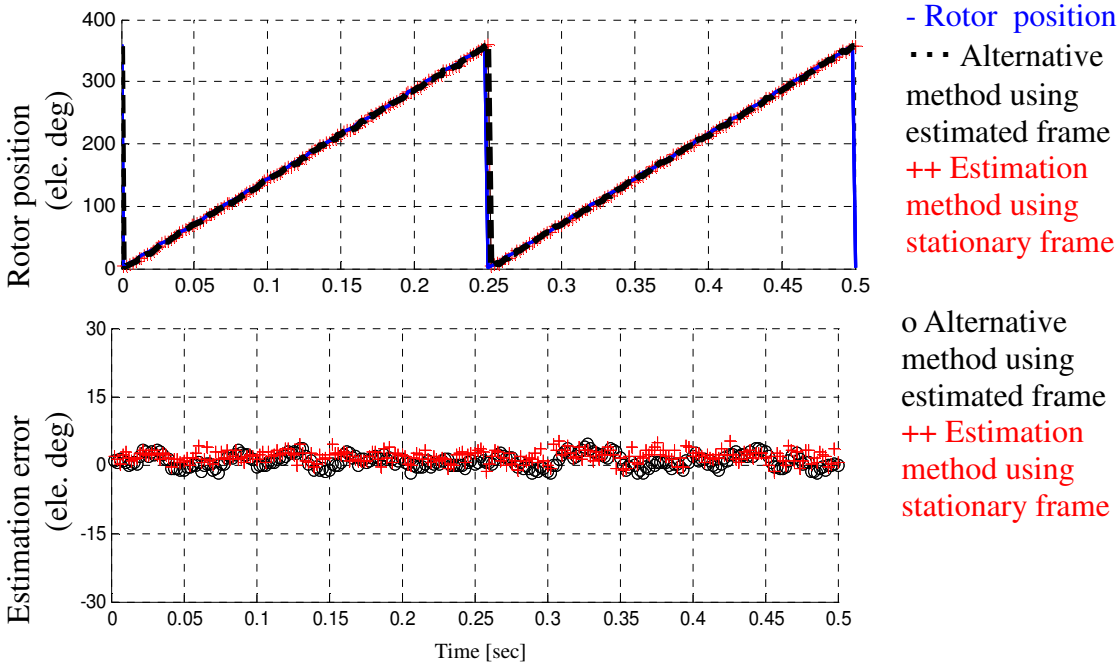

Fig. 2.22The simulation results of rotor position estimation with FW-IPMSM

2.4 **Experimental Setup**

Table 2-1 Test Machine Parameters

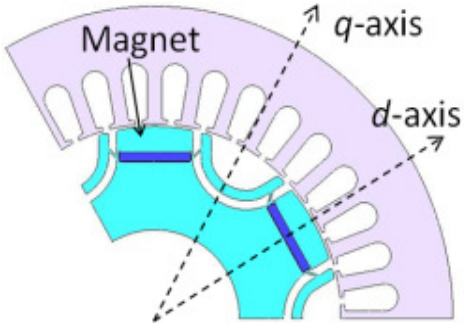

FI-IPMSM

Specifications	**Value**
Rated output power/speed /Rated torque	6.7 kW/6000rpm/13.5 N-m
Rated speed	6000 rpm
Rated current (Phase current)	30 A (peak)
Connection	Wye
Poles/Slots	36/6
Moment of inertia	0.01691 kg-m^2
Winding resistance	0.15 Ω
d-axis inductance	3.1 mH
q-axis inductance	2.5 mH
Saliency (unsaturated)	1.24

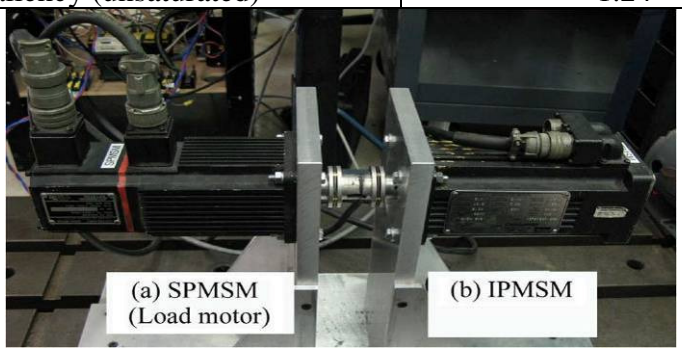

FW-IPMSM#1[127]

Rated power/speed/torque	1.4 kW/ 6200 rpm/2.26 N-m
Poles	4
Moment of inertia	0.0001 kg-m2
Winding resistance	1.5 Ω
L_d/Lq	8 mH/22mH

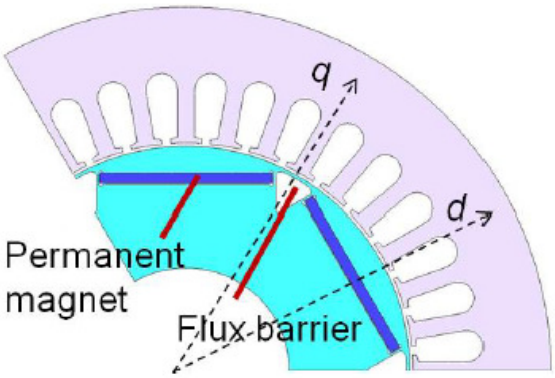

FW-IPMSM#2

Poles	6
Magnet Flux	200.59 mWb
L_d/Lq	2.33 mH/3.61mH

A 10kW FI-IPMSM with 36-slots-6-poles, distributed windings is used to test the self-sensing performance. The FW-IPMSM#1 is used to evaluate square injection method and the FW-IPMSM#2 is used to evaluate the overload self-sensing performance. All machine parameters shown in Table 2-1 correspond to fundamental excitations which normally are at a lower frequency than the carrier frequencies. It should be noted that due to higher reactance, the injected voltage is increased to 40 Volts for the 2500 Hz square wave injection.

This experimental setup consisted of one industrial YASKAWA drive with induction machine and one MYWAY inverter with FI-IPMSM. The induction machine is used as a load machine and FI-IPMSM is used to test the performances of rotor position estimation. The induction machine can be set as speed loop mode or torque mode. The control algorithms for FI-IPMSM machine are implemented with an Analog-to-Digital DSP card in the AIX control system. The PWM is symmetrical regular sampled and has a switching frequency equal to 10 kHz. All of the algorithms are synchronous sampled with the PWM switching frequency. The block diagram of experimental test setup is shown in Fig. 2.23 and the experiment hardware is shown as Fig. 2.24-Fig. 2.26.

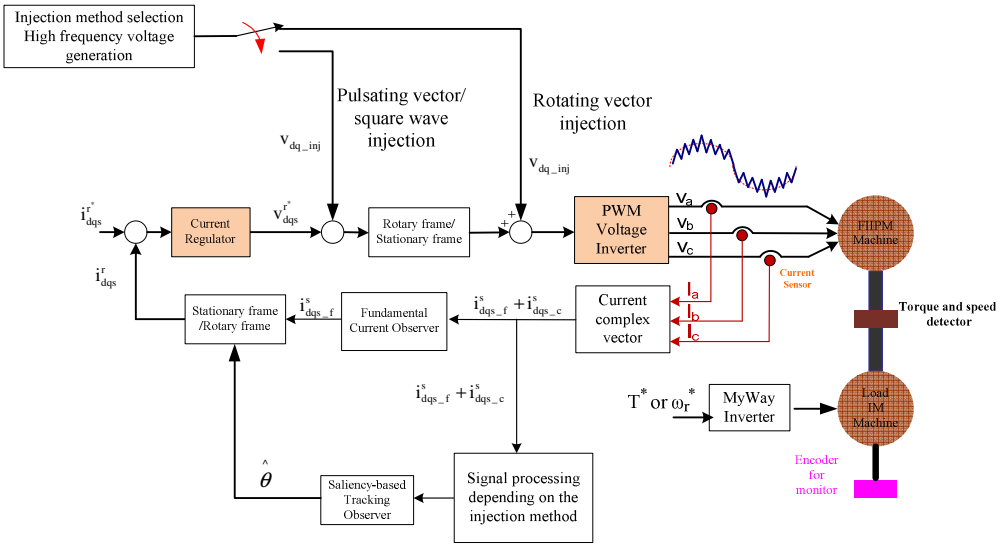

Fig. 2.23 The block diagram of experimental test setup

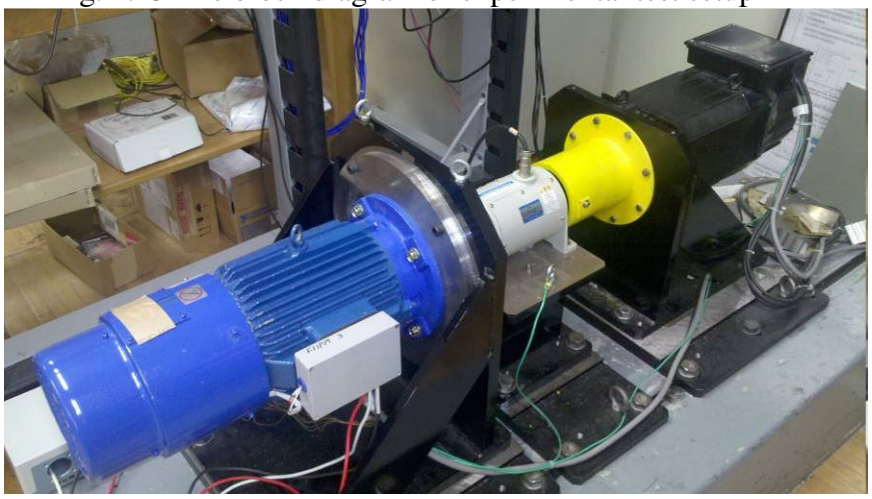

Fig. 2.24 FI-IPMSM motor (left) and induction motor (right)

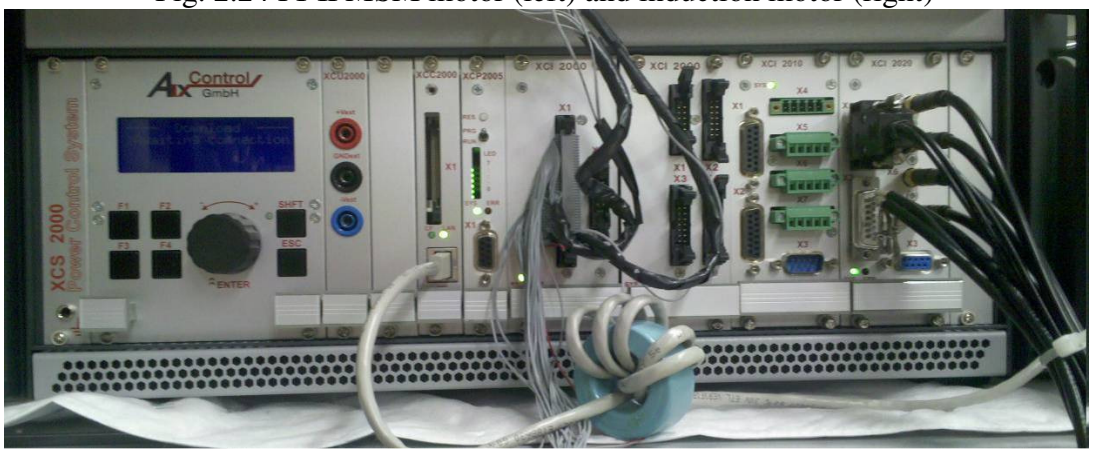

Fig. 2.25 AIX controller for the FI-IPMSM

Fig. 2.26 MYWWAY Inverter for FI-IPMSM and YASAKAWA drive (bottom) for induction machine

2.5 Performance of Rotor Position Estimation

2.5.1 The comparison of square-wave injection

Fig. 2.27 and Fig. 2.28 show the experiment result with FI-IPMSM and FW-IPMSM#1. From the experimental results, it can be observed that prior method leads to 90 degree estimation offset in FI-IPMSM. Decoupling has been performed to reduce the offset. However, it does not solve the instability of the system in the prior method. On the other hand, the rotor position estimation accuracy is greatly improved with the alternative method. As mention in previous section, θ_{err} is forced to zero so the estimation accuracy and system stability are greatly increased.

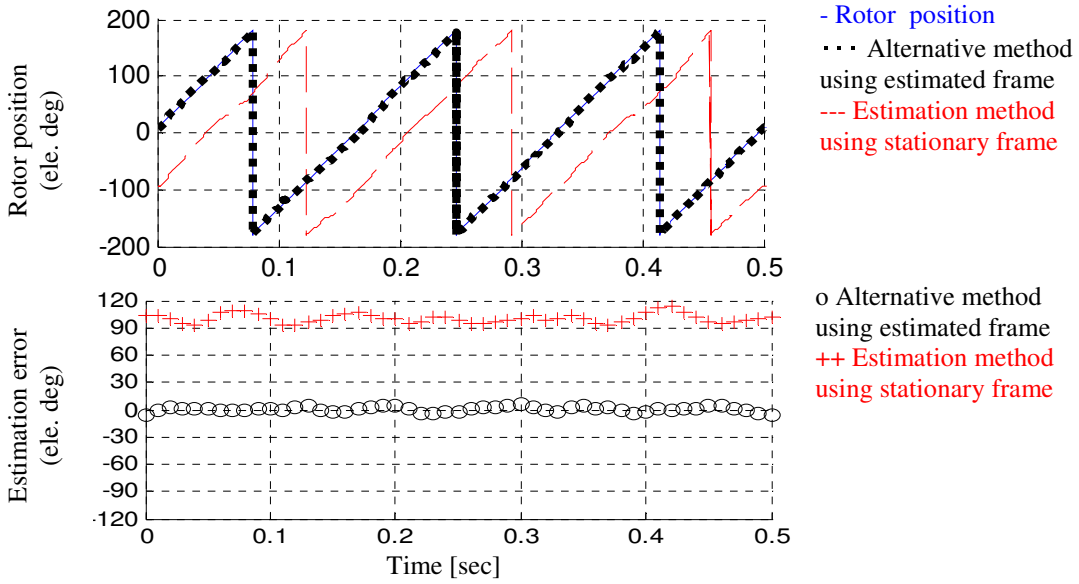

Fig. 2.27. The experiment result of rotor position estimation with **FI-IPMSM** (Test condition: 0.15 pu torque command, Speed 80rpm, DC bus 350V, and 40V square-wave 2500Hz Voltage Injection)

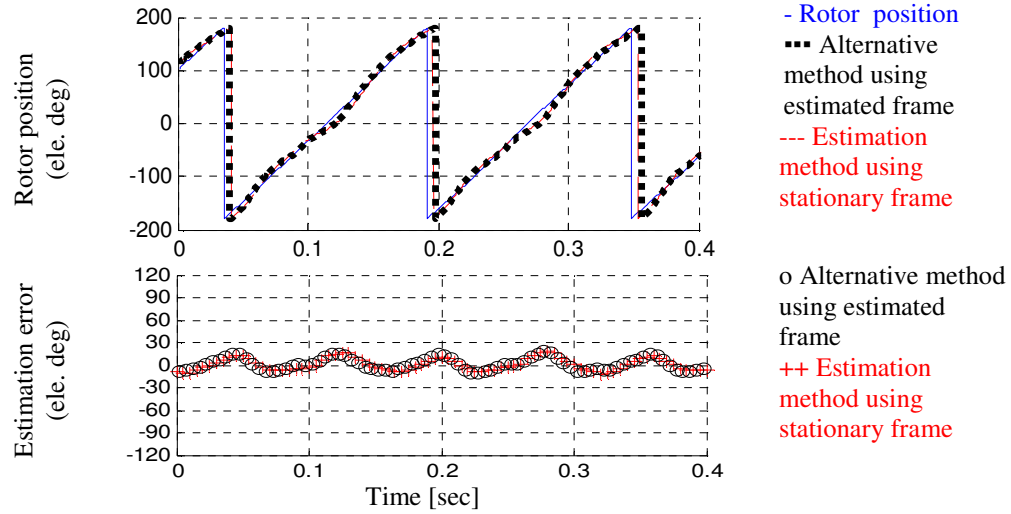

Fig. 2.28. The experiment result of rotor position estimation with FW-IPMSM#1 Test condition: 0.18 pu torque command, Speed 20 rad/sec DC bus 350V, and 30V square-wave 2500Hz Voltage Injection

2.5.2 *Angular offset of FI-IPMSM*

The main advantage of FI-IPMSM is that the angular offset is much smaller during the high load conditions (>1x rated load). Due to the limitation of the test bench, FEA simulation is performed to examine the position offset in the high load conditions. The result is shown in Fig. 2.29. It can be seen that the FI-IPMSM shows the advantage of much less angular offset during the high load conditions than the normal flux-weakening IPMSM (FW-IPMSM#2), which has the same physical dimensions, stator winding configuration and electrical rating of the machines as the FI-IPMSM.

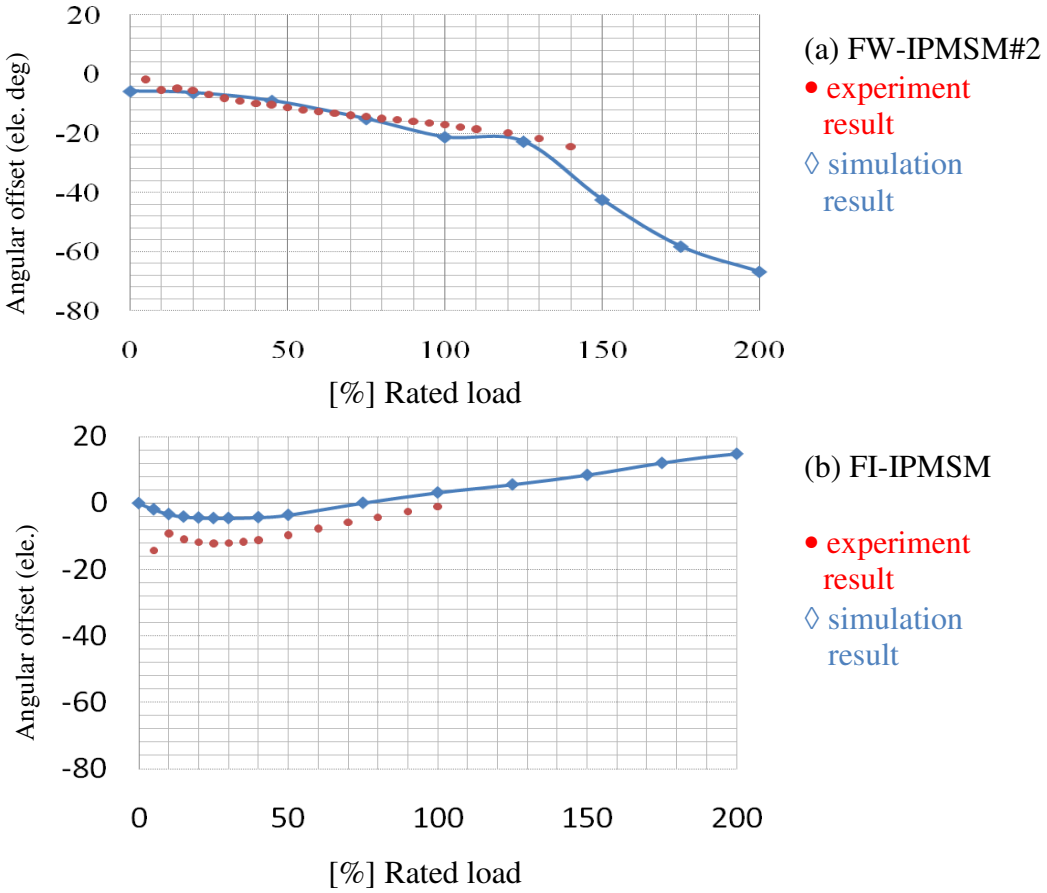

Fig. 2.29. The comparison of angular offset of FW-IPMSM and FI-IPMSM

*2.5.3 **Position estimation with load change***

The experiment results with varying load conditions from zero to 1 pu are shown as Fig. 2.30 - Fig. 2.33. Several observations can be found from the experimental results. First, all of the methods show the increase of offset as the load increase. Cross-coupling effect has been reported as the major cause of phase offset of estimation error and it vary with load conditions[62]. It can be concluded that the cross-coupling in FI-IPMSM causes phase-offset. It can be decoupled by using the model developed in previous sections.

Secondly, rotating vector injection method shows that the error has a one major $+1\omega_e$ component which becomes more evident as the load is increased. It can be known the major error is affected by saturation-induced saliency which increases with load. Comparing to rotating vector injection method, the other methods are less sensitive to saturation-induced saliencies.

Thirdly, for the comparison of the pulsating torque, it can be seen that q-axis pulsating vector injection and rotating vector injection both can induce pulsating torque. As a result, to reduce the pulsating torque, d-axis injection is preferred.

In all cases, the estimation error of all the methods can be greatly reduced if the decoupling techniques are implemented. The pulsating vector injection method and the square-wave injection method show good estimation results if load-dependent phase offset decoupling are implemented.

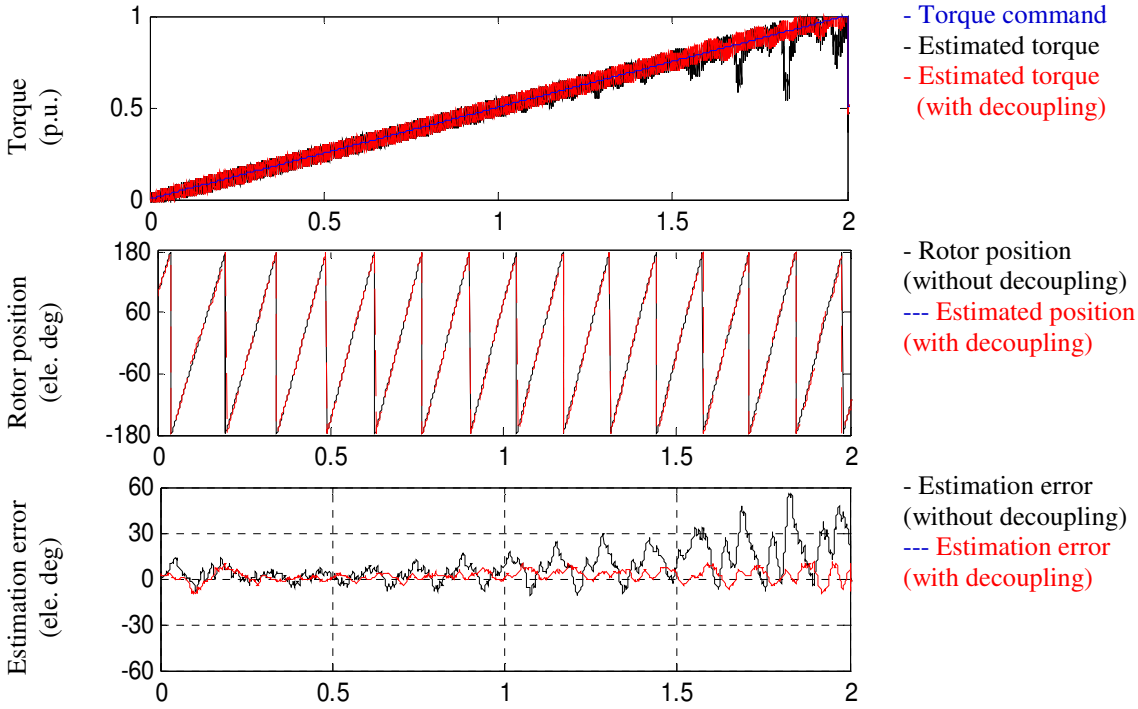

Fig. 2.30 Rotor position estimation using rotating vector injection with zero to 1 p.u torque command

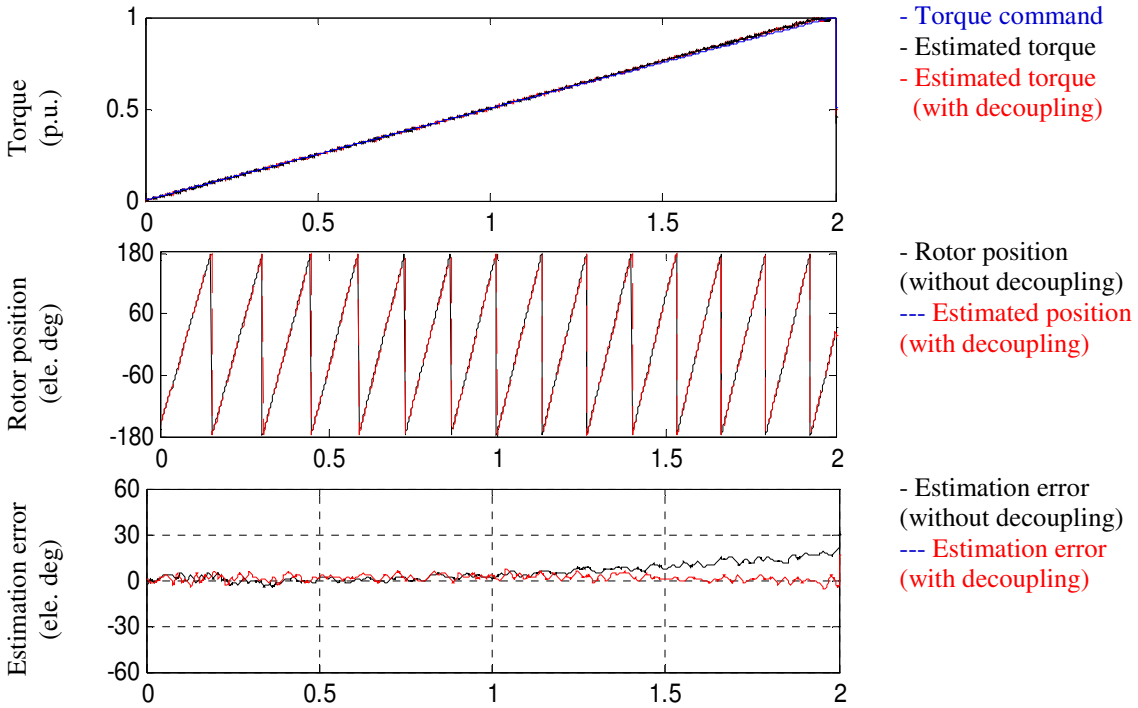

Fig. 2.31 Rotor position estimation using d-axis pulsating vector injection with zero to 1 p.u torque command

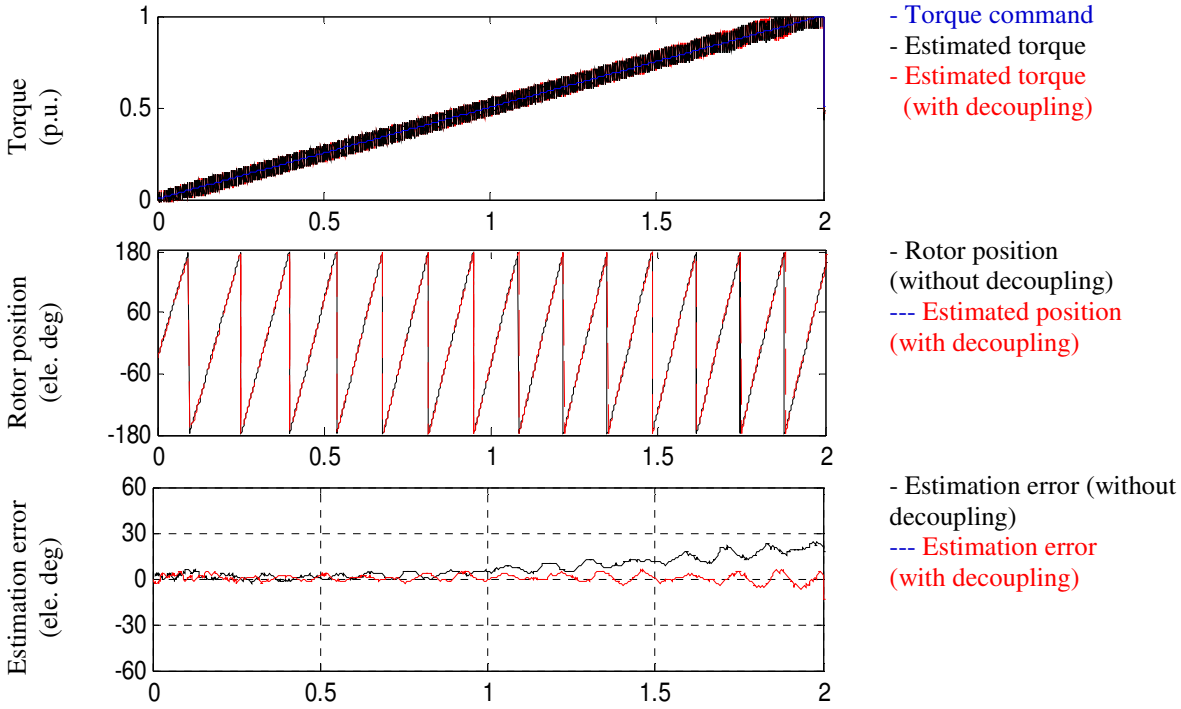

Fig. 2.32 Rotor position estimation using q-axis pulsating vector injection with zero to 1 p.u torque command

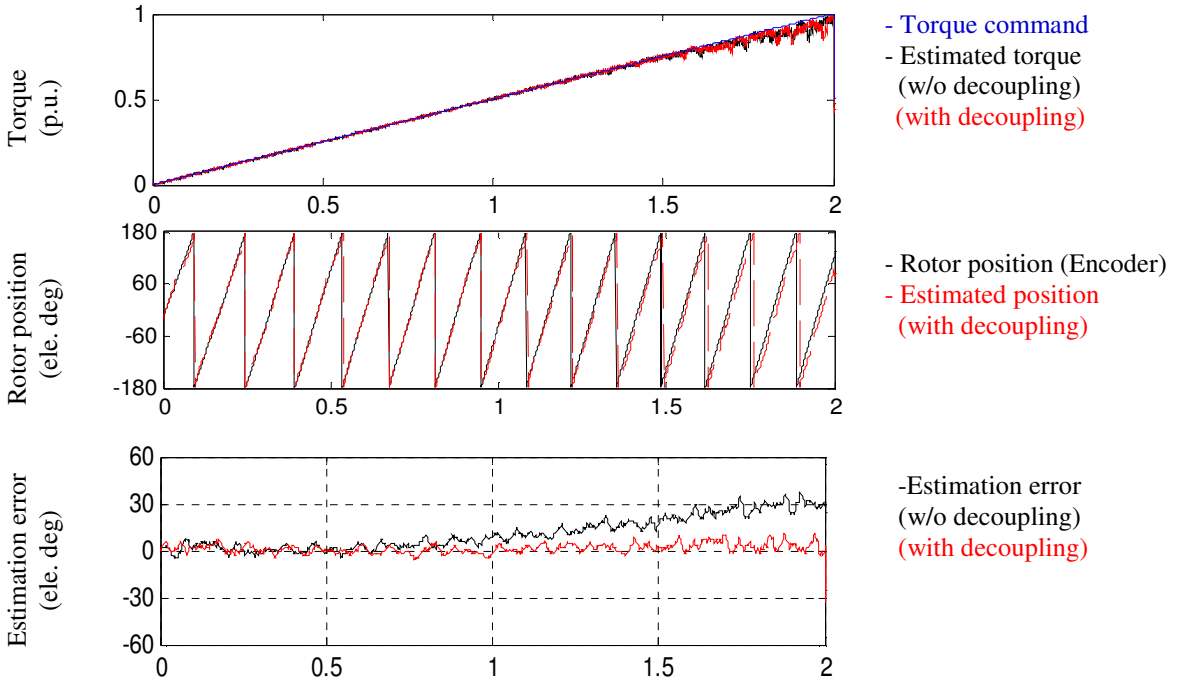

Fig. 2.33 Rotor position estimation using enhanced square wave injection with zero to 1 p.u torque command

2.6 Conclusions and Summary

This chapter presents a thorough evaluation of the self-sensing performance of a FI-IPMSM designed for both self-sensing and power conversion using three well-accepted signal injection methods. In addition, a new robust estimation method for square-wave injection is proposed. The implementation issues are addressed and methods for improving the estimation accuracy are presented. The key observations and conclusions are summarized as following

- Under high frequency injection, the FI-IPMSM has an inductive reactance that is much larger than the high frequency resistance (≈ 90 deg. power factor angle). As a result, the FI-IPMSM shows good estimation accuracy without the need of high frequency resistance decoupling.
- The alternative square-wave injection rotor position estimation method, which uses synchronously demodulated HF current in the estimated frame to extract rotor position, greatly improves the estimation accuracy and system robustness. The analysis is demonstrated and is verified with simulation and experiment.
- Rotating vector injection and q-axis pulsating injection both can induce pulsating HF torque. To avoid the pulsating torque, d-axis pulsating vector injection is preferred
- Saturation-induced saliencies can degrade estimation accuracy performance. The degradation is worst when the rotating vector injection method is used in the FI-IPMSM, but can be greatly improved by using load-dependent multi-saliency decoupling. For both pulsating and square wave injection methods, load-dependent phase offset decoupling is implemented.
- The custom–designed FI-IPMSM yields position estimation results within ±3 RMS electric degree estimation errors for all methods and load conditions if proper decoupling techniques are used.

Chapter 3 - Optimum DC Bus Voltage Analysis and Calculation Method for Inverter/Motor with Variable DC bus Voltage

In this charter, an online method to calculate the optimum DC bus voltage for motor and inverter with variable DC bus voltage is proposed. The required DC bus voltage in the low speed region is much lower than for the rated speed region. As a result, the machine drive system efficiency can be improved with lower DC bus voltage since the switching losses in the inverter are reduced. To simultaneously achieve desired machine output torque and minimized losses, an optimum DC bus voltage is required. However, machine parameter estimation errors and machine spatial harmonics result in calculation errors for the required DC bus voltage. A voltage disturbance state filter, which is formed by a Luenburger-style closed-loop stator current vector observer with voltage command feedforward, is used to mitigate the calculation errors. Voltage errors caused by the parameter deviations and machine spatial harmonics will inherently be estimated by the state feedback controller of the observer. Therefore, the voltage calculation errors can be corrected by the VDSF's disturbance voltage, so that the "nearly" optimum DC bus voltage can be obtained.

3.1 Inverter Loss, Modeling and Properties

In this research, a three phase voltage source inverter (VSI) is used. Losses in the IGBT can be divided into two parts: IGBT loss and diode loss. From [128, 129], the modeling of IGBT losses diode can be expressed as (3-1) - (3-4):

$$\textit{Switching loss per IGBT: } P_{sw} = \frac{6}{\pi}((E_{on}(i_c,t_j,V_{dc}) + E_{off}(i_c,t_j,V_{dc})) * \frac{V_{dc}}{V_{ref}} * \frac{i_L}{i_{ref}} * f_s \quad (3\text{-}1)$$

$$\textit{Conduction loss per IGBT: } P_c = i_L * V_{CE(SAT)} * (\frac{1}{8} + \frac{D}{3\pi}\cos\theta) \quad (3\text{-}2)$$

where: f_s is the switching frequency, E_{on}, E_{off} is the turn-on and turn-off energies loss per switching which is provided by data sheets are given for a certain reference voltage, i_c is the conduction current, t_j is the junction temperature, V_{dc}, is the DC bus voltage, i_L is the peak value of the ac line current, the V_{ref} is to the blocking state voltage of the IGBT, and i_{ref} is the on-state current. $V_{CE(SAT)}$ is IGBT saturation voltage drop at i_L D: PWM duty cycle, θ: Phase angle between output voltage and current. It should be noted this equation is only valid in continuous PWM .

$$\textit{Steady state loss per diode: } P_d = i_L * V_{EC(SAT)} * (\frac{1}{8} - \frac{D}{3\pi}\cos\theta) \quad (3\text{-}3)$$

$$\textit{Reverse recovery loss per diode: } P_{rr} = \frac{1}{8} * i_{RR} * t_{RR} * V_{CE(pk)} * f_s \quad (3\text{-}4)$$

where: VEC is the FWD forward voltage drop, i_{RR} is the diode peak recovery current, t_{RR} is the diode reverse recovery time, and $V_{CE(pk)}$) is the peak voltage across the diode at recovery

From (3-1) - (3-4), it can be seen that lower DC bus voltage or switching frequency can reduce inverter losses. To reduce voltage and current harmonics, the switching frequency has minimum requirement. The other approach is to reduce DC bus voltage. Since only low DC bus voltage is required in the low speed region, it is possible to use lower DC bus voltage if an adjustable DC bus voltage system is available and the inverter efficiency can be increased.

3.2 Inverter/Motor Loss against DC Bus Voltage

In this section, the relationship between DC bus voltage and inverter/motor efficiency is presented. Fig. 3.1 and Fig. 3.2 show the inverter efficiency with several different test conditions (varying speed and current) using different DC bus voltage. It can be seen that in the low speed, light load, high bus voltage conditions degrade efficiency by having switching losses become dominant. This means that inverter efficiency can be improved with a lower DC bus voltage.

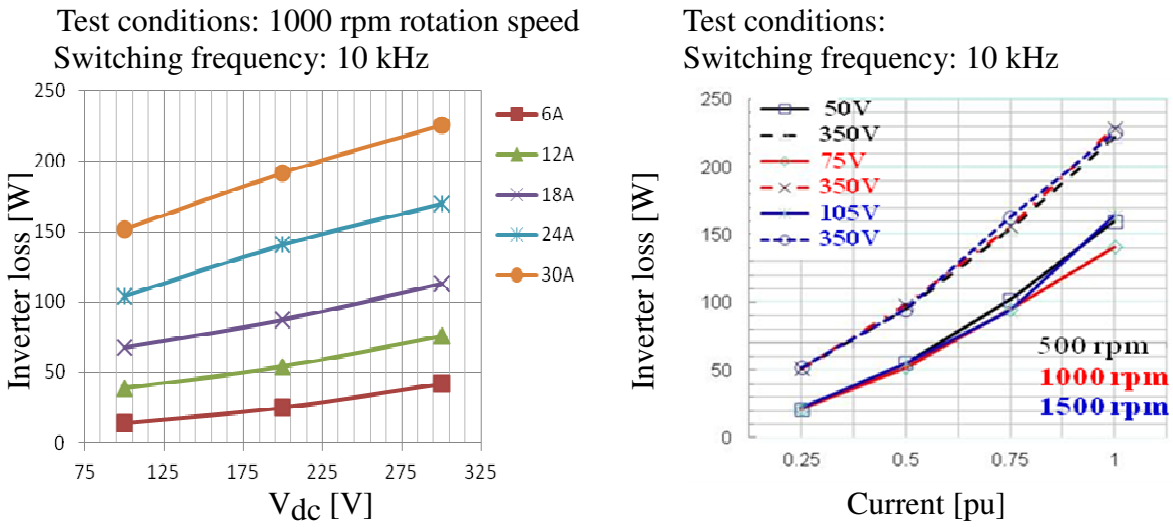

Fig. 3.1 Experimental results of inverter losses under different operating conditions

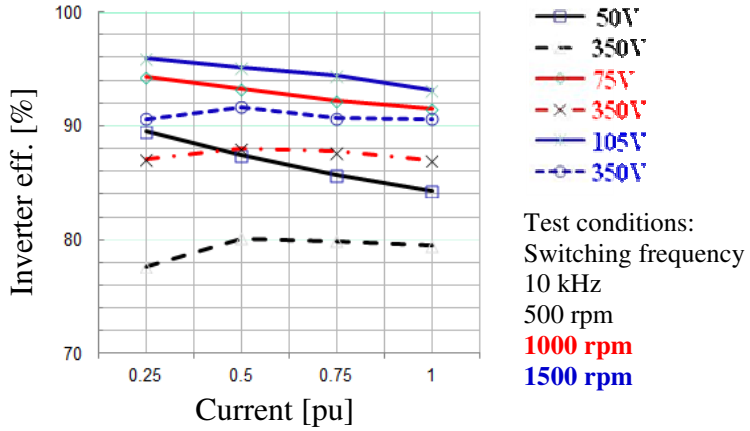

Fig. 3.2 Experimental comparison of inverter efficiency with variable DC bus and fixed DC bus voltage

The motor and inverter efficiency for different DC bus voltages is shown as Fig. 3.3. It can be seen that the motor efficiency is almost not affected by the DC bus voltage. In contrast, the inverter efficiency is improved with lower DC bus voltage. The reason is when the DC bus is reduced, the duty cycle of PWM generator will be increased, and the input voltage/current of motor will nearly remain the same. Therefore, the motor efficiency is almost insensitive to the DC bus voltage variation if same operation is maintained. Since the switching loss is reduced, the total loss (inverter and motor) is reduced.

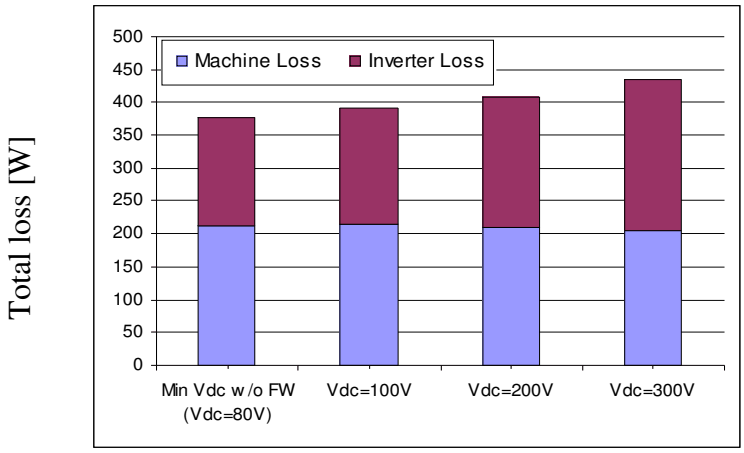

Test conditions:
Switching frequency 10 kHz

500 rpm

Fig. 3.3 Experimental results of total loss distribution under different DC bus voltage conditions

In Fig. 3.4, the current amplitude is increased from 0.1pu to 1pu. The current vector is selected under the motor is operated at loss minimization if the DC bus voltage limit is not reached. The DC voltage limit is based on without over modulation at steady state conditions. If the DC bus voltage is not sufficient, the flux-weakening will be used. Under these conditions, the minimum DC bus voltage can be selected experimentally. The results are shown in Fig. 3.4. Under the linear modulation region assumption, the experimental results of total drive system efficiency under 500 and 1000 rpm are shown in Fig. 3.5.

For the 2000 rpm, the current vector cannot be controlled under the DC bus equal 100V, so only 200V and 300V are tested. In 3000 rpm, the situation is similar to 2000 rpm case, so only 300 V is used. The results are shown in Fig. 3.6. From the experimental shown above, it can be seen that the efficiency is improved by using minimum DC bus voltage. It also can be observed that if the minimum required DC bus voltage cannot be achieved, flux weakening control must be used. However, the system (inverter + motor) efficiency will be decreased. As stated before, the current vector selected is based on machine loss minimization point.

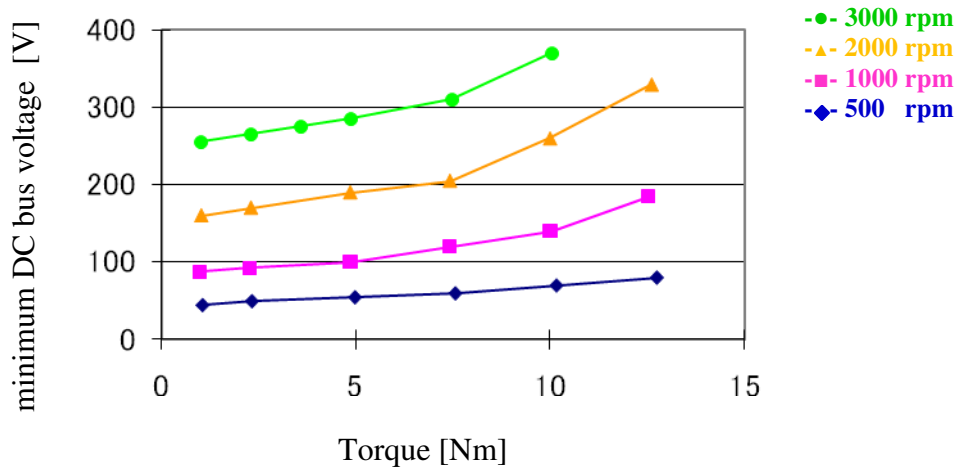

Fig. 3.4 The requirement of minimum DC bus voltage under different machine speed

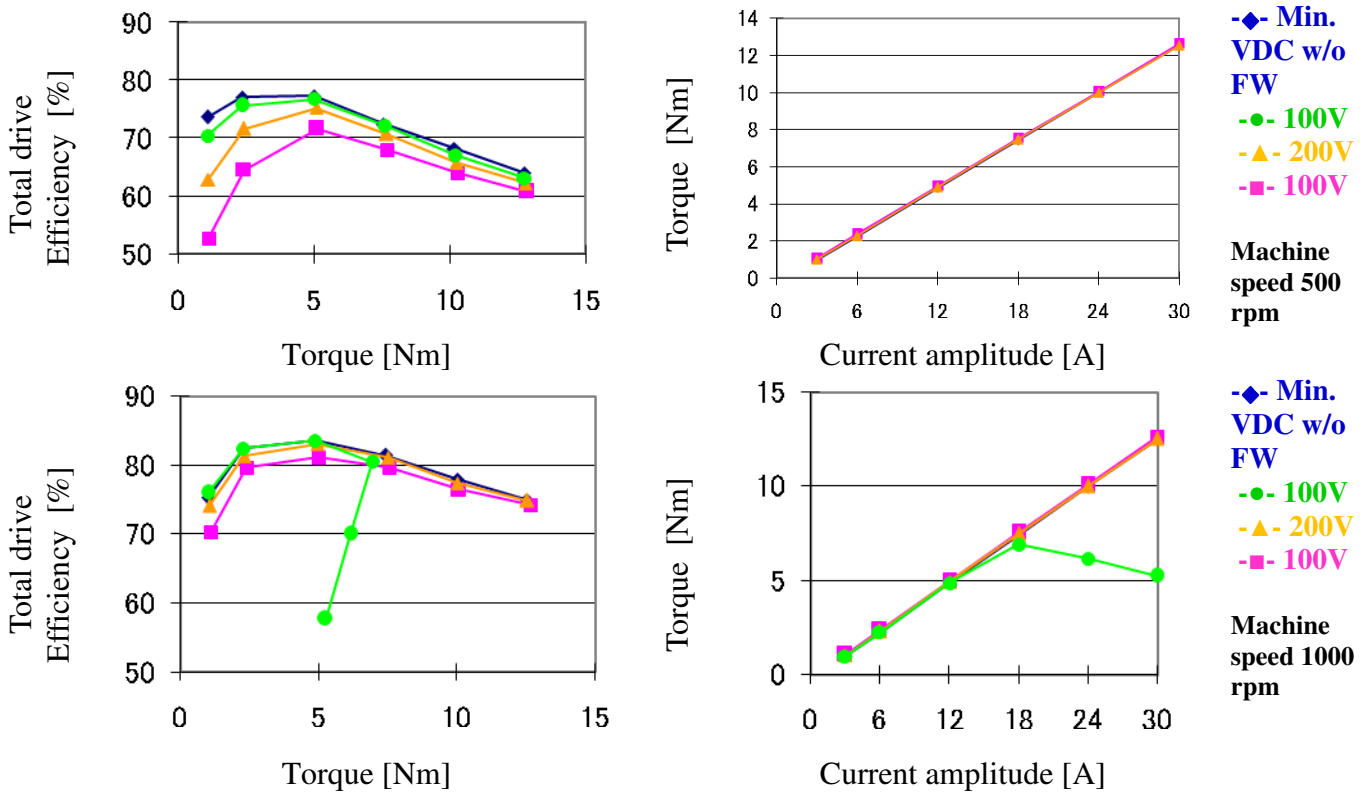

Fig. 3.5 Inverter and motor efficiency under 500 & 1000 rpm conditions

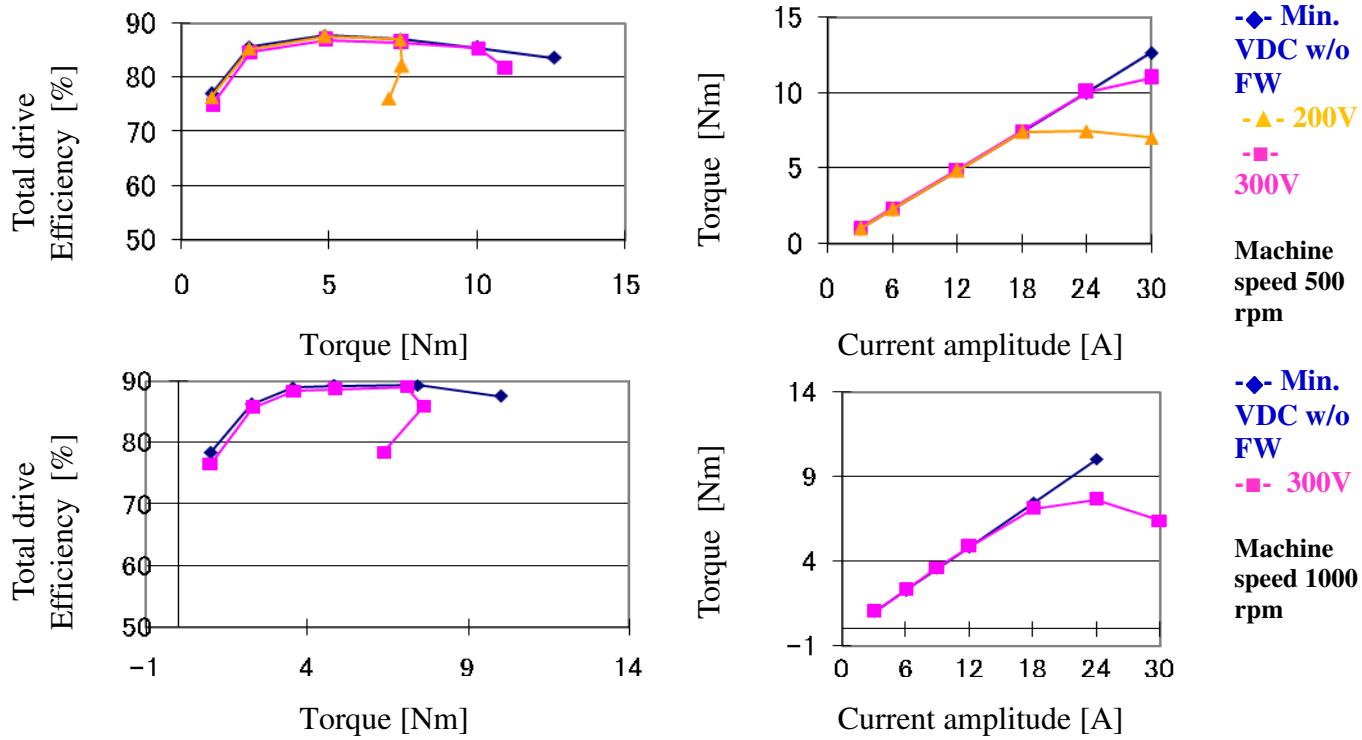

Fig. 3.6 Total drive system efficiency under 2000 & 3000 rpm conditions

3.3 Calculation of the Optimal DC Bus Voltage

In previous section, it was shown that lower DC bus voltage can increase the drive system efficiency. In this section, methods to calculate the optimum DC bus voltage are discussed.

3.3.1 Fundamental component method for calculating DC bus voltage

A fundamental component (FC) method can be used to estimate d-axis and q-axis flux linkage and resulting terminal voltage. Assuming that the machine speed is measured and that over-modulation is not being used for the PWM modulator, the required minimum DC bus voltage can be calculated. The calculation method is shown as Fig. 3.7. In an ideal model, all the machine parameters are constant. . In an ideal model, all the machine parameters are constant. Under the circumstances, the minimum DC bus can be calculated by using the ideal machine equation. The equations are shown as (3-5)-(3-7).

$$V_{dc} = \sqrt{3}\omega\sqrt{\hat{\lambda}_{ds}^{r\,2} + \hat{\lambda}_{qs}^{r\,2}} \tag{3-5}$$

$$\hat{\lambda}_{qs}^{r} = \hat{L}_q i_{qs}^{r} \tag{3-6}$$

$$\hat{\lambda}_{ds}^{r} = \hat{L}_d i_{ds}^{r} + \hat{\lambda}_{pm} \tag{3-7}$$

However, non-ideal effects such as inductance saturation and temperature change cause parameters variations which lead to DC bus voltage calculation error.

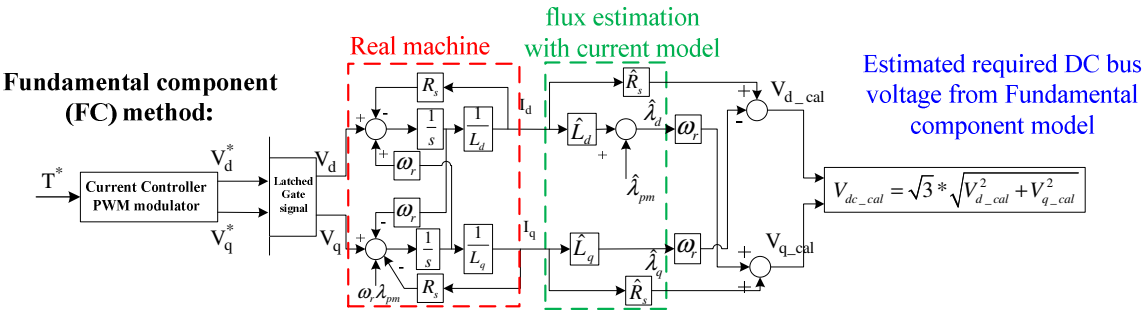

Fig. 3.7 Fundamental component method to calculate DC bus voltage

The estimated required DC bus voltage with fundamental component method and actual required DC bus voltage in the experiment are shown in Fig. 3.8, respectively. The required DC bus voltage is obtained from the experiment that uses MTPA, no flux-weakening and no over-modulation at steady state conditions. It can be seen that the experimentally determined minimum DC bus voltage is much larger than the fundamental component model predicts. This is because the unmodeled spatial harmonics of the FI-IPMSM (flux intensified-interior permanent magnet synchronous machine,) increase the required DC bus voltage. Therefore, a method that mitigates these effects is needed to obtain optimum DC bus voltage. A improvement calculation method is needed and will be introduced in next section

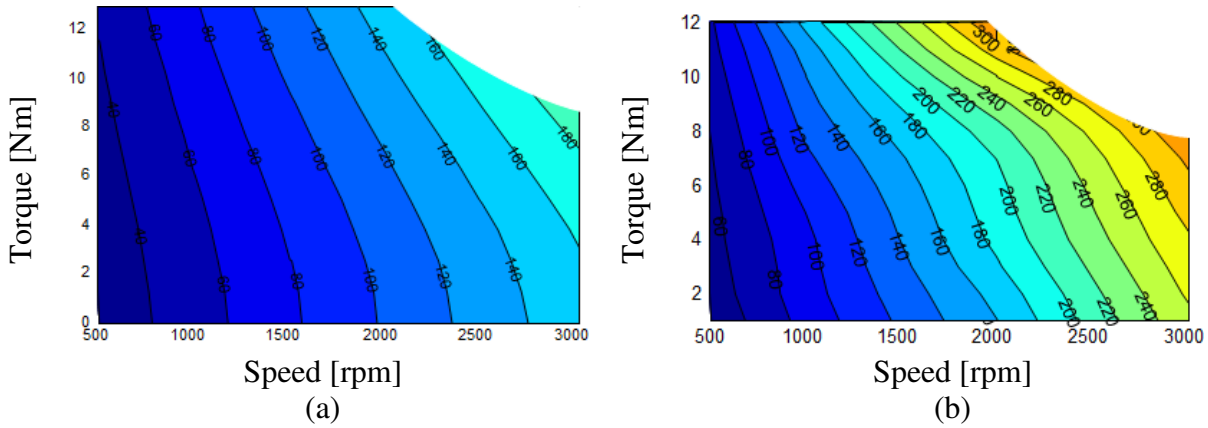

Fig. 3.8 The comparison of experiment result of required DC bus voltage without over modulation inverter efficiency with variable DC bus (a) calculation result (b) experiment result

3.3.2 *Using VDSF to calculate DC bus voltage which corrects errors in the machine model*

A method using a VDSF is proposed to solve calculation error problem caused by parameter variation. The structure of voltage disturbance state filter is shown as Fig. 3.9. Within its bandwidth, the stator current observer (SCO) acts as a VDSF which inherently estimates a disturbance voltage $\hat{\Delta v}_{dq}$, that it uses to overcome parameter errors. With correctly estimated parameters and no harmonics, the estimated current will be equal the measured current and the voltage disturbance estimate would be zero. However, for imperfect models, the voltage disturbance (flux linkage) estimate will contain the effects of parameter errors as shown in (3-8) and (3-9) as well as harmonics.

$$\hat{v}_{ds}^{r} = -\omega_r \hat{\Delta\lambda}_{qs}^{r} = -\omega_r \hat{\Delta L}_q i_{qs}^{r} \tag{3-8}$$

$$\hat{v}_{qs}^{r} = \omega_r \hat{\Delta\lambda}_{ds}^{r} = \omega_r (\hat{\Delta L}_d i_{ds}^{r} + \hat{\Delta\lambda}_{pm}) \tag{3-9}$$

The voltage error information can be used to correct the parameter variation which caused by saturation, temperature, and spatial harmonics so the optimum DC bus voltage can be calculated.

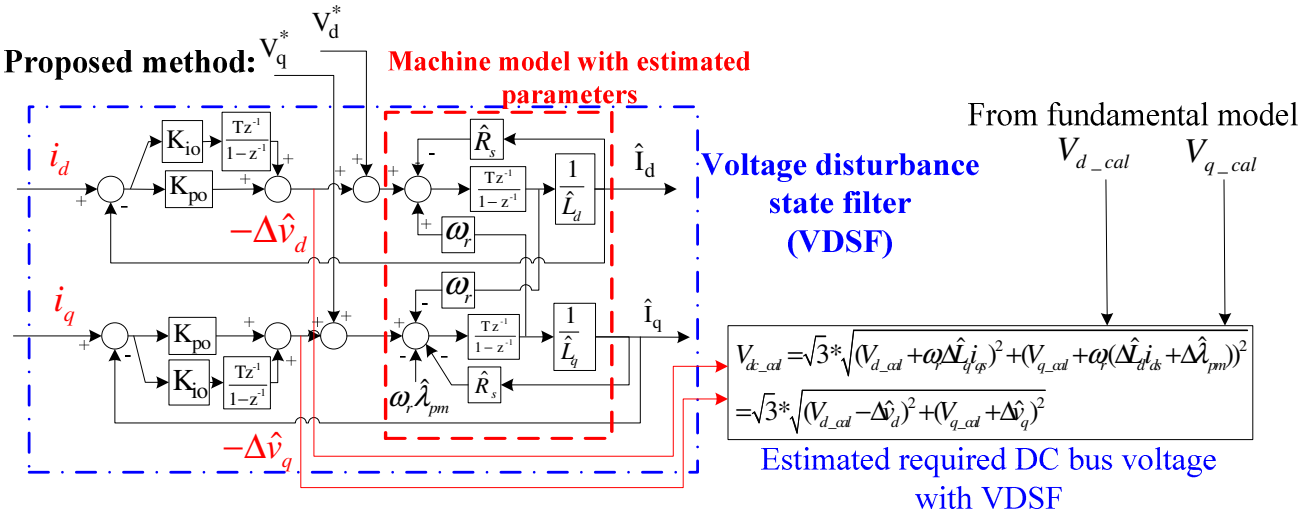

Fig. 3.9 Structure of VDSF and proposed method to calculate nearly optimum DC bus voltage

It should be noted that the DC bus voltage can be further reduced if the nonlinear PWM modulation region is used. The theoretical lowest DC bus voltage (i.e. maximum DC bus voltage utilization) with proposed method can be written as:

$$V_{DC} = \frac{\pi}{2}\sqrt{(V_{d\_cal} + \omega_r \Delta\hat{L}_q\, i_{qs})^2 + (V_{q\_cal} + \omega_r (\Delta\hat{L}_d\, i_{ds} + \Delta\hat{\lambda}_{pm}))^2} = \frac{\pi}{2}\sqrt{(V_{d\_cal} - \Delta\hat{v}_d)^2 + (V_{q\_cal} + \Delta\hat{v}_q)^2)} \quad (3\text{-}10)$$

Since the modulator operates in the nonlinear modulation region, a significant increase in harmonics could occur and cause additional losses. It has been reported that the harmonics can be mitigated with certain forms of PWM modulation methods (e.g. discontinuous PWM) in the nonlinear region[130]. It is also shown that the harmonics components can be as low as in the linear region. Therefore, it is still valid that selections of lowest DC bus voltage could still be the highest efficiency operating points even within the nonlinear PWM modulation region.

3.3.3 *Using VDSF to calculate DC bus voltage with parameter variation*

To investigate the effectiveness of using a VDSF to reduce the effect of parameter errors, simulation using a machine model with varying parameters is performed in Simulink. The DC bus voltage calculation values are evaluated as estimated magnet flux and inductance values are varied. The plots shown in Fig. 3.10 and Fig. 3.11 indicate that using the machine model to calculate DC bus voltage results in significant errors if parameter estimation errors occur. On the other hand, the voltage calculation errors can be greatly mitigated with the proposed method.

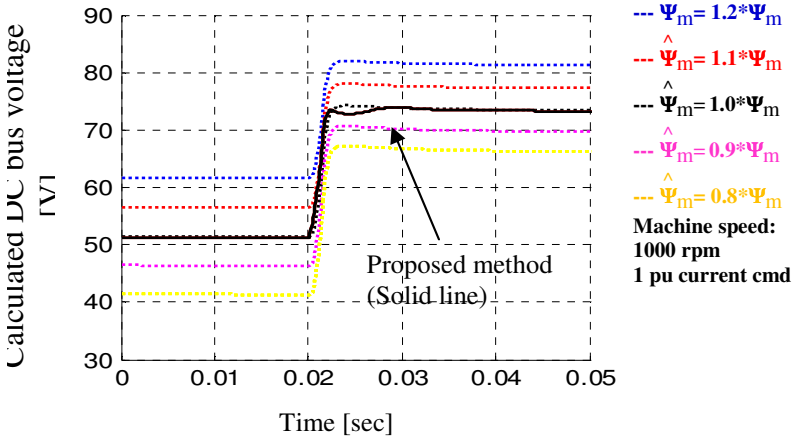

Fig. 3.10 Comparisons of using proposed method and current model with magnet flux estimation errors (Simulation results)

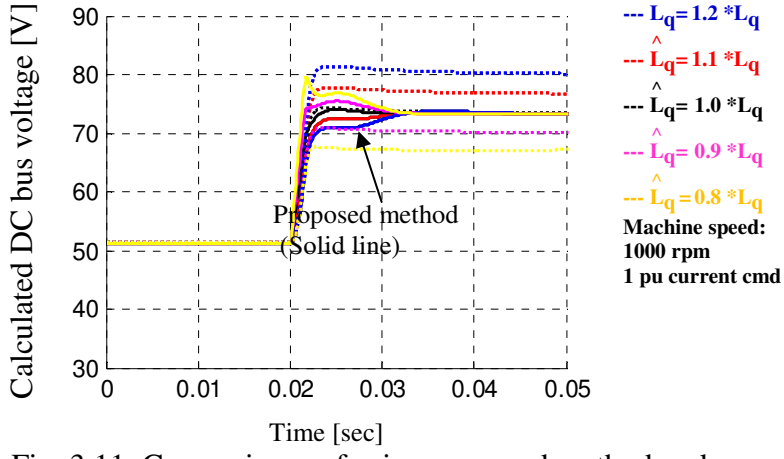

Fig. 3.11 Comparisons of using proposed method and current model with q-axis inductance estimation errors (Simulation results)

*3.3.4 **Using VDSF to calculate bus voltage in the presence of spatial harmonics***

Normally, a perfect sinusoidal flux distribution is assumed in machine equation. However, it is very difficult to have perfect sinusoidal flux distribution because of non-perfect machine geometry configuration (slot/teeth, stator and rotor, and winding). As a result, it is clear that spatial harmonics exist in every real machine. To simulate this effect, a JMAG-RT model is used to investigate the effect of spatial harmonics. The purpose is to see how accurately the VDSF can estimate the spatial harmonic voltage. The result is shown in Fig. 3.12 It can be seen that the frequency of the spatial harmonic is increased with the machine speed and calculation DC bus voltage using proposed method is higher than using ideal model. Furthermore, despite the variations of estimation magnet flux, the calculated DC bus voltage remains the same. It shows that voltage disturbance state-filter is able to nearly eliminate the parameter estimation errors.

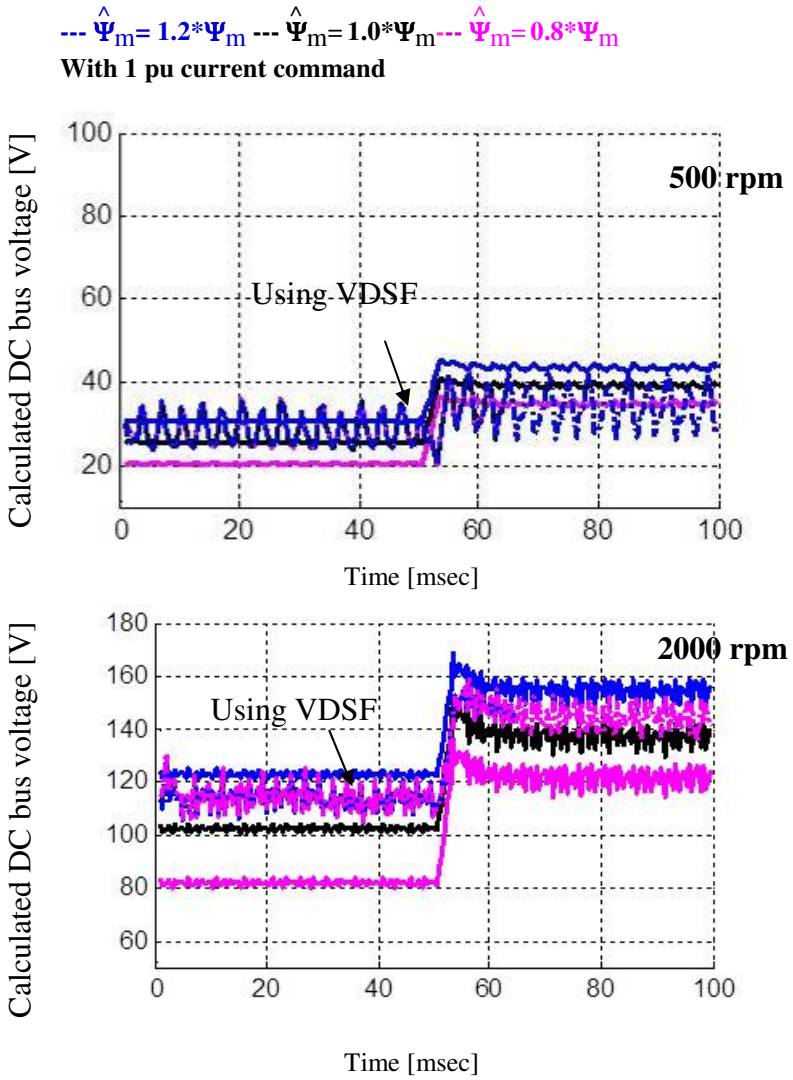

Fig. 3.12 Comparisons of using proposed method and FC model with JMAG-RT model with magnet flux estimation errors

3.4 Impact of Spatial Harmonics on Required DC Bus Voltage

It has been shown that the spatial harmonic will cause the required bus voltage to be larger than the value that the fundamental component method predicted. In this section, the model including spatial harmonic components is discussed. The impact of spatial harmonics on the DC bus voltage will be analyzed.

3.4.1 Back EMF with spatial harmonic contents

A model which describes phase voltage with harmonics can be written as

$$v_a = v_f \cos(\omega t+\theta_{fund}) + v_{har\_p}*\cos(har\_p*\omega t + \theta_{har\_p}) + v_{har\_n} *\cos(har\_n*\omega t + \theta_{har\_n}) + \ldots \quad (3\text{-}11)$$

$$v_b = v_f \cos(\omega t - 2/3\pi + \theta_{fund}) + v_{har\_p}*\cos(har\_p*\omega t - 2/3\pi + \theta_{har\_p}) + v_{har\_n}*\cos(har\_n*\omega t - 2/3\pi + \theta_{har\_n}) + \ldots \quad (3\text{-}12)$$

$$v_c = v_f \cos(\omega t - 4/3\pi + \theta_{fund}) + v_{har\_p}*\cos(har\_p*\omega t - 4/3\pi + \theta_{har\_p}) + v_{har\_n}*\cos(har\_n*\omega t - 4/3\pi + \theta_{har\_n}) + \ldots \quad (3\text{-}13)$$

$$har\_p = 6n+1 \text{ and } har\_n = 6n - 1$$

Where subscript *f,har_p, har_n* represent fundamental, positive spatial harmonic sequence, and negative spatial harmonic sequence component, respectively. v, ω, θ represent voltage, electrical rotational speed, and phase.

From the model described in (3-11)-(3-13), a modeled back-emf voltage can be expressed and compared with experimental results. It should be noted that the spatial harmonic contents are based on the experimental values. The results are shown in Fig. 3.13 It can be seen that the modeled back-emf is very close to the experimental result. As a result, it is possible to conduct more detailed analysis based on the developed model. Illustrations of the concept of the spatial harmonic model are shown in Fig. 3.14 and Fig. 3.15. It can be seen that in the stationary frame, the back-emf voltage contour becomes a certain image instead of unit circle, because of spatial harmonic content. When the

synchronous frame is used, the fundamental component becomes a unit vector and the asynchronous contents causes the variation of back-emf voltage. It is observed that the back-emf voltage will be larger than the case with only the FC. This explains why the required DC bus is much higher in the experimental result.

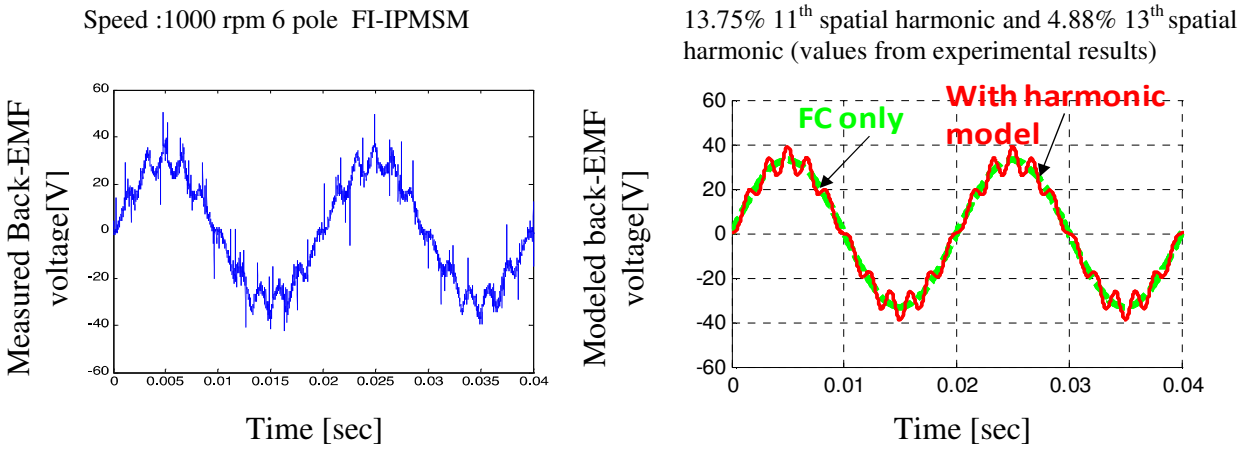

Fig. 3.13 Comparisons of experimental back-emf and modeled back-emf voltage with spatial harmonic components

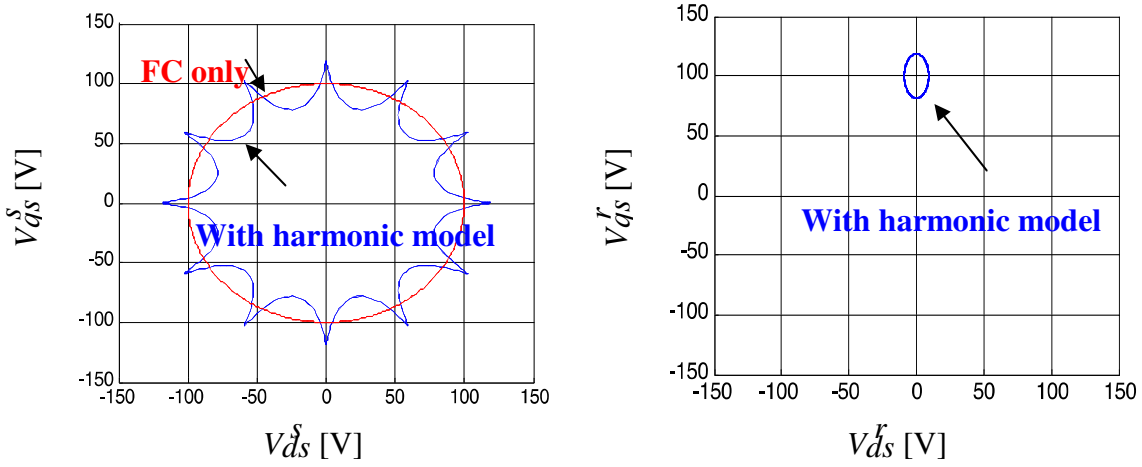

Fig. 3.14 Simulation of V_{dq} with spatial harmonic in the stationary (left) and synchronous (right) ref. frame

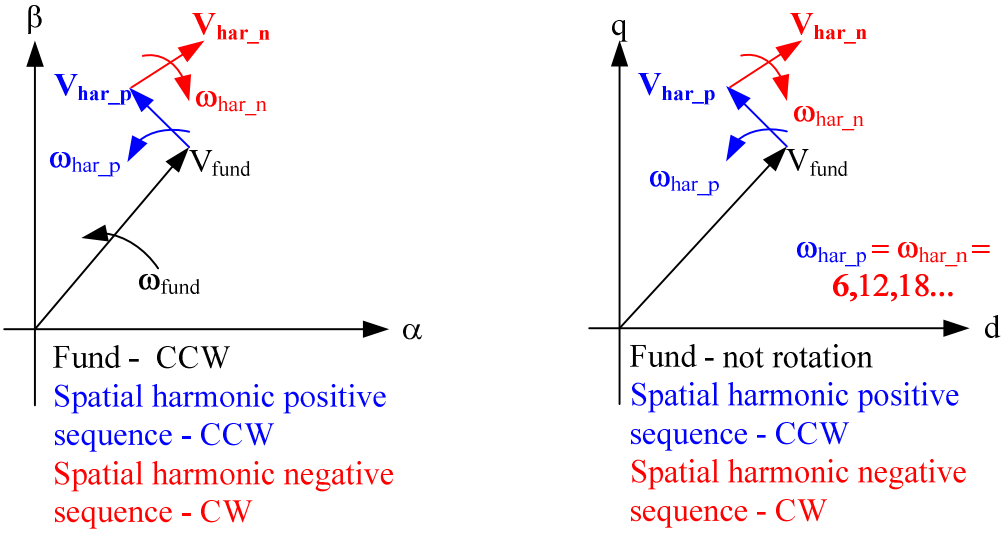

Fig. 3.15 Illustration of voltage vector with spatial harmonic contents in the stationary (left) and synchronous (right) ref. frame

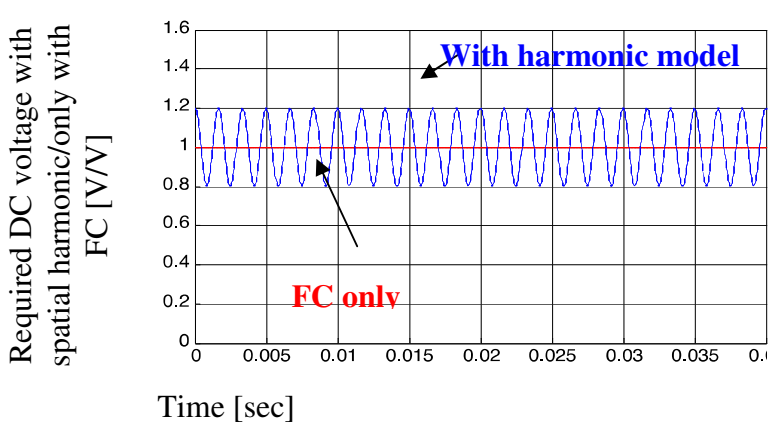

With 15% 11th spatial and 5% 13th spatial harmonic

Fig. 3.16 Simulation with MATLAB tool of required DC bus voltage based model in (3-11)-(3-13)

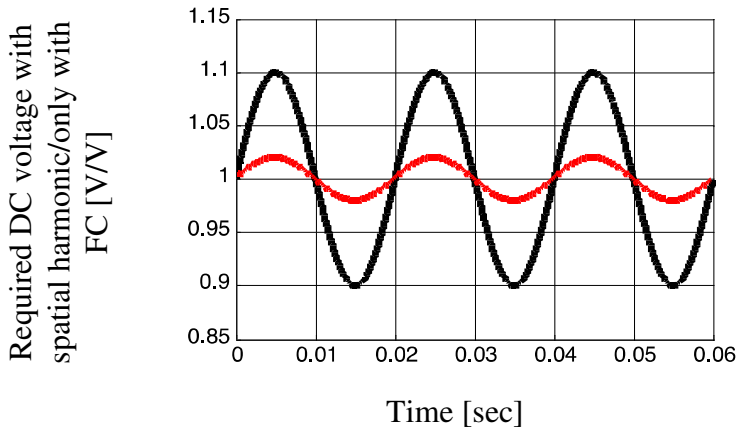

---1 pu inductance machine
— 0.2 pu inductance machine
Both assume 1pu current excitation

Fig. 3.17 Simulation with MATLAB tool of required DC bus voltage for machines with 10% spatial harmonic content based model in (3-15)-(3-18)

Fig. 3.16 shows simulation results of the required DC bus voltage. The required DC bus voltage can be calculated as:

$$\sqrt{3}\sqrt{V_{ds}^{r\,2} + V_{qs}^{r\,2}} = V_{DC} \tag{3-14}$$

It can be seen that the spatial harmonic causes the required DC bus voltage to be 20% larger than the one without any spatial harmonic. It should be noted that the phase of spatial harmonic is assumed in phase with fundamental component. Furthermore, only the 6^{th},12^{th},18^{th} order spatial harmonic are shown in the synchronous frame since 5^{th} and 7^{th} order combine as 6^{th} order and 11^{th} order and 13^{th} order combine as 12^{th} and so on. In Fig. 3.16, it can be seen that the 13^{th} and 11^{th} are combined into 12^{th} order in the synchronous frame. From this analysis, it is apparent that the spatial harmonics will cause the required DC bus to be higher than the value with only the fundamental component. In addition, the spatial harmonic contents will also have other effects. First, the spatial harmonics increase with speed, therefore, it is obvious that additional core loss is produced under high speed conditions. Secondly, spatial harmonics cause phase current distortion and the situation becomes worse as speed increases. The spatial harmonics can be seen as a disturbance voltage increasing with speed. Since the current regulator usually has finite bandwidth, the phase current will be distorted as speed increases.

*3.4.2 **Synchronous inductance with spatial harmonic contents***

The synchronous inductance is often assumed to have a constant value in the spatial domain. The inductance saturation effects only describe how the inductance varies with magnetic saturation. However, due to the structure of the rotor/stator and geometry of the teeth/slot, the synchronous inductance will also vary in the spatial domain. It will also have impact on the required DC bus voltage. The model can be written as

$$L_{q\_total}(i) = L_q(i) + L_{q\_har\_p}(i) + L_{q\_har\_n}(i) \quad (3\text{-}15)$$

$$L_{d\_total}(i) = L_d(i) + L_{d\_har\_p}(i) + L_{d\_har\_n}(i) \quad (3\text{-}16)$$

$$v_{ds}^{r} = -\omega_r L_{q\_total}(i) i_{qs}^{r} \quad (3\text{-}17)$$

$$v_{qs}^{r} = \omega_r (L_{d\_total}(i) i_{ds}^{r} + \lambda_{pm}) \quad (3\text{-}18)$$

where: subscripts *d, q, har_p, har_n* represent d,q synchronous frame, positive spatial harmonic sequence, and negative spatial harmonic sequence, respectively, and v, ω, L, represent voltage, electrical rotational speed and inductance.

It should be noted that the both the synchronous inductance and the spatial harmonic inductance also vary with current level. For the same level of spatial harmonic content, the machine with higher per unit inductance value will have a greater impact on the required DC bus voltage. The results depend on the machine design. Normally, fractional slot concentric winding machines (FSCW) have much larger per unit inductance than integer slot distributing winding machines (ISDW). The simulation results are shown in Fig. 3.17.

3.5 Experimental Evaluation of Proposed Methods

It has been shown that spatial harmonics will have significant impact to the optimum DC bus calculation. In this section, a 10kW FI-IPMSM with 36-slots-6-poles, distributed windings [131] is used to evaluated the proposed method to mitigate non-ideal effects. Several conditions which include parameter estimation errors, spatial harmonic and the minimum DC bus voltage to maintain commanded torque are used to evaluate the proposed methods.

All experimental test conditions are listed in Table I.

Table. I Test conditions

Conditions	Para	Speed[rpm]	Current[p.u.]	Figs.
Steady state	λ_m	500	0.5/1	Fig. 3.18
		1000	0.5/1	Fig. 3.19
	L_d, L_q	500	0.5/1	Fig. 3.20
		1000	0.5/1	Fig. 3.21
Transient	λ_m	1000	0.5/1	Fig. 3.22
	L_d, L_q	1000	0.5/1	Fig. 3.23

*3.5.1 **Evaluation with PM flux variations***

In this part, the PM flux estimation values were varied to evaluate the proposed methods. The experimental results with variation of PM flux, speed and current conditions are shown as Fig. 3.18 and Fig. 3.19. It can be seen that the estimated required DC bus voltage varied with the change of estimated PM flux for the FC method. On the other hand, with the proposed method, the required DC bus voltage is not varied with the variation of estimated PM flux. It can be seen that the DC bus voltage changes with time because of spatial harmonic contents if the proposed method is used. It can be observed that the frequency is increased with the machine speed. Since the major spatial

harmonics are the 11th and 13th in this machine, they appear in the DC value to be a 12th order harmonic.

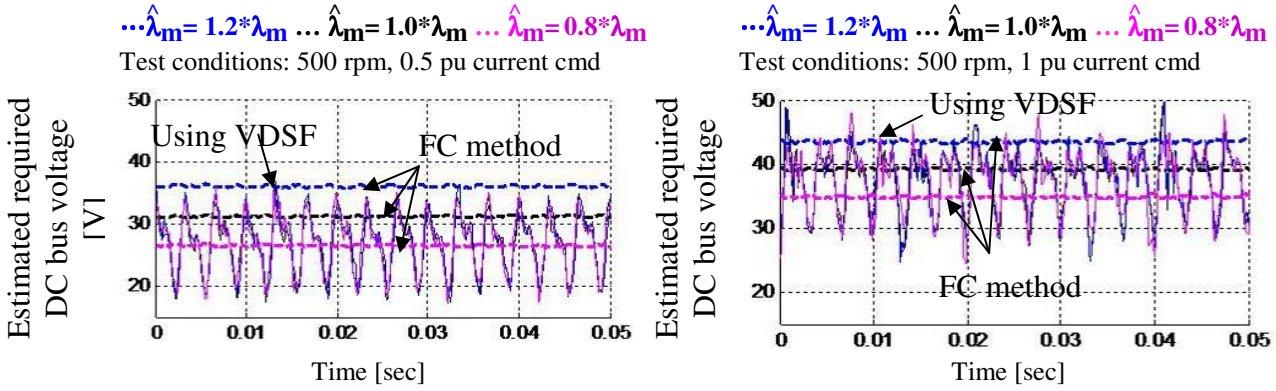

Fig. 3.18 Comparison of FC component method and proposed VDSF method with estimated PM flux variation

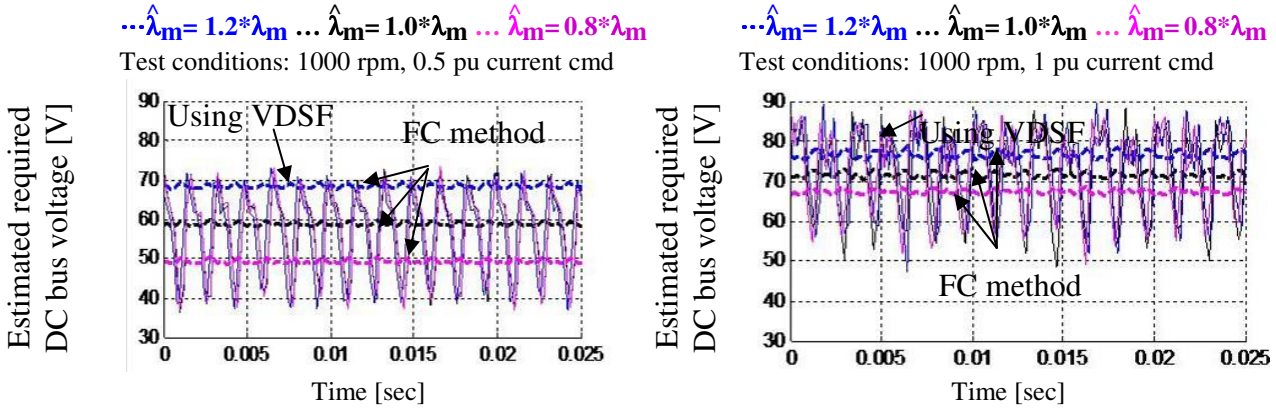

Fig. 3.19 Comparison of FC component method and proposed VDSF method with estimated PM flux variation

*3.5.2 **Evaluation with inductance variations***

Similar experimental procedures were also performed with the variation of estimated inductance. The experiment results are shown in Fig. 3.20 and Fig. 3.21. It can be observed that the proposed methods can mitigate the effects of parameter estimation variation. It can be observed that the variations of estimated required DC bus in the lower current conditions are smaller with FC method. This is because the flux generated by the armature reaction is smaller at lower current conditions.

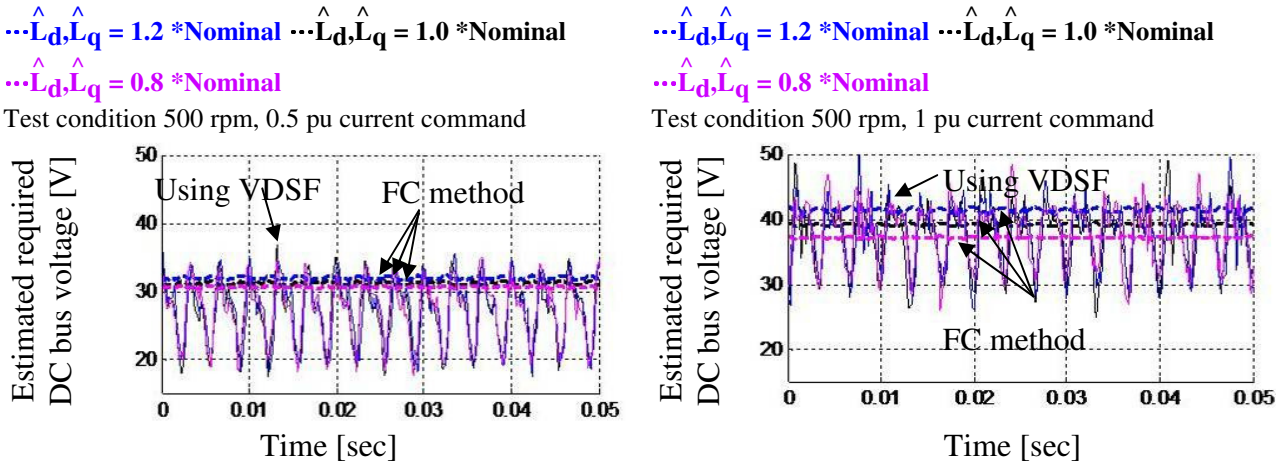

Fig. 3.20 Comparison of FC component method and proposed VDSF method with estimated PM flux variation

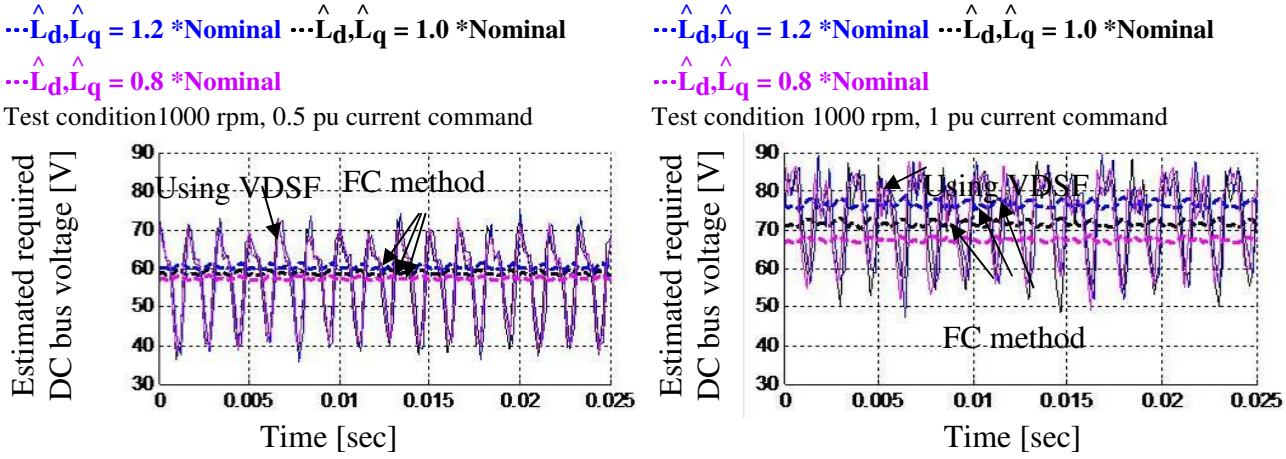

Fig. 3.21 Comparison of FC component method and proposed VDSF method with estimated PM flux variation

*3.5.3 **Evaluation during transient conditions***

The test of the minimum required DC bus voltage with the FC method and proposed methods during the transient conditions are shown as Fig. 3.22 and Fig. 3.23. It can be seen that the proposed method shows similar performance during steady state conditions. During current transient conditions, a voltage spike was observed. Since the inverter needs to produce a significant *Ldi/dt* voltage in the machine during the transient, the required DC bus voltage is higher than the steady state. On the contrast, this physical phenomenon cannot be observed if FC method is used.

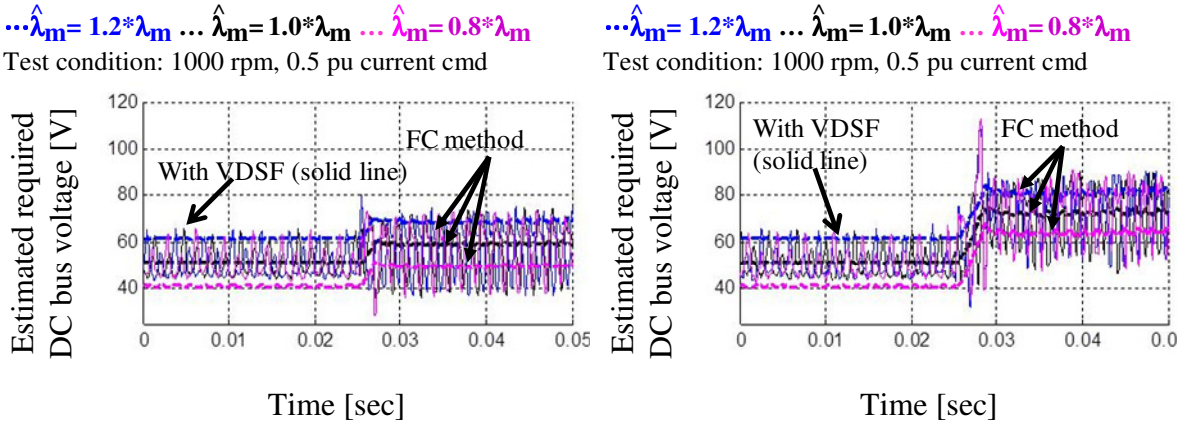

Fig. 3.22 Comparison of FC component method and proposed VDSF method with estimated PM flux variation

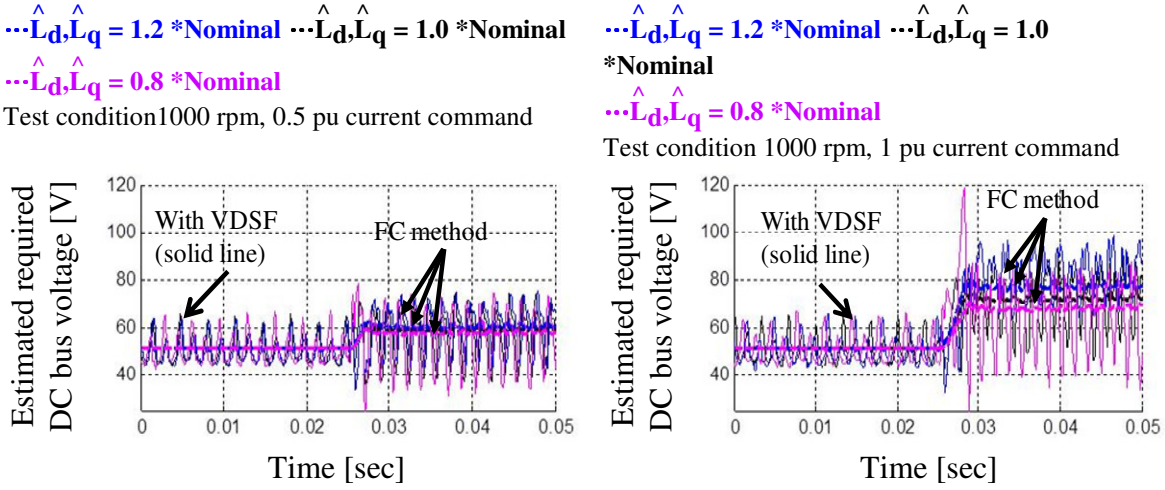

Fig. 3.23 Comparison of FC component method and proposed VDSF method with estimated PM flux variation

*3.5.4 **Estimated required DC bus voltage on loaded conditions***

The test of the minimum required DC bus voltage with the FC method and the proposed methods are shown as Fig. 3.24 and Fig. 3.25. To ensure enough DC bus voltage without saturating the current regulator, the peak DC bus voltage value in VDSF will be used. In real applications, peak value sampling and low pass filter can be used to implement this method. From the experimental results, it is shown that the estimated required DC bus voltage from ideal model is lower than the voltage required by the real

drive. As stated before, if the DC bus voltage is lower than the machine terminal voltage, the desired torque command cannot be achieved. In contrast, with the VDSF method, the calculation errors caused by spatial harmonics can be corrected so that the torque command can be achieved. It also can be seen that the estimated required voltage with VDSF is nearly the minimum DC bus voltage which will thus have the minimum losses. If the DC bus voltage is further reduced, the desired torque command cannot be maintained.

Another important practical issue is how the system recovers from a low bus voltage when the system is hit with a large command for higher velocity. The dynamic response of the booster converter relative to the vehicle dynamics is the key issue. For the switching frequencies used in vehicle applications, it has been shown a high dynamic response can be achieved within 100ms (recovery from 200V to 500V) when a sudden high voltage is required [105].

Test condition: DC bus 60V, 0.5 pu torque command Machine speed 500 rpm

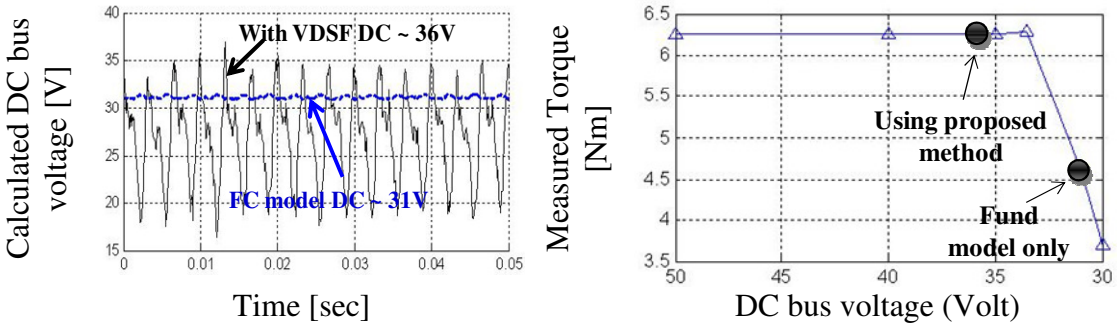

Fig. 3.24 Experiment results using VDSF with a FI-IPMSM drive (left) and Measured torque on a FI-IPMSM drive over a range of DC bus voltages

Test condition: DCbus 120V,0.5 pu torque command Machine speed 1000 rpm

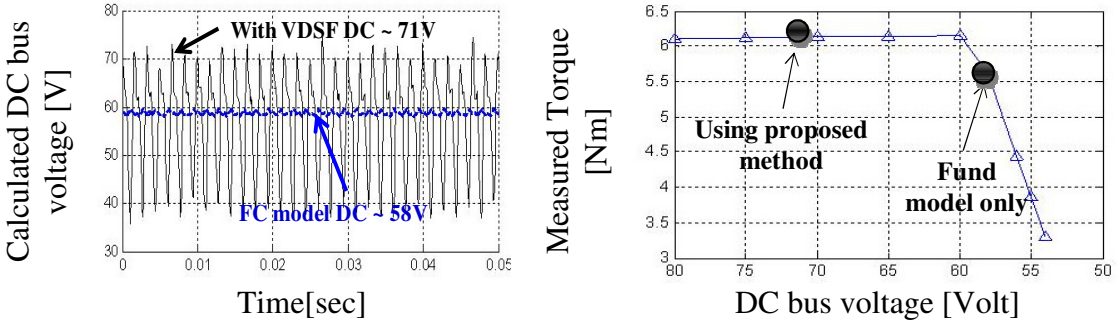

Fig. 3.25 Experiment results using VDSF with a FI-IPMSM drive (left) and Measured torque on a FI-IPMSM drive over a range of DC bus voltages

3.6 Position Estimation with Variable DC Bus Voltage

The investigation of the relationship between DC bus voltage and self-sensing performance is performed. First of all, it has been know that the inverter nonlinearity effect is more severe in the low current conditions [59]. As a result, 0, 0.1, 0.2 pu Torque command are selected for this investigation. Loss minimization operating points are selected in CVC. In this test, lookup table LMC method and MTPA are tested. Because FI-IPMSM have relatively low saliency so the iron loss is very small it in low speed, low current conditions. Therefore, the operating points of MTPA are very close to LMC method. The experimental result of MTPA CVC is shown as Fig. 3.26. It can be seen that the MTPA contour doesn't have significant change even a saturated value is used. The reason is that difference of d- and q- axis inductance FI-IPMSM is relatively small and it is also less insensitive to inductance saturation. The plot torque production with different method is shown as Fig. 3.27. Several observations can be made from Fig. 3.27. First, it can be seen almost no difference exist between MTPA and "i_q only" method during low load conditions. Only 1% torque is increased by the MTPA on the rated load conditions. The experimental result shows that Lorentz torque is dominant in the FI-IPMSM. Secondly, saturation effect cause very small torque production differences. It means that the torque production of FI-IPMSM machine is relatively insensitive to the saturation effect. LMC CVC with pulsating vector injection and variable DC bus voltage is used to test the self-sensing performance in FI-IPMSM. The test results are shown in Fig. 3.28-Fig. 3.30.

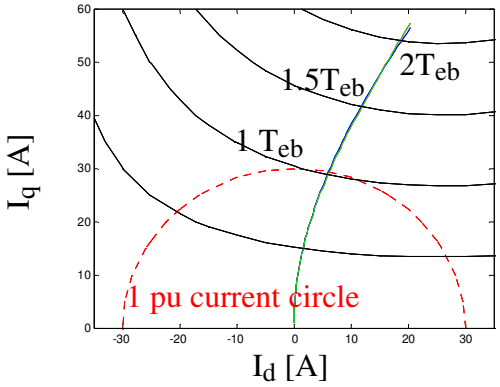

Fig. 3.26 Comparison of the MTPA contour with inductance values saturated/unsaturated

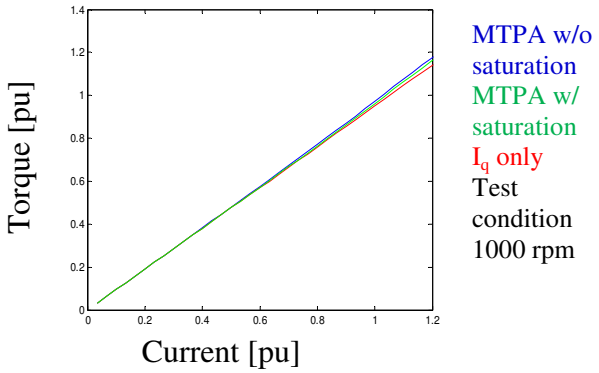

Fig. 3.27 Comparison of torque production with different control method

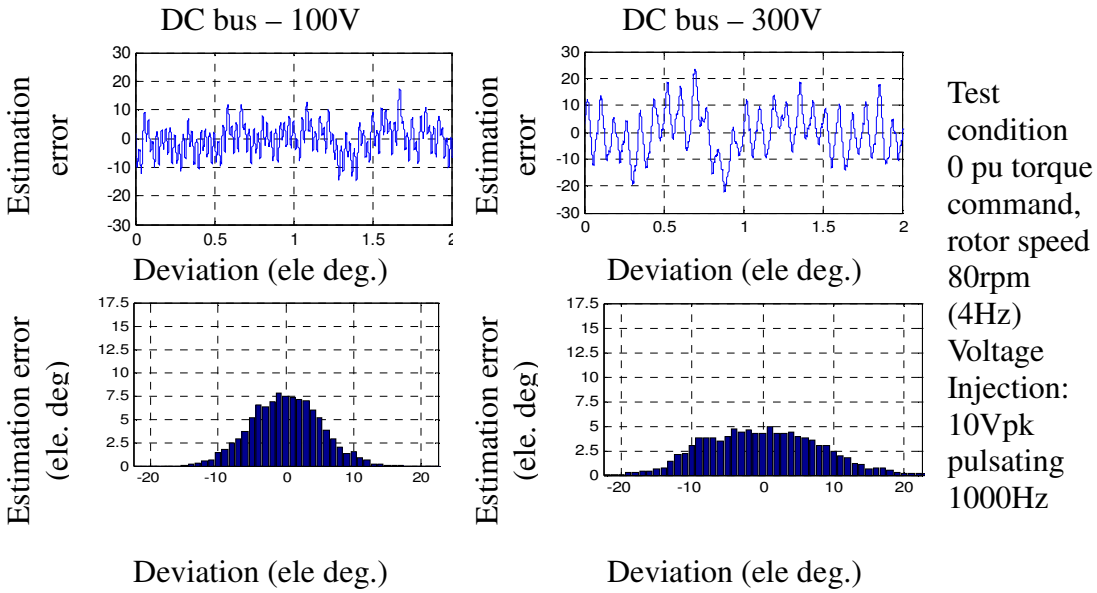

Fig. 3.28 Comparisons of self-sensing performance with LMC CVC and different DC bus voltage under 0 pu torque command

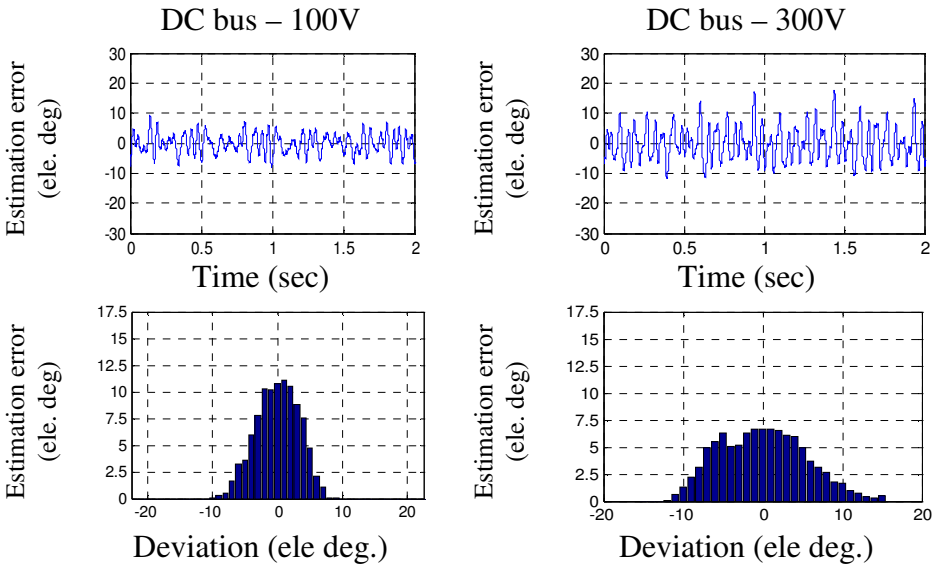

Fig. 3.29 Comparisons of self-sensing performance with LMC CVC and different DC bus voltage under 0.1 pu torque command

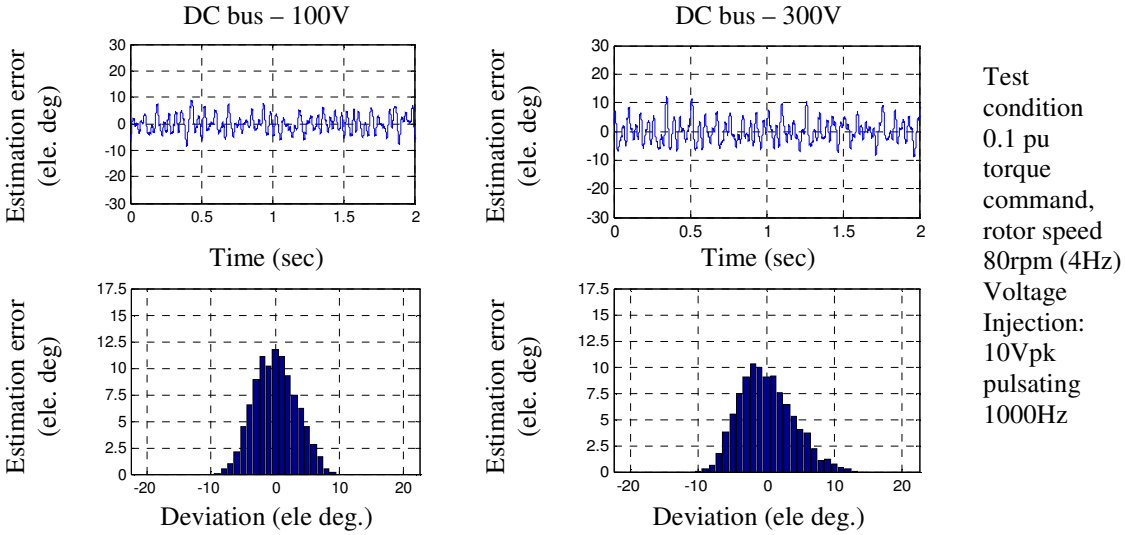

Fig. 3.30 Comparisons of self-sensing performance with LMC CVC and different DC bus voltage under 0.2 pu torque command

From the experiment results of estimation error of time domain waveform and histogram shown above, it can be seen that lower the DC bus voltage improves the self-sensing performance. The error root mean square value of each operating condition is also used to compare the self-sensing performance. The result is shown as Fig. 3.31, it is clear that lower DC bus voltage gives better self-sensing performance. These results align with the optimum DC bus voltage selection control strategy. A dynamically integration of position self-sensing in the proposed DC bus voltage selection control method will become possible.

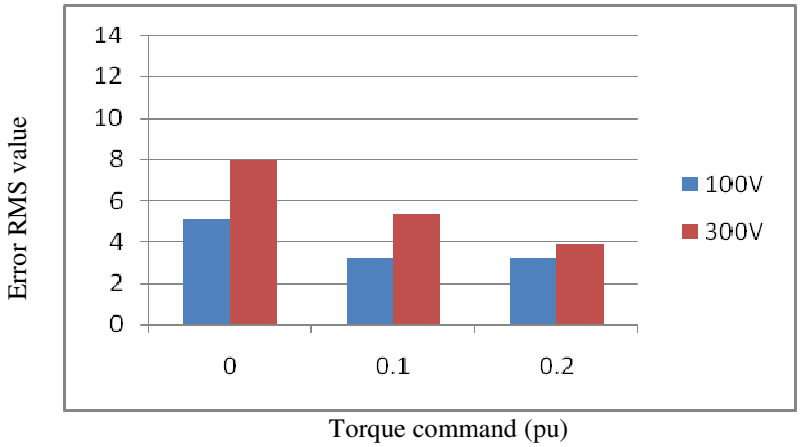

Fig. 3.31 Self-sensing performance against DC bus voltage under 0-0.2 pu command with pulsating injection

3.7 Conclusions and Summary

This chapter conclusions and contributions are summarized as following.

- The optimal DC bus voltage for low speed operation is lower than for rated speed operation. It has been shown both in theory and experiment, that with a lower DC bus voltage, the total drive system (motor and inverter) efficiency can be improved because inverter switching losses are reduced.
- The required DC bus voltage can be calculated by using an ideal fundamental component (FC) machine model. However, it has been shown that the machine parameter errors and spatial harmonics cause errors in the calculated DC bus.
- The impact of spatial harmonics on the required DC bus voltage has been investigated. It is shown that the spatial effect will have significant impact on the required DC bus voltage if the machines have large spatial harmonics. The real value of the required DC bus voltage will be significantly higher than the value calculated from the FC method.
- A method using a voltage disturbance state filter (VDSF) has been developed and shown to be useful in estimating and correcting voltage errors due to parameter estimation and unmodeled spatial harmonics. Therefore, the required ”nearly optimal” DC bus voltage can be calculated on-line. The effectiveness of this method has been demonstrated by experiment results.
- The developed method could be applied on EV, HEV, or PHEV applications as long as a variable DC bus voltage drive is available.
- In the low speed, light load conditions, position self-sensing with variable DC bus voltage are investigated. It can be seen that LMC-CVC with low DC bus voltage and pulsating vector injection improve the self-sensing performance.

Chapter 4 - Variable Flux Machine Torque Estimation and Pulsating Torque Mitigation during Magnetization State Manipulation

This charter focuses on dynamic control, under loaded conditions, of the magnetization state of suitably designed variable flux (VF) permanent magnet (PM) machines. Such VF-PM machines have been shown to achieve low loss operation over a wide range of load and speed. For this type of machine, the PM flux linkage varies during the magnetization manipulation process. Published magnetization techniques have occurred at zero load conditions and thus did not generate torque pulsations. However, under loaded conditions, the existing methods would produce unwanted torque pulsation. This paper proposes a parameter insensitive method to solve this issue. This method generates a decoupling current command which is calculated from accurately estimated stator flux linkage. Accurate flux estimation, i.e. insensitive to inductance saturation and PM flux linkage variation (e.g. temperature or magnetization level) is achieved by using the voltage disturbance estimated by a closed-loop stator current vector observer. In both simulations and experiments, it is shown that even during magnetization processes under loaded conditions, the flux can be estimated correctly and smooth torque output can be achieved.

4.1 VF Machine Magnetization State Manipulation

The machine geometry is shown Fig. 4.1. To achieve wide speed operation, variable flux (VF) machines can operate with high magnet flux in the low speed region and low magnet flux in the high speed region. In Fig. 4.2, a typical operating scenario is depicted. The machine under light load, low speed conditions is operated at reduced magnetization states to achieve high efficiency (low iron and copper loss). Then, if high (maximum) torque is suddenly required, the machine must operate with higher magnet flux to deliver higher torque requirement. Finally, to have wide speed operation, magnetization level should be continuously decreased as speeds increases. The key issue is to change the magnetization state under different working conditions without producing any transient pulsating torque.

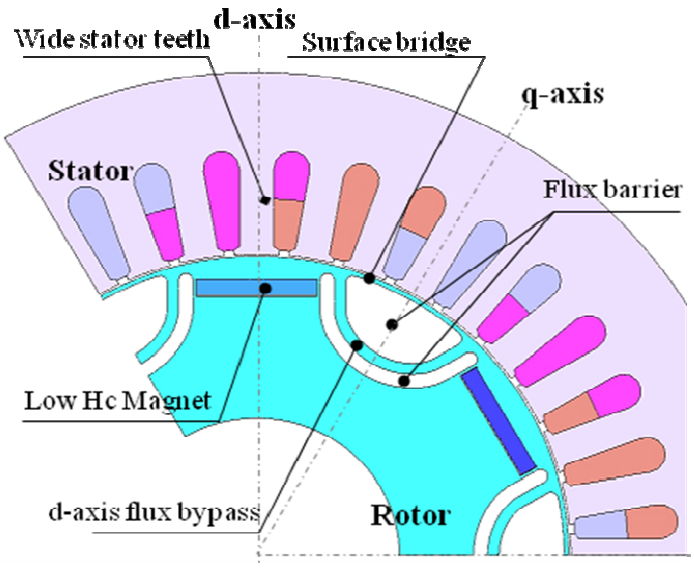

Fig. 4.1 Machine geometry of VFI-IPMSM in [1, 2]

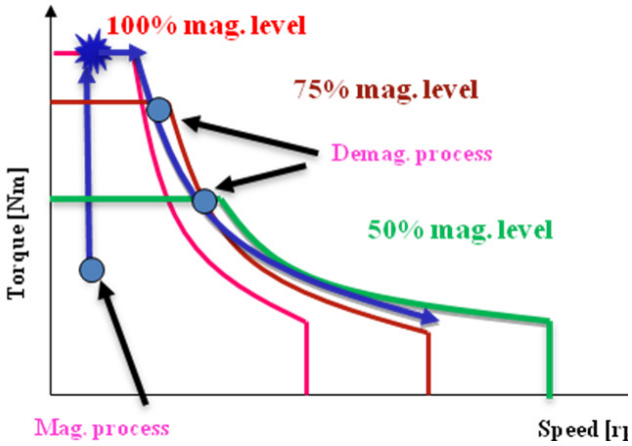

Fig. 4.2 VF Machine magnetization state manipulation under acceleration

4.2 VFI-IPMSM Properties

4.2.1 Magnetization properties with FEA & experiments

To implement proper magnetization state control of VF machines, the magnetization and demagnetization properties of the machine are required. The relationship between the id current pulse amplitude and magnetization properties can be obtained from FEA or through experimental results. The FEA results are shown in Fig. 4.3and Fig. 4.4 and experimental results are shown as Fig. 4.5 and Fig. 4.6.

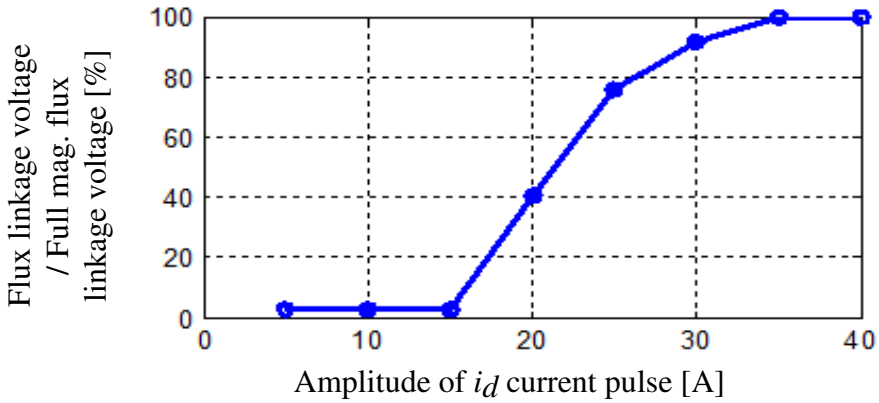

Fig. 4.3 FEA evaluation of normalized magnetization state for a set of positive i_d current pulse amplitudes

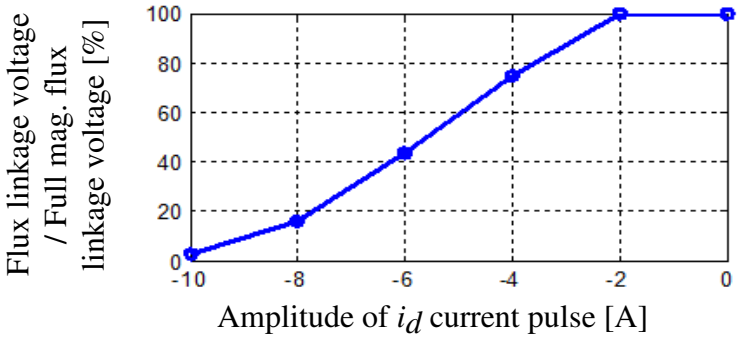

Fig. 4.4 FEA evaluation of normalized magnetization state for a set of negative i_d current pulse amplitudes

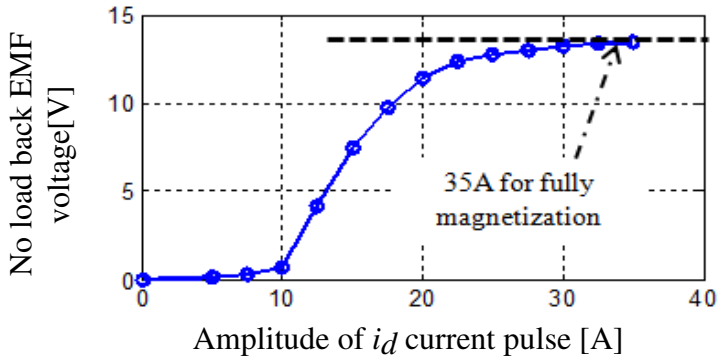

Fig. 4.5 Experimental evaluation of no load back EMF for a set of positive i_d current pulse amplitudes

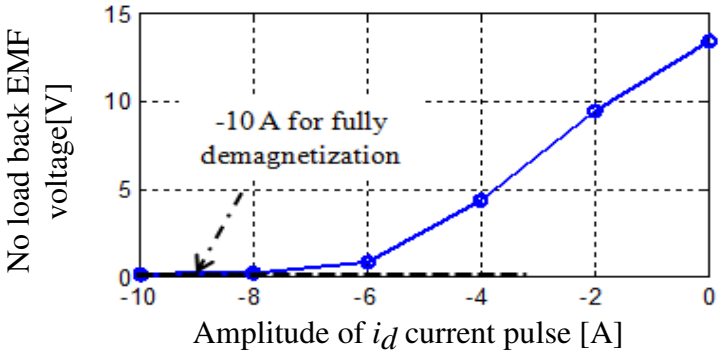

Fig. 4.6 Experimental evaluation of no load back EMF for a set of negative i_d current pulse amplitudes

In both FEA and experimental results, PM flux linkage (back EMF voltage) under no load conditions is used as to estimate magnetization state. It can be seen from both

simulations and experiments that the magnetization state can be changed with a i_d current pulse.

*4.2.2 **Variable flux machine output torque property and energy consumption of the magnetization current***

Fig. 4.7 shows the magnetization level obtained (in percentage) as a function of i_d current pulse amplitude, where 100% refers to fully magnetized condition with pulse amplitude of 3.5x rated current.

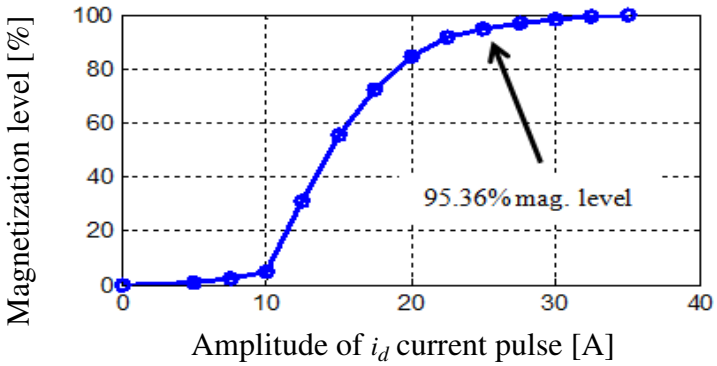

Fig. 4.7 Experimental normalized magnetization state measured for a set of positive i_d current pulse amplitudes

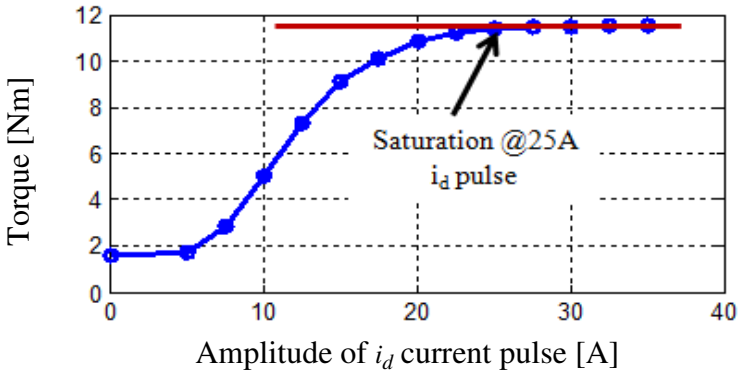

Fig. 4.8 Measured maximum output torque (under 1pu current) measured for a set of positive i_d current pulse amplitudes

Obtaining maximum output torque capability under different magnetization states is done by following procedure: First, the machine is injected with a certain i_d current pulse amplitude to change to specific magnetization state. Secondly, the maximum torque

output for a 1 pu current vector was recorded by a torque meter. It should be noted that the loaded 1 pu current vector doesn't alter the magnetization state under each test condition. The result is shown in Fig. 4.8.

It can be found that the maximum torque is kept constant under 95.36% (25A) or higher magnetization level. This means that the maximum output torque is saturated and increasing magnetization level with larger i_d current pulse amplitude would not result in higher torque. This could be due to the magnet properties or to magnetic saturation in the iron. This issue is the subject of future research. Therefore, it can be concluded that injecting an i_d current pulse amplitude greater than 25A results in increased losses but does very little for increasing output torque capability.

The energy consumption of a magnetization current pulse under different conditions is an important issue. Comparisons were conducted using two metrics: magnetization period (width of the i_d current pulse) and magnetization current amplitude (i_d current pulse amplitude ranging from 2.5 pu to 3.5 pu). A triangle pulse waveform is assumed and all the cases are shown to achieve maximum torque capability. The shortest period is 50 ms. The results are shown as Fig. 4.9. It can be seen that significant reduction of energy consumption can be achieved by properly defining the magnetization current amplitude and reducing the magnetization period. However, it should be noted that reducing the magnetization period to less than 50 ms is challenging because the flux observer bandwidth required tracking details such as machine spatial harmonics and saturation becomes impractical.

The process used for the tested machine required a short 2.5 pu current pulse for full magnetization. Inverters for duty cycle applications are often designed to deliver 3x rated current for transient operating conditions. As a result, a short 2.5 pu current pulse for full magnetization state is a reasonable criteria.

Magnet loss under pulsed conditions can be minimized by proper design. Magnet eddy current loss with 3D FEA simulation has been performed and shown in Fig. 4.10and Fig. 4.11. It was found that with 10 magnet segments in the VFI-IPMSM, magnet loss could be very small (~0.23W).

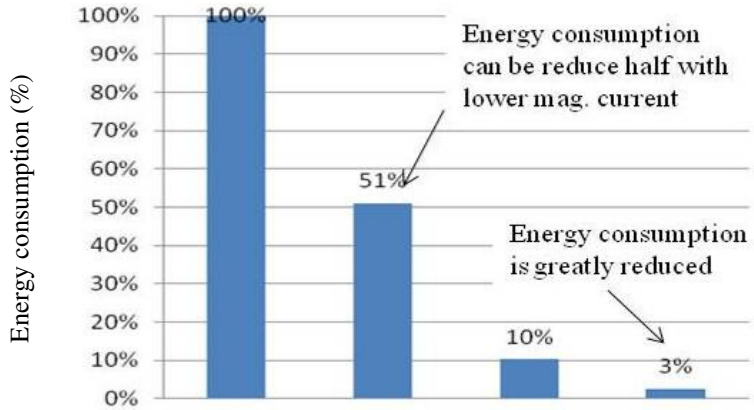

100% = 0.255 (Wh/pulse)Rs = 1.5 ohm

Fig. 4.9 Magnetization current pulse energy consumption for different periods and current amplitudes

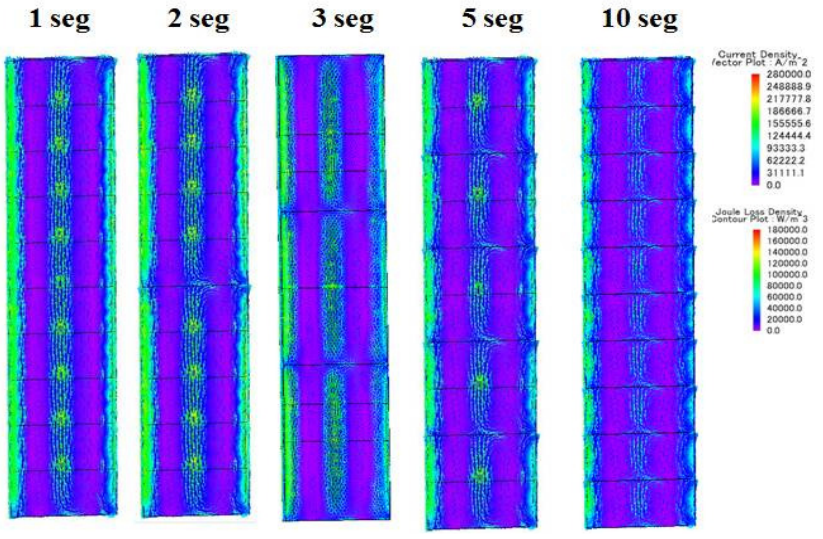

Test conditions
2.5 pu current magnetization current

1500 rpm

Fig. 4.10 Magnet eddy current loss simulation with 3D FEA

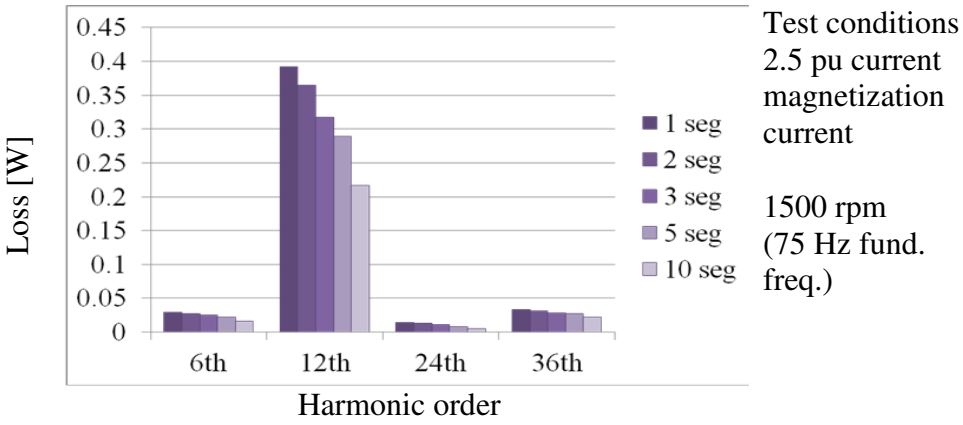

Fig. 4.11 Magnet eddy current loss analysis with different magnet segmentation

4.3 Control Methods for Magnetization State Manipulation

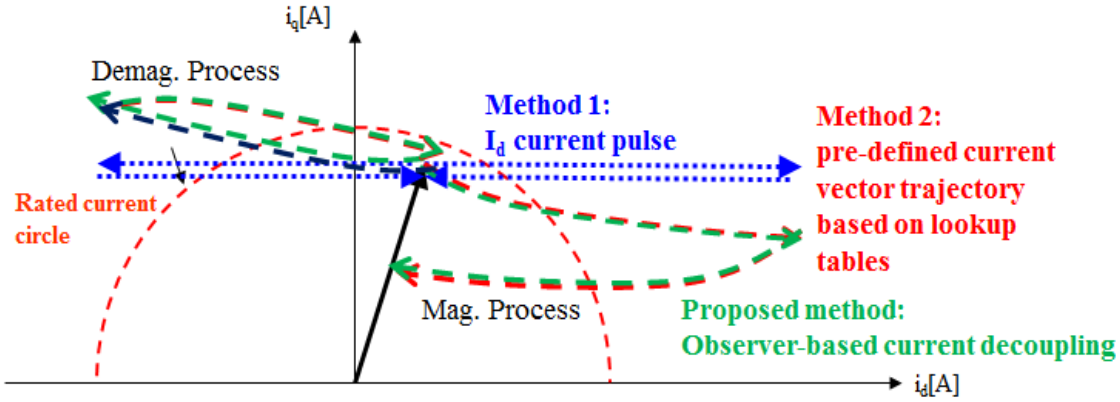

Fig. 4.12 Possible solutions for smooth torque control during magnetization process

To change magnetization state, several possible solutions are shown in Fig. 4.12. Two are existing solutions: direct i_d current pulse injection and using pre-defined current vector trajectory lookup tables. The simplest method is giving a i_d current pulse (blue line in Fig. 4.12) to the machine to achieve the desired magnetization state. This method is only feasible under no load conditions. Otherwise, a severe pulsating torque can be produced. The second method is based on lookup tables. To produce smooth torque, i_q current should be reduced as i_d current increases under loaded conditions based on a pre-recorded current trajectory in a lookup table (red dotted line in Fig. 4.12).

However, time intensive experiments are required because every loaded condition and magnetization state corresponds to a different current trajectory. This paper proposes an observer-based current decoupling method (green dotted line in Fig. 4.12). For smooth torque control during magnetization manipulation process under loaded conditions, the overall control block diagram is shown in Fig. 4.13.

For this method, magnetization state is set within the limit of maximum magnetization state based on the machine properties, speed, and available DC bus voltage. For the observer-based current decoupling method, the i_d current command is generated to achieve the target magnetization level. The decoupling current can be generated based on the torque equation and estimated flux. The flux estimation (the green box in Fig. 4.13) for this method is a key issue for accurate torque control and will be discussed in the following section.

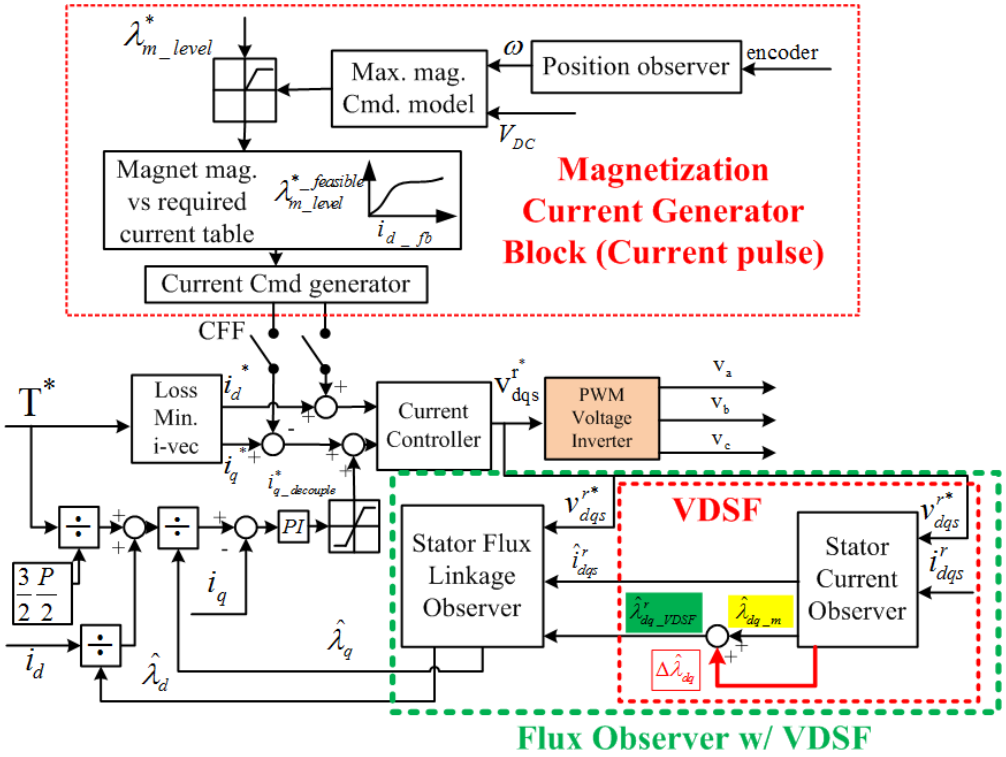

Fig. 4.13 A observer-based current decoupling control method

4.4 Improved Flux Estimation by Using VDSF

In this paper, a cascaded stator flux observer structure is used to mitigate flux estimation error caused by parameter variations. The structure of the stator flux observer is shown as Fig. 4.14. It consists of a stator current observer (SCO) SCO in the first stage and a Gopinath style stator flux linkage observer based on a voltage model [127].

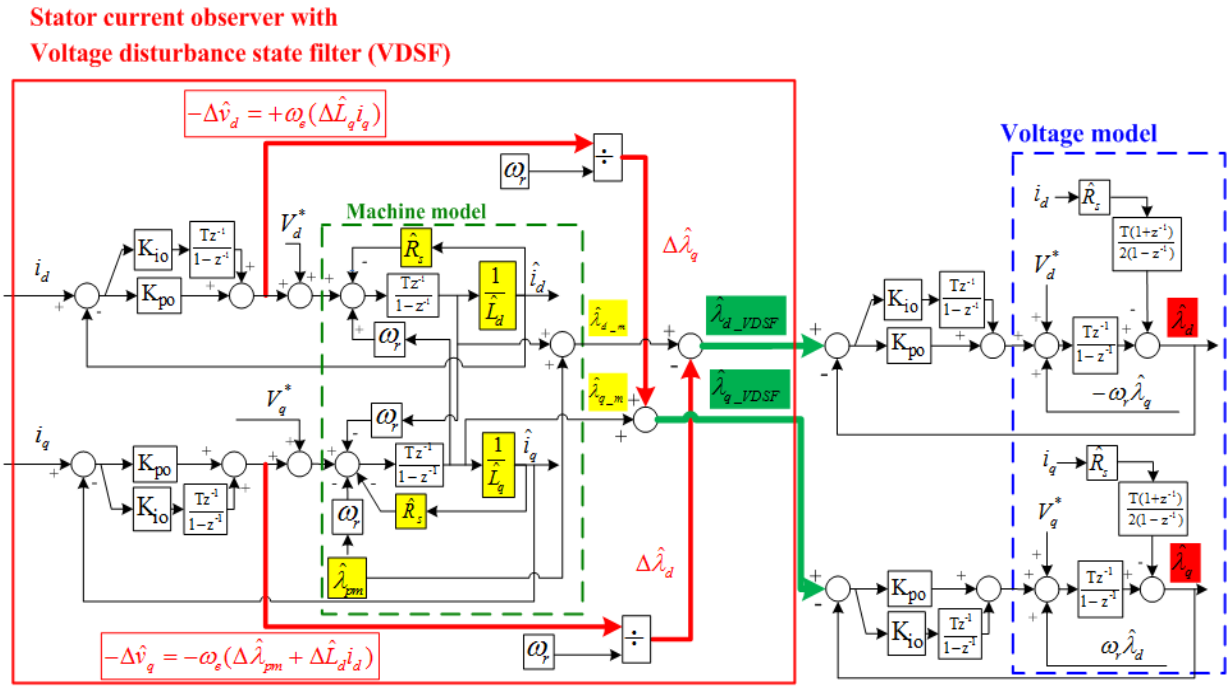

Fig. 4.14 A flux observer structure using VDSF to achieve low sensitivity to PM parameter variations

Within the bandwidth of the SCO, the SCO acts as a VDSF which inherently estimates a disturbance voltage, $\Delta\hat{v}_{dq}$. If exact parameters knowledge of inductance and PM flux linkage are known, the estimated current ($\hat{i}_d, \hat{i}_q$) in SCO will equal to the measured current (i_d, i_q) so disturbance voltage from the output of controller will be very small or zero. However, knowledge of exact parameters is usually difficult to achieve in real cases. With closed-loop SCO structure, the controller forces the estimated current to keep tracking the measured current even under parameter deviations. Under these

conditions, it can be known that the disturbance voltage contains the parameters deviation information (inductance or magnet flux linkage) which can be utilized to decouple the stator flux linkage estimation error.

By decoupling the parameter deviation errors through disturbance voltage in VDSF (red bold line in Fig. 4.14), the stator flux observer becomes less sensitive to both inductance saturation effects and magnet flux linkage variation due to temperature.

However, the disturbance voltage estimation is limited by bandwidth of the SCO. A Gopinath style stator flux linkage observer based on the voltage model (blue dashed box in Fig. 4.14) is cascaded with the SCO. This structure exhibit reduce parameter sensitivity during transient conditions (high frequency), so a better flux estimation can be achieved [132]. This structure also features smooth transition between VDSF and voltage model [132]. VDSF is dominant below a crossover frequency and the voltage model is dominant above the crossover frequency. The crossover frequency is determined by the observer gains depended on different applications.

4.5 Simulation Evaluation during Magnetization State Manipulation

A machine simulation with variable magnetization state capability is used to evaluate the proposed method. The flux and torque estimation with PM parameter variations are used to evaluate the VDSF's ability to reduce PM parameter sensitivity. The simulation results for a 1 pu change in load torque are shown as Fig. 4.15. It can be seen that torque and flux estimation are less sensitive to PM parameters when the VDSF is used.

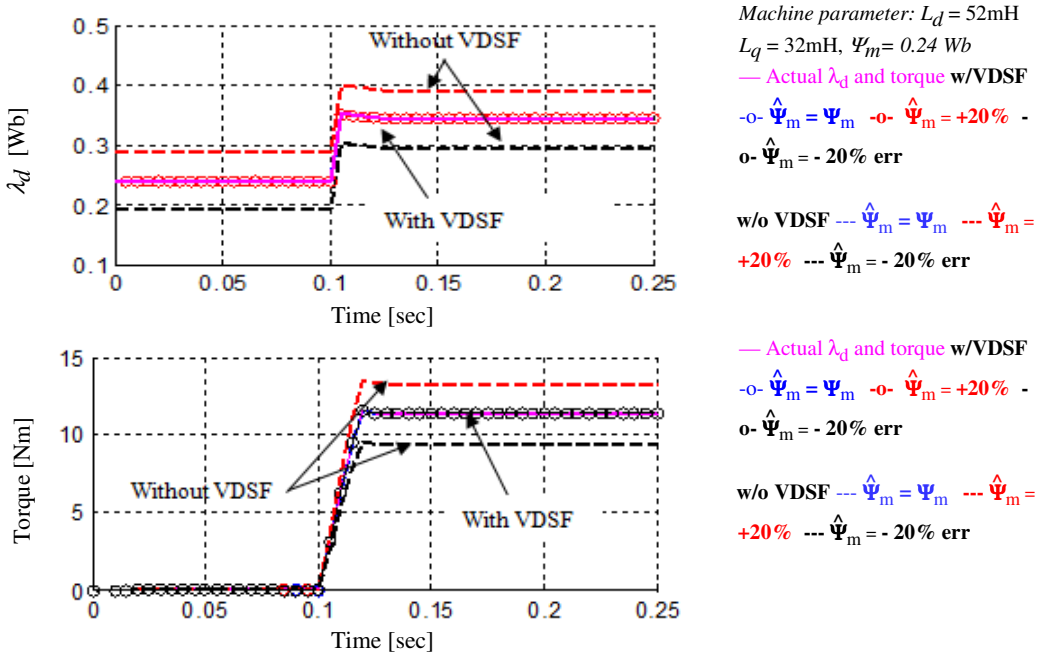

Fig. 4.15 Simulation result of torque and flux estimation with/without VDSF under1 pu current vector change@12.5 deg

The second evaluation is performed with the observer-based current decoupling method during a magnetization manipulation process without/with using VDSF correction. As shown in Fig. 4.16 , if the VDSF is not used, the torque cannot be controlled precisely due to the flux estimation error which is caused by the change of magnetization state. In Fig. 4.17 and Fig. 4.18, it is demonstrated that smooth torque control can be achieved without a lookup table if VDSF is used (proper flux and torque

estimation is achieved). It can be seen that the proposed method can mitigate pulsating torque and torque offset during the magnetization manipulation process unlike the direct i_d current pulse method. The i_d and i_q current plot is shown as Fig. 4.19. It can be seen that the i_q is reduced to decouple the unwanted torque pulsation during the magnetization process.

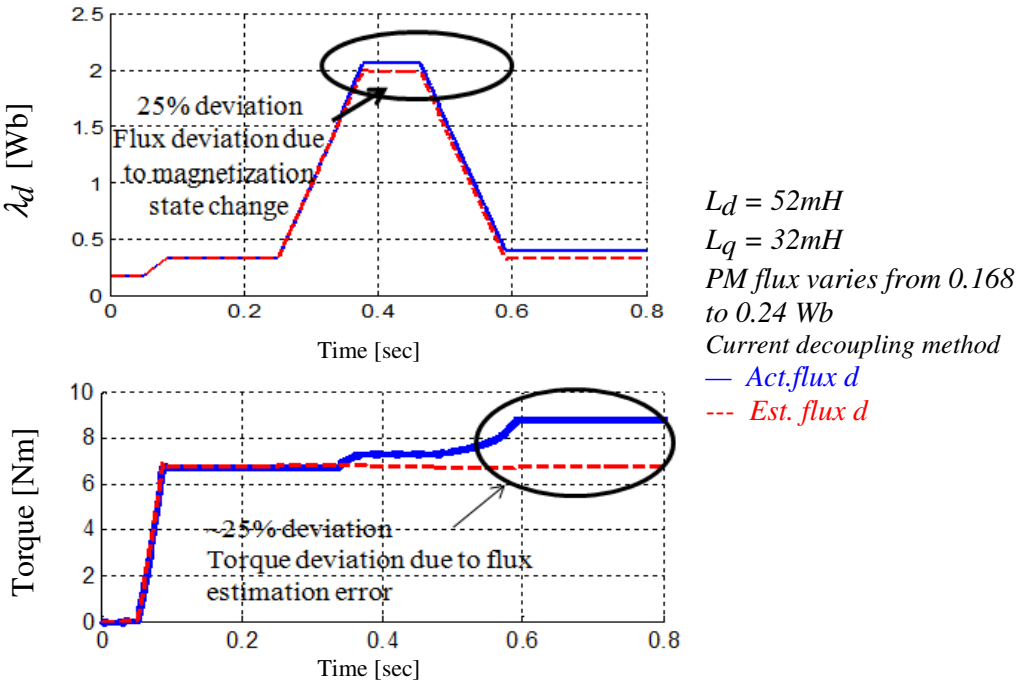

Fig. 4.16 Torque deviations during magnetization manipulation due to flux estimation error (without VDSF correction)

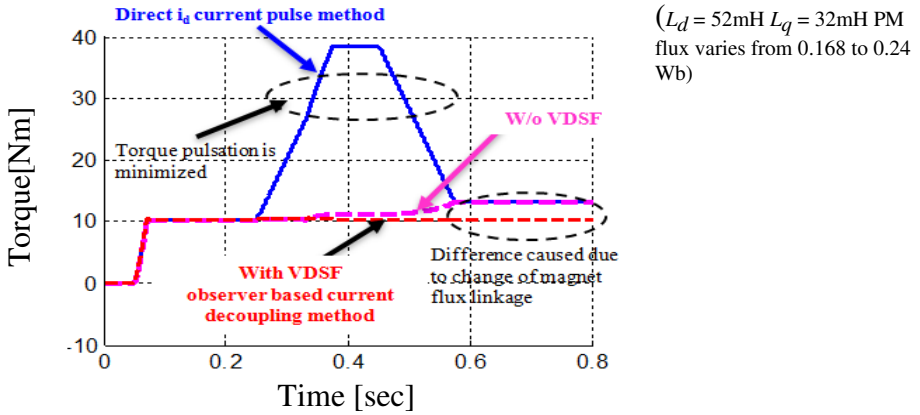

Fig. 4.17 Comparison of output torque characteristic during magnetization manipulation with direct i_d current pulse method and observer-based current decoupling method with/without VDSF

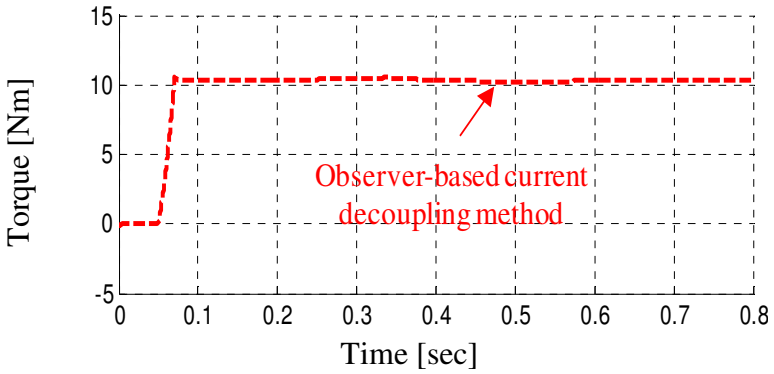

Test condition: fully magnetization process with 10.32 Nm Torque cmd (1 pu rated current) Machine speed: 200 rpm

Fig. 4.18 Zoom in on torque amplitude for observer-based current decoupling method with VDSF)

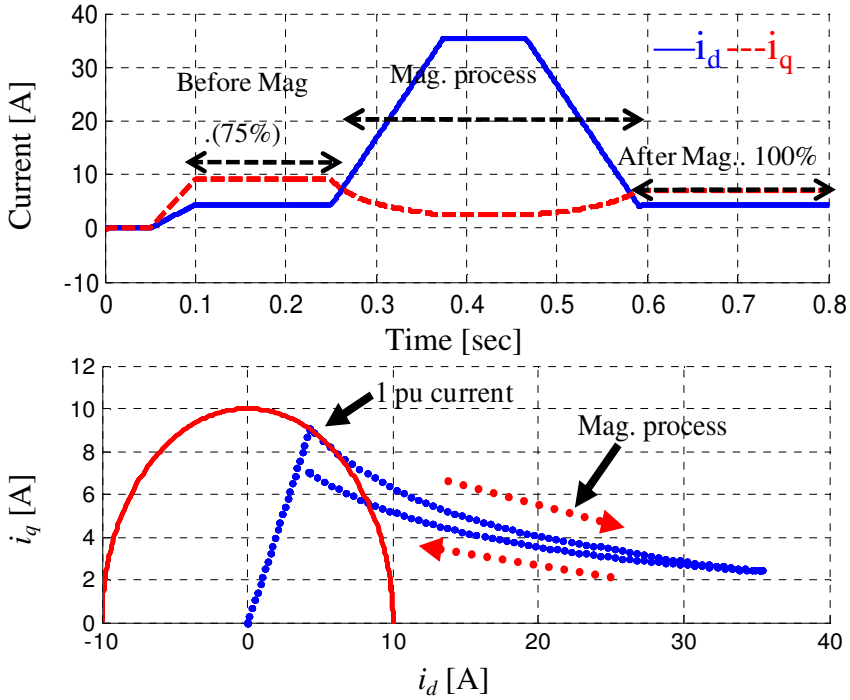

Fig. 4.19 The i_d and i_q current plot in time domain (top) and in d-q plane (bottom)

4.6 Experimental Setup and Evaluation of Proposed Method

A VFI-IPMSM with 36-slots-6-poles and distributed windings is used for experimental evaluation and specification is shown in Table 4.I. The test setup is shown in Fig. 4.20. A torque meter has been installed between two machines and the temperature sensors were installed in both the stator winding and permanent magnet. The temperature is measured by k-type thermal couple and displayed by a PLC controller. During the experiment, the temperature of magnet and winding is monitored in order to produce consistent experimental results.

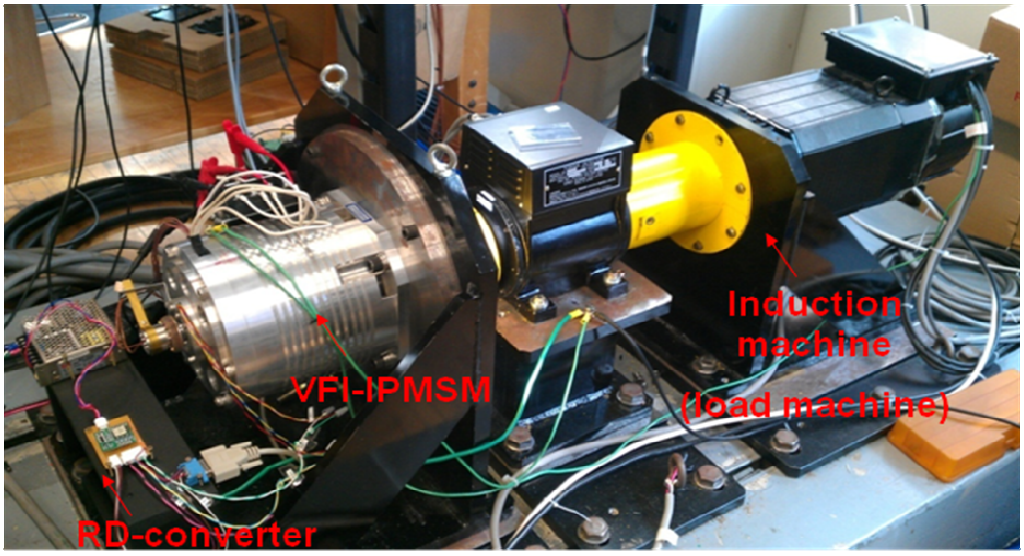

Fig. 4.20 Test setup for VFI-IPMSM

Table 4.I VFI-IPMSM specification	
Specifications	**Value**
Rated speed/ current	1200 rpm/10 A
Rated torque	11.7 N-m (Full magnetization)
Connection	Wye
Poles/Slots/ Turns per slot	6/36/17
Moment of inertia	0.002689 kg-m^2
Ψ_m	0 to 0.138 Wb (Full magnetization)
Winding resistance	1.5 Ω (per phase)

4.6.1 Magnetization process and result

The magnetization process and result is presented in this section. In the beginning, the 3.5x rated current I_d is used to magnetize the magnet. The illustration of phase diagram is shown as Fig. 4.21. To make sure the current vector is properly controlled to have fully magnetization, the voltage and current waveform during the magnetization is recorded and plotted as Fig. 4.22and Fig. 4.23.

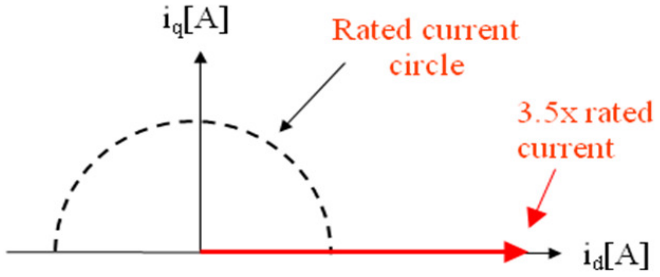

Fig. 4.21 Phase diagram under magnetization process

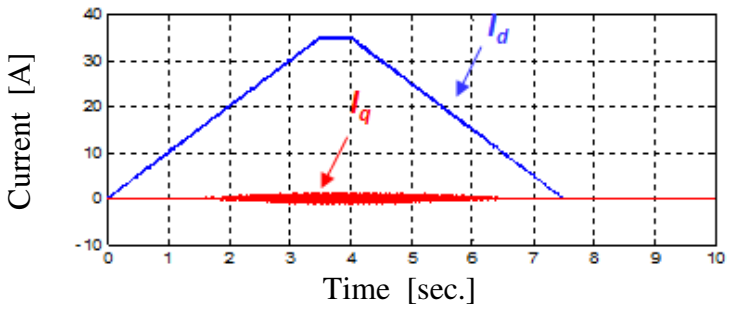

Test condition :
300 rpm

Fig. 4.22 Current waveform during magnetization process

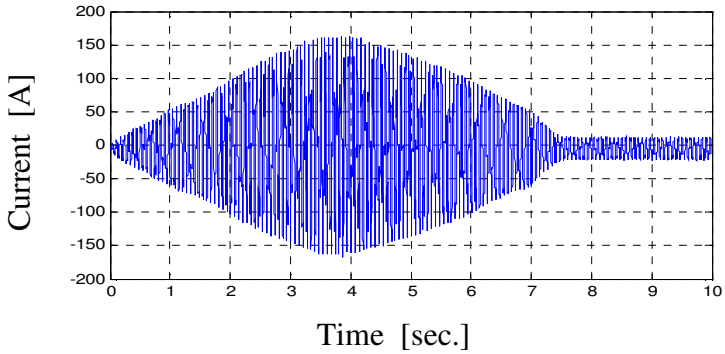

Test condition :
300 rpm
35 A I_d
Magnetization

Fig. 4.23 Voltage waveform during magnetization process

From the voltage and current waveform during the magnetiztion process, it can be seen that the i_d is controlled properly to have 35A. On the other hand, the i_q should be controlled in the zero, but small current ripple (<1A) is observed. The ripple current is caused by the spatial harmonic in this machine. Although current vector may be changed by the i_q current, the current vector variation should be less than 3 electrical degrees. It is also can be observed that the terminal voltage is not above the inverter limit. Fig. 4.24 shows the back-EMF waveform and spectrum before and after the magnetization process. It can be seen that the magnetization level can be successfully controlled by the inverter. A significant harmonics can be observed in VFI-IPMSM after magnetization. It will have impact to the current control and efficiency.

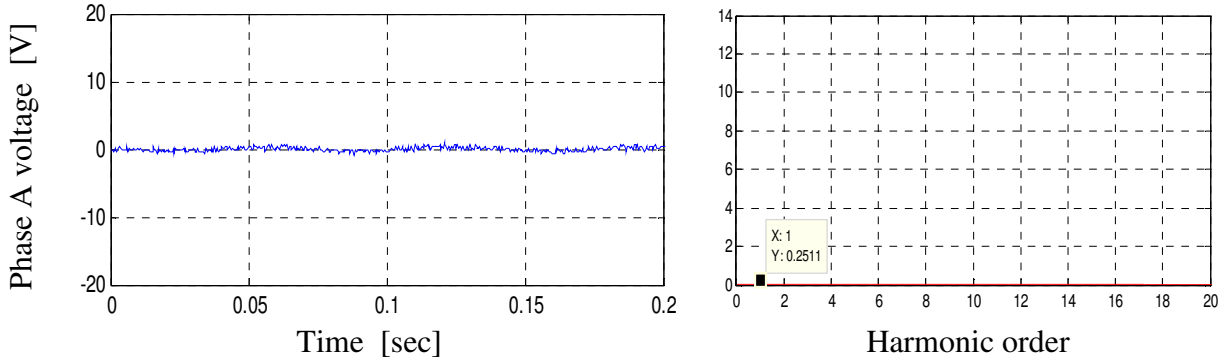

(a) Before magnetized

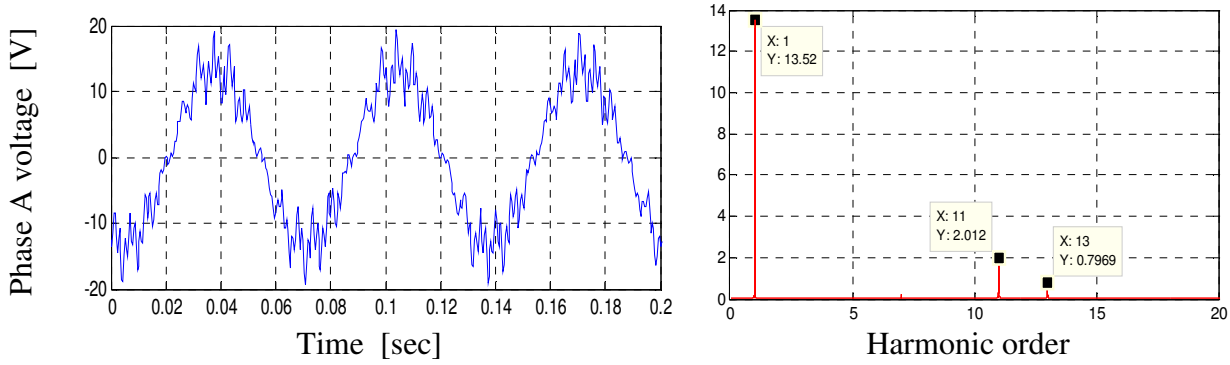

(b) After I_q = 35A magnetized, Test condition : 300 rpm

Fig. 4.24 Back-EMF waveform (left) and spectrum (right) before magnetization control

4.6.2 ***Experimental evaluation of proposed method for magnetization state manipulation***

The proposed method is evaluated during and after magnetization state manipulation processes. The i_d current pulse method is used in comparison to evaluate the effectiveness of proposed method. In the experiment, the magnetization current amplitude is increased to a target i_d current so that a desired magnetization state can be achieved. As discussed in the previous section, the maximum torque can be achieved with 2.5 pu current and a short magnetization period is desirable for energy savings. As a result, a current pulse with 2.5 pu magnetization current amplitude and 50 ms magnetization period is used.

The comparison for current vector trajectory of two methods is shown as Fig. 4.25. It can be seen that the i_q current is kept constant with i_d current pulse method. In contrast, i_q current is reduced for the proposed method in the magnetization manipulation process to reduce the pulsating torque. Measured torque and magnetization current (i_d) are recorded and shown in Fig. 4.26. It can be seen that the pulsating torque is mitigated and smooth torque can be achieved with the proposed method. However, for the i_d current pulse method, a torque pulsation is observed. In addition, due to the change of magnetization, a steady error torque error is found after the magnetization manipulation since the magnetization state is increased and the amplitude of current vector remains the same. Based on machine specific calibration, a pre-defined current vector achieving the torque command (5Nm) at full magnetization can be stored in a lookup table. The pre-defined current vector is commanded at 0.38 sec. It can be seen that both the pre-defined current vector and the proposed method without using lookup table can achieve the commanded torque. It should be noted that the lookup table method must be calibrated for each magnetization state and machine in order to accurately achieve the commanded

torque. In contrast, the proposed method doesn't require a lookup table to achieve similar steady state torque accuracy.

In the second test evaluation, the magnetization is changed and the torque command is increased simultaneously. This evaluation simulates a sudden large torque command requiring a greater level of magnetization. The results are shown in Fig. 4.27 and Fig. 4.28. It can be seen that a large torque transient can be achieved without significant pulsating torque. It should be noted that the delay between command and measured torque is due to the limitation of torque meter bandwidth.

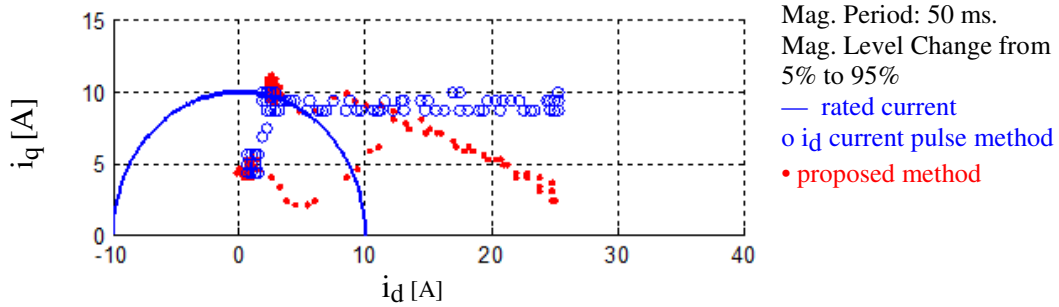

Fig. 4.25 Current vector trajectory before, during, and after magnetization manipulation process

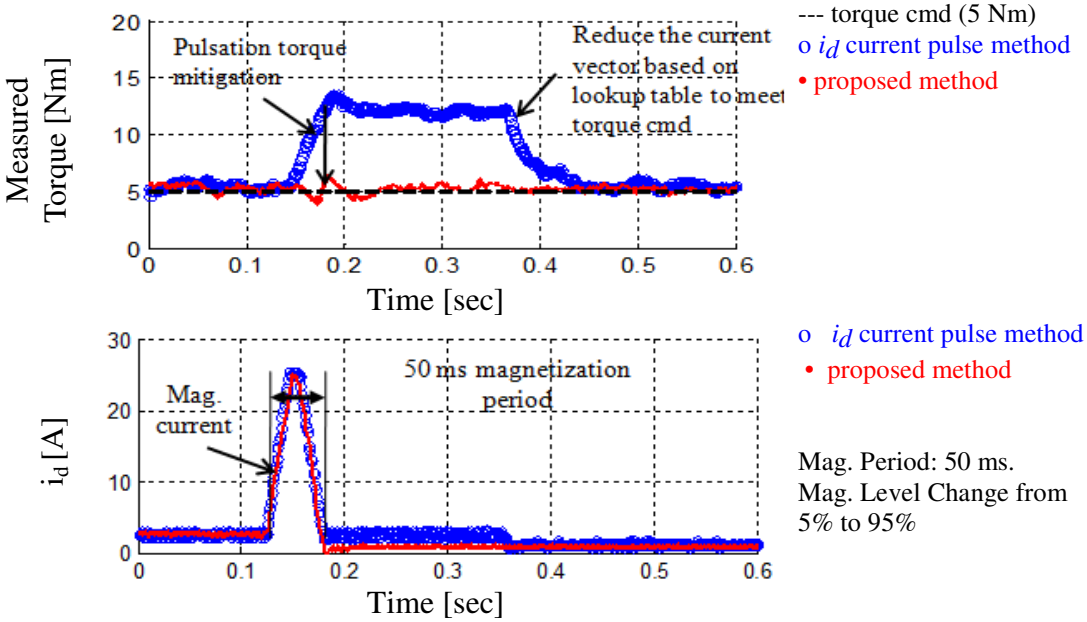

Fig. 4.26 Measured torque, i_d current under constant torque cmd condition before, during, and after magnetization manipulation process

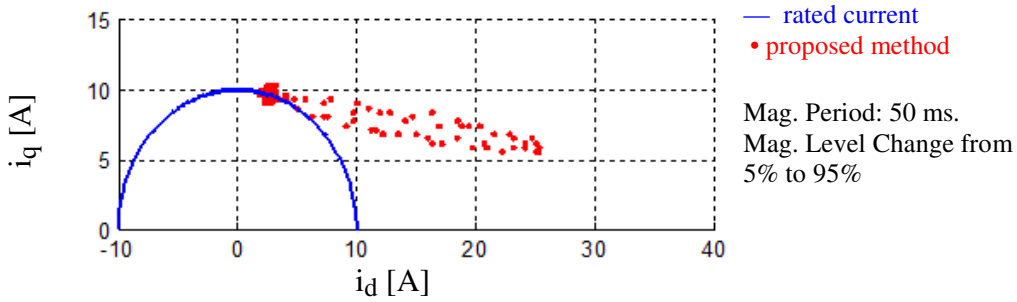

Fig. 4.27 Current vector trajectory before, during, and after magnetization manipulation process with proposed method

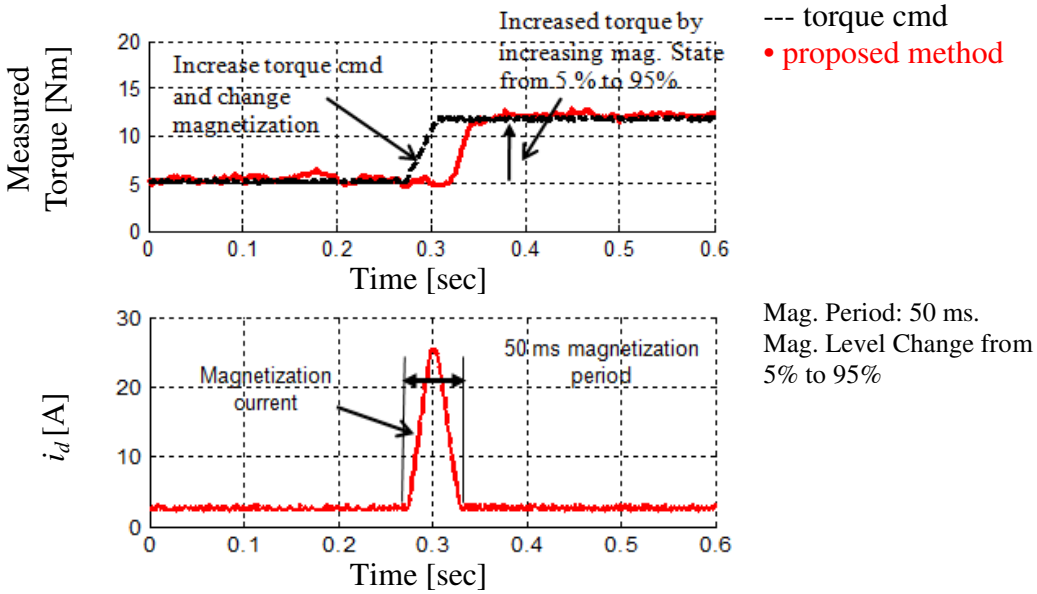

Fig. 4.28 Measured torque, and i_d current before, during, and after magnetization manipulation process with proposed method

4.7 Conclusions and Summary

This chapter conclusions and contributions are summarized as follows.

- It has been shown that both in the FEA and experimental results, magnetization state can be changed with an i_d current pulse on a VFI-IPMSM.
- In the test-bed VFI-IPMSM, maximum torque output can be achieved with 95% magnetization level. Output torque was not increased even when the magnetization level surpassed 95%.
- By evaluating the relationship between output torque capability and magnetization level, a proper i_d current pulse (amplitude and period) can be selected. In this test machine, 2.5 pu magnetization current and 50 ms period was shown to achieve lower energy consumption and also preserve torque output capability.
- An observer-based current decoupling method has been proposed to achieve smooth torque output during magnetization state manipulation.
- Compared to existing methods, the proposed method features reduced parameter sensitivity and less experimental effort since no lookup tables are required.
- A cascaded flux observer has been developed and shown to be useful in estimating and correcting flux estimation errors caused by to machine parameter deviations. The effectiveness of this method has been demonstrated by simulation and experimental results.
- It has been shown that the flux and torque estimation is a crucial issue for torque control. A cascaded observer has been shown to provide improved estimation for smooth torque control.
- Experimental results for magnetization manipulation under loaded conditions are presented. Compared to the direct i_d current pulse method, the proposed observer-

based current decoupling method demonstrated smooth torque output during the magnetization state manipulation without a lookup table.

- Steady state torque accuracy of the proposed method has been shown in experiment to be nearly equivalent to a machine specific calibration (lookup table method). A full torque transient operation during the change of magnetization has also been experimentally demonstrated with the proposed method.

Chapter 5 – Magnetization State Manipulation Strategy for Loss Minimization over a Driving Cycle

In this chapter, a magnetization state manipulation method for loss minimization for a novel interior permanent magnet (IPM) machine with variable-flux characteristics using low coercive force magnets is presented. The variable-flux characteristics allow improving the efficiency of machine and also reducing the usage of rare-earth material in the high-coercive magnets, which are currently used for the IPM machines in electrified vehicles. A flux-intensifying interior permanent magnet (FI-IPM) type having positive saliency is employed for a positive d-axis current to mitigate a demagnetizing field in the magnet due to a q-axis current. A proof-of principle prototype machine is designed, fabricated and evaluated. A series of experiments are conducted to capture the efficiency contours with different magnetization states of the low coercive force magnets. The designed machine shows benefits in improving efficiency when the magnetization state is optimally operated. With these results, the loss over a driving cycle is then simulated and the benefits of changing the magnetization state are quantified.

5.1 Machine Operation Principle

As shown in Fig. 5.1, the VFI-IPM prototype machine has six poles and each pole has a single low-coercive-force magnet. This magnet changes in its magnetization state during the machine operation. The basic equation for torque in a d-q frame and for voltage in the synchronous reference frame are described in (1) and (2) respectively

$$T = 3/2\ p\ \{f + (L_d - L_d)\ i_d\}\ i_q \qquad (5\text{-}1)$$

$$V = w\ \{(f + L_d\ i_d)_2 - (L_d\ i_q)_2\}_{1/2} \qquad (5\text{-}2)$$

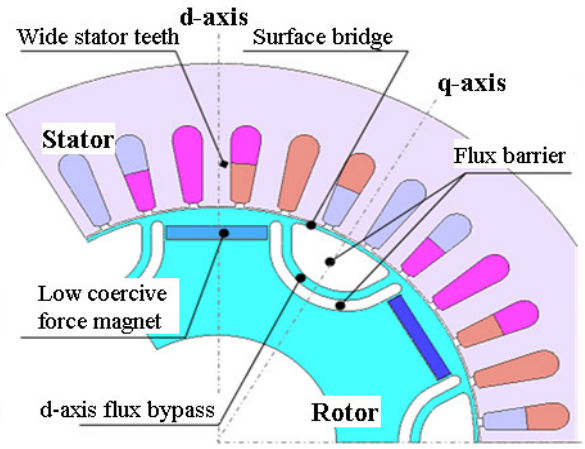

Fig. 5.1 Machine geometry of VFI-IPMSM

To achieve high torque capability and wide speed operation simultaneously, the machine was designed to have high magnet flux (i.e. high magnetization state of the magnet) in the low speed condition and low magnet flux (i.e. low magnetization state of the magnet) in the high speed condition. The approach used to change the magnetization state of the low-coercive-force magnets is shown in Fig. 5.2.

According to (5-2), when the machine speeds up, machine voltage will increase. For the proposed variable flux machine, a negative i_d pulse current is used to reduce the magnetization state of the magnet, i.e. reduce magnet flux ϕ, which reduces back EMF. Or conversely, when the machine slows down, a positive i_d pulse current is used to

increase the magnetization state of the magnet to be ready for a high torque production, since larger ϕ will help producing large torque according to (2-27).

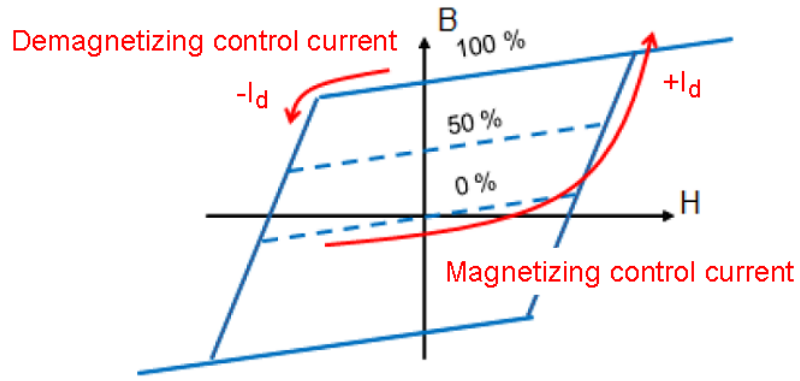

Fig. 5.2 Illustration of magnetizing and demagnetizing control pulse current for magnet magnetization state manipulation

The experimentally obtained magnetization state characteristics in the i_d-i_q frame are shown in Fig. 5.3.a. The area enclosed in the yellow lines is the region where 100% magnetization could be maintained. The results in Fig. 5.3.b indicate that the maximum torque was produced in the region of FI control due to the positive saliency. The results of these two experiments confirm that the VFI-IPM prototype machine can generate maximum torque while maintaining the magnetization state even though it uses low-coercive-force magnets

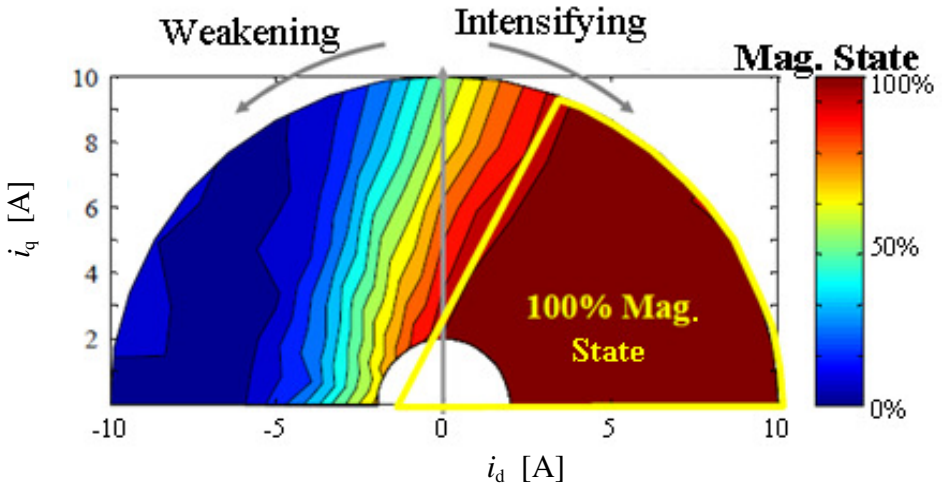

(a) Magnetization state

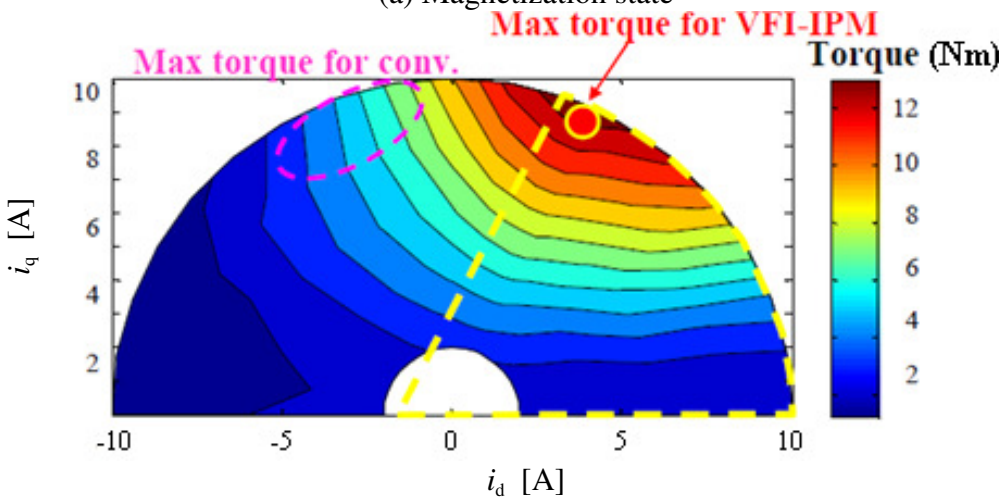

(b) Torque characteristics

Fig. 5.3 Experimental results for magnetization state and torque characteristics in the i_d-i_q frame

5.2 Efficiency Contours of The First Prototype VFI-IPMSM

5.2.1 Efficiency contours obtained by FEA and experiment

Torque/speed efficiency contours were calculated using FEA simulation of minimum total loss current vector control at 100%, 75%, 50%, and optimally manipulated magnetization states and are shown in Fig. 5.4. A comparable set of experimental efficiency contours are shown in Fig. 5.5. They were obtained by a series of experiments on the proof-of-principle prototype. Because of the power source limitation, the experiments were done only in a speed range up to 3,000 rpm. Both Fig. 5.4 and Fig. 5.5 indicate that in much of the most relevant portion of a high-speed low-torque region, the efficiency can be improved if a lower magnetization state, instead of 100%, is selected.

Since the actual coercive force of the magnets in the prototype fabrication was lower than the original magnet specification which was used in the simulations, the magnetization state labeled in the experiments did not have the same magnet flux linkage as in the simulations. Thus, the maximum toque was 16.5 Nm for FEA whereas only 11.5 Nm could be seen in experiment as shown in Fig. 5.4.a and Fig. 5.5.a.

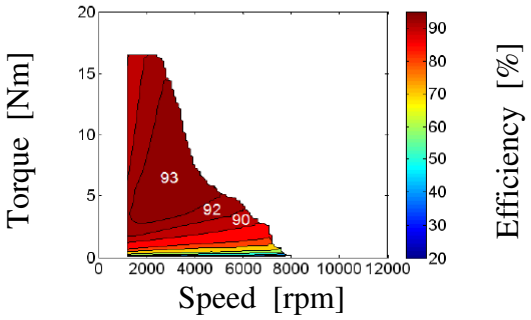

(a) 100% magnetization state

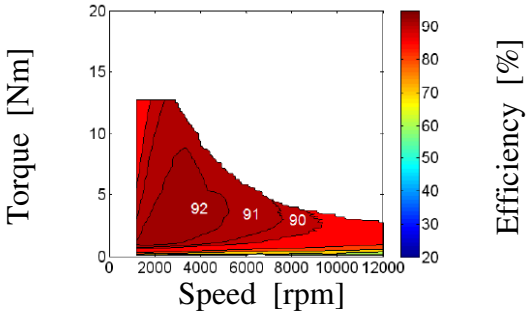

(b) 75% magnetization state

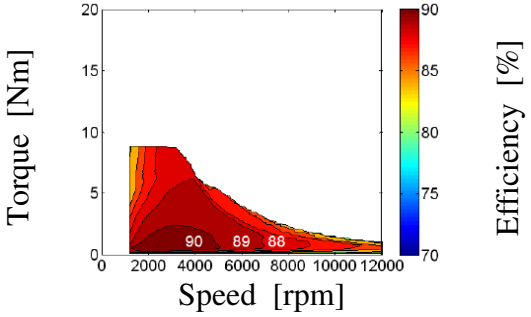

(c) 50% magnetization state

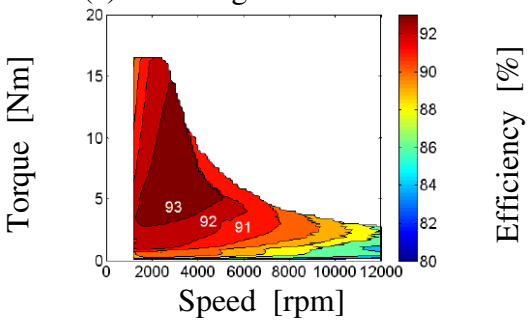

(d) magnetization state optimally operated

Fig. 5.4 Simulated efficiency maps with minimum total loss current vector control of the VFI-IPM machine at three magnetization states

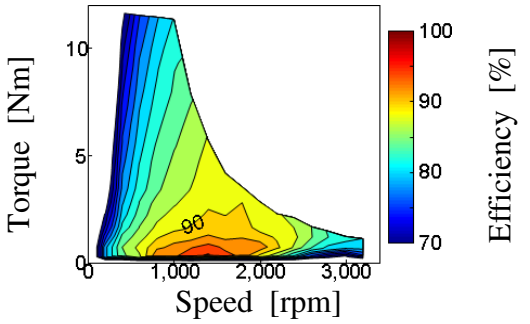

(a) 100% magnetization state

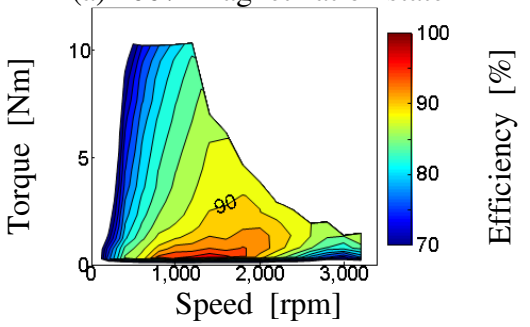

(b) 75% magnetization state

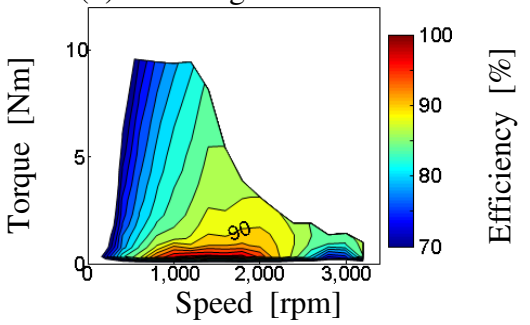

(c) 50% magnetization state

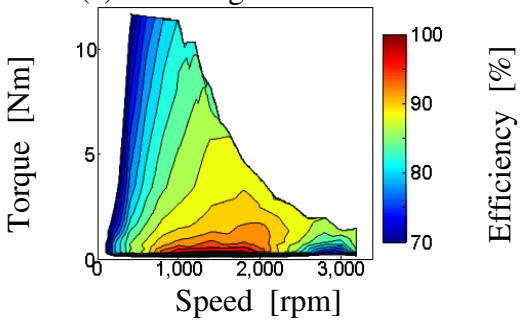

(d) magnetization state optimally operated

Fig. 5.5 Experimental efficiency maps with minimum total loss current vector control of the fabricated VFI-IPM machine at four magnetization states

Furthermore, in the experiments, more current was required than in that used in the FEA to produce the same torque. This can be seen in the FEA and experimental comparison of the torque contours in the current vector plane shown in Fig. 5.6. For instance, the required current to produce a torque of 6.2 Nm with 100% magnetization state was 4.7 A for FEA and 6.0 A for the experiment. This indicates that the current is larger by 28% for the experiment. This results in a 64% copper loss discrepancy. Accordingly, the efficiency seen in the experiments was lower than the simulation especially in high load conditions.

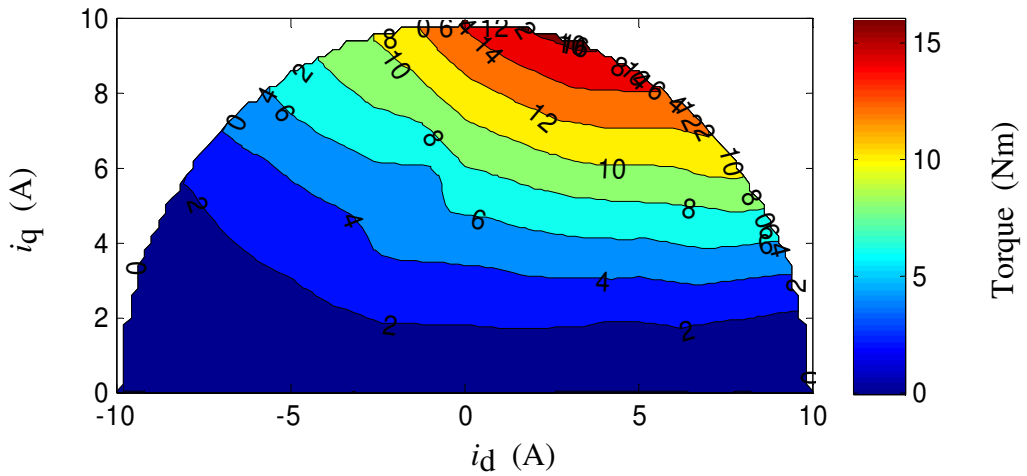

(a) FEA

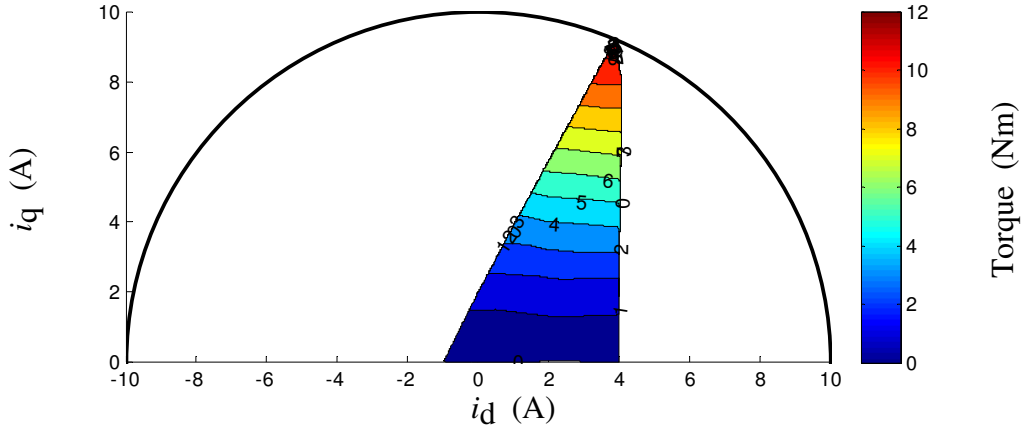

(b) Experiment

Fig. 5.6 Torque contours on the current vector plane for a 100% magnetization state.

5.2.2 Eddy current loss by PWM harmonics

In the FEA, the eddy current loss due to PWM harmonics was not included. Although the magnets have segmentations, PWM harmonics may have significant impact on eddy current loss in the magnets. A series of line-to-line impedance measurements using high frequency injection revealed that the equivalent secondary resistance was 3.5k Ω It can be considered that this is mainly because of the resistance for the magnet eddy current path.

Using the equivalent secondary resistance value, the loss due to PWM harmonics was calculated as shown in Fig. 5.7. The loss only depends on terminal voltage and doesn't depend on rotation speed, current amplitude or power factor. PWM carrier frequency was 10kHz and the DC bus voltage was 350V.

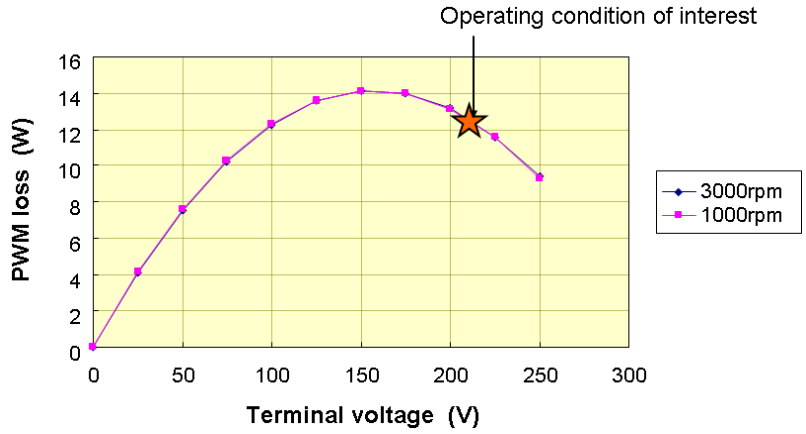

Fig. 5.7 Eddy current loss due to PWM harmonics

5.2.3 Overall discrepancy analysis

The discrepancies between the FEA and experimental loss evaluation are depicted in Fig. 5.8 for one set of test condition, i.e. 1,200 rpm, 6.2 Nm and 100% magnetization state. The data includes the losses due to flux linkage discrepancy in section B and the losses due to magnet eddy current losses in section C. The data also includes measured interconnections losses on the cables between the drive and the machine and the effect of measured winding resistance being different from that included in the FEA model. With all of this data included, 74 % of the total difference between FEA and the experiment could be explained. The remaining 26% are not explained, but could be because of measurement accuracy or deviations in physical tolerances for fabrication.

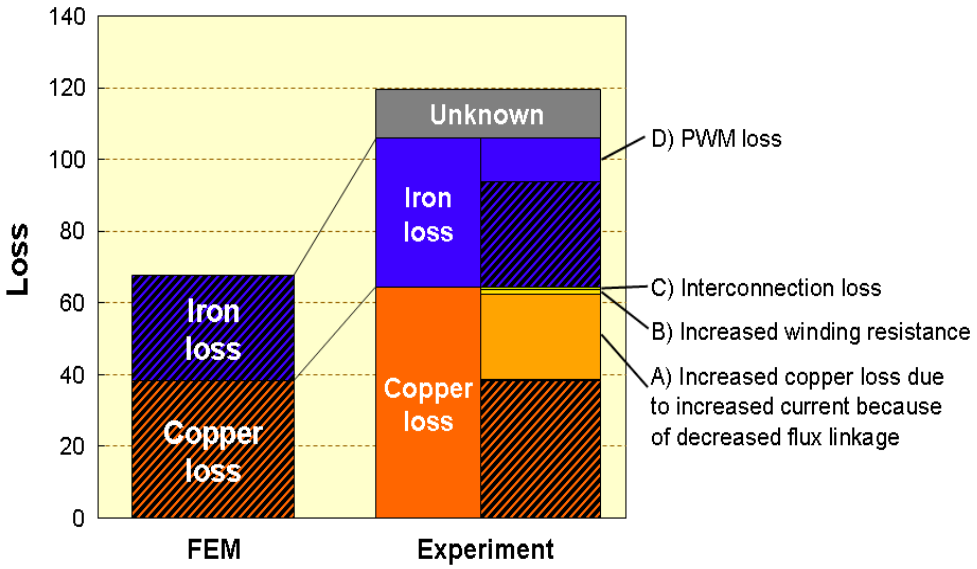

Fig. 5.8 Discrepancy analysis result for test conditions of 1,200 rpm, 6.2 Nm and 100% magnetization state

5.3 Efficiency Contours of The Second Prototype VFI-IPMSM

From previous section, it is known that the magnet properties are the major issue for the discrepancy between the simulation and experiment. To achieve the target specification, magnets close to the specific value were fabricated and installed to the second prototype machine. The stator slot number for the VFI-IPMSM is also changed to reduce the spatial harmonic in the EMF waveform.

5.3.1 Mechanical comparison for two prototype VF machines

The stators for the two VF machines are shown in Fig. 5.11. The stator of 2nd VF machine is increased to 45 slots so the slot per pole per phase is change from 2.0 to 2.5. Changing to a fractional slot combination is to reduce the spatial harmonic induced from the flux barrier design of rotor.

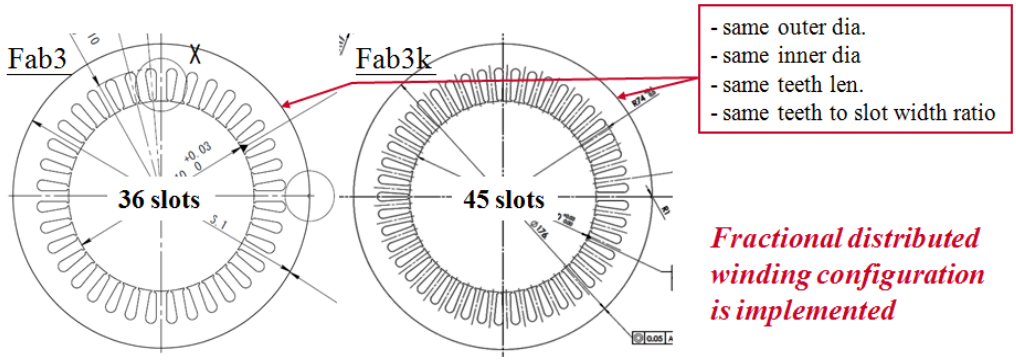

Fig. 5.9 Stator core design for two VFI-IPMSMs: (left) the first prototype VFI-IPMSM with integer slot design and (right) the second prototype VFI-IPMSM with fractional slot design

Table 5. I Machine design parameters of two machines

Design item		Integer slot design	Fractional slot design
Slot/pole number combination	Pole Slot	6/36	6/45
	Slot per pole per phase	2.0	2.5
Stator	Phase current rating	10.0 A_{rms}	22.3 A_{rms}
	Current density	6.25 A_{rms} /mm^2	9.28 A_{rms} /mm^2
Rotor		Same	
Magnet	B_r [T] =	1.07	1.16
	H_c [kA/m]	115	167

The detailed machine design parameters for two VF machine are shown in Table 5.I. It can be seen that the current density is also increased to have a better usage of core. The magnet properties are also better than the previous VF machine.

5.3.2 Mag/Demag and torque properties for the second prototype VFI-IPMSM

The experimentally obtained magnetization, demagnetization, and torque properties in the i_d-i_q frame for second prototype VF machine are shown in Fig. 5.10.a. The region where 100% magnetization could be maintained is similar as the first prototype VF machine. It indicates that the two prototype machine have similar magnetic property.

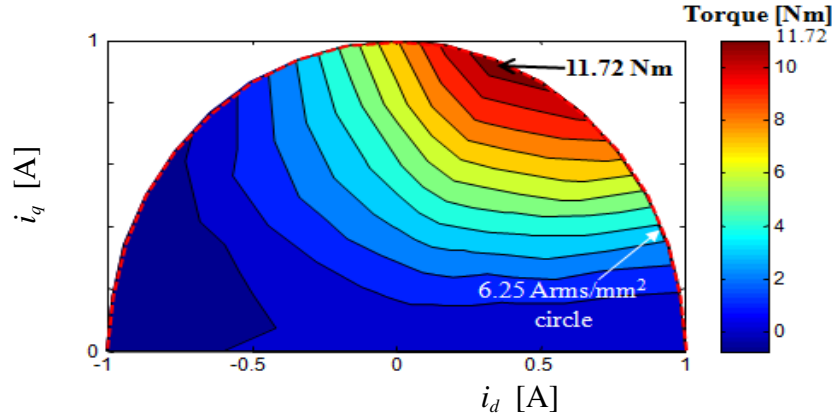

(a) Magnetization state

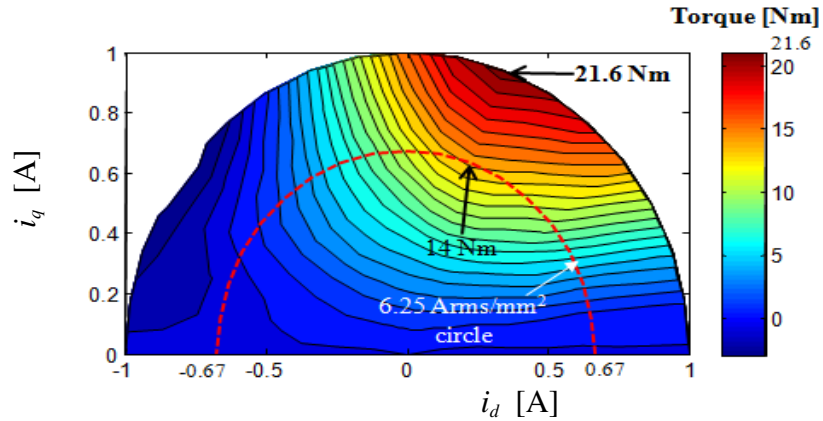

(b) Torque characteristics

Fig. 5.10 Experimental results for the second prototype VFI-IPMSM magnetization state and torque characteristics in the i_d-i_q frame

The results in Fig. 5.10.b demonstrate that the maximum torque was produced in the region of FI control due to the positive saliency. The results are similar as the 1st prototype machine and confirmed that the second prototype VFI-IPMSM can also generate maximum torque while maintaining the magnetization state with the low-coercive-force magnets. For the torque output comparison, a same current density was tested for both machines to have a fair comparison of two machines. The results show second prototype VFI-IPMSM have a better output torque under the same current density condition since the magnets close to the specifications are installed.

5.3.3 ***Efficiency contours obtained by FEA and experiments for the second prototype VFI-IPMSM***

The FEA simulation and experimental torque/speed efficiency contours of the second prototype VFI-IPMSM were shown in Fig. 5.11 and Fig. 5.12, respectively. These diagrams demonstrate minimum total loss current vector control at 100%, 75%, 50%, and optimally manipulated magnetization states.

The experiments were done in a speed range up to 6,000 rpm with the newly installed high voltage inverter which is capable to deliver up to 600V. The results for the second proof-of-concept machine demonstrate that in the most relevant portion of a high-speed low-torque region, the efficiency can be improved with a lower magnetization state, instead of 100%, is selected.

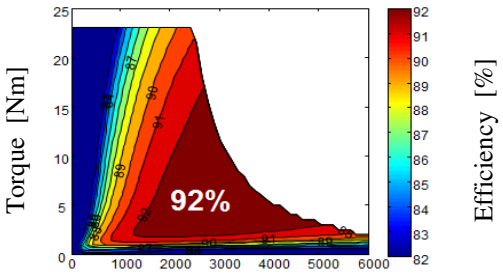

(a) 100% magnetization state

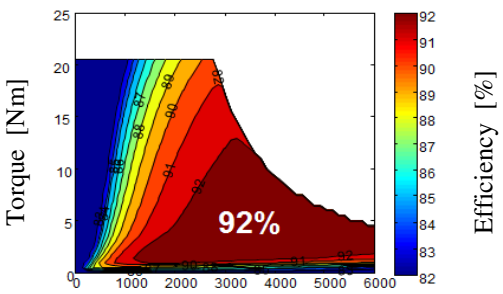

(b) 75% magnetization state

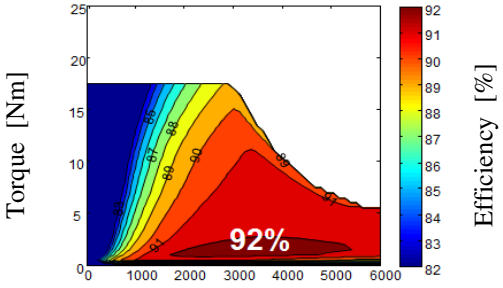

(c) 50% magnetization state

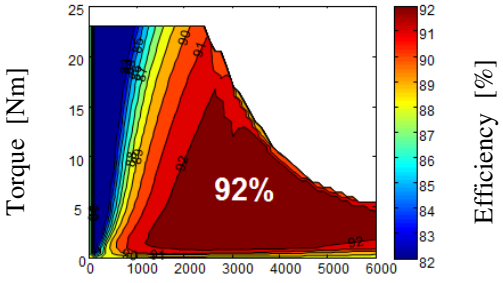

(d) magnetization state optimally operated

Fig. 5.11 Simulated efficiency maps with minimum total loss current vector control of the VFI-IPM machine

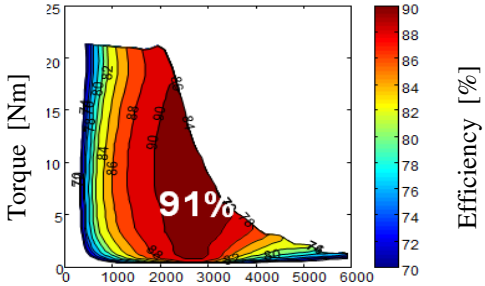

(a) 100% magnetization state

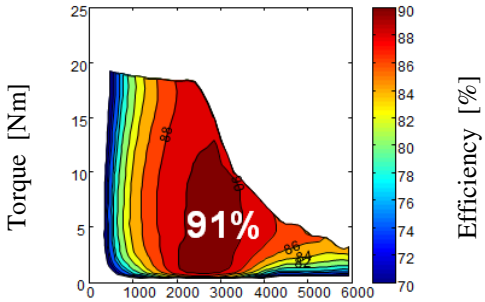

(b) 75% magnetization state

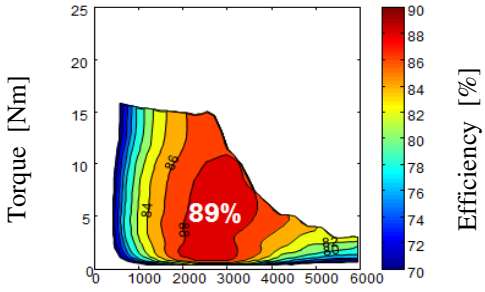

(c) 50% magnetization state

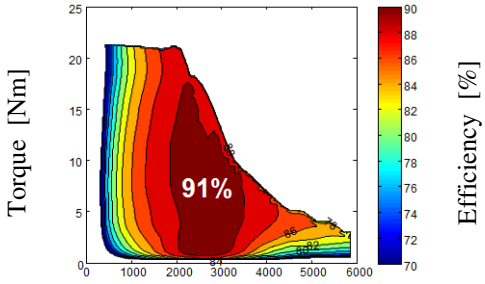

(d) magnetization state optimally operated

Fig. 5.12 Experimental efficiency maps with minimum total loss current vector control of the fabricated VFI-IPM machine

5.4 Loss Minimization over a Driving Cycle

5.4.1 Magnetization state selection

Based on the experimental results presented in section 5.3, losses over a driving cycle are then calculated. The driving cycle selected here is the FTP's Los Angeles Route Four City. The machine operating speed and torque is then calculated with typical EV parameters. The fabricated prototype has about 1/30th of the power capability of the EV used for this evaluation. Therefore during the calculation, the EV was scaled to be the equivalent of thirty machines.

The magnetization state was manipulated to reduce the losses. Too frequent manipulation of magnetization state would result in larger net losses due to the loss caused by magnetization current even if the conventional loss decreases via manipulation of the magnetization state. Thus, hysteresis control of the magnetization operation was implemented as shown in Fig. 5.13.

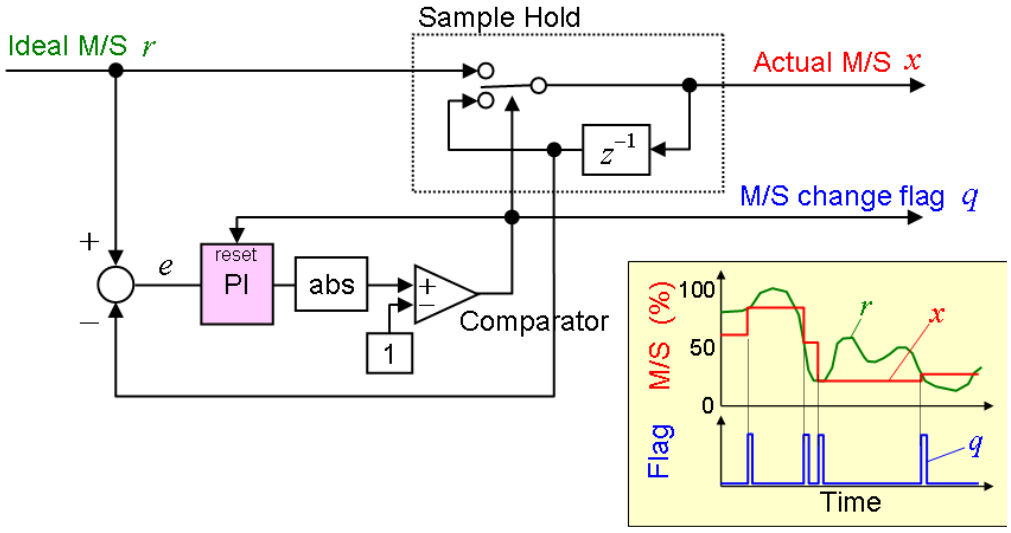

Fig. 5.13 Schematic diagram for the magnetization state selection controller

In Fig. 5.13, the input signal is the ideal magnetization state, which is a continuous value and ideally minimizes the steady loss of machine without taking into

account the loss due to the changing of magnetization state. The output is the actual magnetization state, which has reduced frequency of change and goes to the machine controller.

As shown in Fig. 5.14, the controller keeps the magnetization state from changing with a small step. The integral compensator in the controller helps to remove the steady state error brought by hysteresis controller. Smaller gains for PI compensator reduce the number of changes of the magnetization state.

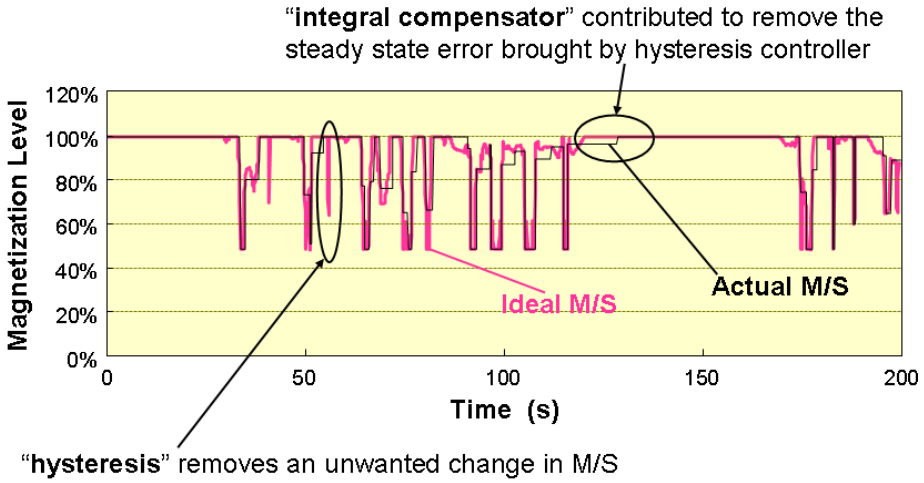

Fig. 5.14 The input and output wave form of the magnetization state selection controller

5.4.2 Energy consumption for the first prototype VFI-IPMSM

The magnetization selection controller has a PI compensator in it, thus the gains were investigated to find the optimal point to minimize the total loss energy over a driving cycle. During the optimization, a 50msec. magnetization changing pulse period was assumed. The controller gain loss properties are shown in Fig. 5.15. The total loss energy is minimized at k_p of 2.4, k_i of 0.25.

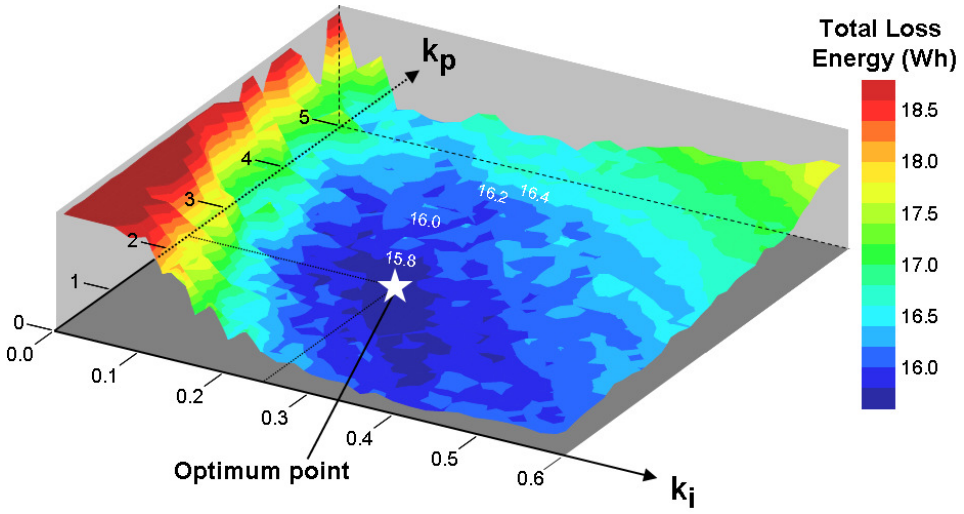

Fig. 5.15 Optimum Point for Controller Gain Based on Experimental Data

The total losses for three different magnetization selection methods are shown in Fig. 5.16. For the method depicted in the left most column, the magnetization state was fixed at 75%, thus there is no change in the magnetization states. For the method depicted in the center column, the nearest magnetization state is selected from four possible levels: 25%, 50%, 75% and 100%. For the method depicted in the right most column, the PI gains were optimized. The count of changing was reduced to half, while the driving loss is also decreased by 24% compare to the nearest 3 level strategy.

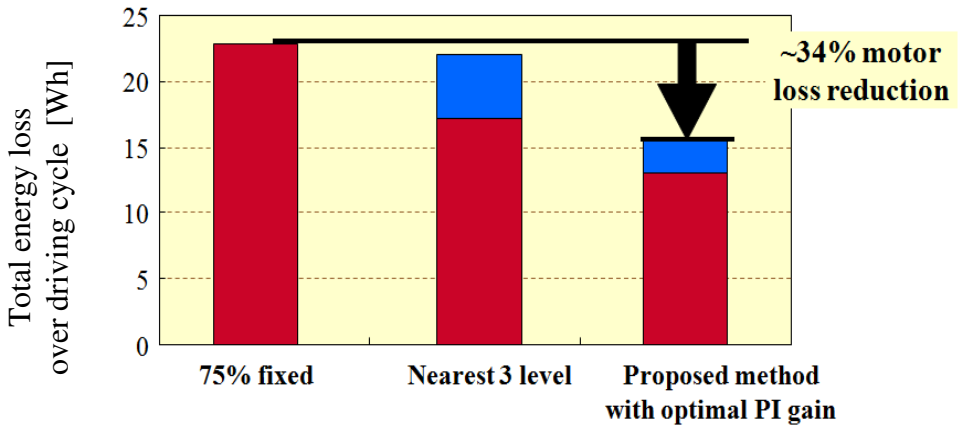

Fig. 5.16 Total loss comparison among different magnetization selection methods

5.4.3 Energy consumption for the second prototype VFI-IPMSM

Fig. 5.17 shows the simulation results of energy consumption for second prototype VFI-IPMSM. Same metrics, fixed 75%, nearset 3 level method, are used for the comparisons. The proposed method is also selected with the optimum PI gains. It can be seen that the total energy consumption with the proposed method is reduced by 10% compare to the fixed 75% method.

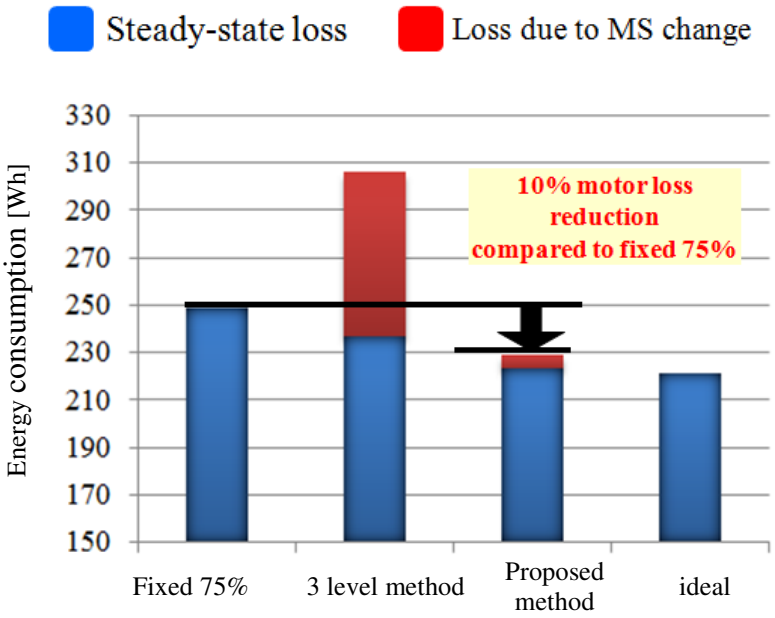

Fig. 5.17 Fifteen motors energy loss among different MS selection methods under UDDS driving cycle

5.5 Scalability Analysis for Vehicle-Sized VFI-IPMSM

A scalability analysis of energy consumption for vehicle-sized VFI-IPMSM is discussed in this section. A commercial FW machine is used as the baseline machine. The comparisons of energy consumption for both machines are discussed as following sections.

5.5.1 Specifications for the baseline machine and the VFI-IPMSM

Fig. 5.18 shows the machines geometries for both machines. Table 5. II shows the key design parameters for both machines. The major differences for the vehicle-sized VFI-IPMSM are the magnets and winding method. The VFI-IPMSM uses low coercive force magnets (SmCo) so changing MS is feasible. Similar property is shown in the test of proof-of-concept machine. A segment conductor design is also used to increase the slot fill of the VF machine.

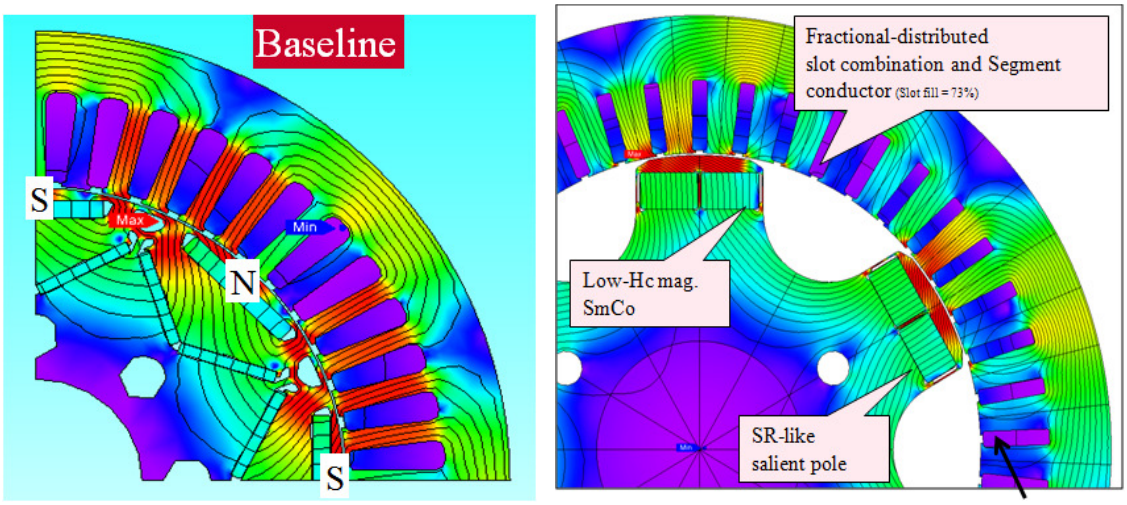

Fig. 5.18 Machine geometries for the baseline machine (left) and the vehicle-sized VFI-IPMSM (right)

Table 5. II Machine design parameters of baseline and VF machine 5.7

Item	Baseline	VF
Pole/slot/SPP /Diameter (mm)	8/48/2/200	6/45/2.5/200
N of turns per coil/Wires in bundle	8/8	3/1
Res. per phase (mohm) /Slot filling	8.245/49.8%	8.38/73.0%
Rotor Geometry/Magnet Type	FW-IPM/Neodymium	FI-IPM/SmCO

5.5.2 *Efficiency contour comparison between the baseline machine and VFI-IPMSM*

The efficiency contours for the vehicle size machine are shown in Fig. 5.19. There are four efficiency contours including 100%, 75%, 50% and optimum MS. It can be seen that the high efficiency region shift to light load and high speed as the magnetization state reduced to lower MS. With optimum MS selection, the VFI-IPMSM can achieve highest efficiency around 98% and greater than 97% in most region.

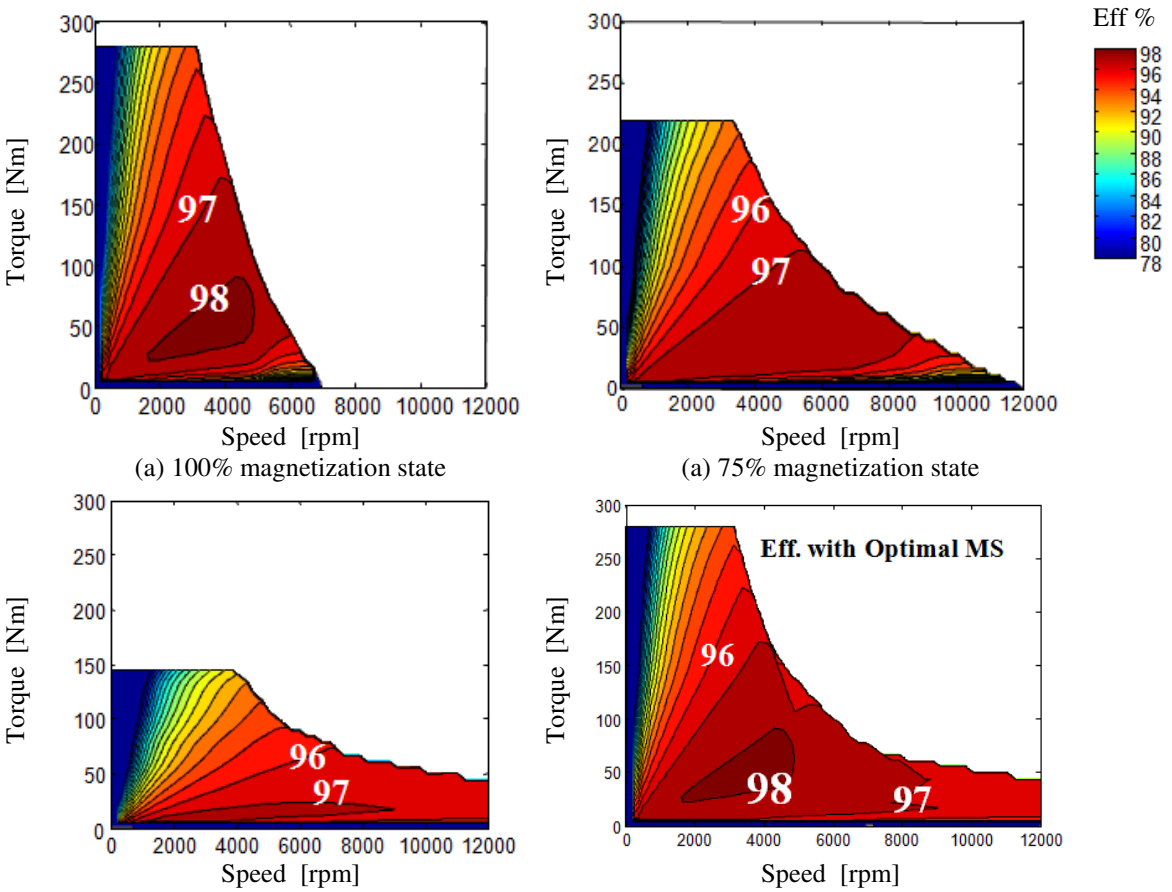

(a) 100% magnetization state (a) 75% magnetization state

(c) 50% magnetization state (d) magnetization state optimally operated

Fig. 5.19 Simulated efficiency maps with minimum total loss current vector control of the vehicle-sized VFI-IPMSM

5.5.3 Loss minimization over a driving cycle with the vehicle-sized baseline machine and VFI-IPMSM

The efficiency contours overlaid with UDDS driving cycle is shown in Fig. 5.20. It can be seen that the vehicle is mostly operating in the light load condition. The VFI-IPMSM demonstrates more efficient than the baseline machine in the light load operating conditions if optimum magnetization states are selected. In Fig. 5.21, the VFI-IPMSM demonstrates that the loss is reduced compared to baseline machine in most operating conditions.

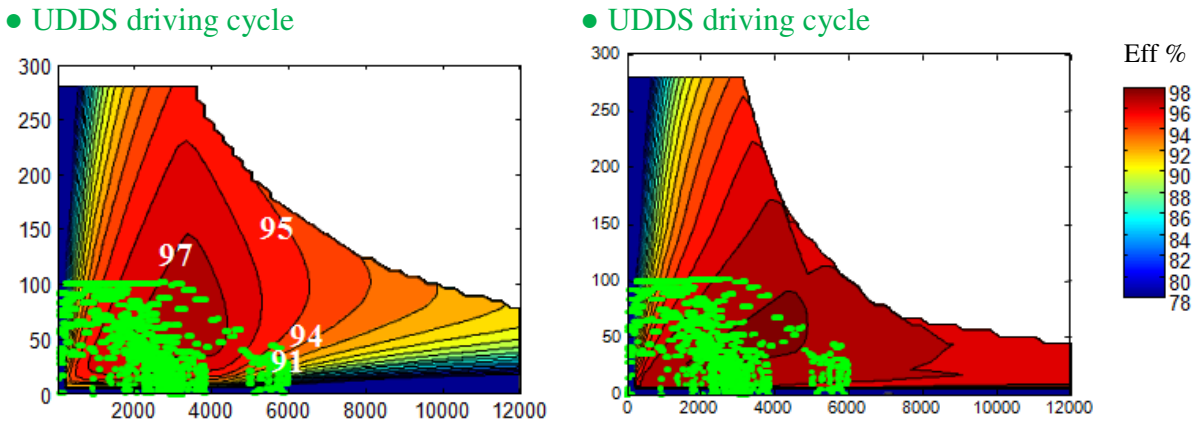

Fig. 5.20 The efficiency contours overlaid with UDDS driving cycle for the baseline machine (left) and the VFI-IPMSM (right)

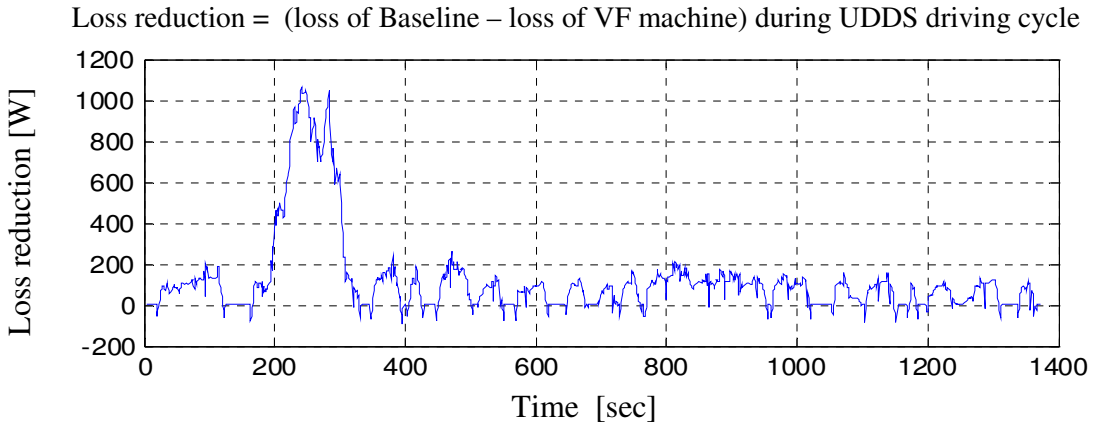

Fig. 5.21 Loss reduction of VFI-IPMSM over a UDDS driving cycle

Fig. 5.22 and Fig. 5.23 demonstrate the energy consumption for baseline machine and vehicle size machine with 3 level MS method and proposed MS selection method over a UDDS and HFET driving cycle, respectively. It can be seen that the vehicle size VF machine with the proposed MS selection method demonstrate 37% and 70.8% energy loss reduction and 3.6% and 7% fuel economy improvement over a UDDS and HFET driving cycle, respectively.

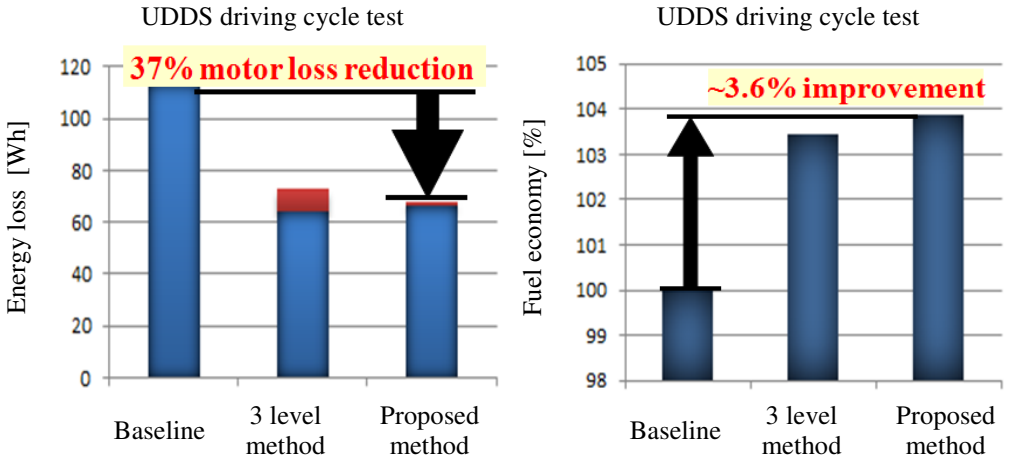

Fig. 5.22 The comparison of energy loss and fuel economy for the baseline machine, the VFI-IPMSM with 3 level method, and VFI-IPMSM with the proposed method over a UDDS driving cycle

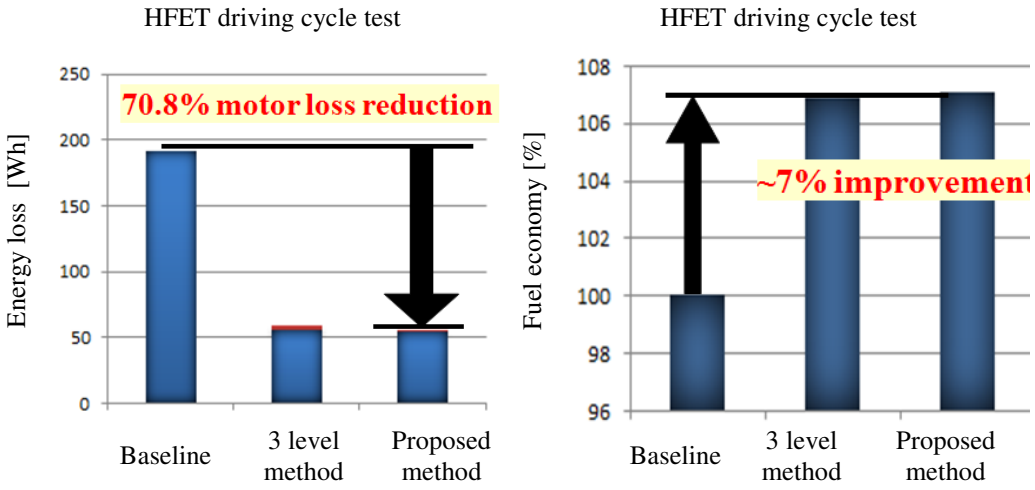

Fig. 5.23 The comparison of energy loss and fuel economy for the baseline machine, the VFI-IPMSM with 3 level method, and VFI-IPMSM with the proposed method over a HFET driving cycle

5.6 Conclusions and Summary

This chapter conclusions and contributions are summarized as follows.

- The contours show benefits in improving efficiency when magnetization state is optimally operated.
- The discrepancy between FEA and the experiment was analyzed and found to be mainly because of the reduction in magnetization state in fabricated machine and the eddy current loss brought by PWM harmonics.
- It was also found that a hysteresis controller for the magnetization state operating algorithm could reduce the total loss. With the experimental results, the loss over a driving cycle have been simulated and found to be reduced by 10% and compared to fixed magnetization state control for the second prototype VFI-IPMSM.
- The optimum theoretical loss over a driving cycle can be reduced to 15% in the second prototype VFI-IPMSM, when compared to fixed magnetization state control under the assumptions of no additional loss due to the magnetization pulse and ideal MS selection.
- A scalability analysis of proposed method for a vehicle-sized VFI-IPMSM is explored. The VFI-IPMSM with the proposed method demonstrates a reduction of 37% energy loss over a UDDS driving cycle and a reduction of 70% over a HFET driving cycle compared to the baseline machine.

Chapter 6 – Zero/Low Speed Magnet Magnetization State Estimation Using High Frequency Injection

This charter focuses on zero/low speed magnetization state (MS) estimation using high frequency injection for a fractional slot variable flux-intensifying interior permanent magnet synchronous machine (VFI-IPMSM). For VFI-IPMSMs, the knowledge of the MS is necessary to achieve loss minimizing control since loss properties vary with MS. The MS can be estimated by measuring EMF, however, voltage sensors are not commonly used in standard drives. If a flux observer is used, accurate estimation is difficult at zero/low speed due to the diminishing EMF signal. To solve this issue, a superimposed high frequency (HF) injection method for MS estimation is proposed. Physically, higher MS implies a higher saturation condition which results in lower differential inductance. With a constant HF voltage injection, lower inductance (higher MS) results in a larger HF current response and vice versa. As a result, by imposing a HF voltage signal, the MS can be estimated through the HF current response. The proposed MS estimation methodology is evaluated experimentally with a fabricated fractional slot VFI-IPMSM and demonstrates effective MS estimation within 5 % error

6.1 Machine Modeling and Properties for Magnetization State Estimation

6.1.1 Machine modeling for MS estimation

This section discusses machine modeling for MS estimation. The equation for HF current in the stator can be written as (6 - 1) and the HF resistance and inductance including MS effects can be modeled as (6 - 2) and (6 - 3).

$$\textit{HF current: } i^{s}_{dqc} = V^{s}_{dqc} / Z^{s}_{dqc} \text{ , where } V^{s}_{dqc} = V_c e^{j\omega_c t}, \text{ and } \Sigma Z^{s}_{dqc} = \Sigma R + j\omega_c \Sigma L \quad (6 - 1)$$

$$\textit{HF resistance: } \Sigma R = R_s + R_r = R_{so}(1+\alpha\Delta T_s) + R_{ro}(1 + \beta\Delta T_r + \gamma_r B(MS,T_r)) \quad (6 - 2)$$

where R_s: stator resistance, R_r:rotor resistance, R_{so}: nominal stator resistance, R_{ro}: nominal rotor resistance,
T_s: stator temperature, T_r: rotor temperature, α: copper resistive thermal coefficient, β : magnet resistive thermal coefficient,
γ_r: magnet resistive coefficient due to change of magnetization state, B, flux density, MS: magnetization state

$$\textit{HF inductance: } \Sigma L = L_{so}(1 + \delta B(MS,T_r)) \quad (6 - 3)$$

where L_{so}: nominal inductance, δ: magnet inductive coefficient due to change of magnetization state

Therefore, the HF current can be represented as

$$i^{s}_{dqc}(T_s,T_r,B) = V_c / \sqrt{\Sigma R(T_s,T_r,MS)^2 + \omega_c^2 \Sigma L(T_r,MS)^2} * e^{j\omega_c t - \varphi \Sigma Z^{s}_{dqc}(T_s,T_r,MS)} \quad (6 - 4)$$

From (6 - 4), it can be seen that the MS directly affects HF current. Therefore, the MS can be estimated by measuring HF current. Physically, HF inductance and resistance both affect the HF current as shown in (6 - 4). Therefore, MS estimation should be possible through either HF resistance or inductance. The relationship between the HF inductance and MS can be explained as Fig. 6.1. As the MS changes, the operating points in BH loop varies. When a HF signals is imposed, the amplitude of HF current will change with the MS. Therefore, the MS can be estimated from the HF current.

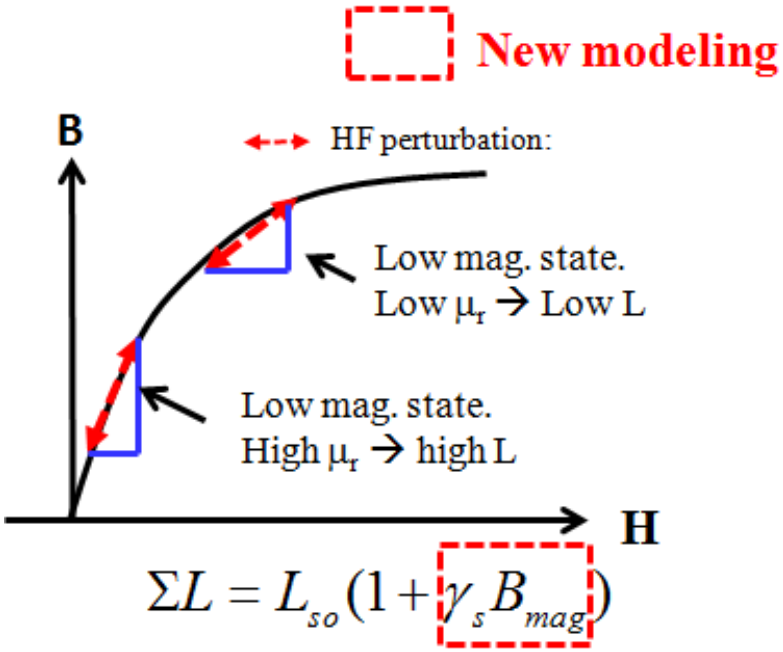

Fig. 6.1 Illustration of the relationship between MS and HF current

*6.1.2 **Properties of the tested machine***

Most machines act more like a purely inductive load, but some machines exhibit a significant resistive property [133]. Therefore, it is important to know the impedance property of the test machine. If the machine is dominated by inductance, accurate estimation should still be possible without decoupling the HF resistance. Experiments were performed to measure the reactance property of the test VFI-IPMSM and results are shown in Fig. 6.2 and Fig. 6.3. It can be seen that the machine demonstrates an almost purely inductive property (~90 degree) in 100 Hz ~ 1 kHz frequency region. This effect can be also seen in Fig. 6.3. The VFI-IPMSM shows a nearly 90 degree power factor angle with 1 kHz HF injection after various current pulse conditions (different MS conditions). As a result, it can be concluded that the tested VFI-IPMSM reveals an almost purely inductive property.

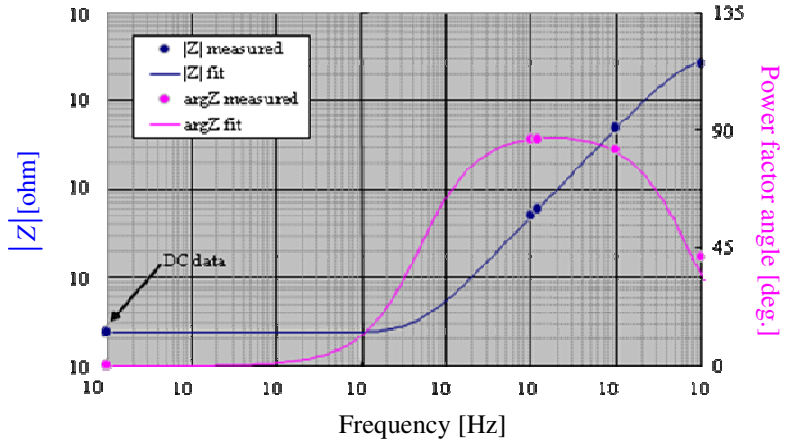

Fig. 6.2 Power factor angle angle versus frequency

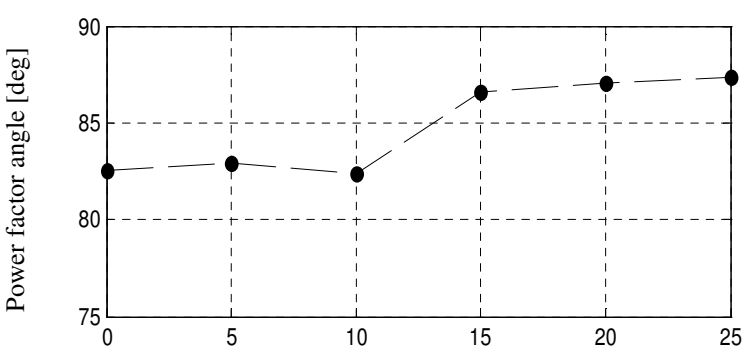

Test conditions:
1000 Hz HF injection
40 V rotating voltage
Magnet temp: 25 degree

Fig. 6.3 Power factor angle at 1 kHz HF injection measured after the i_d current pulse

6.2 Magnetization State Estimation Methodology

A methodology for MS estimation will be discussed in this section. As a rotating voltage vector is injected in the stationary frame, the induced current in the stationary frame can be modeled as (6-5) [134]

$$\begin{bmatrix} i_{dsh}^{s} \\ i_{qsh}^{s} \end{bmatrix} = I_{c\_p}\begin{bmatrix} cos\omega_c t \\ sin\omega_c t \end{bmatrix} - I_{c\_n}\begin{bmatrix} 2\theta_e - cos\omega_c t \\ 2\theta_e - sin\omega_c t \end{bmatrix} \tag{6-5}$$

where I_{c_p} is a positive sequence current which is equal to $v_c.\frac{\Sigma Z}{Z_d^r Z_q^r}$, I_{c_n} is a negative sequence current which is equal to $v_c.\frac{\Delta Z}{Z_d^r Z_q^r}$, and v_c is the injection voltage.

It should be noted that both positive and negative sequence current can be used for MS estimation. Normally, the amplitude of the positive sequence current is larger than the amplitude of the negative sequence current. To improve the signal-to-noise ratio, the positive sequence current is used for MS estimation. To investigate the relationship between MS and HF current, an experiment is performed by injecting various i_d current pulses to change the MS. The test machine used here will be described in the next section. EMF voltage is used as an MS indicator and shown in green in Fig. 6.4. It also can be seen that HF current varies with MS. Through (6-5), the relationship between flux linkage and HF current can be obtained and is shown in Fig. 6.5. By converting the MS to become a function of HF current, the MS can be estimated through HF current even at zero speed. The overall block diagram for MS estimation is shown as Fig. 6.6. A HF rotating vector voltage command is added with the command voltage from current regulator to produce the HF voltage injection. To separate fundamental and HF current from measured current, a fundament current observer for fundamental current and a synchronous frame filter for HF current are used. After the HF current amplitude is

extracted using a heterodyne detection process, the flux linkage then can be estimated based on the relationship between HF current and flux linkage. It should be noted that rotating vector injection is simply used as example here; pulsating voltage injection can also be used for MS estimation.

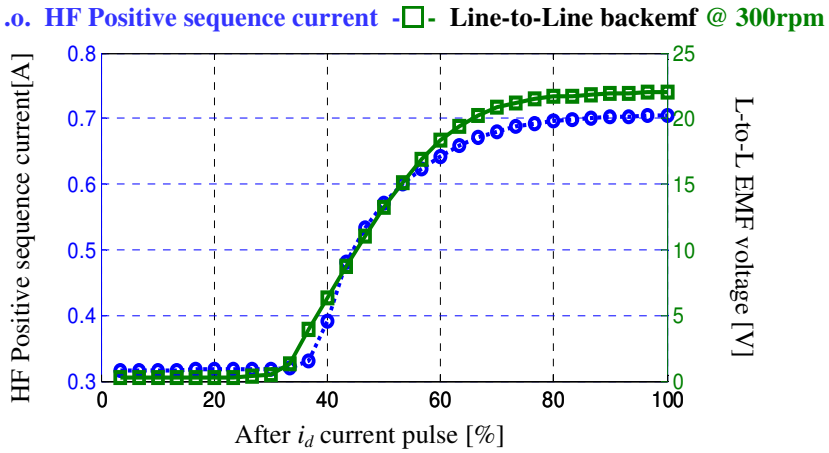

Fig. 6.4 HF Positive sequence current and line-to-line EMF after various i_d current pulses

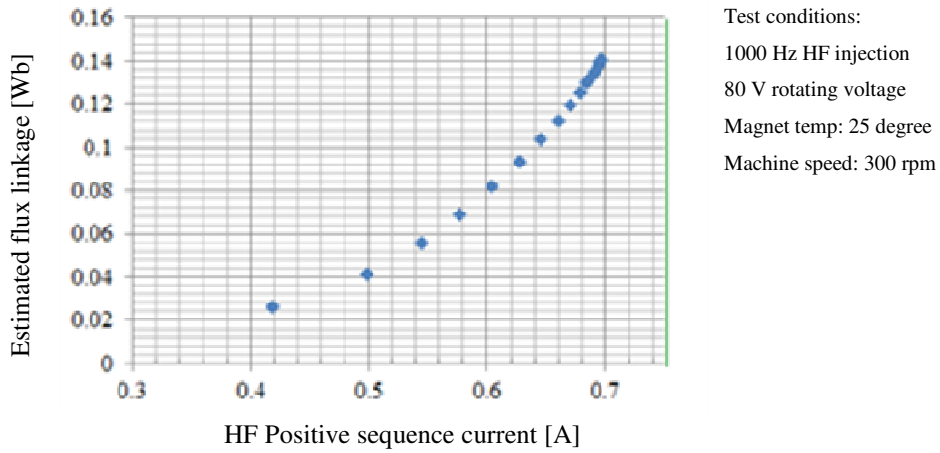

Fig. 6.5 Relationship between HF current and flux linkage

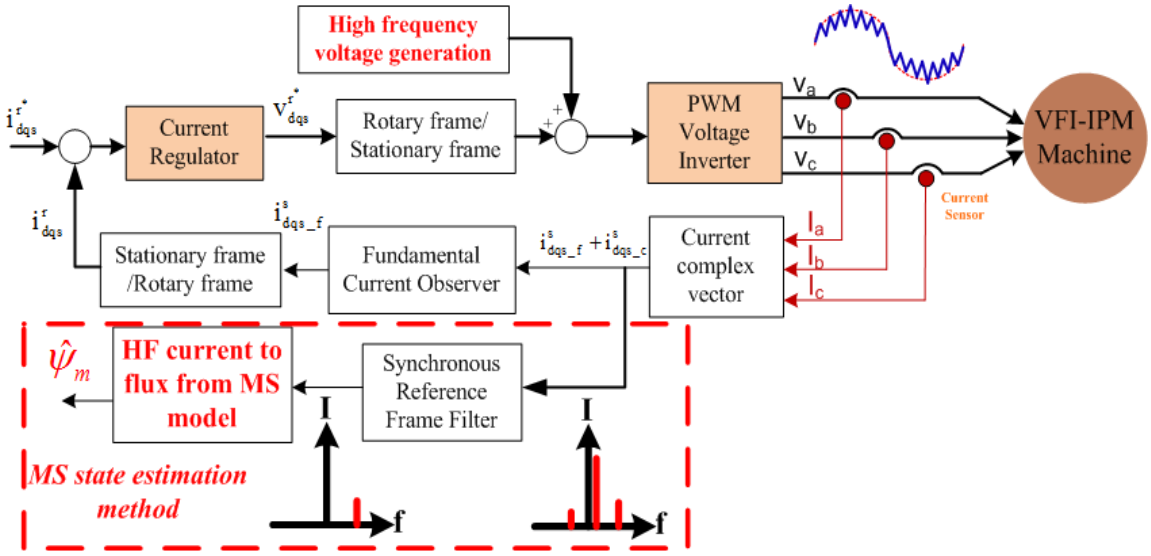

Fig. 6.6 Block diagram for flux/magnetization state estimation

6.3 Finite Element Analysis Evaluation With Different Magnet Resistivity

In this section, a FEA evaluation is conducted to examine the effect of magnet electrical resistivity to the trend of HF current under different MS. The purpose is to investigate the applicability of the proposed methodology for not only SmCo magnet but also Neodymium magnet. The machine geometry used for simulation and test is shown in Fig. 6.7. The electrical resistivity of the two magnets are shown in Table 6.I.

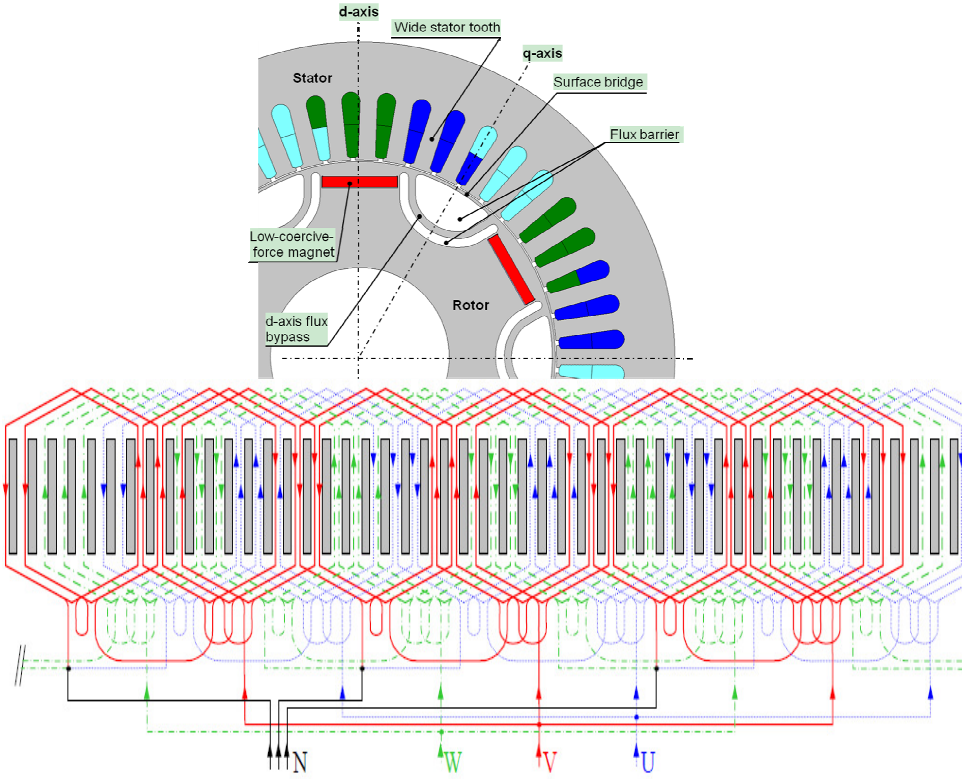

Fig. 6.7 Machine geometries and winding diagram for the fractional slot VFI-IPMSM test machine

Table 6.I. Electrical resistivity: ρ (Ω·cm) of magnet [135]

Neodymium	$(110 – 170)\times10^{-6}$
SmCo	$(70 – 90)\times10^{-6}$

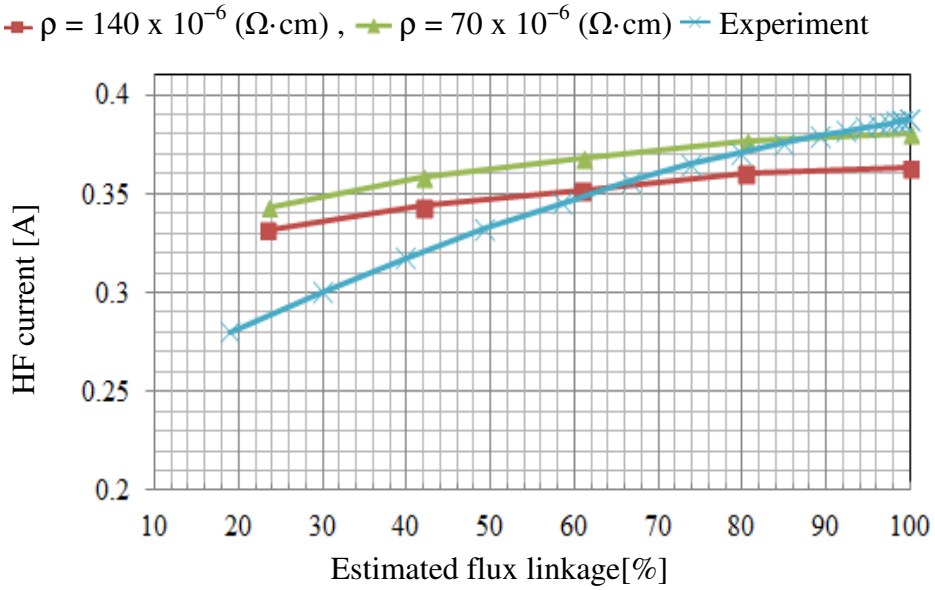

Fig. 6.8 Relationship between HF current and flux linkage. Test condition: voltage injection @ 40V, 1000 Hz

The simulation and test results are shown in Fig. 6.8. It can be seen that the HF current increased with the estimated flux linkage. In general, the trend is similar for both magents with different magnet resistivity. Magnet electrical resistivity changes the absolute value of HF current response but not the trend. Therefore, the proposed methodology should be able to use in both magnet. It should be noted that the absolute value of simulation results are not identical to the experiment results. The reasons are due to the BH loop curvature are not available in the material and it is also very difficult to measure. In addition, to save the simulation time, a 2D simulation is performed and additional errors could occur. Since the trend is much more important than the absolute value, this research will focus more on the trend.

6.4 Experiment Evaluation

A fractional slot VFI-IPMSM with 45 slots, 6 poles, and distributed windings was fabricated and used to evaluate the proposed MS estimation method. The machine geometry and winding diagram of this fractional slot machine are shown in Fig. 6.7. The temperature of magnet is maintained in a specific value during the experiment to assure the consistence of the evaluation. The temperature are monitored with two thermocouples which are attached to the surface of magnet. The temperature signal is then transmitted through a slip ring. The setup of temperature is shown as Fig. 6.9.

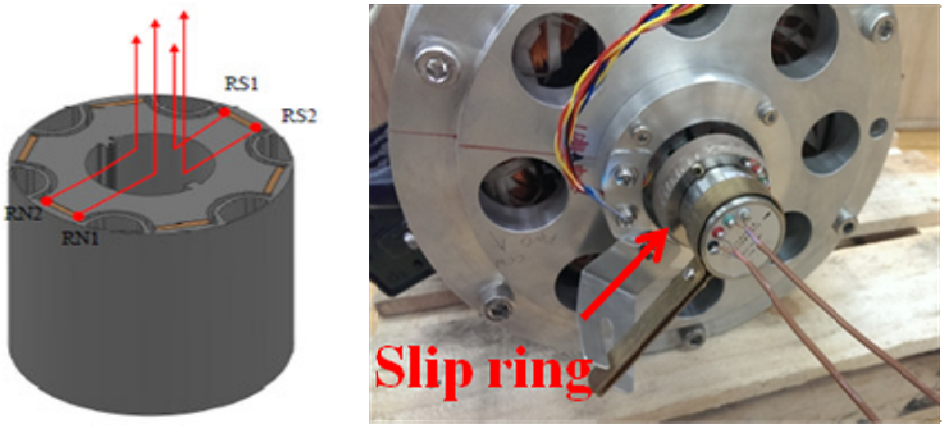

(a) (b)

Fig. 6.9 Illustration of magnet temperature measurement tools. (a) thermocouples location (b) slip ring

6.4.1 Machine specification and experiment evaluation

A VFI-IPMSM test bench used for experimental evaluation is shown in Fig. 6.10 and the machine specification is shown in Table 6.II. Previously, an integer slot VFI-IPMSM has been fabricated and evaluated. However, the harmonics of voltage waveform and the torque ripple were significant. In order to solve this issue, the slot number was increased to have a fractional slot per pole per phase number (i.e. 2.5) configuration. As shown in Table 6.III, table IV, Fig. 6.11 and Fig. 6.12, the torque ripple and the voltage

waveform harmonics were greatly reduced. Table 6.III describes the design parameters of the machines. The current density has also been modified to test the fractional slot machine at severe core saturation conditions

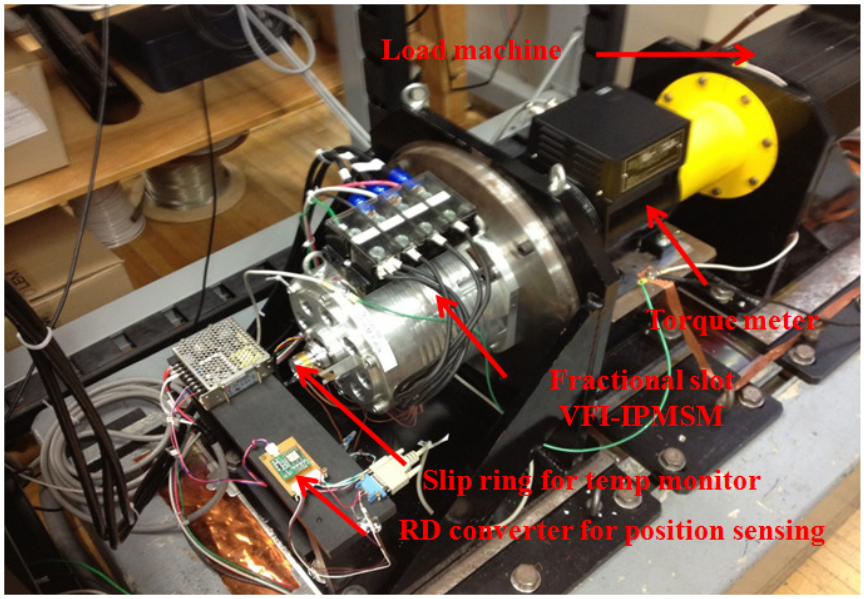

Fig. 6.10 Experimental setup for fractional slot VFI-IPMSM

Table 6.II VFI-IPMSM specification	
Specifications	**Value**
Rated speed/ current	1200 rpm/22.3 A
Rated torque	22.2 N-m (Full magnetization)
Connection	Wye
Poles/Slots/	6/45
Ψ_m	0 to 0.141 Wb (Full magnetization)
Winding resistance	0.55 Ω (per phase)

Table 6. III Machine design parameters of two machines

Design item		Integer slot design [1, 2]	Fractional slot design (test machine)
Slot/pole number combination	Pole Slot	6/36	6/45
	Slot per pole per phase	2.0	2.5
Stator	Phase current rating	10.0 A_{rms}	22.3 A_{rms}
	Current density	6.25 A_{rms} /mm^2	9.28 A_{rms} /mm^2
Rotor		Same	

Table. 6. IV Comparison of torque properties of the two machines (Experimental results)

Machine	Current density	Average torque	Torque ripple	Torque ripple reduction
Integer slot design [1, 2]	6.25 A_{rms} /mm^2 [1 pu]	11.48 Nm	3.5 Nm (27%)	-
Fractional slot design	6.25 A_{rms} /mm^2 [0.67 pu]	14.9 Nm	0.89 Nm (5.8%)	75%
	9.28 A_{rms} /mm^2 [1 pu]	22.22 Nm	1.06 Nm (4.8%)	70%

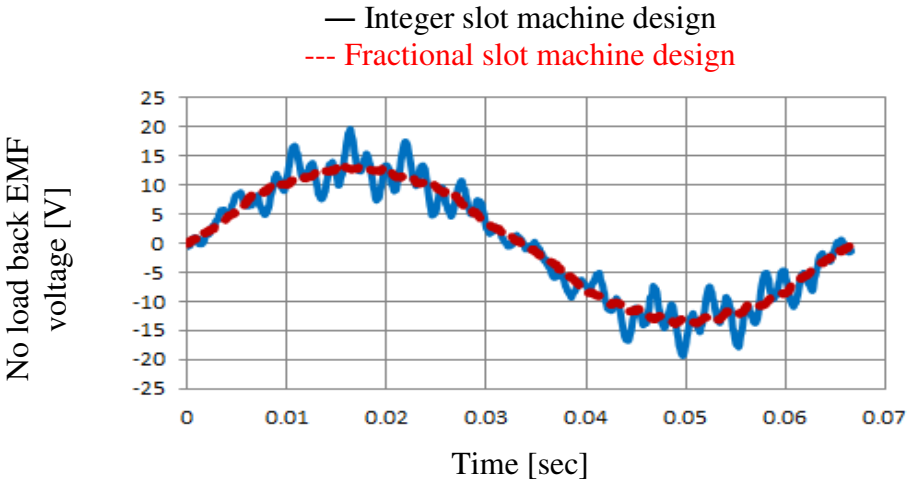

Fig. 6.11 Time domain comparison of phase A back EMF for two machines (Experiment at 300 rpm condition)

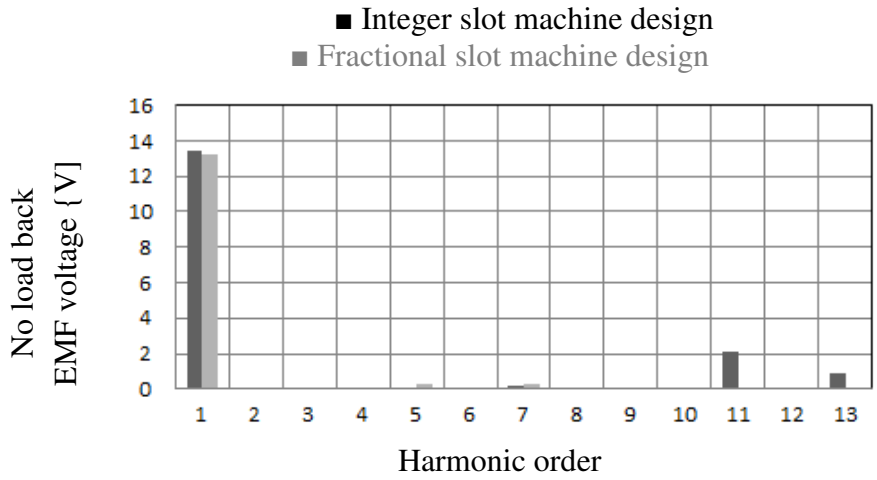

Fig. 6.12 Frequency domain comparison of phase A back EMF for two machines (Experiment at 300 rpm condition)

6.4.2 *Proposed method MS estimation evaluation*

The MS experimental results in constant speed condition is shown in Fig. 6.13. The EMF measured with a voltage sensor at 300 rpm is used as the benchmark. MS estimation results at other speed conditions are obtained by applying the proposed methodology described in previous section. It can be seen that the proposed method can work at zero/low speed conditions within a 5% deviation from the back EMF based results.

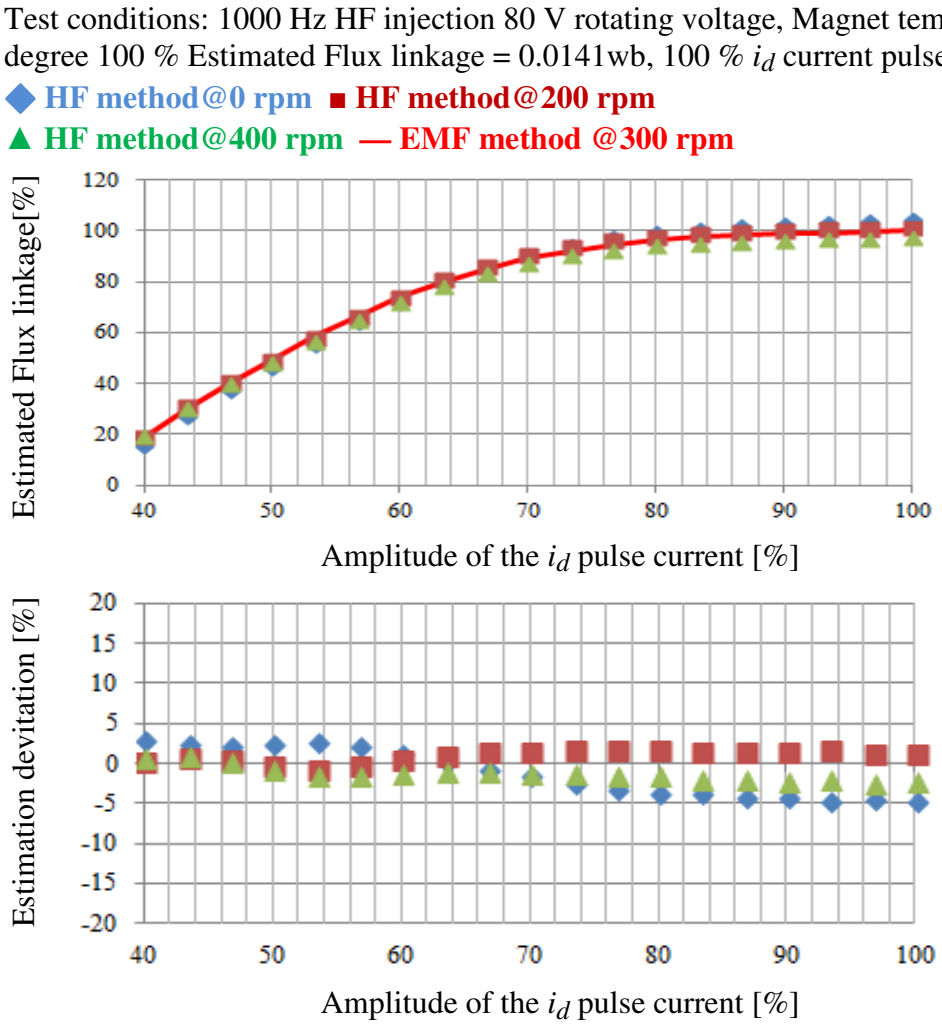

Fig. 6.13 Magnetization estimation experimental results

*6.4.3 **Proposed method MS estimation evaluation under speed variant condition***

The purpose of the evaluation is to investigate the effectiveness of proposed method under speed varying conditions. Since most of the applications are under variable speed conditions, the MS estimation is very crucial under speed changing conditions. The evaluation results is shown in Fig. 6.14. The slew rate of the test condition is set at 600 rpm/s which is much higher than the most critical condition in LA4 city drive cycle (350 rpm/s). The proposed method also demonstrates within a 5% deviation from the back EMF based results.

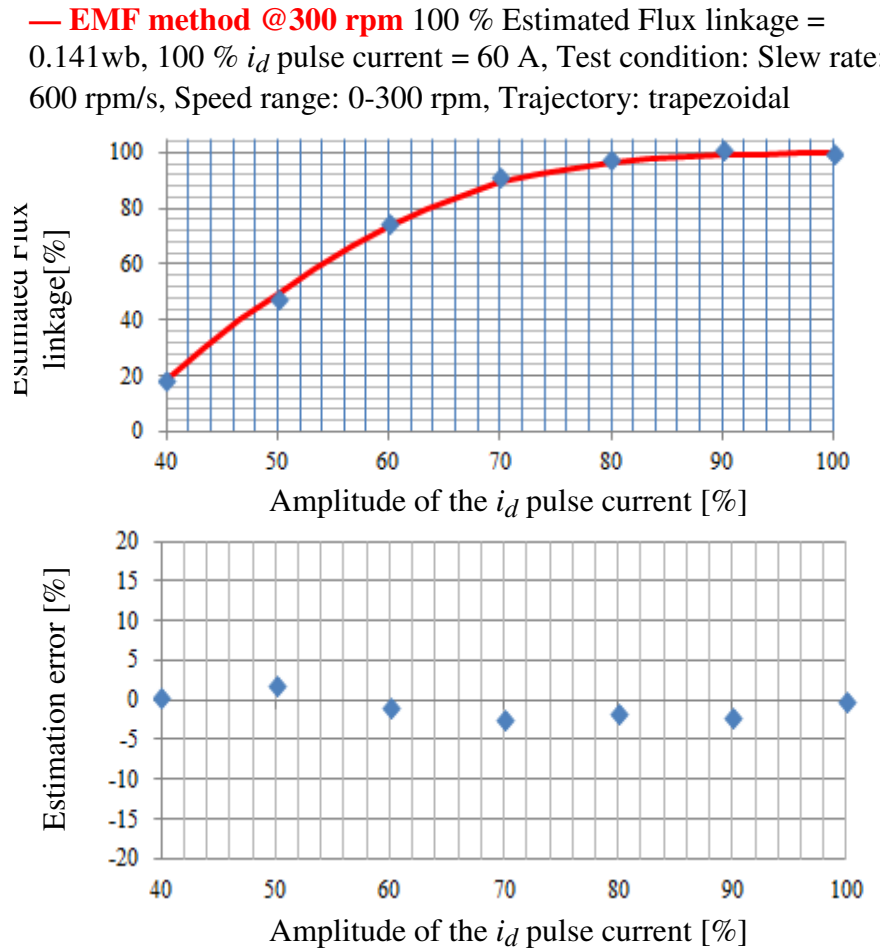

Fig. 6.14 Magnetization estimation experimental results@ speed varying condition

6.5 Conclusions and Summary

This chapter conclusions and contributions are summarized as follows.

- An effective MS estimation methodology suitable for zero/low speed conditions using HF injection has been proposed. By combining the CVC, FCO, and SRFF, the impact of EMF at machine rotating conditions on MS estimation accuracy can be reduced.
- A HF machine model has been proposed to describe the physical relationship between HF current and MS. By using this relationship, the MS can be estimated by measuring HF current.
- The resistivity of the magnet has been found to not to have a significant impact on the trend of HF current versus MS in the VFI-IPMSM.
- Using amplitude of positive sequence HF current extracted through a synchronous reference frame filter and a vector tracking method can achieve better signal-to-noise ratio and noise immunity.
- A fractional slot machine has been fabricated for MS estimation evaluation and features low EMF harmonics/torque ripple compared to previous integer slot machine design.
- The proposed MS estimation methodology has been evaluated in a fractional slot VFI-IPMSM. The experiment results demonstrate that the estimation errors are within 5%.

Chapter 7 – Conclusions, Contributions, and Recommended Future Work

7.1 Research Conclusions

The following list summarizes the key conclusions offered by this research:

7.1.1 Methodology of self-sensing control of FI-IPMSM

- Reliable low speed position estimation was achieved within 3 rms electric degrees deviation for three injection methods under load conditions as proper decoupling techniques were applied.
- For the self-sensing control, the main saliency of the FI-IPMSM increases as the loading conditions increase. Therefore, the signal-to-noise ratio (SNR) improves with increased loading conditions.
- It was observed that with the selection of d-axis pulsating carrier voltage injection to extract the rotor saliency signal followed by a saliency tracking observer, the induced saliency and multi-saliencies have the least impact on position tracking estimation performance.
- For cross-coupling effects of cross-saturation that cause position errors, all the signal injection and saliency tracking methods share the same position error sensitivity. The cross-coupling effects can be mitigated by proper implementation of adaptive decoupling techniques.

- The FI-IPMSM has an inductive reactance that is much larger than the high frequency resistance (≈ 90 deg. power factor angle). The FI-IPMSM demonstrates good estimation accuracy without need of high frequency resistance decoupling.
- Using conventional position estimation methods with square wave injection caused large estimation errors (~90 elec. degree) due to the reverse saliency ($L_d > L_q$) of FI-IPMSMs. An alternative method was proposed and evaluated to show accurate position estimation for both FW-IPMSMs and FI-IPMSMs.

7.1.2 ***Optimum DC bus voltage selection for FI-IPMSM drive to achieve loss minimization with variable DC bus voltage***

- Through theoretical and experimental results, the total losses in the machine and the inverter can be reduced with optimum DC bus voltage selection. It is dominated by reduction of inverter switching losses.
- To achieve both the desired machine output torque and loss minimization simultaneously, an optimum DC bus voltage is required. The optimum DC bus voltage in the low speed region is the lowest voltage that can operate the machine without entering the flux weakening region.
- The optimum DC bus voltage calculation, which is based on an ideal machine model, is severely affected by the spatial harmonics of the FI machine and machine parameter estimation errors.
- A method using a VDSF has been developed for correcting voltage errors due to parameter estimation errors and unmodeled spatial harmonics. Therefore, a nearly optimal DC bus voltage calculation can be achieved.
- The self-sensing performance can be dynamically improved with the optimum DC bus voltage control method.

7.1.3 Variable magnetization state control in VFI-IPMSMs

- The magnetization state of VFI-IPMSM can be manipulated with i_d current.
- Magnetization state can be maintained during loss minimizing operation because positive i_d current is used for loss minimization.
- A significant reduction in the magnetization current losses can be achieved by using lower amplitude and shorter duration pulses of magnetization current.
- With proper magnet segmentation, the losses in the magnets can be reduced to a very small percentage of the total machine loss.
- Several possible control solutions for magnetization state manipulation during loaded conditions have been compared. It was shown that using a direct current pulse method without decoupling caused severe pulsating torque in simulations and experiments.
- Pre-recorded current lookup table methods for decoupling require intensive experimental efforts. These methods are also limited by machine manufacturing imperfections (e.g. magnet property, air gap distance.)
- Accurate flux and torque estimation can be achieved by the proposed VDSF. Therefore, closed loop torque control can be realized and smooth torque output can be preserved during the magnetization state manipulation process.
- Using the proposed VDSF-based methods, magnetization state change is feasible and smooth torque can be achieved over a wide speed range with loss minimization.

7.1.4 Magnetization state manipulation strategy for loss minimization over a driving cycle

- Efficiency improvement is demonstrated as the magnetization state of VFI-IPMSM is optimally controlled.

- Frequently changing magnetization state could cause significant losses. Keeping the magnetization state at specific condition does not fully utilize the benefits of the variable flux machine. A balance is needed for loss increases due to the magnetization pulse current and loss savings with changing magnetization state.
- It was also found that a hysteresis controller for the magnetization state operating algorithm could reduce the total loss. With the experimental results, the loss over a driving cycle have been simulated and found to be reduced by 10% and compared to fixed magnetization state control for the second prototype VFI-IPMSM.
- The optimum theoretical loss over a driving cycle can be reduced by as much as 15% for the second prototype VFI-IPMSM, when compared to fixed magnetization state control under the assumptions of no additional loss due to the magnetization pulse and ideal MS selection.
- A scalability analysis of proposed method for a vehicle-sized VFI-IPMSM is explored. The VFI-IPMSM with the proposed method demonstrates a reduction of 37% energy loss over a UDDS driving cycle and a reduction of 70% over a HFET driving cycle compared to the baseline machine.

*7.1.5 **Zero/Low speed magnetization state estimation using high frequency injection***

- With a high frequency injection, the induced high frequency current was found to have a significant correlation with magnetization state.
- The resistivity of the magnet has been found to not to have a significant impact on the trend of HF current versus MS in the VFI-IPMSM.
- To reduce the impact of EMF during machine rotation on MS estimation accuracy, the high frequency current is extracted by using CVC, FCO, and SRFF.

- To have better signal-to-noise ratio and noise immunity, the amplitude of positive sequence HF current is extracted through SRFF and vector tracking.
- A fractional slot machine has been fabricated for MS estimation evaluation and features low EMF harmonics/torque ripple compared to the previous integer slot machine design.
- The proposed MS estimation methodology has been evaluated in a fractional slot VFI-IPMSM under no load conditions. The experimental results demonstrate that the estimation errors are within 5% in both constant speed and speed varying conditions (in zero/low speed region).

7.2 Research Contributions

Key major contributions of this work are listed as follows:

*7.2.1 **Methodology for self-sensing control of FI-IPMSM***

- Three saliency based injection methods were implemented for comparative evaluation of low speed position tracking self-sensing performance for a FI-IPMSM.
- Multi-saliency effects on FI-IPMSMs were explored and shown to have decreased sensitivity under saturated load conditions. Based on this attribute, recommendation of signal injection method (pulsating vector injection) was made for effective reduction of the effects of multi-saliencies.
- Position estimation errors (90 degree offset) caused by square wave injection methods in FI-IPMSM were theoretically and experimentally identified and its cause isolated.
- An alternative position estimation method for square-wave injection was developed and shown to achieve robustness of rotor position estimation in FI-

IPMSM. Theoretical analysis, simulation and experiment results are provided to evaluate the effectiveness of this method.

7.2.2 ***Optimum DC bus voltage selection for FI-IPMSM drive to achieve loss minimization with variable DC bus voltage***

- Rigorous inverter/motor efficiency evaluations under different DC bus voltage and torque speed conditions were implemented on a FI-IPMSM drive. The relationship between losses distribution on the machine and inverter versus DC bus voltage were established through experimental results.
- Using rigorous experimental loss results, an optimum DC bus voltage selection strategy for loss minimization was proposed. Energy saving capabilities with the optimum DC bus selection was experimentally documented.
- The key limitations of an ideal machine model for optimum DC bus voltage estimation were identified. Spatial harmonic models were proposed to understand and explain the causes of the limitations.
- Using the disturbance voltage from the VDSF for accurate estimation of the optimum DC bus voltage (loss minimization operation) was proposed and loss reduction was demonstrated.
- Control methods for optimum DC bus voltage calculations with reduced sensitivity to machine parameter estimation errors and unmodeled machine spatial harmonics were proposed.
- Effectiveness and limitations of proposed optimum DC bus voltage control methods were evaluated via simulation and experiments.

*7.2.3 **Variable magnetization state control in VFI-IPMSMs***

- Magnetization state manipulation capabilities of VFI-IPMSM were identified and documented through simulation and experimental evaluation.
- A loss assessment of the magnetization manipulation current was performed by different durations and amplitudes of magnetization current pulse. The maximum torque capabilities with different magnetization state manipulation currents were also identified.
- The causes of pulsating torque during magnetization state manipulation were explored and documented.
- Using the disturbance voltage from the VDSF for accurately estimating the flux and torque in VFI-IPMSM was proposed and evaluated.
- Magnetization state manipulation methods that achieve a continuous and wide range of magnetization state change were proposed. Proposed methods were shown via simulation and experimental results to mitigate torque pulsations and yield smooth torque control during magnetization state manipulation without using lookup tables during non-zero speed and non-zero load conditions.

*7.2.4 **Magnetization state manipulation strategy for loss minimization over a driving cycle***

- Loss profiles for different MS of VF machines were identified and documented through simulation and experimental evaluation.
- An optimum MS manipulation control method was proposed to balance losses induced by the current used to change MS and the energy savings from MS selection.
- Loss assessment of the VF machines was performed by utilizing driving cycles. Losses of fixed MS and proposed optimum MS selection were analyzed. The

proposed method was shown via dynamic MS selection to achieve larger energy savings.

- A scalability analysis for VFI-IPMSM is explored. A comparative duty cycle loss analysis between a vehicle-sized VFI-IPMSM and an actual production vehicle machine is demonstrated. The VFI-IPMSM with the proposed MS selection method was shown to save energy compared to the actual production machine.

*7.2.5 **Zero/Low speed magnetization state estimation using high frequency injection***

- A physical model is proposed to describe the relationship between the MS and HF injection current. It is demonstrated that both HF resistance and inductance can be used to estimate MS.
- This research identified and documented a VF machine showing an almost pure inductive reactance in the HF range (100Hz - 1000 Hz) for MS estimation. It implies that the MS estimation accuracy should not be affected even without resistance decoupling.
- This research explores the impact of the magnet resistivity effects on MS estimation with HF injection methods and demonstrates that the magnet resistivity would not affect the trend of HF current versus MS in the VFI-IPMSM.
- A reliable MS estimation with HF injection for zero/low speed was proposed. The combination of CVC, SRFF, and vector tracking is used to extract MS information during machine rotating conditions.
- The proposed method provided an initial diagnostic methodology during the zero/varying speed and no load conditions. The MS information can be used as the basis for torque control and MS selection. The key limitation for the proposed method on the loaded condition was identified as the cross-coupling between magnet flux and stator flux.

7.3 Recommendations for Future Work

This research mainly focuses on the control aspects of FI-IPMSMs and VFI-IPMSMs. Several recommendations for future work are discussed here.

7.3.1 MS estimation under loaded conditions

At this time, the proposed MS estimation method is limited to no load conditions. Due to the cross-coupling between the magnet flux and the stator flux, decoupling is needed for the MS estimation under loaded conditions. A model reference adaptive control (MRAC) method would be a good candidate to estimate the MS under loaded conditions. In addition, the current sensor accuracy could also affect the precision of the MS estimation since the proposed MS estimation method relies on the accurate current measurement. MRAC can also be implemented to reduce the measurement errors in the current sensors.

7.3.2 Control methodology experimental evaluation with vehicle size VFI-IPMSM

Downsized proof-of-concept machines were fabricated and used to evaluate several control algorithms. As the control algorithms have been demonstrated to be effective in simulation, a vehicle size VFI-IPMSM will be needed to experimentally evaluate the limits of the proposed control algorithm.

7.3.3 Methods for changing MS under high speed conditions

Due to insufficient DC bus voltage, it is difficult to change magnetization state under high speed conditions. At this time, speed limitations for magnetization state changing still exist. An improved method for changing magnetization state in higher speed conditions will be needed. An additional boost converter could be used for increasing the DC bus voltage for changing MS within a short period of time. Several

boost converter topology could be investigated from several points of view including complexity, cost and size. Other methods such as pulse current shaping and changing MS under zero torque conditions could be explored for changing the MS in the high speed conditions.

*7.3.4 **Variable DC bus voltage control with VF machine for loss minimization***

The test bench has been modified to have variable DC bus voltage capability. A variable DC bus voltage was shown in the literature and this research to have better system efficiency. By adding the variable DC bus voltage, an additional control variable can be added in the control algorithms. For example, as the VF machine flux is reduced at mid speed range conditions, the DC bus voltage can also be reduced to further reduce the total system loss. A control methodology for the loss minimization has not yet been explored. Additionally, the dynamic properties of the DC bus voltage will have to be properly investigated and dealt with during the changing magnetization state condition.

*7.3.5 **Position self-sensing control in VFI-IPM machines***

Self-sensing attributes could be affected by different magnetization states and this phenomenon has not yet been explored. Impact of spatial harmonics in VFI-IPMSMs on position self-sensing is important. Techniques including the use of information about harmonic content or decoupling can be explored to further improve position self-sensing estimation. The limitations and the impacts of magnetization state conditions on position self-sensing estimation are unexplored areas.

*7.3.6 **Loss minimization control of MS manipulation including the inverter losses on duty cycle loaded conditions***

As shown in this research, machine loss reduction by proposed MS manipulation method can be achieved. However, inverter loss during normal operation and additional

inverter loss due to MS manipulation current are not considered. A more comprehensive control methodology should be developed to consider the tradeoff between the motor/inverter losses and loss reduction from manipulating MS. The consideration of inverter losses can help to develop new control methodologies for selecting an optimum number of changing states so energy savings on duty cycle load can be achieved.

7.3.7 ***Investigation of magnet properties variation due to temperature effects, aging effects, and residual flux***

Understanding the magnet properties are the key to design and control VF machines. At this time, the impacts of several effects on magnet properties are still unknown. First of all, temperature effects on variable magnetization state control are unknown and not discussed in this research. Since magnet flux is affected by temperature, the control of MS manipulation might be affected. Secondly, frequent changing of the MS is required for the duty cycle load conditions. Therefore, the investigation of aging effects and life-cycle in low-H_c magnets due to MS manipulation procedures will be very crucial. Thirdly, manipulating MS from a non-zero MS is also common in the duty cycle load conditions. The impact of residual flux on changing (MS ex. 40% → 80 % VS. 0% → 80%) is also unknown and should be explored.

Bibliography

[1] N. Limsuwan, T. Kato, K. Akatsu, and R. Lorenz, "Design and Evaluation of a Variable-Flux Flux-Intensifying Interior Permanent Magnet Machine," *Industry Applications, IEEE Trans. on,* vol. PP, pp. 1-1, 2013.

[2] T. Kato, N. Limsuwan, C. Y. Yu, K. Akatsu, and R. D. Lorenz, "Rare Earth Reduction Using A Novel Variable Magnetomotive Force, Flux Intensified IPM Machine," *Industry Applications, IEEE Trans. on,* vol. PP, pp. 1-1, 2013.

[3] A. M. El-Refaie, "High speed operation of permament magnet machines," University of Wisconsin--Madison, 2005., 2005, pp. xix, 572 p.

[4] A. M. El-Refaie and T. M. Jahns, "Optimal flux weakening in surface PM machines using fractional-slot concentrated windings," *Industry Applications, IEEE Transactions on,* vol. 41, pp. 790-800, 2005.

[5] F. Magnussen, P. Thelin, and C. Sadarangani, "Performance evaluation of permanent magnet synchronous machines with concentrated and distributed windings including the effect of field-weakening," in *Proc. of Power Electronics, Machines and Drives, 2004. (PEMD 2004). Second International Conference on (Conf. Publ. No. 498)*, pp. 679-685 Vol.2.

[6] W. Jiabin, X. Zhen Ping, and D. Howe, "Three-phase modular permanent magnet brushless Machine for torque boosting on a downsized ICE vehicle," *Vehicular Technology, IEEE Transactions on,* vol. 54, pp. 809-816, 2005.

[7] D. Raca, "Permanent magnet synchronous machines terminal attributes for self-sensing and automatic identification," University of Wisconsin--Madison, Thesis (Ph D), 2009, pp. xvii, 326 p.

[8] N. Limsuwan, Y. Shibukawa, D. Reigosa, and R. D. Lorenz, "Novel design of flux-intensifying interior permanent magnet synchronous machine suitable for power conversion and self-sensing control at very low speed," in *Proc. of Energy Conversion Congress and Exposition (ECCE), 2010 IEEE*, pp. 555-562.

[9] D. D. Reigosa, K. Akatsu, N. Limsuwan, Y. Shibukawa, and R. D. Lorenz, "Self-Sensing Comparison of Fractional Slot Pitch Winding Versus Distributed Winding for FW- and FI-IPMSMs Based on Carrier Signal Injection at Very Low Speed," *Industry Applications, IEEE Transactions on,* vol. 46, pp. 2467-2474, 2010.

[10] S. Ogasawara and H. Akagi, "An approach to position sensorless drive for brushless DC motors," *Industry Applications, IEEE Transactions on,* vol. 27, pp. 928-933, 1991.

[11] N. Matsui, "Sensorless PM brushless DC motor drives," *Industrial Electronics, IEEE Transactions on,* vol. 43, pp. 300-308, 1996.

[12] N. Matsui and M. Shigyo, "Brushless DC motor control without position and speed sensors," *Industry Applications, IEEE Transactions on,* vol. 28, pp. 120-127, 1992.

[13] N. Matsui, T. Takeshita, and K. Yasuda, "A new sensorless drive of brushless DC motor," in *Proc. of Industrial Electronics, Control, Instrumentation, and Automation, 1992.* , pp. 430-435 vol.1.

[14] C. Zhiqian, M. Tomita, S. Doki, and S. Okuma, "An extended electromotive force model for sensorless control of interior permanent-magnet synchronous motors," *Industrial Electronics, IEEE Transactions on,* vol. 50, pp. 288-295, 2003.

[15] S. Morimoto, K. Kawamoto, M. Sanada, and Y. Takeda, "Sensorless control strategy for salient-pole PMSM based on extended EMF in rotating reference frame," *Industry Applications, IEEE Transactions on,* vol. 38, pp. 1054-1061, 2002.

[16] S. Ichikawa, Z. Chen, M. Tomita, S. Doki, and S. Okuma, "Sensorless controls of salient-pole permanent magnet synchronous motors using extended electromotive force models," *Electrical Engineering in Japan,* vol. 146, pp. 55-64, 2004.

[17] K. Hyunbae, M. C. Harke, and R. D. Lorenz, "Sensorless control of interior permanent-magnet machine drives with zero-phase lag position estimation," *Industry Applications, IEEE Transactions on,* vol. 39, pp. 1726-1733, 2003.

[18] S. Morimoto, M. Sanada, and Y. Takeda, "Mechanical Sensorless Drives of IPMSM With Online Parameter Identification," *Industry Applications, IEEE Transactions on,* vol. 42, pp. 1241-1248, 2006.

[19] Y. Inoue, K. Yamada, S. Morimoto, and M. Sanada, "Effectiveness of Voltage Error Compensation and Parameter Identification for Model-Based Sensorless Control of IPMSM," *Industry Applications, IEEE Transactions on,* vol. 45, pp. 213-221, 2009.

[20] R. W. Hejny and R. D. Lorenz, "Evaluating the practical low speed limits for back-EMF tracking-based sensorless speed control using drive stiffness as a key metric," in *Proc. of Energy Conversion Congress and Exposition, 2009.* , pp. 2481-2488.

[21] P. L. Jansen and R. D. Lorenz, "Transducerless position and velocity estimation in induction and salient AC machines," *Industry Applications, IEEE Transactions on,* vol. 31, pp. 240-247, 1995.

[22] L. A. S. Ribeiro, M. W. Degner, F. Briz, and R. D. Lorenz, "Comparison of carrier signal voltage and current injection for the estimation of flux angle or rotor position," in *Proc. of Industry Applications Conference, 1998. Thirty-Third IAS Annual Meeting. The 1998 IEEE*, pp. 452-459 vol.1.

[23] M. W. Degner, "Flux, position, and velocity estimation in AC machines using carrier signal injection," University of Wisconsin--Madison, 1998., 1998, pp. xii, 303 leaves.

[24] F. Briz, A. Diez, and M. W. Degner, "Dynamic operation of carrier-signal-injection-based sensorless direct field-oriented AC drives," *Industry Applications, IEEE Transactions on,* vol. 36, pp. 1360-1368, 2000.

[25] A. Consoli, G. Scarcella, and A. Testa, "Industry application of zero-speed sensorless control techniques for PM synchronous motors," *Industry Applications, IEEE Transactions on,* vol. 37, pp. 513-521, 2001.

[26] A. Consoli, G. Scarcella, G. Bottiglieri, and A. Testa, "Harmonic Analysis of Voltage Zero-Sequence-Based Encoderless Techniques," *Industry Applications, IEEE Transactions on,* vol. 42, pp. 1548-1557, 2006.

[27] M. W. Degner and R. D. Lorenz, "Using multiple saliencies for the estimation of flux, position, and velocity in AC machines," *Industry Applications, IEEE Transactions on,* vol. 34, pp. 1097-1104, 1998.

[28] F. Briz, M. W. Degner, A. Diez, and R. D. Lorenz, "Measuring, modeling, and decoupling of saturation-induced saliencies in carrier-signal injection-based sensorless AC drives," *Industry Applications, IEEE Transactions on,* vol. 37, pp. 1356-1364, 2001.

[29] P. Garcia, F. Briz, D. Raca, and R. D. Lorenz, "Saliency-Tracking-Based Sensorless Control of AC Machines Using Structured Neural Networks," *Industry Applications, IEEE Transactions on,* vol. 43, pp. 77-86, 2007.

[30] M. J. Corley and R. D. Lorenz, "Rotor position and velocity estimation for a salient-pole permanent magnet synchronous machine at standstill and high speeds," *Industry Applications, IEEE Transactions on,* vol. 34, pp. 784-789, 1998.

[31] T. Aihara, A. Toba, T. Yanase, A. Mashimo, and K. Endo, "Sensorless torque control of salient-pole synchronous motor at zero-speed operation," *Power Electronics, IEEE Transactions on,* vol. 14, pp. 202-208, 1999.

[32] J. Ji-Hoon, S. Seung-Ki, H. Jung-Ik, K. Ide, and M. Sawamura, "Sensorless drive of surface-mounted permanent-magnet motor by high-frequency signal injection based on magnetic saliency," *Industry Applications, IEEE Transactions on,* vol. 39, pp. 1031-1039, 2003.

[33] J. Ji-Hoon, H. Jung-Ik, M. Ohto, K. Ide, and S. Seung-Ki, "Analysis of permanent-magnet machine for sensorless control based on high-frequency signal injection," *Industry Applications, IEEE Transactions on,* vol. 40, pp. 1595-1604, 2004.

[34] R. Kennel, "Encoderless control of synchronous machines with permanent magnets - impact of magnetic design," in *Proc. of Optimization of Electrical and Electronic Equipment (OPTIM), 2010 12th International Conference on*, pp. 19-24.

[35] M. Linke, R. Kennel, and J. Holtz, "Sensorless speed and position control of synchronous machines using alternating carrier injection," in *Proc. of Electric Machines and Drives Conference, 2003. IEMDC'03. IEEE International*, pp. 1211-1217 vol.2.

[36] H. Jung-Ik and S. Seung-Ki, "Sensorless field-orientation control of an induction machine by high-frequency signal injection," *Industry Applications, IEEE Transactions on,* vol. 35, pp. 45-51, 1999.

[37] K. Sungmin, K. Yong-Cheul, S. Seung-Ki, P. Joonho, and K. Sang-Min, "Position sensorless operation of IPMSM with near PWM switching frequency signal injection," in *Proc. of Power Electronics and ECCE Asia (ICPE & ECCE), 2011 IEEE 8th International Conference on*, pp. 1660-1665.

[38] Y. Young-doo, S. Seung-ki, S. Morimoto, and K. Ide, "High bandwidth sensorless algorithm for AC machines based on square-wave type voltage injection," in *Proc. of Energy Conversion Congress and Exposition, 2009. ECCE 2009. IEEE*, pp. 2123-2130.

[39] W. Hammel and R. M. Kennel, "Integration of alternating carrier injection in position sensorless control without any filtering," in *Proc. of Energy Conversion Congress and Exposition, 2009. ECCE 2009. IEEE*, pp. 3830-3836.

[40] R. Leidhold and P. Mutschler, "Improved method for higher dynamics in sensorless position detection," in *Proc. of Industrial Electronics, 2008. IECON 2008. 34th Annual Conference of IEEE*, pp. 1240-1245.

[41] Y. Young-doo and S. Seung-ki, "Sensorless control for induction machines using square-wave voltage injection," in *Proc. of Energy Conversion Congress and Exposition (ECCE), 2010 IEEE*, pp. 3147-3152.

[42] Y. Young-Doo, S. Seung-Ki, S. Morimoto, and K. Ide, "High-Bandwidth Sensorless Algorithm for AC Machines Based on Square-Wave-Type Voltage Injection," *Industry Applications, IEEE Transactions on,* vol. 47, pp. 1361-1370, 2011.

[43] K. Sungmin, H. Jung-Ik, and S. Seung-Ki, "PWM switching frequency signal injection sensorless method in IPMSM," in *Proc. of Energy Conversion Congress and Exposition (ECCE), 2011 IEEE*, pp. 3021-3028.

[44] W. Hammel and R. M. Kennel, "Position sensorless control of PMSM by synchronous injection and demodulation of alternating carrier voltage," in *Proc. of Sensorless Control for Electrical Drives (SLED), 2010 First Symposium on*, pp. 56-63.

[45] C. Dae-Woong, K. Joohn-Sheok, and S. Seung-Ki, "Unified voltage modulation technique for real-time three-phase power conversion," *Industry Applications, IEEE Transactions on,* vol. 34, pp. 374-380, 1998.

[46] S. Ogasawara, T. Matsuzawa, and H. Akagi, "A position-sensorless IPM motor drive system using a position estimation based on magnetic saliency," *Electrical Engineering in Japan,* vol. 131, pp. 68-79, 2000.

[47] S. Ogasawara and H. Akagi, "Implementation and position control performance of a position-sensorless IPM motor drive system based on magnetic saliency," *Industry Applications, IEEE Transactions on,* vol. 34, pp. 806-812, 1998.

[48] S. Ogasawara and H. Akagi, "An approach to real-time position estimation at zero and low speed for a PM motor based on saliency," *Industry Applications, IEEE Transactions on,* vol. 34, pp. 163-168, 1998.

[49] E. Robeischl and M. Schroedl, "Optimized INFORM-measurement sequence for sensorless PM synchronous motor drives with respect to minimum current distortion," in *Proc. of Industry Applications Conference, 2002. 37th IAS Annual Meeting.* , pp. 92-98 vol.1.

[50] M. Schroedl, "Sensorless control of AC machines at low speed and standstill based on the “INFORM” method," in *Proc. of Industry Applications Conference, 1996. Thirty-First IAS Annual Meeting*, pp. 270-277 vol.1.

[51] M. Schroedl and P. Weinmeier, "Sensorless control of reluctance machines at arbitrary operating conditions including standstill," *Power Electronics, IEEE Transactions on,* vol. 9, pp. 225-231, 1994.

[52] J. Holtz and P. Hangwen, "Acquisition of rotor anisotropy signals in sensorless position control systems," in *Proc. of Industry Applications Conference, 2003. 38th IAS Annual Meeting. Conference Record of the*, pp. 1165-1172 vol.2.

[53] J. Holtz and J. Juliet, "Sensorless acquisition of the rotor position angle of induction motors with arbitrary stator windings," *Industry Applications, IEEE Transactions on,* vol. 41, pp. 1675-1682, 2005.

[54] A. Consoli, G. Scarcella, and A. Testa, "A new zero-frequency flux-position detection approach for direct-field-oriented-control drives," *Industry Applications, IEEE Transactions on,* vol. 36, pp. 797-804, 2000.

[55] F. Briz, M. W. Degner, P. Garcia, and J. M. Guerrero, "Rotor position estimation of AC machines using the zero-sequence carrier-signal voltage," *Industry Applications, IEEE Transactions on,* vol. 41, pp. 1637-1646, 2005.

[56] F. Briz, M. W. Degner, P. G. Fernandez, and A. B. Diez, "Rotor and flux position estimation in delta-connected AC Machines using the zero-sequence carrier-signal current," *Industry Applications, IEEE Transactions on,* vol. 42, pp. 495-503, 2006.

[57] F. Briz, M. W. Degner, P. Garcia, and R. D. Lorenz, "Comparison of saliency-based sensorless control techniques for AC machines," *Industry Applications, IEEE Transactions on,* vol. 40, pp. 1107-1115, 2004.

[58] D. D. Reigosa, P. Garcia, F. Briz, D. Raca, and R. D. Lorenz, "Modeling and Adaptive Decoupling of High-Frequency Resistance and Temperature Effects in Carrier-Based Sensorless Control of PM Synchronous Machines," *Industry Applications, IEEE Transactions on,* vol. 46, pp. 139-149, 2010.

[59] J. M. Guerrero, M. Leetmaa, F. Briz, A. Zamarron, and R. D. Lorenz, "Inverter nonlinearity effects in high-frequency signal-injection-based sensorless control methods," *Industry Applications, IEEE Transactions on,* vol. 41, pp. 618-626, 2005.

[60] Y. Xinmei, I. Brown, R. D. Lorenz, and Q. Arui, "Observer-based inverter disturbance compensation," in *Proc. of Energy Conversion Congress and Exposition, 2009. ECCE 2009. IEEE*, pp. 2520-2527.

[61] Y. Shih-Chin, T. Suzuki, R. D. Lorenz, and T. M. Jahns, "Surface-Permanent-Magnet Synchronous Machine Design for Saliency-Tracking Self-Sensing Position

Estimation at Zero and Low Speeds," *Industry Applications, IEEE Transactions on,* vol. 47, pp. 2103-2116, 2011.

[62] P. Guglielmi, M. Pastorelli, and A. Vagati, "Cross-Saturation Effects in IPM Motors and Related Impact on Sensorless Control," *Industry Applications, IEEE Transactions on,* vol. 42, pp. 1516-1522, 2006.

[63] L. Yi, Z. Q. Zhu, D. Howe, C. M. Bingham, and D. A. Stone, "Improved Rotor-Position Estimation by Signal Injection in Brushless AC Motors, Accounting for Cross-Coupling Magnetic Saturation," *Industry Applications, IEEE Transactions on,* vol. 45, pp. 1843-1850, 2009.

[64] D. Raca, P. Garcia, D. D. Reigosa, F. Briz, and R. D. Lorenz, "Carrier-Signal Selection for Sensorless Control of PM Synchronous Machines at Zero and Very Low Speeds," *Industry Applications, IEEE Transactions on,* vol. 46, pp. 167-178, 2010.

[65] D. D. Reigosa, P. Garcia, D. Raca, F. Briz, and R. D. Lorenz, "Measurement and Adaptive Decoupling of Cross-Saturation Effects and Secondary Saliencies in Sensorless Controlled IPM Synchronous Machines," *Industry Applications, IEEE Transactions on,* vol. 44, pp. 1758-1767, 2008.

[66] N. Bianchi and S. Bolognani, "Sensorless-Oriented Design of PM Motors," *Industry Applications, IEEE Transactions on,* vol. 45, pp. 1249-1257, 2009.

[67] Y. Kano, T. Kosaka, N. Matsui, and T. Nakanishi, "Design of Saliency-Based Sensorless Drive IPM Motors for General Industrial Applications," in *Proc. of Industry Applications Society Annual Meeting, 2008. IAS '08. IEEE*, pp. 1-6.

[68] S. Morimoto, M. Sanada, and Y. Takeda, "Wide-speed operation of interior permanent magnet synchronous motors with high-performance current regulator," *Industry Applications, IEEE Transactions on,* vol. 30, pp. 920-926, 1994.

[69] T. G. Habetler, F. Profumo, M. Pastorelli, and L. M. Tolbert, "Direct torque control of induction machines using space vector modulation," *Industry Applications, IEEE Transactions on,* vol. 28, pp. 1045-1053, 1992.

[70] I. Takahashi and Y. Ohmori, "High-performance direct torque control of an induction motor," *Industry Applications, IEEE Transactions on,* vol. 25, pp. 257-264, 1989.

[71] M. Depenbrock, "Direct self-control (DSC) of inverter-fed induction machine," *Power Electronics, IEEE Transactions on,* vol. 3, pp. 420-429, 1988.

[72] I. Takahashi and T. Noguchi, "A New Quick-Response and High-Efficiency Control Strategy of an Induction Motor," *Industry Applications, IEEE Transactions on,* vol. IA-22, pp. 820-827, 1986.

[73] C. French and P. Acarnley, "Direct torque control of permanent magnet drives," *Industry Applications, IEEE Transactions on,* vol. 32, pp. 1080-1088, 1996.

[74] L. Zhong, M. F. Rahman, W. Y. Hu, and K. W. Lim, "Analysis of direct torque control in permanent magnet synchronous motor drives," *Power Electronics, IEEE Transactions on,* vol. 12, pp. 528-536, 1997.

[75] L. Zhong, M. F. Rahman, W. Y. Hu, K. W. Lim, and M. A. Rahman, "A direct torque controller for permanent magnet synchronous motor drives," *Energy Conversion, IEEE Transactions on,* vol. 14, pp. 637-642, 1999.

[76] M. F. Rahman, L. Zhong, and L. Khiang Wee, "A direct torque-controlled interior permanent magnet synchronous motor drive incorporating field weakening," *Industry Applications, IEEE Transactions on,* vol. 34, pp. 1246-1253, 1998.

[77] B. H. Kenny, "Deadbeat direct torque control of induction machines using self-sensing at low and zero speed," University of Wisconsin--Madison, 2001., 2001, pp. x, 274 p.

[78] N. T. West and R. D. Lorenz, "Digital Implementation of Stator and Rotor Flux-Linkage Observers and a Stator-Current Observer for Deadbeat Direct Torque Control of Induction Machines," *Industry Applications, IEEE Transactions on,* vol. 45, pp. 729-736, 2009.

[79] T. R. Obermann, Z. D. Hurst, and R. D. Lorenz, "Deadbeat-direct torque & flux control motor drive over a wide speed, torque and flux operating space using a single control law," in *Proc. of Energy Conversion Congress and Exposition (ECCE), 2010 IEEE*, pp. 215-222.

[80] R. D. Lorenz, "The emerging role of dead-beat, direct torque and flux control in the future of induction machine drives," in *Proc. of Optimization of Electrical and Electronic Equipment, 2008. OPTIM 2008. 11th International Conference on*, pp. XIX-XXVII.

[81] J. M. Burton, "Loss manipulation using Deadbeat-Direct Torque & Flux Control for induction machines," University of Wisconsin--Madison, 2009., 2009, pp. vii, 125 p.

[82] L. Jae Suk, C. Chan-Hee, S. Jul-Ki, and R. D. Lorenz, "Deadbeat direct torque and flux control of interior permanent magnet machines with discrete time stator current

and stator flux linkage observer," in *Proc. of Energy Conversion Congress and Exposition, 2009. ECCE 2009. IEEE*, pp. 2504-2511.

[83] T. R. Obermann, Z. D. Hurst, B. F. Bradley, and R. D. Lorenz, "Deadbeat-direct torque and flux control motor drive using a single control law to minimize motor losses," in *Proc. of Electrical Machines and Systems (ICEMS), 2010 International Conference on*, pp. 742-747.

[84] T. M. Jahns, G. B. Kliman, and T. W. Neumann, "Interior Permanent-Magnet Synchronous Motors for Adjustable-Speed Drives," *Industry Applications, IEEE Transactions on,* vol. IA-22, pp. 738-747, 1986.

[85] S. Morimoto, M. Sanada, and Y. Takeda, "Effects and Compensation of Magnetic Saturation in Flux-Weakening Controlled Permanent Magnet Synchronous Motor Drives," *Industry Applications, IEEE Transactions on,* vol. 30, p. 1632, 1994.

[86] J. Yu-seok, S. Seung-Ki, S. Hiti, and K. M. Rahman, "Online Minimum-Copper-Loss Control of an Interior Permanent-Magnet Synchronous Machine for Automotive Applications," *Industry Applications, IEEE Transactions on,* vol. 42, pp. 1222-1229, 2006.

[87] S. Morimoto, Y. Tong, Y. Takeda, and T. Hirasa, "Loss minimization control of permanent magnet synchronous motor drives," *Industrial Electronics, IEEE Transactions on,* vol. 41, pp. 511-517, 1994.

[88] J. B. Adawey, S. Yamamoto, T. Kano, and T. Ara, "Maximum efficiency drives of interior permanent magnet synchronous motor considering iron loss and cross-magnetic saturation," in *Proc. of Electrical Machines and Systems, 2009. ICEMS 2009. International Conference on*, pp. 1-6.

[89] D. S. Kirschen, D. W. Novotny, and T. A. Lipo, "Optimal Efficiency Control of an Induction Motor Drive," *Energy Conversion, IEEE Transactions on,* vol. EC-2, pp. 70-76, 1987.

[90] D. S. Kirschen, D. W. Novotny, and T. A. Lipo, "On-Line Efficiency Optimization of a Variable Frequency Induction Motor Drive," *Industry Applications, IEEE Transactions on,* vol. IA-21, pp. 610-616, 1985.

[91] D. S. Kirschen, D. W. Novotny, and W. Suwanwisoot, "Minimizing Induction Motor Losses by Excitation Control in Variable Frequency Drives," *Industry Applications, IEEE Transactions on,* vol. IA-20, pp. 1244-1250, 1984.

[92] K. Sungmin, Y. Young-Doo, S. Seung-Ki, K. Ide, and K. Tomita, "Parameter independent maximum torque per ampere (MTPA) control of IPM machine based

on signal injection," in *Proc. of Applied Power Electronics Conference and Exposition (APEC), 2010 Twenty-Fifth Annual IEEE*, pp. 103-108.

[93] K. Sungmin, S. Seung-Ki, K. Ide, and S. Morimoto, "Maximum efficiency operation of Synchronous Reluctance Machine using signal injection," in *Proc. of Power Electronics Conference (IPEC), 2010 International*, pp. 2000-2004.

[94] S. Bolognani, R. Petrella, A. Prearo, and L. Sgarbossa, "Automatic tracking of MTPA trajectory in IPM motor drives based on AC current injection," in *Proc. of Energy Conversion Congress and Exposition, 2009. ECCE 2009. IEEE*, pp. 2340-2346.

[95] X. Wei and R. D. Lorenz, "Dynamic loss minimization using improved deadbeat-direct torque and flux control for interior permanent magnet synchronous machines," in *Proc. of Energy Conversion Congress and Exposition (ECCE), 2012 IEEE*, pp. 4000-4007.

[96] R. W. De Doncker and R. D. King, "Technique for decoupling the energy storage system voltage from the DC link voltage in AC electric drive systems," U.S. Patent No. 5,373,195. 13 Dec., 1994.

[97] N. Akao, "Controller for driving a permanent magnet type synchronous motor," U.S. Patent No. 5,883,484. 16 Mar., 1999.

[98] H. Jonokuchi, "Motor driver having a booster circuit and an inverter both controlled by pulse width modulation," US Patent No. 6,060,859,May 9, 2000.

[99] R. D. King, "Traction motor drive system," U.S. Patent No. 6,737,822. 18 May 2004.

[100] K. Yamamoto, K. Shinohara, and H. Makishima, "Comparison between flux weakening and PWM inverter with voltage booster for permanent magnet synchronous motor drive," in *Proc. of Power Conversion Conference, 2002. PCC Osaka 2002. Proceedings of the*, pp. 161-166 vol.1.

[101] K. Yamamoto, K. Shinohara, and A. Imakiire, "Steady State Characteristics of PWM Inverter with Voltage Boosters for Permanent Magnet Synchronous Motor Drives," in *Proc. of Power Conversion Conference - Nagoya, 2007. PCC '07*, pp. 296-301.

[102] K. Yamamoto, K. Shinohara, and T. Nagahama, "Characteristics of permanent-magnet synchronous motor driven by PWM inverter with voltage booster," *Industry Applications, IEEE Transactions on,* vol. 40, pp. 1145-1152, 2004.

[103] E. S. M. Okamura, and S. Sasaki,, "Development of Hybrid Electric Drive System Using a Boost Converter," in *EVS-20, Session 5, The 20th International Electric Vehicle Symposium and Exposition* Long Beach, California, 2003.

[104] S. Shinn-Ming, L. Jenn-Horng, H. Yi-Shuo, and L. Yi-Hung, "Design and Implementation of a Dynamic Voltage Boosting Drive for Permanent Magnet Synchronous Motors," in *Proc. of Power Electronics Conference (IPEC), 2010 International*, pp. 1398-1402.

[105] K. Asano, Y. Inaguma, H. Ohtani, E. Sato, M. Okamura, and S. Sasaki, "High Performance Motor Drive Technologies for Hybrid Vehicles," in *Proc. of Power Conversion Conference (PCC), Nagoya*, pp. 1584-1589.

[106] M. Okamura and T. Yamashita, "Motor drive apparatus capable of accurately estimating demagnetization of permanent magnet motor," Google Patents, 2009.

[107] V. Ostovic, "Memory motors," *Industry Applications Magazine, IEEE,* vol. 9, pp. 52-61, 2003.

[108] V. Ostovic, "Memory motors-a new class of controllable flux PM machines for a true wide speed operation," in *Proc. of Industry Applications Conference,Thirty-Sixth IAS Annual Meeting. IEEE*, pp. 2577-2584 vol.4.

[109] K. Sakai, H. Hashimoto, and S. Kuramochi, "Principle and basic characteristics of hybrid variable-magnetic-force motors," in *Proc. of the European Power Electronics Conference (EPE),Birmingham UK*.

[110] K. Sakai, K. Yuki, Y. Hashiba, N. Takahashi, and K. Yasui, "Principle of the variable-magnetic-force memory motor," in *Proc. of Electrical Machines and Systems, Nov15-18 . 2009, Tokyo*, pp. 1-6.

[111] K. Yuuki, K. Sakai, and H. Mochikawa, "Variable-flux motor drive system," U.S. Patent No. 8,179,068. 15 May 2012., 2012.

[112] K. Sakai and K. Yuuki, "Permanent-magnet-type rotating electrical machine and permanent magnet motor drive system," US Patent 8,269,390, 2012.

[113] K. Yuuki, K. Sakai, and H. Mochikawa, "VARIABLE MAGNETIC FLUX DRIVE SYSTEM," U.S. Patent Application 12/678,929, filed September 16, 2008.

[114] T. Kato, N. Limsuwan, C. Yu, K. Akatsu, and R. D. Lorenz, "Rare earth reduction using a novel variable magnetomotive force, flux intensified IPM machine," in *Proc. of Energy Conversion Congress and Exposition (ECCE), IEEE, 2012*, pp. 4346-4353.

[115] N. Limsuwan, T. Kato, K. Akatsu, and R. D. Lorenz, "Design and evaluation of a variable-flux flux-intensifying interior permanent magnet machine," in *Proc. of Energy Conversion Congress and Exposition (ECCE), IEEE,2012*, pp. 3670-3677.

[116] C. Y. Yu, T. Fukushige, N. Limsuwan, T. Kato, D. Reigosa, and R. D. Lorenz, "Variable flux machine torque estimation and pulsating torque mitigation during magnetization state manipulation," in *Proc. of Energy Conversion Congress and Exposition (ECCE)*, pp. 852-859.

[117] C. W. Cheng, H. C. Man, and F. T. Cheng, "Magnetic and corrosion characteristics of Nd-Fe-B magnet with various surface coatings," *Magnetics, IEEE Trans. on,* vol. 33, pp. 3910-3912, 1997.

[118] Y. Anno and S.-K. Sul, "Design of Flux Observer Robust to Interior Permanent-Magnet Synchronous Motor Flux Variation," *Industry Applications, IEEE Trans. on,* vol. 45, pp. 1670-1677, 2009.

[119] S. Rajagopalan, W. Roux, T. G. Habetler, and R. G. Harley, "Dynamic Eccentricity and Demagnetized Rotor Magnet Detection in Trapezoidal Flux (Brushless DC) Motors Operating Under Different Load Conditions," *Power Electronics, IEEE Trans. on,* vol. 22, pp. 2061-2069, 2007.

[120] J. Urresty, J. R. Riba Ruiz, M. Delgado, and L. Romeral, "Detection of Demagnetization Faults in Surface-Mounted Permanent Magnet Synchronous Motors by Means of the Zero-Sequence Voltage Component," *Energy Conversion, IEEE Trans. on,* vol. 27, pp. 42-51, 2012.

[121] H. Jongman, H. Doosoo, L. Sang-Bin, Y. Ji-Yoon, and L. Kwang-Woon, "Automated Monitoring of Magnet Quality for Permanent-Magnet Synchronous Motors at Standstill," *Industry Applications, IEEE Trans. on,* vol. 46, pp. 1397-1405, 2010.

[122] H. Jongman, P. Sanguk, H. Doosoo, K. Tae-june, L. Sang Bin, C. Kral, and A. Haumer, "Detection and Classification of Rotor Demagnetization and Eccentricity Faults for PM Synchronous Motors," *Industry Applications, IEEE Trans. on,* vol. 48, pp. 923-932, 2012.

[123] S. J. Underwood and I. Husain, "Online Parameter Estimation and Adaptive Control of Permanent-Magnet Synchronous Machines," *Industrial Electronics, IEEE Transactions on,* vol. 57, pp. 2435-2443, 2010.

[124] S. Ichikawa, M. Tomita, S. Doki, and S. Okuma, "Sensorless control of permanent-magnet synchronous motors using online parameter identification based on system

identification theory," *Industrial Electronics, IEEE Transactions on,* vol. 53, pp. 363-372, 2006.

[125] C. Jong-Woo and S. Seung-Ki, "A new compensation strategy reducing voltage/current distortion in PWM VSI systems operating with low output voltages," *Industry Applications, IEEE Transactions on,* vol. 31, pp. 1001-1008, 1995.

[126] D. Reigosa, P. Garcia, F. Briz, D. Raca, and R. D. Lorenz, "Modeling and Adaptive Decoupling of Transient Resistance and Temperature Effects in Carrier-Based Sensorless Control of PM Synchronous Machines," in *Proc. of Industry Applications Society Annual Meeting, 2008. IAS '08. IEEE*, pp. 1-8.

[127] L. Jae Suk, C. Chan-Hee, S. Jul-Ki, and R. D. Lorenz, "Deadbeat-Direct Torque and Flux Control of Interior Permanent Magnet Synchronous Machines With Discrete Time Stator Current and Stator Flux Linkage Observer," *Industry Applications, IEEE Transactions on,* vol. 47, pp. 1749-1758, 2011.

[128] M. H. Bierhoff and F. W. Fuchs, "Semiconductor losses in voltage source and current source IGBT converters based on analytical derivation," in *Proc. of Power Electronics Specialists Conference, 2004. PESC 04. 2004 IEEE 35th Annual*, pp. 2836-2842 Vol.4.

[129] Powerex, "App. Note of IGBT/Intelligent Power Modules," *in http://www.pwrx.com/.*

[130] A. M. Hava, R. J. Kerkman, and T. A. Lipo, "Simple analytical and graphical methods for carrier-based PWM-VSI drives," *Power Electronics, IEEE Transactions on,* vol. 14, pp. 49-61, 1999.

[131] N. Limsuwan, Y. Shibukawa, D. D. Reigosa, and R. D. Lorenz, "Novel Design of Flux-Intensifying Interior Permanent Magnet Synchronous Machine Suitable for Self-Sensing Control at Very Low Speed and Power Conversion," *Industry Applications, IEEE Transactions on,* vol. 47, pp. 2004-2012, 2011.

[132] W. Xu and R. D. Lorenz, "Reduced Parameter Sensitivity Stator Flux Linkage Observer in Deadbeat-Direct Torque and Flux Control for IPMSMs," in *Proc. of Int'l Electric Machines and Drives Conf (IEMDC), May 12-15, 2013, Chicago, IL.*

[133] D. D. Reigosa, F. Briz, P. Garcia, J. M. Guerrero, and M. W. Degner, "Magnet Temperature Estimation in Surface PM Machines Using High-Frequency Signal Injection," *Industry Applications, IEEE Trans. on,* vol. 46, pp. 1468-1475, 2010.

[134] C. Y. Yu, J. Tamura, D. D. Reigosa, and R. D. Lorenz, "Position Self-Sensing Evaluation of a FI-IPMSM Based on High-Frequency Signal Injection Methods," *Industry Applications, IEEE Trans. on,* vol. 49, pp. 880-888, 2013.

[135] "Retrieved from http://en.wikipedia.org/wiki/Neodymium_magnet."